



WILSON KNOX LIBRARY
200 L FOSTER AVENUE SCHOOL
MANTERLY, CALIFORNIA 95943-5002

NAVAL POSTGRADUATE SCHOOL

Monterey, California



DISSERTATION

THESIS
W5581

WIND AND WAVE FORCING
OF LONGSHORE CURRENTS
ACROSS A BARRED BEACH

by

Dennis James Whitford

June 1988

Thesis Advisor

E.B. Thornton

Approved for public release; distribution is unlimited.

T239318

REPORT DOCUMENTATION PAGE

Report Security Classification Unclassified		1b Restrictive Markings	
Security Classification Authority		3 Distribution Availability of Report	
Declassification Downgrading Schedule		Approved for public release; distribution is unlimited.	
Performing Organization Report Number(s)		5 Monitoring Organization Report Number(s)	
Name of Performing Organization Naval Postgraduate School	6b Office Symbol (if applicable) 35	7a Name of Monitoring Organization Naval Postgraduate School	
Address (city, state, and ZIP code) Monterey, CA 93943-5000		7b Address (city, state, and ZIP code) Monterey, CA 93943-5000	
Name of Funding Sponsoring Organization	8b Office Symbol (if applicable)	9 Procurement Instrument Identification Number	
Address (city, state, and ZIP code)		10 Source of Funding Numbers	
		Program Element No	Project No
		Task No	Work Unit Accession No

Title (include security classification) **WIND AND WAVE FORCING OF LONGSHORE CURRENTS ACROSS A BARRED BEACH**

Personal Author(s) Dennis James Whitford			
Type of Report Doctoral Dissertation	13b Time Covered From To	14 Date of Report (year, month, day) June 1988	15 Page Count 226

Supplementary Notation The views expressed in this thesis are those of the author and do not reflect the official policy or position of the Department of Defense or the U.S. Government.

Cosati Codes			18 Subject Terms (continue on reverse if necessary and identify by block number) longshore current, wind stress, nearshore, radiation stress, surf zone, modeling, wave forcing
Field	Group	Subgroup	

Abstract (continue on reverse if necessary and identify by block number)
 Previous investigations of longshore currents have included various simplifying assumptions and restrictions including a planar beach, a steady and depth uniform flow, spatially-invariant bed shear stress and turbulent momentum exchange, and the exclusion of surface wind stress. These assumptions are quantitatively investigated by calculating the relative importance of each term in the longshore momentum balance with an emphasis on the relative importance of wind forcing across the barred nearshore. Wind and wave forcing of longshore currents across a barred beach are examined using both a numerical model and field measurements. A local momentum balance was measured at various locations across the surf zone during the SUPERDUCK experiment held at the U.S. Army Corps of Engineers, CERC Field Research Facility, Duck, N.C., U.S.A. in October 1986. A moveable sled was instrumented with pressure, current, and wind sensors to measure the various terms in the longshore momentum equation. Stability-dependent atmospheric drag coefficients for the surf zone are determined from wind stress measurements acquired just beyond the surf zone and wind speed measurements acquired from an anemometer atop the 9 m sled mast. Breaking waves were visually identified and electronically marked on the data tapes. Mean current velocities at three levels were measured across the barred surf zone to examine the effects of a bar on the vertical structure of the flow. A modified longshore current model is used to study the effects of barred topography. The predicted longshore current profiles are compared with field data and bed shear stress coefficients are determined from model-fitting. Significant spatial variability of longshore current [$O(1.0 \text{ ms}^{-1})$] is observed across the bar with depth uniform longshore flow. Wind force is found to be a first-order term along with wave force under certain wind and wave conditions. Spatially-dependent bed shear stress coefficients relative to the bar are determined from a local momentum balance. Mean bed shear stress coefficients were 0.004 ± 0.0010 , 0.002 ± 0.0006 , and 0.001 ± 0.0003 for offshore the bar, on top and immediately before the bar, and in the trough. Mean bed shear stress coefficients determined from model-fitting and from the momentum balance are in excellent agreement. Longshore current velocities are modeled within $\pm 20\%$ of observed velocities across the barred beach at SUPERDUCK with a mean least square error of 7-15%.

Distribution Availability of Abstract Unclassified unlimited <input type="checkbox"/> same as report <input type="checkbox"/> DTIC users		21 Abstract Security Classification Unclassified	
22a Name of Responsible Individual B. Thornton		22b Telephone (include Area code) (408) 646-2847	22c Office Symbol 68Tm

Approved for public release; distribution is unlimited.

Wind and Wave Forcing
of Longshore Currents
Across a Barred Beach

by

Dennis James Whitford
Commander, United States Navy
B.S., United States Naval Academy, 1972
M.S., Naval Postgraduate School, 1979

Submitted in partial fulfillment of the
requirements for the degree of

DOCTOR OF PHILOSOPHY IN PHYSICAL OCEANOGRAPHY

from the

NAVAL POSTGRADUATE SCHOOL
June 1988

ABSTRACT

Previous investigations of longshore currents have included various simplifying assumptions and restrictions including a planar beach, a steady and depth uniform flow, spatially-invariant bed shear stress and turbulent momentum exchange, and the exclusion of surface wind stress. These assumptions are quantitatively investigated by calculating the relative importance of each term in the longshore momentum balance with an emphasis on the relative importance of wind forcing across the barred nearshore. Wind and wave forcing of longshore currents across a barred beach are examined using both a numerical model and field measurements. A local momentum balance was measured at various locations across the surf zone during the SUPERDUCK experiment held at the U.S. Army Corps of Engineers, CERC Field Research Facility, Duck, N.C., U.S.A. in October 1986. A moveable sled was instrumented with pressure, current, and wind sensors to measure the various terms in the longshore momentum equation. Stability-dependent atmospheric drag coefficients for the surf zone are determined from wind stress measurements acquired just beyond the surf zone and wind speed measurements acquired from an anemometer atop the 9 m sled mast. Breaking waves were visually identified and electronically marked on the data tapes. Mean current velocities at three levels were measured across the barred surf zone to examine the effects of a bar on the vertical structure of the flow. A modified longshore current model is used to study the effects of barred topography. The predicted longshore current profiles are compared with field data and bed shear stress coefficients are determined from model-fitting. Significant spatial variability of longshore current [$O(1.0 \text{ ms}^{-1})$] is observed across the bar with depth uniform longshore flow. Wind force is found to be a first-order term along with wave force under certain wind and wave conditions. Spatially-dependent bed shear stress coefficients relative to the bar are determined from a local momentum balance. Mean bed shear stress coefficients were 0.004 ± 0.0010 , 0.002 ± 0.0006 , and 0.001 ± 0.0003 for offshore the bar, on top and immediately before the bar, and in the trough. Mean bed shear stress coefficients determined from model-fitting and from the momentum balance are in excellent agreement. Longshore current velocities are modeled within $\pm 20\%$ of observed velocities across the barred beach at SUPERDUCK with a mean least square error of 7-15%.

11/25/11
115581
C.1

TABLE OF CONTENTS

I. INTRODUCTION	1
II. LITERATURE REVIEW	6
A. INTRODUCTION	6
B. RADIATION STRESS	6
C. SURFACE WIND STRESS	9
D. BOTTOM SHEAR STRESS	11
1. Momentum Balance	15
2. Model-fitting	17
3. Profile Method	17
E. TURBULENT MOMENTUM FLUX	18
F. TEMPORAL VARIABILITY	20
G. VERTICAL DISTRIBUTION OF MEAN LONGSHORE FLOW	20
H. BARRED BEACHES	22
III. WIND FORCING OF LONGSHORE CURRENTS FROM A FINITE-DEPTH SPECTRAL WAVE MODEL APPROACH	23
A. THE TMA SPECTRUM	23
B. NUMERICAL APPROACH	26
C. RESULTS AND DISCUSSION	28
IV. FIELD EXPERIMENT	36
A. INTRODUCTION	36
B. SITE DESCRIPTION	36
C. EQUIPMENT DESIGN AND OPERATION	38
V. PRELIMINARY DATA ANALYSIS	45
A. INITIAL DATA SCREENING	45
B. SLED INTER-ORIENTATION	46
C. BEACH ANGLE ORIENTATION	47
D. CURRENT METER ORIENTATION PRIOR TO A TRANSECT.	50

E.	MEAN CURRENT OBSERVATIONS	51
1.	Overview	51
2.	Discussion	56
3.	Stationarity and Homogeneity	56
VI.	SURFACE WIND STRESS (τ_y^x)	62
A.	INTRODUCTION	62
B.	DETERMINATION OF AN ATMOSPHERIC DRAG COEFFICIENT FOR THE SURF ZONE	65
C.	ADJUSTMENT OF C_d FOR THE SURF ZONE ENVIRONMENT	70
1.	Uniqueness of surf zone air-sea interaction	70
a.	Shoaling effect	70
b.	Refraction	70
c.	Wave Breaking	70
2.	Surf Zone C_d Adjustment Formulation and Results	71
VII.	LONGSHORE MOMENTUM BALANCE	74
A.	TEMPORAL, OR ACCELERATION TERM ($\partial M_y / \partial t$)	74
B.	RADIATION STRESS GRADIENT ($\partial S_{yx}^T / \partial x$)	77
C.	SEA SURFACE ELEVATION (η)	80
D.	RESULTS OF THE MOMENTUM BALANCE	83
1.	Bed Shear Stress Coefficient	83
2.	Relative Contributions of the Longshore Momentum Balance Terms ..	84
E.	ERROR ANALYSIS	90
1.	Incident Wave Angle Error	90
a.	Beach Angle Orientation Error	90
b.	Current Meter Orientation Error	94
c.	Current Meter Directional Gain Error	94
2.	Measurement Error	94
3.	Finite Differencing Error	99
4.	Combined Error	101
VIII.	LONGSHORE CURRENT MODEL	105
A.	INTRODUCTION	105

B. MODEL THEORY	105
1. Wave Height Transformation	105
2. Longshore Current	108
C. MODIFICATION OF MODEL BASED ON FIELD DATA	109
1. A Slope Dependent γ	109
2. Breaking Wave Weighting Function	110
D. MODEL RESULTS	115
1. Wave Height Transformation	115
2. Longshore Current Model Results	117
3. Bed Shear Stress Coefficients	124
IX. SUMMARY AND CONCLUSIONS	125
APPENDIX A. DATA ANALYSIS FIGURES FOR DAYS OTHER THAN OCTOBER 16, 1986	129
APPENDIX B. CURRENT VECTORS OVERLAYED ON BATHYMETRY ..	149
APPENDIX C. ATMOSPHERIC STABILITY DETERMINATION	157
APPENDIX D. SURFACE WEATHER MAPS	159
APPENDIX E. ANALYSIS PARAMETERS FOR ALL SLED DATA RUNS .	164
APPENDIX F. RADIATION STRESS, SEA SURFACE ELEVATION, SIG- NIFICANT WAVE ANGLE, AND CURRENT VELOCITY SPECTRA	169
APPENDIX G. MEAN CURRENT VELOCITIES AND TOTAL RADIATION STRESS FOR EACH SLED CURRENT METER AND RUN	192
REFERENCES	194
INITIAL DISTRIBUTION LIST	203

LIST OF TABLES

Table 1.	BED SHEAR STRESS COEFFICIENTS PROPOSED AND UTILIZED BY VARIOUS INVESTIGATORS	16
Table 2.	CASE PARAMETERS FOR WIND VERSUS WAVE FORCE COMPARISONS	28
Table 3.	RATIO OF WIND FORCE TO WAVE FORCE FOR A GENTLE BEACH SLOPE ($\tan \beta = 0.01$)	33
Table 4.	RATIO OF WIND FORCE TO WAVE FORCE FOR A STEEP BEACH SLOPE ($\tan \beta = 0.10$)	34
Table 5.	BATHYMETRY SELECTION AND BEACH ORIENTATION ANGLES.	49
Table 6.	INSTRUMENT ORIENTATION PARAMETERS	53
Table 7.	SUPERDUCK SYNOPTIC-SCALE METEOROLOGICAL DATA (OCTOBER 1986)	63
Table 8.	SUPERDUCK SURF ZONE WIDTH FOR SLED DEPLOYMENT DAYS	72
Table 9.	ATMOSPHERIC DRAG COEFFICIENTS ($C_{d10} \times 10^3$) FOR EACH SLED DATA RUN.	73
Table 10.	SUPERDUCK BED SHEAR STRESS COEFFICIENTS (OCTOBER 15-18, 1986)	85
Table 11.	RELATIVE CONTRIBUTIONS OF THE LONGSHORE MOMENTUM BALANCE TERMS FOR SUPERDUCK	87
Table 12.	RELATIVE IMPORTANCE OF MOMENTUM BALANCE TERMS FOR LOCATIONS RELATIVE TO THE BAR	88
Table 13.	MEAN BED SHEAR COEFFICIENTS DETERMINED FOR LOCATIONS RELATIVE TO THE BAR	89
Table 14.	MEASUREMENT ACCURACY	95
Table 15.	SLED CURRENT METER CALIBRATION	96
Table 16.	ERROR PROPAGATION ANALYSIS	99
Table 17.	FINITE DIFFERENCE RELATIVE ERRORS	102
Table 18.	FINITE DIFFERENCE RELATIVE ERRORS	103
Table 19.	COMBINED ERROR RELATIVE TO THE BAR ON THE BED	

SHEAR STRESS COEFFICIENT AS DETERMINED FROM A MO- MENTUM BALANCE	104
Table 20. MODEL-FITTING RESULTS FOR B , c_f AND N	124

LIST OF FIGURES

Figure 1.	Section and plan definition for the SUPERDUCK experiment	2
Figure 2.	Calculated dependence of C_{dn} on the 10 m height wind speed for five depths.	12
Figure 3.	Vector Relationship of \vec{u}_t due to presence of waves and currents.	14
Figure 4.	Kitaigorodskii et al. (1975) finite-depth spectral transformation function, $\Phi_K(\omega, h)$	25
Figure 5.	Comparison of wind and wave force for a gentle beach slope ($\tan \beta = 0.01$) with associated wave spectra.	29
Figure 6.	Comparison of wind and wave force for a steep beach slope ($\tan \beta = 0.10$) with associated wave spectra.	30
Figure 7.	Comparison of wind and wave force for increasing wind speed at constant wind direction ($\theta = 20^\circ$).	32
Figure 8.	Wind to wave force ratio versus beach slope for a typical mid-latitude cold frontal passage.	35
Figure 9.	SUPERDUCK field experiment site.	37
Figure 10.	SUPERDUCK field experiment instrument locations.	39
Figure 11.	Three-dimensional bathymetry example, 16 October 1986.	40
Figure 12.	Two-dimensional bathymetry example, 16 October 1986.	41
Figure 13.	Side and top view of the SUPERDUCK sled.	42
Figure 14.	Sled data run locations.	48
Figure 15.	Constraints on current meter rotation or gain correction for bi-directional spectra outside the surf zone.	52
Figure 16.	Mean current structure across the bar on 16 October 1986.	54
Figure 17.	Mean cross-shore U and longshore velocity V profiles versus normalized water depth for 15-18 October.	57
Figure 18.	Offshore S_{yx} spectra and S_{yx}^T from 'puv' gage 621 for 16 October 1986.	59
Figure 19.	H_{mo} ('x') and wave incidence angle ('o') versus time for 15 - 18 October 1986.	61
Figure 20.	Wind speed, wave height, atmospheric stability, and initial C_d data for October 15-16, 1986	67
Figure 21.	An empirically-derived stability-dependent drag coefficient obtained un-	

	der a sea-breeze condition	69
Figure 22.	Linear wave theory transfer function used to calculate $S_{yx}(f)$ from current velocity	78
Figure 23.	Finite differencing scheme for $\partial S_{yx}^T / \partial x$	81
Figure 24.	c_f and percent breaking wave (Q) values as a function of offshore distance (October 15-18, 1986)	91
Figure 25.	Sensitivity of $\partial S_{yx} / \partial x$ to beach angle orientation error for varying incident wave angles and depths and $\tan \beta = 0.03$.	93
Figure 26.	Periodic bore used to describe spilling breakers	107
Figure 27.	Ratio H_{rms}/h versus beach slope for various data sets.	111
Figure 28.	Example $p_h(t)$ and $\eta(t)$ time series with corresponding $G_\eta(f)$ spectra.	113
Figure 29.	Wave height and breaking wave height distributions (hatched area) normalized to offshore H_{rms} for 16 October.	114
Figure 30.	Breaking wave fraction (Q) versus the ratio $H_{rms}/\gamma h$.	116
Figure 31.	Model-generated H_{rms} and V compared with field observations versus distance for invariant c_f and B and including turbulent momentum exchange, 16 October.	118
Figure 32.	Model-generated V compared to field observations versus offshore distance for constant c_f no turbulent momentum exchange, 15-16 October.	120
Figure 33.	Example of a least square error solution surface for model-fitted longshore current for various c_f and N combinations.	122
Figure 34.	Scatter diagram of breaking wave periods and heights for 17	123
Figure 35.	Mean current structure on 11 October 1986.	130
Figure 36.	Mean current structure on 12 October 1986.	131
Figure 37.	Mean current structure on 15 October 1986.	132
Figure 38.	Mean current structure on 17 October 1986.	133
Figure 39.	Mean current structure on 18 October 1986.	134
Figure 40.	Mean current structure on 21 October 1986.	135
Figure 41.	Offshore S_{yx} spectra and S_{yx}^T from 'puv' gage 621 for 15 October 1986.	136
Figure 42.	Offshore S_{yx} spectra and S_{yx}^T from 'puv' gage 621 for 17 October 1986.	137
Figure 43.	Offshore S_{yx} spectra and S_{yx}^T from 'puv' gage 621 for 18 October 1986.	138
Figure 44.	Wind speed, wave height, atmospheric stability, and initial C_d data for October 11-12, 1986.	139
Figure 45.	Wind speed, wave height, atmospheric stability, and initial C_d data for	

	October 17-18, 1986.	140
Figure 46.	Wind speed, wave height, atmospheric stability, and initial C_d data for October 21, 1986.	141
Figure 47.	Wave height and breaking wave height distributions (hatched area) normalized to offshore H_{rms} for 15 October.	142
Figure 48.	Wave height and breaking wave height distributions (hatched area) normalized to offshore H_{rms} for 17 October.	143
Figure 49.	Wave height and breaking wave height distributions (hatched area) normalized to offshore H_{rms} for 18 October.	144
Figure 50.	Model-generated H_{rms} and V compared with field observations versus distance for invariant c_f and B and including turbulent momentum exchange, 15 October.	145
Figure 51.	Model-generated H_{rms} and V compared with field observations versus distance for invariant c_f and B and including turbulent momentum exchange, 17 October.	146
Figure 52.	Model-generated H_{rms} and V compared with field observations versus distance for invariant c_f and B and including turbulent momentum exchange, 18 October.	147
Figure 53.	Model-generated V compared to field observations versus offshore distance for constant c_f and no turbulent momentum exchange, 17-18 October.	148
Figure 54.	Sled and alongshore array mean current vectors for 11 October 1986 overlaid on bathymetry.	150
Figure 55.	Sled and alongshore array mean current vectors for 12 October 1986 overlaid on bathymetry.	151
Figure 56.	Sled and alongshore array mean current vectors for 15 October 1986 overlaid on bathymetry.	152
Figure 57.	Sled and alongshore array mean current vectors for 16 October 1986 overlaid on bathymetry.	153
Figure 58.	Sled and alongshore array mean current vectors for 17 October 1986 overlaid on bathymetry.	154
Figure 59.	Sled and alongshore array mean current vectors for 18 October 1986 overlaid on bathymetry.	155
Figure 60.	Sled and alongshore array mean current vectors for 21 October 1986	

overlayed on bathymetry.	156
Figure 61. Surface weather analysis for 0700 E.S.T. 15 October 1986.	160
Figure 62. Surface weather analysis for 0700 E.S.T. 16 October 1986.	161
Figure 63. Surface weather analysis for 0700 E.S.T. 17 October 1986.	162
Figure 64. Surface weather analysis for 0700 E.S.T. 18 October 1986.	163
Figure 65. Radiation stress (S_{yx}), sea surface elevation (η), significant wave angle ($\hat{\alpha}$), and current velocity spectra for sled run 15-1.	170
Figure 66. Radiation stress (S_{yx}), sea surface elevation (η), significant wave angle ($\hat{\alpha}$), and current velocity spectra for sled run 15-2.	171
Figure 67. Radiation stress (S_{yx}), sea surface elevation (η), significant wave angle ($\hat{\alpha}$), and current velocity spectra for sled run 15-3.	172
Figure 68. Radiation stress (S_{yx}), sea surface elevation (η), significant wave angle ($\hat{\alpha}$), and current velocity spectra for sled run 15-4.	173
Figure 69. Radiation stress (S_{yx}), sea surface elevation (η), significant wave angle ($\hat{\alpha}$), and current velocity spectra for sled run 16-2.	174
Figure 70. Radiation stress (S_{yx}), sea surface elevation (η), significant wave angle ($\hat{\alpha}$), and current velocity spectra for sled run 16-3.	175
Figure 71. Radiation stress (S_{yx}), sea surface elevation (η), significant wave angle ($\hat{\alpha}$), and current velocity spectra for sled run 16-4.	176
Figure 72. Radiation stress (S_{yx}), sea surface elevation (η), significant wave angle ($\hat{\alpha}$), and current velocity spectra for sled run 16-5.	177
Figure 73. Radiation stress (S_{yx}), sea surface elevation (η), significant wave angle ($\hat{\alpha}$), and current velocity spectra for sled run 16-6.	178
Figure 74. Radiation stress (S_{yx}), sea surface elevation (η), significant wave angle ($\hat{\alpha}$), and current velocity spectra for sled run 17-1.	179
Figure 75. Radiation stress (S_{yx}), sea surface elevation (η), significant wave angle ($\hat{\alpha}$), and current velocity spectra for sled run 17-2.	180
Figure 76. Radiation stress (S_{yx}), sea surface elevation (η), significant wave angle ($\hat{\alpha}$), and current velocity spectra for sled run 17-3.	181
Figure 77. Radiation stress (S_{yx}), sea surface elevation (η), significant wave angle ($\hat{\alpha}$), and current velocity spectra for sled run 17-4.	182
Figure 78. Radiation stress (S_{yx}), sea surface elevation (η), significant wave angle ($\hat{\alpha}$), and current velocity spectra for sled run 17-5.	183
Figure 79. Radiation stress (S_{yx}), sea surface elevation (η), significant wave angle	

	($\hat{\alpha}$), and current velocity spectra for sled run 17-6.	184
Figure 80.	Radiation stress (S_{yx}), sea surface elevation (η), significant wave angle ($\hat{\alpha}$), and current velocity spectra for sled run 17-7.	185
Figure 81.	Radiation stress (S_{yx}), sea surface elevation (η), significant wave angle ($\hat{\alpha}$), and current velocity spectra for sled run 17-8.	186
Figure 82.	Radiation stress (S_{yx}), sea surface elevation (η), significant wave angle ($\hat{\alpha}$), and current velocity spectra for sled run 18-1.	187
Figure 83.	Radiation stress (S_{yx}), sea surface elevation (η), significant wave angle ($\hat{\alpha}$), and current velocity spectra for sled run 18-2.	188
Figure 84.	Radiation stress (S_{yx}), sea surface elevation (η), significant wave angle ($\hat{\alpha}$), and current velocity spectra for sled run 18-3.	189
Figure 85.	Radiation stress (S_{yx}), sea surface elevation (η), significant wave angle ($\hat{\alpha}$), and current velocity spectra for sled run 18-4.	190
Figure 86.	Radiation stress (S_{yx}), sea surface elevation (η), significant wave angle ($\hat{\alpha}$), and current velocity spectra for sled run 18-5.	191

LIST OF SYMBOLS AND ABBREVIATIONS

Symbols (Greek)

α	wave incident angle; Phillips constant
$\hat{\alpha}$	mean incident wave angle for narrow-banded waves
$\hat{\alpha}(f)$	significant wave incident angle
β	beach slope
γ	ratio of H_{rms} to h for saturated wave breaking conditions
γ_J	JONSWAP spectral peak enhancement factor
$\Delta\alpha_e$	beach angle orientation error
Δf	frequency resolution
$\langle \varepsilon_b \rangle$	ensemble-averaged dissipation due to wave breaking
$\langle \varepsilon_f \rangle$	ensemble-averaged dissipation due to friction
η	sea surface
θ	angle of rotation; wind direction
θ_c	combined angle used to coordinate transform current velocities determined at the sled location to the FRF coordinate system
κ	von Karman's constant (0.4)
ν	degrees of freedom; eddy viscosity coefficient
ρ	water density
ρ_a	atmospheric density
σ	standard deviation; peak spectral width
σ_a^2	variance of the variable a
τ	stress
τ_x^s	surface wind stress in the longshore direction
τ_y^b	bed or bottom shear stress in the longshore direction
ϕ_m	atmospheric stability function
Φ_K	finite-depth spectral transformation function
Ψ_h, Ψ_q	integral diabatic term for temperature and humidity, respectively
ω	radian frequency

Symbols (Roman)

a	wave amplitude
b	bed (or bottom) when used as a subscript
B	breaker coefficient
C_{ab}	Co-spectrum or real part of the cross-spectrum of quantities of a and b
C_{d10}	stability-dependent atmospheric drag coefficient for a height of 10 m above MSL
C_{dn10}	neutral, or stability-independent, atmospheric drag coefficient for a height of 10 m above MSL
c_f	dimensionless bed shear stress coefficient due to waves and current
C(f)	wave celerity as a function of frequency
C_g	wave group velocity
E	wave energy density
f	frequency
\bar{f}	mean wave frequency
f_m	peak spectral frequency
g	gravitational acceleration
G_a	spectral density function of the variable a
h	water depth measured from mean water level
H	wave height
H(f)	linear theory transfer function
H_{mo}	significant wave height (energy based); four times the standard deviation of sea surface elevation
H_{rms}	root-mean-square wave height
H_{sig}	significant wave height (statistically based); average height of highest one-third of waves for a specified time period
\hat{i}, \hat{j}	unit vectors in the x and y directions, respectively
J	joules
k	wave number
k_m	wave number for peak spectral frequency
L	Monin-Obukhov length
m	meters; number of ensembles used in ensemble averaging for spectral estimation

M	time-averaged depth-integrated mean momentum per unit area; includes steady (\bar{M}) and unsteady (M') components
M_y	longshore component of M
n	ratio of wave group speed to wave phase speed
N	dimensionless adjustable coefficient used in turbulent momentum flux theory
p	absolute pressure
p_{atm}	atmospheric pressure
$p(H)$	Rayleigh wave height probability density function
$p_b(H)$	breaking wave height distribution
p_h	pressure head (m)
q	specific humidity
Q	specific humidity; percentage of waves which are breaking
R	relative error due to finite difference space approximation
S_{yx}	longshore momentum flux (radiation stress) due to unsteady motion (i.e., waves and turbulence)
\tilde{S}_{yx}	longshore momentum flux due to waves
S_{yx}''	longshore momentum flux due to turbulence
S_{yx}^T	total S_{yx} integrated over frequency
t	time
T_a	air temperature
T_s	sea temperature measured at depth 0.6 m below MSL
T_v	virtual temperature
T_v^*	virtual temperature scaling parameter
T_d	dewpoint temperature
u, v, w	current velocities in the x, y, and z directions, respectively; includes mean (\bar{U}, \bar{V}) and fluctuating (u', v') components
u', v'	fluctuating flow velocities in the x, y directions, respectively; includes wave-induced (\tilde{u}, \tilde{v}) and turbulent (u'', v'') components
u_t	resultant vector sum of the mean longshore current velocity and the instantaneous wave orbital speed near the bottom in the longshore direction.
u_w	wave orbital speed
u_*, v_*	shear or friction velocities in the x and y directions associated with the averaged flow; may apply to the atmosphere or ocean.

V_x	coefficient of variation
W	wind speed
W(H)	breaking wave weighting function
x,y,z	axes of a right-handed Cartesian coordinate system with x increasing off-shore and z increasing upward
\bar{X}	arithmetic mean of variable X
x_b	surf zone width
z_m	depth of measurement
z_o	roughness height
z_q, z_T	humidity and temperature measurement heights, respectively
z_{0q}, z_{0T}	humidity and temperature roughness lengths, respectively

Abbreviations

c/m	current meter
cov	covariance
EM	electromagnetic
FFT	Fast Fourier Transform
FGAIN	front current meter gain calibration factor
FRF	Field Research Facility
FTWIST	front current meter rotation angle
KE	kinetic energy
MSL	mean sea level
MWL	mean water level
O	order of magnitude
Paro	Paroscientific pressure sensor
PCM	pulse code modulated
pdf	probability density function
rc	relative contribution
RGAIN	rear current meter gain calibration factor
RH	relative humidity
rms	root-mean-square
RTWIST	rear current meter rotation angle

STWIST side current meter rotation angle
SWL still water level
TOT total contribution

MKS units are used throughout this dissertation.

ACKNOWLEDGMENTS

I wish to express my sincere appreciation to my adviser, Prof. Edward B. Thornton, who became not only my mentor, but also my friend. His guidance and wealth of knowledge were given to me freely over the entire time of this endeavor. I also wish to express appreciation to my entire doctoral committee for their unwavering support for my work, and especially to Dr. C. S. Wu for our many helpful discussions of longshore current forcing.

I wish to thank the entire staff of the U.S. Army Corps of Engineers, CERC Field Research Facility in Duck, N.C., for not only hosting the SUPERDUCK experiment, but for providing assistance whenever and wherever it was requested. Special thanks to Bill Birkemeier and Carl Miller for their continued assistance after the experiment with data support. Appreciation is expressed for Don Martens for his technical support before and during the experiment. Support for this field investigation and data analysis was received from the Office of Naval Research under Contract NR 388-114.

Lastly, I wish to express my gratitude to my entire family, especially to my wife Dorothy, for supporting me over the years with an inexhaustible supply of love, encouragement, and understanding.

I. INTRODUCTION

Previous investigations of longshore currents have utilized many simplifying restrictions and assumptions. Major assumptions and restrictions include a *planar* beach, a steady and depth uniform longshore current, spatially-invariant bed shear stress and turbulent mixing, and the exclusion of surface wind stress. These assumptions are often too restrictive to permit realistic results. This research quantitatively investigates these assumptions by measuring the *relative* importance of each term in the longshore momentum balance equation (see equation (1)).

Modern theories for mean longshore currents are based on a longshore momentum balance (Bowen, 1969; Thornton, 1970; and Longuet-Higgins, 1970a, 1970b) with a radiation stress approach (Longuet-Higgins and Stewart, 1964). For a plane-parallel beach, the complete longshore momentum equation is:

$$\frac{\partial M_y}{\partial t} + \frac{\partial \tilde{S}_{yx}}{\partial x} = -\tau_y^b + \tau_y^\eta - \frac{\partial S''_{yx}}{\partial x} \quad (1)$$

term: 1 2 3 4 5

where a right-handed Cartesian system is adopted with x increasing offshore (see Figure 1), and

- term 1 = temporal change of the time-averaged depth-integrated mean momentum per unit area in the longshore direction due to both steady (\overline{M}_y) and unsteady flow (M_y'),
- term 2 = cross-shore gradient of the wave-induced longshore momentum flux (also called the wave-induced radiation stress gradient),
- term 3 = bottom shear stress in the longshore direction,
- term 4 = surface wind stress in the longshore direction, and
- term 5 = cross-shore gradient of the longshore momentum flux due to turbulence.

Most investigators (Longuet-Higgins, 1970a; Jonsson et al., 1974; Kraus and Sasaki, 1979; Thornton and Guza, 1986; Losada et al., 1987; Baum and Basco, 1987; among others) apply the previously mentioned assumptions and restrictions and then reduce the

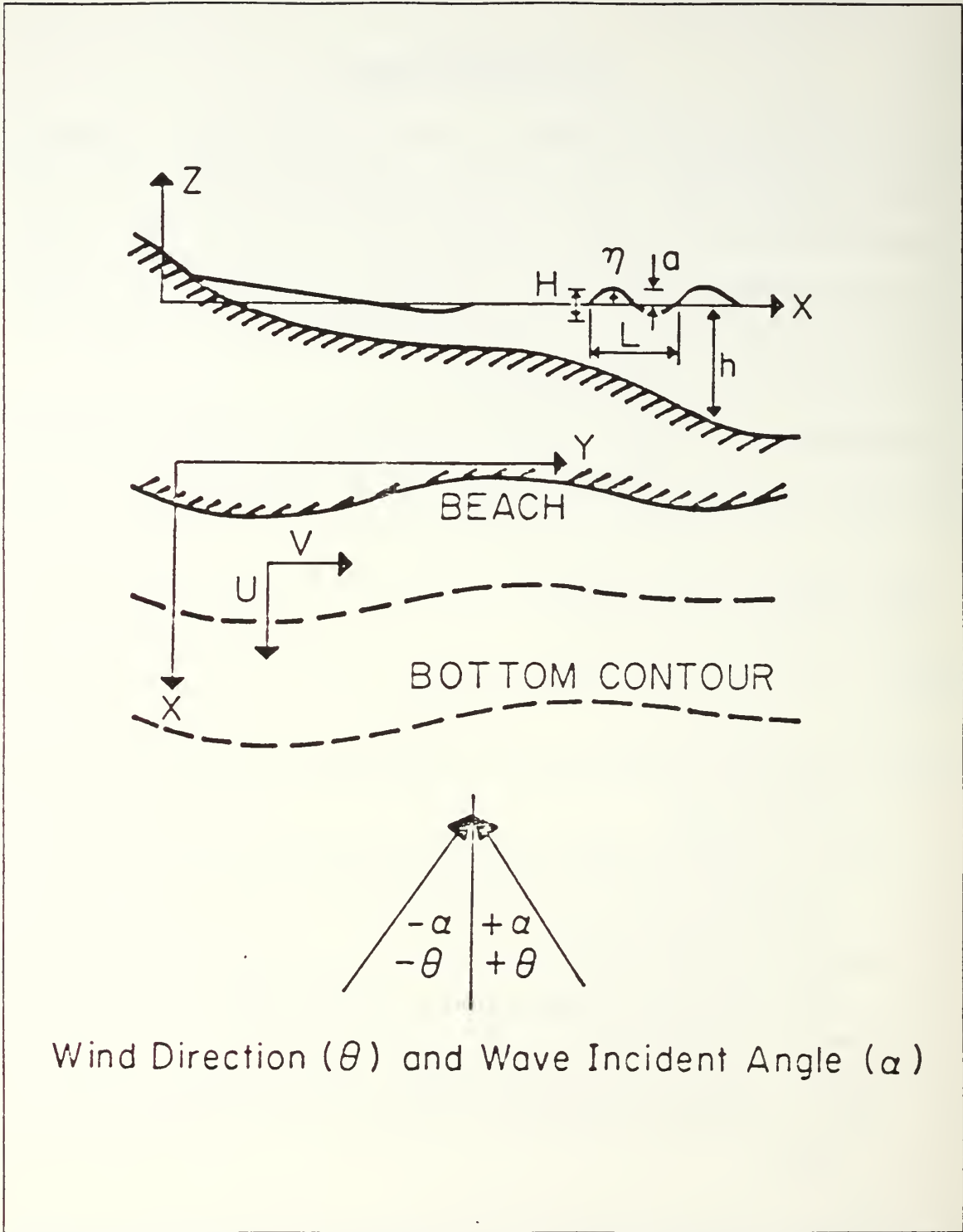


Figure 1. Section and plan definition for the SUPERDUCK experiment (modified from Birkemeier and Dalrymple, 1975).

equation for longshore momentum to a simplified balance between the wave-induced radiation stress gradient, the bottom shear stress, and the turbulence-induced radiation stress gradient. The most restrictive of these assumptions is that of a planar beach, since barred beaches are more common than planar beaches (Wright et al., 1986). Temporal variability of longshore currents, often exceeding $\pm 100\%$ of the mean flow, have been measured in the field (Dette and Fuhrboter, 1974; Wood and Meadows, 1975; Meadows, 1976). The depiction of spatially-invariant bed shear stress and turbulent mixing across the dynamic surf zone, especially over a barred beach, may be unrealistic. Additionally, recent investigations addressing combined currents and waves indicate that the bed shear stress coefficient, which is directly proportional to bed shear stress itself, may be 1.5 to 3.5 times larger in magnitude (Grant et al., 1984) than the invariant values universally used by longshore current investigators.

Longshore current forcing is studied utilizing the data sets acquired during the SUPERDUCK experiment. This experiment was held at the U.S. Army Corps of Engineers, Waterways Experiment Station's Coastal Engineering Research Center (CERC), Field Research Facility (FRF) in Duck, NC in September and October 1986. A unique instrumentation system designed specifically for this experiment was utilized to measure a local momentum balance at various locations across the surf zone of this single-barred beach under various wave, current, and wind conditions. Instruments were mounted on a mobile sled to measure the various terms in the momentum balance of equation (1). Two triangular, differential pressure sensor slope arrays were spaced approximately 2 m apart. Coupled with an absolute pressure reference, the slope arrays can be used to measure the gradient of the wave-induced momentum flux. Marsh-McBirney electromagnetic (EM) current meters located at the centroid of the slope arrays can be used to determine both mean momentum as well as the total, or combined, momentum flux due to the wave-induced and turbulent components. The difference between the current meter determination of the total momentum flux (S_{yx}) and the slope array determination of the wave-induced momentum flux (\tilde{S}_{yx}) yields a measure of the depth-integrated Reynolds stress, or turbulent component of the momentum flux. The surface stress can be inferred from the wind velocity measured using a wind anemometer mounted atop the 9 m sled mast.

Three methods for calculating the bed shear stress coefficient are attempted -- measuring the momentum balance, model-fitting to field data, and the mean profile method. By operating in areas where a plane-parallel beach assumption is valid and by

precisely orienting dynamic measurements perpendicular to the local bottom contours, all the terms contributing to the longshore momentum can be measured. Having measured all the terms in the balance, the unspecified bed shear stress coefficient is then determined. Theoretical mean longshore current distributions generated by a numerical model are compared with field-measured longshore current speeds. The bed shear stress coefficients in the numerical model are then adjusted until the modeled and observed current distributions coincide in a least square sense. Preliminary indications from an on-going surf zone investigation suggest that the mean longshore velocity profile in the vertical appears to be logarithmic (personal communication, R. T. Guza, 1987). Hence, the bed shear stress coefficient might also be determined by the profile method of boundary layer physics. However, logarithmic profiles were not found in the SUPERDUCK data.

The sled was designed to make transects anywhere along the shoreline and as far offshore as the mast height would allow. Sled mobility was provided by U.S. Army Corps of Engineers equipment. The sled was tethered by a 300 m chain to a heavy-duty forklift on the beach. The sled was towed offshore by the Coastal Research Amphibious Buggy (CRAB) to the desired location beyond the surf zone and then detached from the sled. The forklift dragged the sled onshore along its pre-planned transect of data collection locations.

A previous difficulty with directly measuring momentum flux in the field was the precise orientation required of the instrumentation (Thornton and Guza, 1981). In the SUPERDUCK experiment, precise orientation of the sled (and attached slope arrays) was achieved to within 0.5° using laser ranging to triangulate on two prisms mounted 2.4 m apart on a mast spreader above the sled. A daily calibration of current meter orientation was accomplished by initially positioning the sled *beyond* the surf zone for the first data run of a surf zone transect. Based on conservation of radiation stress outside the surf zone, the current meters were numerically oriented so that their respective radiation stress values were identical. This orientation was then held constant for the remaining sled locations along that transect. This calibration procedure is essential to obtaining realistic physical results from the data and is a distinguishing feature of the research.

A primary improvement between the SUPERDUCK experiment and previous large-scale nearshore experiments was the extensive bathymetric data. Daily

bathymetric profiles of the entire experiment area were accurately measured with the CRAB and the laser ranging system.

Pertinent literature is reviewed in the following chapter. A numerical model is developed in Chapter III to compare wind and wave forces for various wind speeds and directions. The SUPERDUCK field experiment is described in Chapter IV. Data analysis of the field experiment is extensive and therefore is addressed in separate chapters. Preliminary data analysis is described in Chapter V and includes an overview of the observed mean current structure over the bar. Since surface wind stress is of major importance to this research and few wind stress studies have been conducted in the surf zone, Chapter VI is entirely devoted to the parameterization of the surf zone surface wind stress for this field experiment. Calculation of the longshore momentum balance, determination of the relative contributions of each term in the balance, and calculation of spatially-variable bed shear stress coefficients are addressed in Chapter VII. A longshore current model for planar beaches is modified to account for barred topography and is applied to the data. The model's longshore current results are compared to observations and bed shear stress coefficients are determined by model-fitting in Chapter VIII. Summary and conclusions are presented in Chapter IX. Because of the large quantity of data presented graphically for each day of data analysis, only a single typical day (October 16) is illustrated within the text. Data analysis figures for other days are referenced in the text by figure number but are collectively grouped in Appendix A.

The data obtained from this field experiment represents the first quantitative data set, including directional wave, surface wind stress, bathymetry, and breaking wave measurements, for the study of longshore current over barred beaches. In most previous studies, wind forcing of longshore currents has not been considered due to the absence of quantitative data. This research quantitatively determines the role of wind forcing in driving longshore currents from both field measurements and a simple numerical model. Wind forcing, as well as a variable bed shear stress coefficient, can represent measurable and reasonably significant terms in the momentum balance equation, and therefore must be taken into account in any quantification of longshore currents.

II. LITERATURE REVIEW

A. INTRODUCTION

One of the earliest works on coastal hydrodynamics and processes was that of Johnson (1919). He qualitatively discussed wave set-up, longshore currents, and rip currents (undertow) as hydraulic currents due to waves. He utilized incident wave angle as his criterion for rip currents (waves approaching perpendicular to shore) and for longshore currents (waves approaching oblique to shore).

In World War II, amphibious landing craft had difficulty landing their troops in the presence of a longshore current. The current often represented a greater hazard than the breakers themselves by causing the craft to broach inside the breaker zone. The U.S. Navy's concern for this effect prompted Putnam et al. (1949) to conduct one of the first applied research studies on longshore currents.

Since that time, various theories have been postulated to account for the basic physics of longshore currents and their predicted velocity distribution across the surf zone. These theories include conservation of energy, conservation of mass, empirical formulation, and conservation of momentum .

B. RADIATION STRESS

Modern longshore current theory is based on conservation of momentum. One of Putnam et al.'s (1949) approaches was the application of conservation of momentum. The momentum flux of an obliquely incident wave was averaged over a wave period to give a mean momentum flux entering the surf zone. The longshore component of the change (due to wave breaking) in this momentum flux provided a driving force for longshore currents. They assumed a steady-state longshore current, and therefore the driving force was balanced by a bottom frictional force.

The momentum flux approach was formalized and the physics clarified when the concept of *radiation stress* was introduced. Longuet-Higgins and Stewart (1964) defined radiation stress as the "excess flow of momentum due to the presence of the waves." Elaborations on the concept of radiation stress are contained in Longuet-Higgins and Stewart (1960, 1961, 1962, 1963, 1964), Bowen (1969), Longuet-Higgins (1970a, 1970b, 1972a, 1972b), and Thornton (1970).

Theory was further formalized with the derivation of time-averaged and depth-integrated conservation of mass and conservation of momentum which separates the

mean and fluctuating momentum contributions (Phillips, 1977; Mei, 1983). This approach has been used extensively in the study of wave set-up and set-down, horizontal longshore current profiles, rip currents, and surf beat generation. This approach forms the foundation of modern longshore current theory, as well as the foundation for the momentum balance of equation (1) on which this dissertation is based.

When there is an oblique wave approach to the shoreline, the longshore component of radiation stress (or longshore momentum flux due to unsteady motion) is given by (Longuet-Higgins, 1970a):

$$S_{yx} = \overline{\int_{-h}^{\eta} \rho u' v' dz} \quad (2)$$

where η = the sea surface.

h = water depth as measured from the still water line (SWL).

ρ = water density,

u', v' = fluctuating (x, y) components of the flow velocity, and the overbar denotes a time-averaging operator.

The basic concept is that the longshore current velocity is related to the change in incoming wave momentum, which in turn relates to the radiation stress. This change of momentum flux in the cross-shore direction is proportional to the rate of wave energy dissipation, where dissipation is due primarily to surface breaking but can include bottom, and internal (turbulent) dissipation. By using linear wave theory, radiation stress for monochromatic waves can be related to the incident wave angle (α) at the measurement location by:

$$S_{yx} = E n \sin \alpha \cos \alpha \quad (3)$$

where E is total wave energy density, α is the wave incident angle, or angle between the wave crest and a line parallel to the shoreline, and n is the ratio of wave group velocity to wave phase velocity expressed in terms of wave number (k) as:

$$n = \frac{1}{2} \left(1 + \frac{2kh}{\sinh(2kh)} \right) \quad (4)$$

Radiation stress has also been applied to random waves (Collins, 1972; Battjes, 1972a; Thornton and Guza, 1986) and non-linear wave theory (James, 1974a, 1974b) to solve for the longshore current.

The conservation laws of mass, horizontal momentum flux, and radiation stress by Phillips (1977) and Mei (1983) are both widely applied and similar. Both develop the equations for mean water motion by integrating over depth and averaging over a wave period. They differ in their approach to the mean flow due to unsteady motion (i.e. waves). Separating the mean and fluctuating horizontal velocity components (u_i) as:

$$u_i = U_i + \tilde{u}_i \quad i = 1, 2, \quad (5)$$

Mei(1983) defines the mean flow as:

$$U_i(x,y,t) = \frac{1}{\bar{\eta} + h} \overline{\int_{-h}^{\eta} u_i dz} \quad i = 1, 2 \quad (6)$$

and

$$\overline{\int_{-h}^{\eta} \tilde{u}_i dz} = 0 \quad i = 1, 2 \quad (7)$$

Thus he incorporates the mean flow due to unsteady motion in the mean velocity term, U_i , resulting in a mean momentum per unit area defined as:

$$M_i = \overline{M}_i = \rho U_i(\bar{\eta} + h) \quad (8)$$

Phillips (1977) utilizes equation (5) and (6), however he does not include the mean flow due to unsteady motion in the term U_i . He evaluates the time-averaged depth-integrated current flow by partitioning the integration of \tilde{u} (equation 7) into two separate regions:

$$\overline{\int_{-h}^{\eta} \tilde{u}_i dz} = \overline{\int_{-h}^0 \tilde{u}_i dz} + \overline{\int_0^{\eta} \tilde{u}_i dz} \quad (9)$$

where the first term on the right-hand side is zero by definition. This results in a mean momentum per unit area of

$$M_i = \rho U_i (\bar{\eta} + h) + \rho \overline{\int_0^{\eta} \tilde{u}_i dz} \quad i = 1, 2 \quad (10)$$

Phillips approach is adopted for this research.

Since the momentum balance of equation (1) represents the basis for this research, each remaining term -- surface wind stress, bottom shear stress, turbulent momentum flux, and temporal variability -- will now be examined.

C. SURFACE WIND STRESS

Surface wind stress is a shear stress imparted to the water column when the wind flows across the water surface. For simplicity, surface wind stress has been historically neglected as a forcing function for longshore currents. Although no physically-based model has specifically evaluated the wind stress contribution to longshore currents, there is empirical evidence suggesting wind stress can be important, and therefore should be included as a driving force for longshore currents. Nummedal and Finley (1978) used a stepwise multiple regression procedure utilizing surf zone environmental parameters to explain the variability of longshore current velocities. Although this procedure was empirical and not theoretical, the longshore current component of the wind velocity was found to account for more of the observed current variance than any single parameter, or combination of parameters, descriptive of the breakers.

Fox and Davis (1973) were able to relate longshore currents with barometric pressure at Lake Michigan. Although wind is certainly related to barometric pressure, they did not expand their work to directly deal with wind. Komar (1976) mentioned that winds blowing in the longshore direction may contribute to the observed flow.

Birkemeier and Dalrymple (1975) are one of the few nearshore modelers who did incorporate a wind forcing term (albeit, an underweighted term) in their longshore current model. Notwithstanding the different spatial scales involved, it is noted that lake (e.g., Sheng et al., 1978) and offshore modelers do consider wind stress whereas nearshore modelers do not. Nearshore modelers either assume that wave stress dominates over surface wind stress or that no wind is present.

Hubertz (1986) calculated the spectra of the mean longshore wind component and mean longshore current for a four-month period at the FRF in Duck, N.C. Longshore current spectral peaks were present at periods of 4.6 days, 23.8 hours, and 12.5 hours. Longshore wind component spectral peaks were present at 5.9 days and 24.4 hours. He

related the two longest period current peaks to wind forcing by synoptic weather systems and by sea breeze conditions, respectively. The 12.5 hours peak was attributed to tides.

There are several methods for calculating surface wind stress on the water surface. These methods are:

- the direct method (also called the covariance or eddy correlation method),
- the profile method,
- the dissipation method, and
- the drag coefficient method (also called the bulk aerodynamic method).

Each method has its own inherent advantages, disadvantages, and accuracy. The drag coefficient method was selected for this research based on equipment availability, the rough environment and platform involved (surf zone measurements by a mobile sled), and the availability of wind stress measurements acquired by other field investigators at the SUPERDUCK experiment.

The drag coefficient method formulation for surface wind stress (Taylor, 1916) in the longshore direction is:

$$\tau_y^{\eta} = \rho_a C_d |W| W_y \quad (11)$$

where τ_y^{η} = time-averaged surface wind stress vector in the longshore (y) direction (hereafter referred to as surface wind stress),

ρ_a = atmospheric density,

C_d = an atmospheric drag coefficient (generally of $O(10^{-3})$ for a height of 10 m above the water surface) for the specific height above the water surface at which W is measured,

W = the total wind speed, and

\bar{W}_y = the longshore component of the wind velocity.

The absolute value is used in equation (11) to retain directionality.

A large quantity of research has been directed at determining values for C_d for land and the open ocean. Garratt (1977) provides an excellent review for investigations of C_d for land and the open ocean prior to 1977. More recent investigations include Wu (1980, 1982), Safaie (1984), Geernaert and Katsaros (1986), Geernaert et al. (1986, 1987a, 1987b), and Hsu (1986a, 1986b, 1987). Unfortunately, few investigations have dealt with determining C_d near the land-sea interface and in the surf zone. C_d magnitudes

of $O(1.7 \times 10^{-3}$ to $2.4 \times 10^{-3})$ were determined for nearly calm conditions outside the surf zone of a Chukchi Sea barrier island (Walters, 1975) and C_d magnitudes of $O(2.0 \times 10^{-3}$ to $7.0 \times 10^{-3})$ for the upper swash zone of a Florida beach (Hsu, 1970). Walter's (1975) investigation was conducted under adiabatic and onshore wind conditions, whereas Hsu's (1970) investigation included adiabatic as well as non-adiabatic conditions with onshore wind conditions.

Hsu (1973) determined surf zone wind stress values for onshore winds of 0.5 to 8.5 ms^{-1} under adiabatic conditions for a two-week period at Santa Rosa Island, FL. C_d magnitudes of $O(1.0 \times 10^{-2}$ to $1.5 \times 10^{-3})$ are obtained upon conversion of his surface wind stress values. No breaker wave height values were indicated; however, it is assumed that they were small due to the experiment's location (northwest Florida coast), month (June), wind speeds, and a photograph accompanying the published results.

Vugts and Cannemeijer (1981) calculated C_d for non-adiabatic and onshore wind conditions from field measurements at a Danish beach. They instrumented two 20 m masts with multi-level cup anemometers and temperature sensors and placed one at the high-tide line and one directly inland at a distance of 127 m. They concluded from approximately 100 half-hour profiles that the drag coefficient during unstable conditions over the surf zone is the same as over the ocean. They calculated C_d magnitudes of $O(1.3 \times 10^{-3}$ to $1.5 \times 10^{-3})$ for wind speeds at 10 m height from 3-10 ms^{-1} .

Geernaert et al. (1987) measured wind stress using a sonic anemometer from a research platform in the North Sea. They found an empirical relation between the neutral drag coefficient (C_{dn}) and the ratio c_o/u_* , where c_o is the dominant long wave phase speed and u_* is the surface wind friction velocity. They applied this relationship to other data sets taken in varying water depths. They found increased C_{dn} values for shallower depths (Figure 2). As wind speed increased to 25 ms^{-1} , the C_{dn} value for 10 m depth was increased by a factor of 2 (to $O(3.0 \times 10^{-3})$) over that for deep water.

D. BOTTOM SHEAR STRESS

Putnam and Johnson (1949) conducted one of the earliest investigations of nearshore bottom stress or bottom friction. They assumed sinusoidal oscillatory bottom motion, an invariant friction coefficient, negligible perpendicular flow at the bottom due to percolation, a planar bottom slope, and a constant water density. Based on their investigations, bottom shear stress (τ^b) may be represented by:

$$\vec{\tau}^b = \rho c_f |u_t| \vec{u}_t \quad (12)$$

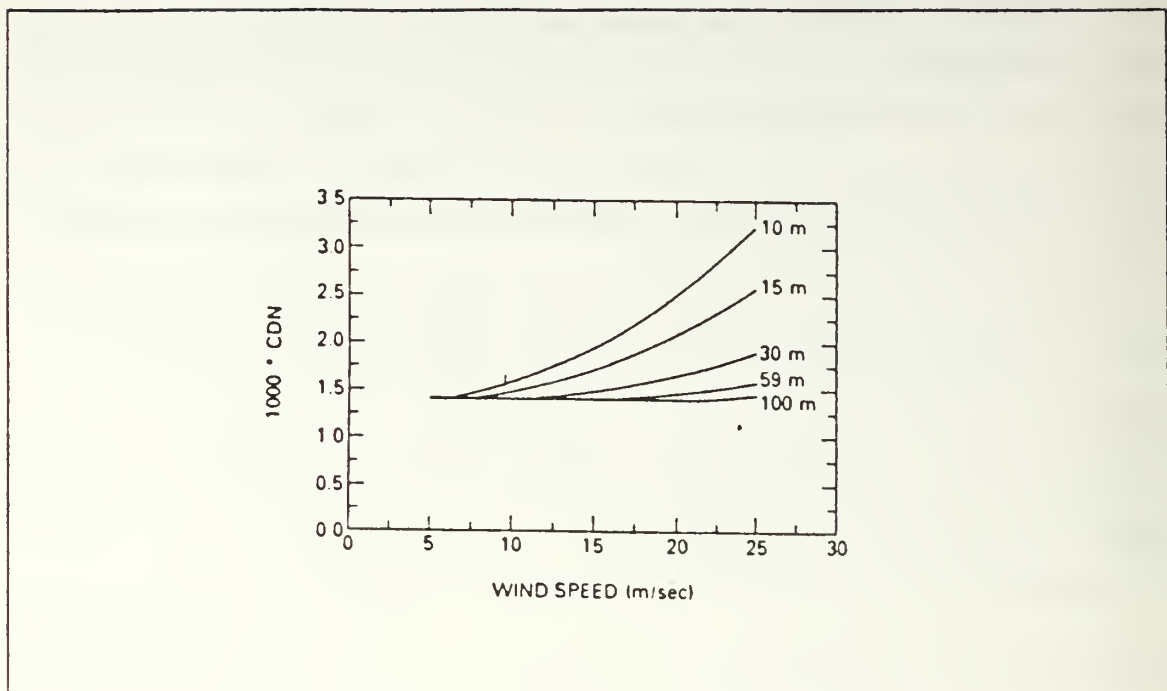


Figure 2. Calculated dependence of C_{dn} on the 10 m height wind speed for five depths (from Geerneart et al., 1987b).

where c_f = the dimensionless bed shear stress coefficient due to waves and currents and generally of $O(10^{-2})$, and

u_t = resultant vector sum of the mean longshore current velocity (V) and the instantaneous wave orbital speed near the bottom (see Figure 3).

As with wind stress, the absolute value is used in equation (12) to retain directionality. This equation has essentially formed the basis for modern bottom friction studies. In general, later investigators have worked toward its modification as well as solving for empirical values for c_f .

One can decompose u and v into a steady or mean velocity (U, V) and an unsteady or fluctuating velocity (u', v'). The unsteady velocity may be further separated into wave-induced (\tilde{u}, \tilde{v}) and turbulence-induced (u'', v'') components (Mei, 1983):

$$u = U + u' = U + \tilde{u} + u'' \quad (13)$$

$$v = V + v' = V + \tilde{v} + v'' \quad (14)$$

Incorporating the above decomposition, the bottom shear stress is represented as a vector oscillating in both direction and magnitude due to the interaction of a quasi-steady current with superimposed wave motion. From conservation of mass flux and the assumption of straight-and-parallel bathymetric contours, the mean cross-shore current velocity (U) is assumed zero. u_t is then expressed as:

$$\vec{u}_t = u_x \hat{i} + (V + u_y) \hat{j} = u \hat{i} + v \hat{j} = u + v \quad (15)$$

where $u_x = u_w \cos \alpha$,
 $u_y = u_w \sin \alpha$,
 u_w = wave orbital speed just above the bottom and immediately outside the bottom boundary layer, and
 \hat{i} , & \hat{j} unit vectors in the x and y directions, respectively.

Bottom shear stress (τ^b) can be written as:

$$\vec{\tau}^b = \tau_x^b \hat{i} + \tau_y^b \hat{j} \quad (16)$$

and from equations (12) and (15):

$$\vec{\tau}^b = \rho c_f |u_t| u + \rho c_f |u_t| v \quad (17)$$

The longshore component of time-averaged bottom shear stress can then be written as:

$$\tau_y^b = \overline{\rho c_f |u_t| v} = \overline{\rho c_f (u^2 + v^2)^{\frac{1}{2}} v} \quad (18)$$

The time-averaging procedure must be performed after evaluating the velocity components.

The bed shear stress coefficient is a function of bottom roughness and flow intensity near the bed. Bottom roughness is a function of both sand characteristics and bed form, where density and grain size define sand characteristics and bed form is described by the existence of ripples, which are in turn, a function of the flow field. Hence, the bed shear stress coefficient, bottom roughness, and flow intensity are all interrelated.

Often in geophysical research, laboratory results complement field measurements and assist in building a particular data base as well as increasing our knowledge of the phenomena being studied. Unfortunately, very few of the large number of laboratory studies of c_f are appropriate for extrapolation to the field. The flow field in nature will

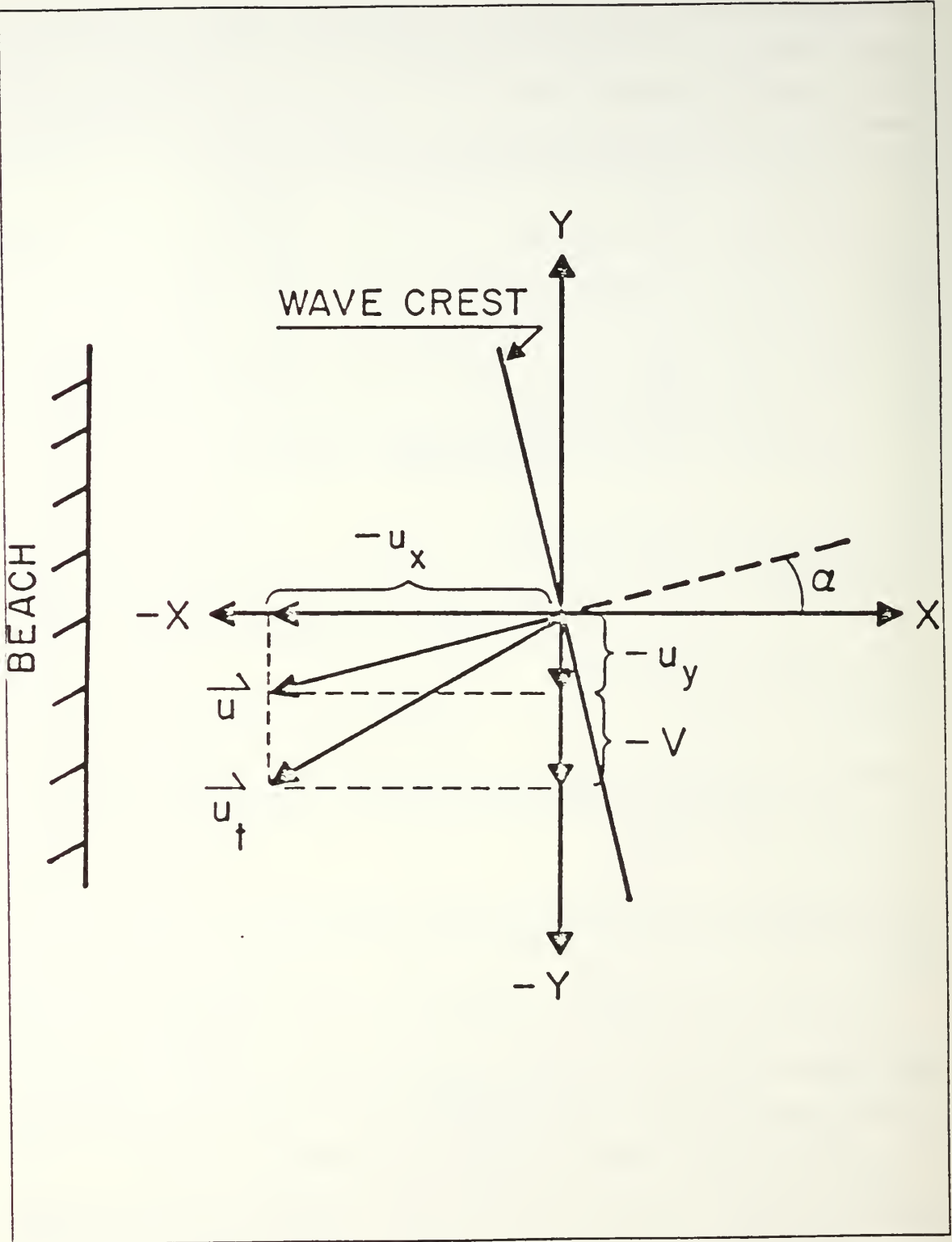


Figure 3. Vector Relationship of \vec{u}_i due to presence of waves and currents.

almost always be in the rough turbulent flow regime (Jonsson, 1966). Since the Reynolds number is the appropriate dynamical similitude scale parameter, large Reynolds numbers are required to be in this flow regime. Hence, only laboratory studies performed in large wave flumes or oscillating water tunnels, where longer wave periods can be obtained, appear appropriate.

Numerous investigators have solved for c_f under waves (Table 1) with results ranging from $O(10^{-1}$ to $10^{-3})$ for different beaches. Most have sought an invariant value for c_f based on a given set of conditions (e.g., bottom roughness, beach slope, or for only one particular beach), without regard for any spatial or temporal variability. Vitale (1979) states that a common engineering practice is to assume $c_f = 0.01$. Johns and Jefferson (1980) showed the variation of bottom stress within a wave cycle in a numerical analysis. They found increasing c_f with increasing bottom roughness and decreasing wave period.

There are four methods of bottom shear stress, and subsequent c_f , determination: -- momentum balance, model-fitting, the profile method, and direct shear measurements. The first three are indirect methods and are addressed below. The direct shear measurement method involves directly measuring the shear force, such as with pressure plates fixed on the bottom or measuring the Reynolds stress at the bed. This has not been done in a surf zone and is therefore omitted from further discussion.

1. Momentum Balance

Forcing terms and assumptions are specified (often based on data availability) to form an appropriate longshore momentum balance equation. The bottom stress term and its accompanying bed shear stress coefficient are then determined as residual values. The strength of this method depends on how complete the momentum balance is and how realistic are the restrictions and assumptions. Thornton and Guza (1981) utilized this method at Torrey Pines Beach, CA (a near-planar, unbarred beach) in connection with the Nearshore Sediment Transport Study (NSTS) experiments. Assuming steady-state conditions, neglecting wind forcing, and operating in an area of straight-and-parallel contours, they assumed a simple balance where the cross-shore gradient of the total longshore momentum flux (both wave-induced and turbulent components) was balanced by the mean longshore bottom shear stress. For simplicity, they neglected the temporal variation term. They found considerable temporal and spatial variation of c_f with a mean value of 0.01 ± 0.01 . However they stated that the results were to be used with caution due to the difficulties in directly measuring the radiation stress (S_{yx}) and its

Table 1. BED SHEAR STRESS COEFFICIENTS PROPOSED AND UTILIZED BY VARIOUS INVESTIGATORS

Investigator	c_f	Comments
Bretschneider and Reid (1954)	0.01	
Kishi ¹ (1954)	0.03 - 0.04	
Iwagaki and Tsuchiya ¹ (1966)	0.01 - 0.04	
Iwagaki and Kakinuma (1967)	0.01 - 1.16	various data sets
Jonsson (1966)	0.01	
Hasselman and Collins (1968)	0.015	
Longuet-Higgins (1970a)	0.01	
James ² (1972)	0.0025 - 0.001	
Jonsson et al. (1974)	0.05 - 0.10	
Kamphius (1975)	0.004 - 0.250	f(bottom roughness)
Komar ² (1975, 1976)	0.017 \pm 0.0225	
Huntley (1976)	0.0026 \pm 0.0006	non-linear eqn.
Liu and Dalrymple (1978)	0.04	
Hsiao and Sheindin (1978)	0.002 - 0.100	various data sets
Madsen et al. ² (1978)	0.01	
Kraus and Sasaki (1979)	0.011 - 0.024	
Vitale (1979)	0.003 - 0.250	
Johns and Jefferson (1980)	0.0096 - 0.00319	
Grant et al. (1984)	0.005 - 0.011	
Wind and Vreugdenhil (1986)	0.0015	
Guza et al. (1986b)	0.008	
Thornton and Guza (1986)	0.006 \pm 0.0007	
<p>• if required, the investigator's friction factor was converted to a bed shear stress coefficient from $c_f = (\text{friction factor} / 2)$.</p> <p>¹ from Sonu (1975)</p> <p>² from Basco (1982)</p>		

gradients. These difficulties were due to angularity errors caused by lack of instrument resolution, installation misalignment, and errors associated with choosing the correct alongshore direction. All of these errors prevented accurate directional resolution of waves with small angles of incidence ($< 3^\circ$). Resolution of these difficulties was addressed in the SUPERDUCK experiment by utilizing a precise surveying system and selecting days for analysis when the mean wave incident angle was large ($> 8^\circ$). In the following determination of c_f by the momentum balance method, both the temporal variability and wind stress terms in equation (1) are included.

2. Model-fitting

Theoretical horizontal mean longshore current distributions generated by a numerical model are compared with field-measured longshore current speeds. The c_f in the numerical model is then adjusted so that the two profiles agree. The resulting numerical model values for c_f can then be assumed to apply for the field measurements. Selecting the appropriate physics for the numerical model is obviously important for this method. Thornton and Guza (1986) used this method with a narrow-band, random-wave transformation model for data collected in another NSTS experiment at Leadbetter Beach, CA. A hierarchy of c_f solutions were derived for linear and non-linear formulations for bottom shear stress, and with and without turbulent momentum exchange. Thornton and Guza (1986) found a least-squares "best fit" value of $c_f = 0.006 \pm 0.0007$ using the full non-linear, and presumably more correct, formulation for the bed shear stress.

3. Profile Method

The profile method (e.g., see Roll, 1965; Schlichting, 1968) has been utilized in boundary layer physics for years to determine friction or shear velocities and roughness heights. It assumes a constant stress layer with a mean logarithmic vertical flow structure and requires at least two simultaneous speed values at different heights above the same location.

Grant et al. (1984) conducted high-quality near-bottom boundary layer measurements at a continental shelf location in 90 m water depth. Even at this substantial depth, they found the near-bottom flow field to be composed of oscillatory currents due to swell superimposed on mean currents, a situation similar to Figure 3. The mean, near-bottom (< 2 m) velocity profiles were found to be logarithmic. Using the profile method, mean stress values were 3 to 7 times larger than expected from predictions of mean current alone using a typical smooth-bottom drag coefficient, and 1.5 to 3.5 times larger than expected for predictions using a drag coefficient based on the observed rough bottom. This significant increase in mean stress magnitudes was attributed to the presence of the swell wave oscillatory currents. These results may apply to the surf zone, if the surf zone's entire vertical extent of chaotic flow may be likened to a fully developed, neutral, turbulent boundary layer in the longshore direction.

Analogous to surface wind stress (e.g., see Roll, 1965; Schlichting, 1968), the longshore bottom shear stress may be written as:

$$\tau_y^b = \rho v_*^2 \quad (19)$$

where v_* is the longshore shear or friction velocity associated with the mean flow. Combining equations (18) and (19):

$$c_f = \frac{v_*^2}{(|u_t|v)} = \frac{v_*^2}{(u^2 + v^2)^{\frac{1}{2}}v} \quad (20)$$

The time-averaged velocity profile in a neutral turbulent boundary layer over a topographically simple bottom is logarithmic and may be expressed as:

$$V(z) = \left(\frac{v_*}{\kappa} \right) \ln \left[\frac{(h+z)}{z_o} \right] \quad (21)$$

where κ is von Karman's constant and z_o is the roughness height. By simultaneously measuring current speed at two different heights ($V(z_1)$ and $V(z_2)$), two equations in the form of (21) may be written. The two unknowns, v_* and z_o , are first solved, and then c_f is obtained from equation (20). Grant et al. (1984) employed a similar profile method in their deep water (90 m depth) investigation where friction velocity was measured in a downstream direction and u and v were measured in the streamwise and cross-stream directions, respectively.

E. TURBULENT MOMENTUM FLUX

The horizontal transfer of momentum due to turbulent mixing processes is not well understood. When the classical analytical solutions for the horizontal profile of the longshore current were initially solved using monochromatic breaking waves (Bowen, 1969; Longuet-Higgins, 1970a, 1970b; Thornton, 1970), a velocity maximum and discontinuity was observed at the breaker line, with zero longshore velocity at the shoreline as well as beyond the breaker line. This occurred since there were no driving forces outside the sharply defined breaker line to generate a longshore current and there was maximum forcing occurring at the breaker line. However, field and laboratory data showed a smooth transition of the longshore current from outside the surf zone to a maximum inside the breaker line. This observation was attributed to turbulent mixing (lateral shear stress). Analytical solutions for longshore currents on a planar beach were proposed with the assumptions of isotropic turbulence, a planar beach, monochromatic waves, and the parameterization of a lateral shear stress in terms of an eddy viscosity coefficient multiplied by a horizontal velocity gradient. Values for the eddy viscosity coefficient were obtained by model-fitting.

Whereas the bed shear stress coefficient is a physical quantity related to bottom roughness and flow intensity, the eddy viscosity coefficient is a function of the flow field and is a parameterization used to remove the longshore current discontinuity at the breaker line. An alternative approach to a monochromatic wave model is to describe breaking wave heights in terms of a probability distribution. This results in a more realistic *region* of wave breaking rather than a distinct breaker *line*. This spreading out of the breaker line results in a smooth horizontal profile of the longshore current, thus eliminating the need to include an eddy viscosity (Collins, 1970; Battjes, 1972a).

Thornton and Guza (1986) utilized a random wave model and model-fitting to determine values of the bed shear stress coefficient and eddy viscosity coefficient for both a linear and non-linear expression for the bed shear stress. Eddy viscosity coefficients (ξ) were represented by an adjustable coefficient, N , in the range of $0 \leq N \leq 0.016$, expressed by (Longuet-Higgins, 1970a, 1970b):

$$\xi = N|x|(gh)^{\frac{1}{2}} \quad x > 0, \quad (22)$$

where g is the acceleration due to gravity. Optimal c_f and N coefficients were determined by least-squares fitting between calculated and measured longshore current speeds shoreward of the mean breaker line. Using a non-linear bed shear stress formulation, a c_f value of 0.006 was determined. Eddy viscosity was found not to be important for the near planar topography of their field experiment.

The last term in equation (1) represents an expression for horizontal diffusion or lateral mixing of turbulent momentum in terms of a depth-integrated Reynolds stress. The longshore component of momentum flux due to unsteady motion (equation 1) is the depth-integrated covariance between the fluctuating velocity components of u and v , measured by the current meters. By partitioning the unsteady motion as that due to waves and turbulence (equations 13 and 14), the excess momentum flux (equation 2) can be separated into a wave-induced (\tilde{S}_{yx}) and turbulent component (S''_{yx}):

$$S_{yx} = \tilde{S}_{yx} + S''_{yx} = \overline{\int_{-h}^{\eta} \rho \tilde{u} \tilde{v} dz} + \overline{\int_{-h}^{\eta} \rho u'' v'' dz} \quad (23)$$

It has been assumed for this separation that the characteristic time scales of the two fluctuations are vastly different (i.e., \tilde{u}_i and u''_i are uncorrelated and $\overline{\tilde{u}_i u''_j} = 0$). integrated viscous stresses are negligible, and that the horizontal scales of depth and mean velocity are comparable. The turbulent component of the excess momentum flux due

to unsteady motion may be obtained by comparing the total radiation stress (S_{yx}) measured by a current meter to the wave-induced radiation stress (\tilde{S}_{yx}) measured by a slope array.

F. TEMPORAL VARIABILITY

Most previous investigators have assumed steady-state conditions for longshore momentum. However, significant temporal variations in longshore current velocity measurements have been observed (Putnam et al., 1949; Inman and Quinn, 1951; Inman and Bagnold, 1963; Dette and Fuhrboter, 1974; Dette, 1974; Huntley and Bowen, 1975; Wood and Meadows, 1975; Meadows, 1976, 1978; Guza and Thornton, 1978; Guza et al., 1986b; and others). The temporal variability of mean currents ($\partial M_y / \partial t$) will be included in the analysis where M_y is the time-averaged and depth-integrated mass flux per unit area, or momentum per unit area, in the longshore direction due to steady (\bar{M}_y) and unsteady (M_y') flow:

$$M_y = \bar{M}_y + M_y' = \rho V(\bar{\eta} + h) + \overline{\int_{-h}^{\eta} \rho v' dz} \quad (24)$$

Inman and Bagnold (1963) ascribed temporal variability of longshore currents to the wave groupness. Meadows (1976) concluded that the total observed longshore current velocity was composed of three components:

$$V = V_{\text{steady}} + V_{\text{wave}} + V_{\text{long}} \quad (25)$$

where V_{steady} is the steady longshore component, V_{wave} is the coincident wave period fluctuating component, and V_{long} is the long period (as related to surf beat or low mode edge waves) fluctuating component. He defined the steady state component as the velocity component whose period of variation was greater than 200 seconds. The selection of 200 seconds was not explained. Guza and Thornton (1978) concluded that a temporal averaging period for mean longshore currents was not well-understood. Various researchers utilize different averaging times to determine the steady state component, based more on record length or data analysis, than on rationale.

G. VERTICAL DISTRIBUTION OF MEAN LONGSHORE FLOW

The equations by Phillips (1977) and Mei (1983) integrate the water motion over depth. For simplicity, the longshore current is assumed uniform from the surface to the bottom. No longshore current theories account for a depth-dependent longshore cur-

rent. Theoretical work on the depth-dependency of longshore currents (Stive and de Vriend, 1987) and cross-shore currents (Svendsen et al., 1987) has only recently been undertaken. Most laboratory and field investigations have not measured the depth-dependence of longshore currents, and as a result, there is little field data on vertical current structure.

Greenwood and Sherman (1983) measured vertical structure of the longshore current at the Wendake Beach, Ontario field experiment. They calculated mean flows for three elevations as well as a depth-averaged mean longshore current velocity. Their maximum mean variability was only 10% of the depth-averaged flow. Thus their data, as well as Meadows' (1978) and Hubertz's (1986) data, suggests that modeling longshore currents as uniform over depth is appropriate. Although they assumed a logarithmic boundary layer velocity profile in order to calculate a boundary roughness length (z_o), their logarithmic plots of only two points are inconclusive regarding the existence of a logarithmic vertical velocity profile in the surf zone. However, their linear plots of vertical profiles show a "consistent deformation of the velocity field strongly suggestive of the influence of bed friction," and hence a logarithmic profile within at least 0.5 - 1.0 m of the bed remains a possibility for their data.

Wright et al. (1986) obtained field data of vertical profiles from 0.1 to 1.0 m above the bottom of longshore currents in a bar trough. Although the longshore velocities were on the same order of magnitude as the wave orbital velocities, the bottom boundary layer was dominated by the waves acting in the shore-normal direction, orthogonal to the longshore currents. The velocity profiles were not logarithmic and it appeared that they were strongly influenced by wave-generated vortices from the bed ripples present.

Theoretical investigations by Lundgren (1972), Smith (1977), and Grant and Madsen (1979), laboratory studies by Bakker and Van Dorn (1978) and Grant and Madsen (1982), and field measurements by Grant et al. (1984) assume that the mean velocity profile is comprised of an inner region (close to the bed which is directly affected by wave-induced turbulence) and an outer region above it, and that the outer region has a logarithmic profile which is also affected by wave-induced turbulence. Preliminary indications from an on-going surf zone field investigation suggest that the mean longshore velocity profile in the vertical might be logarithmic (personal communication, R.T. Guza, 1987). The existence of a logarithmic profile would allow bed shear stress coefficients to be determined by the profile method.

H. BARRED BEACHES

Although barred beaches are more common (Wright et al., 1986), far less is known about surf zone currents on barred beaches than on planar beaches. Allender and Ditmars (1981) found little spatial variability in the horizontal longshore current profile across the entire surf zone of a steep, barred beach during storm conditions on Lake Michigan. No significant cross-shore flow or vertical variability of current flow was observed. Greenwood and Sherman (1983, 1986) studied surf zone currents in Lake Huron off a steep, multi-barred beach at Georgian Bay. They found significant cross-shore variability in the longshore current, and up to a four-fold variation during storm conditions. These two contrasting conclusions are indicative of the embryonic state of knowledge concerning the surf zone dynamics of barred beaches. The SUPERDUCK experiment was conducted on a barred beach. Data analysis of the surf zone currents will be used to improve the understanding of surf zone dynamics at a barred beach.

III. WIND FORCING OF LONGSHORE CURRENTS FROM A FINITE-DEPTH SPECTRAL WAVE MODEL APPROACH

To assess the importance of the wind contribution to longshore currents, wave and wind forcing terms in the longshore momentum equation are integrated across the surf zone in a simple model and compared. Wave and wind forcing are coupled by assuming the waves driving the longshore currents are generated by the local wind. The TMA wind-wave shallow water wave spectrum is used as input to the radiation stress.

A. THE TMA SPECTRUM

The TMA spectrum (Bouws et al., 1985) was developed from data obtained from two extensive shallow-water wave measurement programs. MARSEN (Marine Remote Sensing Experiment at the North Sea) and ARSLOE (Atlantic Ocean Remote Sensing Land-Ocean Experiment), and data from a prolonged storm near lightship TEXEL in the southern North Sea. The MARSEN and ARSLOE sites were both on the continental shelf with depths less than 40 m. The combined data set was named TMA, after the 3 sub-data sets, and includes water depths from 6 - 42 m, wind speeds up to 30 ms⁻¹, bottom composition from fine to coarse sands, and beach slopes ranging from 1:150 to nearly flat. The uniqueness of the TMA data set to this research is that the ARSLOE data, which comprises two-thirds of the nearly 3000 wind-wave spectra, were measured at the CERC Field Research Facility in Duck, N.C.

Bouws et al. (1985) proposed, and then verified, that a finite-depth wind-wave spectrum could be approached through application of the similarity principles by Kitaigorodskii et al. (1975). The TMA spectrum is an extension of the self-similar JONSWAP (Joint North Sea Wave Project) spectral shape (Hasselmann et al., 1976) to include the effects of finite water depth embodied in the Kitaigorodskii et al. (1975) finite-depth transformation factor, $\Phi_K(\omega, h)$:

$$E_{\text{TMA}}(f, h) = E_{\text{PM}}(f, f_m, \alpha) \Phi_J(f, f_m, \gamma_J, \sigma_a, \sigma_b) \Phi_K(\omega, h) \quad (26)$$

where

$$E_{\text{PM}}(f) = \alpha g^2 f^{-5} (2\pi)^{-4} \exp\left[-1.25\left(\frac{f}{f_m}\right)^{-4}\right] \quad (27)$$

$$\Phi_J(f, f_m, \gamma_J, \sigma_a, \sigma_b) = \gamma_J^{\exp\left[\frac{-(f-f_m)^2}{2\sigma_f^2}\right]} \quad (28)$$

$$\Phi_K(\omega, h) = \frac{(k(\omega, h))^{-3} \frac{\partial k(\omega, h)}{\partial f}}{(k(\omega, \infty))^{-3} \frac{\partial k(\omega, \infty)}{\partial f}} \quad (29)$$

and

- α = Phillips constant,
- ω = $2\pi f$,
- f = frequency,
- f_m = peak spectral frequency,
- γ_J = peak enhancement factor, and
- σ = σ_a = peak spectral width on low frequency side of f_m ,
= σ_b = peak spectral width on high frequency side of f_m .

$E_{PM}(f, f_m, \alpha)$ is the Pierson-Moskowitz (1964) spectral shape for fully-developed deepwater waves, and $\Phi_J(f, f_m, \gamma_J, \sigma_a, \sigma_b)$ is the JONSWAP spectral shape function.

Thompson and Vincent (1983) developed an approximation for $\Phi_K(\omega, h)$ using linear theory and redefining the two independent variables (ω, h) as a single variable (ω_h):

$$\Phi_K(\omega, h) \simeq \Phi(\omega_h) = \begin{cases} \frac{1}{2} \omega_h^2 & \omega_h \leq 1 \\ 1 - \frac{1}{2} (2 - \omega_h)^2 & \omega_h > 1 \end{cases} \quad (30)$$

where

$$\omega_h = 2\pi f \left(\frac{h}{g} \right)^{\frac{1}{2}} \quad (31)$$

However, the approximation (equation 30) is incorrect for $\omega_h > 2$ and therefore is modified here as:

$$\Phi_K(\omega, h) = \begin{cases} \frac{1}{2} \omega_h^2 & \omega_h \leq 1 \\ 1 - \frac{1}{2} (2 - \omega_h)^2 & 1 < \omega_h \leq 2 \\ 1 & \omega_h > 2 \end{cases} \quad (32)$$

$\Phi(\omega_h)$ approaches a value of one in deep water and a value of zero as the depth decreases (Figure 4).

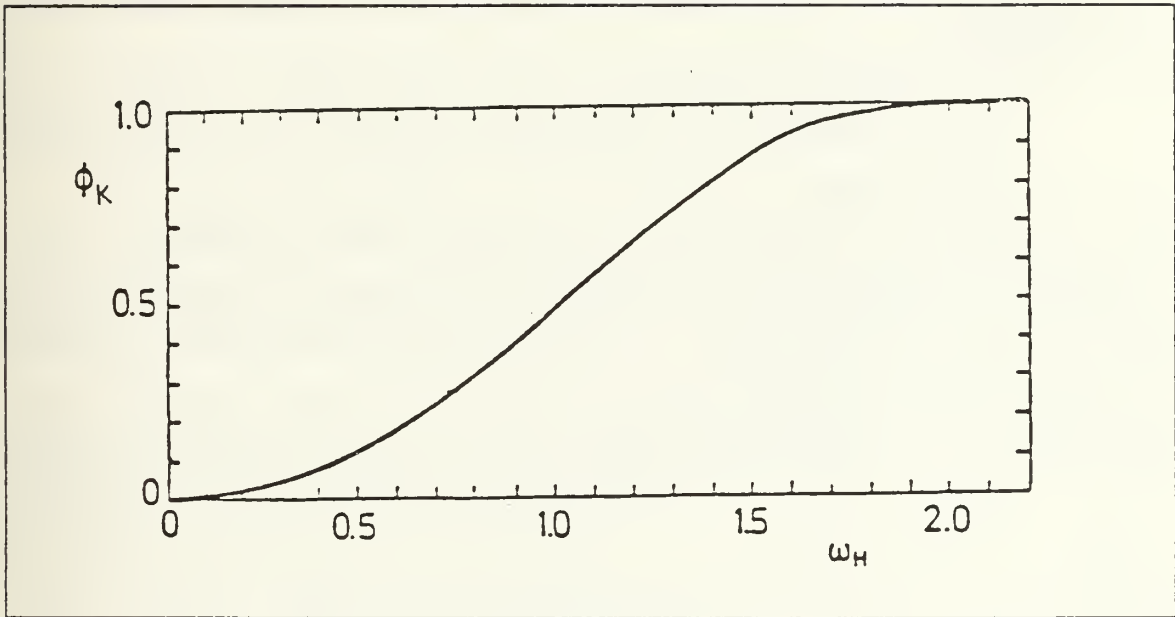


Figure 4. Kitaigorodskii et al. (1975) finite-depth spectral transformation function, $\Phi_K(\omega, h)$ (from Bouws et al., 1985).

Bouws et al. (1985) developed the following empirical parameter expressions for input into the TMA data set:

$$\alpha = 0.0078 K^{0.49} \quad (33)$$

$$\gamma_J = 2.47 K^{0.39} \quad (34)$$

$$K = \left(\frac{H_{10}^2}{g} \right) k_m \quad (35)$$

$$\sigma = \begin{cases} \sigma_a = 0.07 & f \leq f_m \\ \sigma_b = 0.09 & f > f_m \end{cases} \quad (36)$$

where W_{10} = wind speed at $z = 10$ m and
 k_m = wave number for waves at peak frequency.

These expressions are valid for all water depths in the TMA data set. Thus, the TMA spectrum requires specification of W_{10} , h , and f_m .

B. NUMERICAL APPROACH

To compare wind and wave forcing for various conditions using finite-depth spectra, it is assumed that:

- 1) Wave conditions are solely the result of a local wind (i.e. there is no swell present), and therefore the wind direction (θ) and mean incident wave direction are identical, and
- 2) Sea conditions are fully arisen (i.e., the sea is not duration-limited).

Comparisons are made for inputs of gentle and steep planar beach slopes ($\tan \beta = .01$ and $.10$), wind speeds (10 - 30 ms^{-1}), all wind directions, and peak spectral frequencies commensurate with wind speed.

Surface wind stress is determined from equation (11). C_d is determined from measurements taken by Geernaert et al. (1987b) in open waters of the North Sea for a depth of 10 m (Figure 2). These C_d values are increased by 33% to account for surf zone roughness. The 33% increase will be addressed later in the Chapter VI. Peak frequency is determined for the Pierson-Moskowitz spectrum (Carter, 1982):

$$f_m = \frac{1.27}{W_{10}} \quad (37)$$

Peak frequency is assumed not to shift during shoaling (Hughes, 1984).

After input of $\tan \beta$ and W_{10} , peak wavenumber (k_m) is calculated using the linear theory relationship starting at an initial water depth of 20 m. The TMA spectrum is determined from equation (26). The RMS wave height is obtained by integrating the TMA spectrum:

$$(H_{\text{rms}})_{\text{TMA}} = \left[8 \sum_{0.0}^{0.5} E_{\text{TMA}}(f) \right]^{\frac{1}{2}} \quad (38)$$

where only sea waves (maximum frequency of 0.5 Hz) are considered.

Thornton and Guza (1982, 1983) found an envelope curve relating H_{rms} to depth in the inner surf zone:

$$H_{rms} \approx 0.42 h \quad (39)$$

The H_{rms} determined by equation (38), which includes the effects of variable depth, is checked against equation (39) to ascertain if wave breaking due to shoaling had commenced. If the ratio H_{rms}/h is less than required for surf zone wave breaking, water depth is reduced and a new H_{rms} determined. This process for calculating breaker depth iterates until equation (39) is satisfied. Surf zone width (x_b) is then determined from:

$$x_b = \frac{h}{\tan \beta} \quad (40)$$

The radiation stress gradient ($\partial S_{yx} / \partial x$) and surface wind stress (τ_y) are both integrated with respect to x_b to allow comparison of a wave force (S_{yx}) and a wind force ($\tau_y x_b$), with units of force per unit longshore length. The integration is confined to x_b since the radiation stress gradient is conserved outside the surf zone where there is no wave breaking. Momentum exchange between the wind-driven longshore current outside x_b and the wind- and wave-driven longshore current inside x_b is assumed negligible. Using equation (2), wave force is expressed as:

$$S_{yx} = \int_0^{x_b} \frac{\partial S_{yx}}{\partial x} dx = \frac{1}{2} \sigma_{TMA \times n(f)}^2 \rho g \sin \theta \cos \theta \quad (41)$$

where the energy is expressed in terms of variance, which is:

$$\sigma_{TMA \times n(f)}^2 = \sum_{0.0}^{0.5} E_{TMA}(f) n(f) \Delta f \quad (42)$$

and $n(f)$ is expressed in a frequency-dependent form. The factor of 1/2 is an adjustment factor for broad-banded wind-driven waves which incorporates the effect of short-crestedness on the ratio of radiation stress to the average energy content of the waves (Battjes, 1972b).

Wind force is constant over the surf zone and is determined from equation (11):

$$\tau_y^\eta x_b = \int_0^{x_b} \tau_y^\eta dx = \rho_a C_d |W| W \sin \theta x_b \quad (43)$$

C. RESULTS AND DISCUSSION

Resultant spectra, wind force, and wave force for both a gentle beach slope and a steep beach slope are illustrated as cases A through F in Figure 5 and Figure 6. H_{rms} , h , f_m , wind speed, C_d , and x_b for each of the six cases are listed in Table 2. Increasing wind speed effect for a gentle beach slope ($\tan \beta = 0.01$) is depicted in cases A, B, and C, and for a steep beach slope ($\tan \beta = 0.10$) in cases D, E, and F. Wind and wave direction are relative to normal beach incidence. The three spectra previously described (Pierson-Moskowitz, JONSWAP, and TMA) are included to illustrate the effect of shoaling on the wind-wave spectra, as well as the expected shift to lower peak spectral frequency as wind speed increases. The H_{rms} and depth (h) at commencement of breaking also increase with increasing wind speed.

Table 2. CASE PARAMETERS FOR WIND VERSUS WAVE FORCE COMPARISONS (see Figure 5 and Figure 6).

Case	$\tan \beta$	wind speed (ms ⁻¹)	H_{rms} (m)	h (m)	x_b (m)	f_m (Hz)	C_d
A	0.01	10	0.7	1.6	160	0.13	0.0021
B	0.01	20	3.0	7.0	700	0.06	0.0033
C	0.01	30	7.6	18.0	1800	0.04	0.0053
D	0.10	10	0.7	1.6	16	0.13	0.0021
E	0.10	20	3.0	7.0	70	0.06	0.0033
F	0.10	30	7.6	18.0	180	0.04	0.0053

The wind force is directly proportional to the width of the surf zone (x_b), which is a function of $\tan \beta$. As a beach steepens, surf zone width narrows and thus there is a reduced area for surface wind stress to act. Wave force is independent of $\tan \beta$.

Wind direction dependency is inherent in equations (41) and (43) where:

$$S_{yx}^T \propto \sin \theta \cos \theta = \frac{1}{2} \sin(2\theta) \quad (44)$$

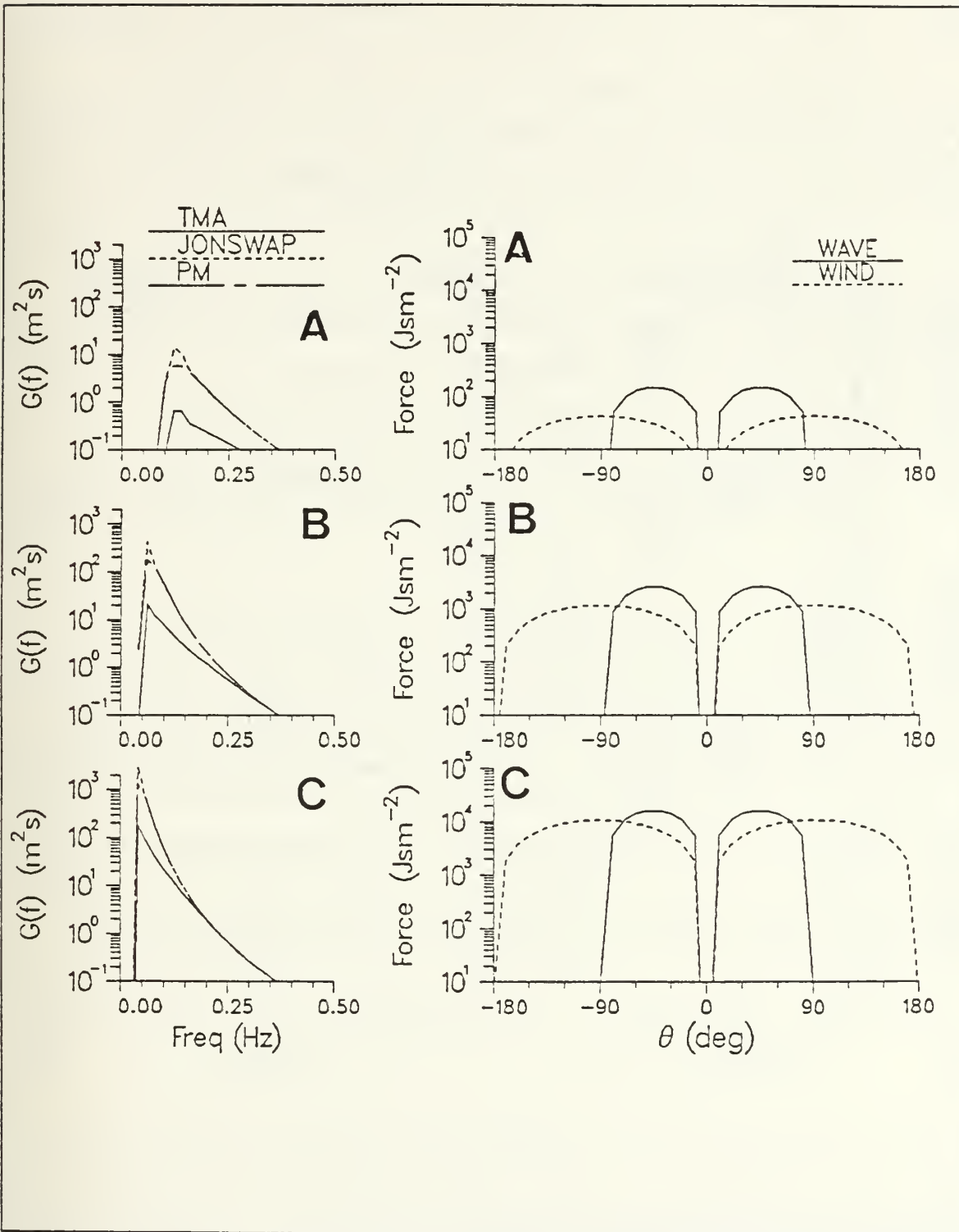


Figure 5. Comparison of wind and wave force for a gentle beach slope ($\tan \beta = 0.01$) with associated wave spectra.

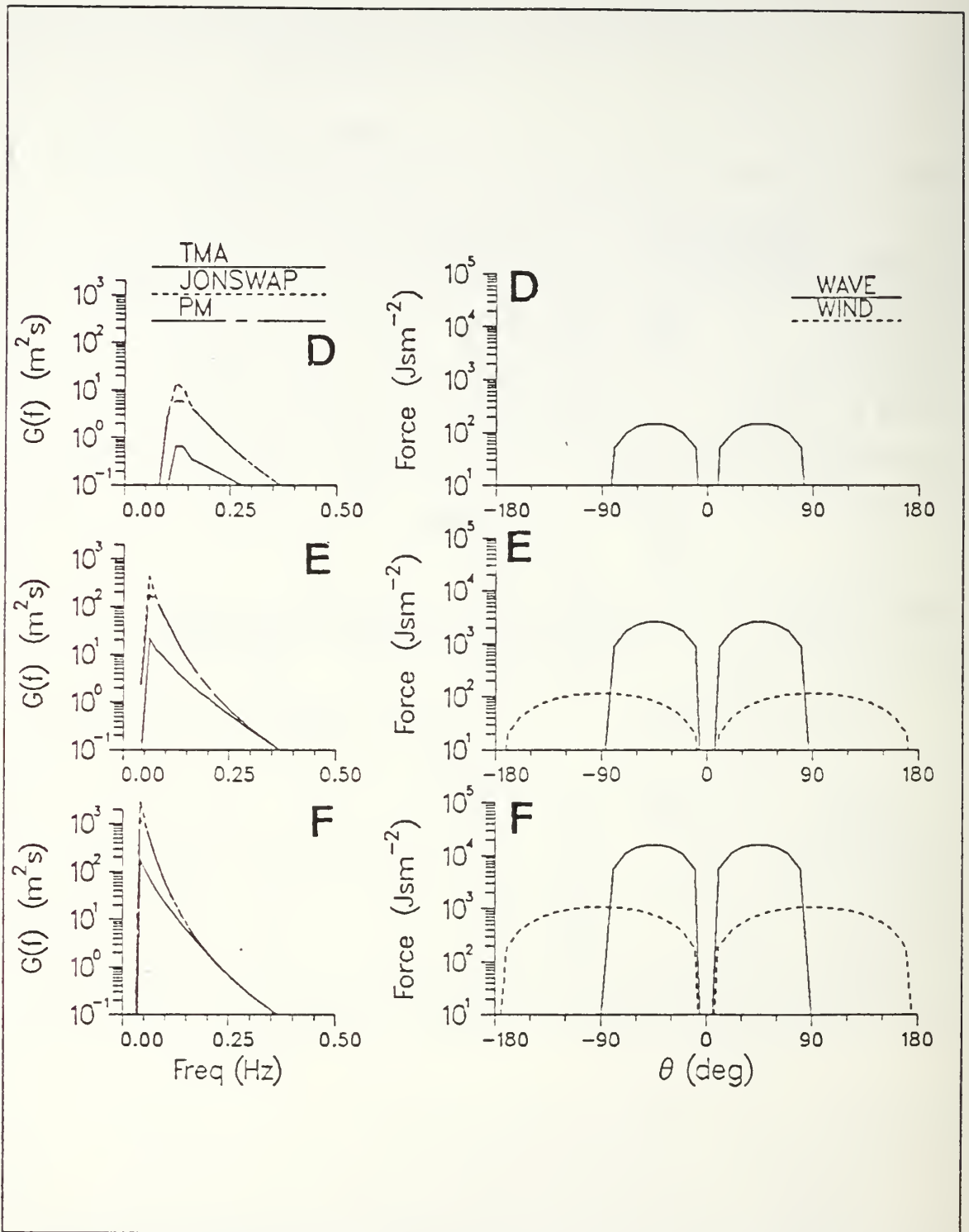


Figure 6. Comparison of wind and wave force for a steep beach slope ($\tan \beta = 0.10$) with associated wave spectra.

$$\tau_y^{\eta} \propto \sin \theta \quad (45)$$

Thus the maximum force occurs at $\pm 90^\circ$ (alongshore) for wind and $\pm 45^\circ$ for waves. Wind force increases more rapidly than wave force for increasing θ . When winds are blowing offshore (i.e. absolute wind directions $> 90^\circ$), waves do not form because of fetch limitations and thus only wind force exists, creating a weak, but *totally wind-driven* longshore current.

The dependency of wind and wave force on wind speed is not as readily apparent because of the interrelationship of wind speed with the various TMA parameterizations (equations 33 to 37). The absolute force of both wind and waves increases as wind speed increases. The increase in wave force is due to the increase in spectral energy. The increase in wind force is through the wind speed and the increase in surf zone width caused by larger waves (generated from the TMA spectrum) breaking farther offshore. Thus the wind force's dependency on wind speed is indirectly dependent on the spectral wave energy.

Wave and wind force are compared for increasing wind speed and constant wave incident angle (Figure 7). Since wave force is independent of β , only wind force is illustrated for both gentle (solid line) and steep (dashed) beach slopes. The amount of increase for both wind and wave force over the wind speed range of 5 ms^{-1} to 30 ms^{-1} is nearly four orders of magnitude. Wind force is seen to increase more rapidly than wave force for increasing wind speed and constant incident wave angle. Varying the incident wave angle results in the same conclusion; therefore only θ equal to 20° is illustrated.

The more rapid rate of increase for wind force is quantified in terms of a wind force to wave force ratio:

$$\frac{\tau_y^{\eta} x_b}{S_{yx}} \quad (46)$$

The ratio of forces is depicted in Table 3 ($\tan \beta = 0.01$) and Table 4 ($\tan \beta = 0.10$) for the quadrant of wind direction from $0 - 90^\circ$. The ratio is symmetric for wind directions of 0 to -90° and is a function of slope, wind speed, and wind direction. For steep beach slopes, wind force is much less than wave force and thus may be neglected. However, for gentle slopes, wind force increases as the wind becomes more alongshore in direction. For a given wind direction, an increase of 10 ms^{-1} in wind speed results in a 50% in-

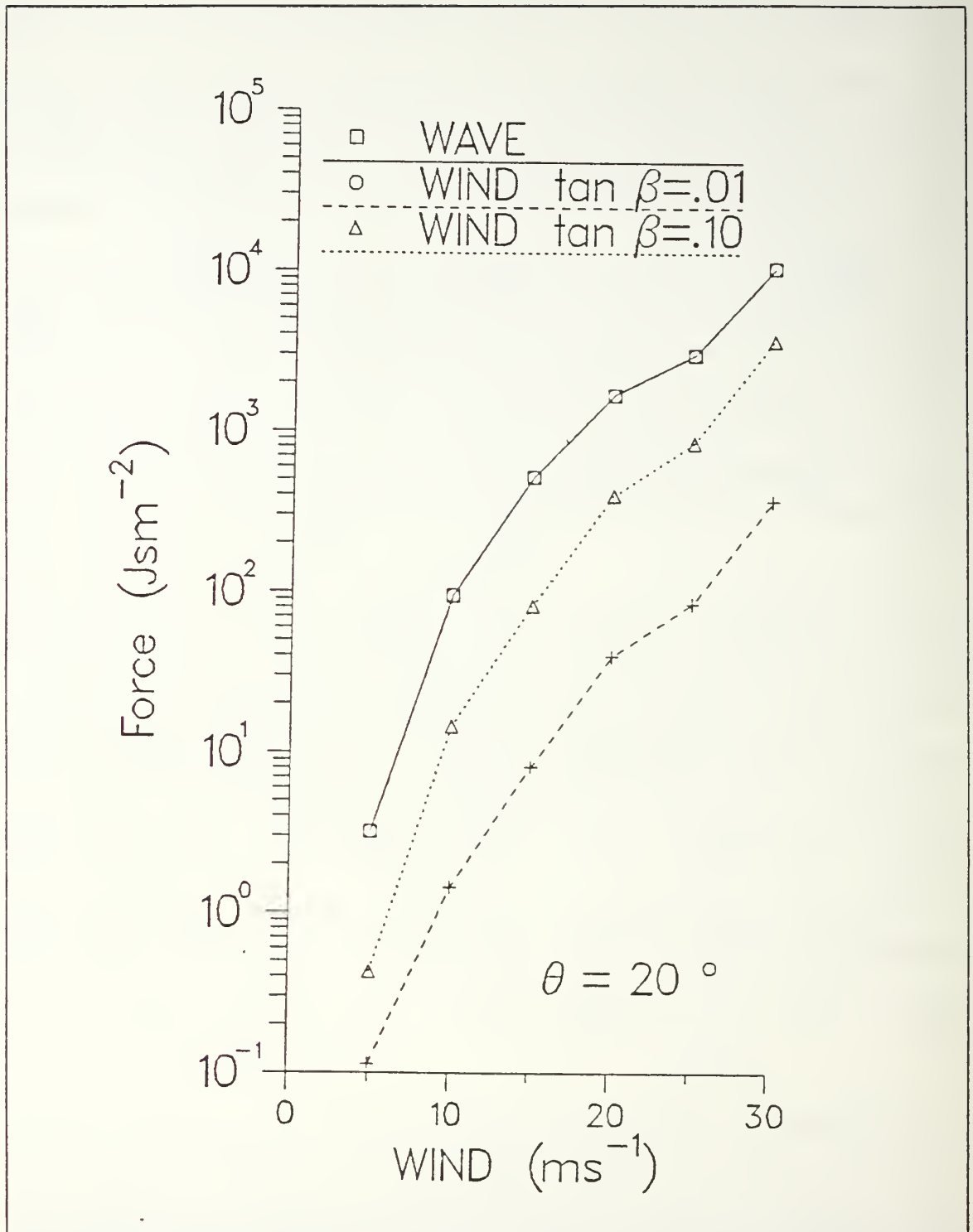


Figure 7. Comparison of wind and wave force for increasing wind speed at constant wind direction ($\theta = 20^\circ$).

crease in the ratio. Although this ratio for gentle beach slope is generally less than unity for all wind speed and direction combinations, wind force is never less than an order of magnitude compared to wave force. Wind to wave force ratio versus beach slope for a typical mid-latitude cold frontal passage is depicted in Figure 8. Wind and wave frontal conditions are defined as a wind speed of 15 ms^{-1} and $\theta = 20^\circ$. The wind to wave force ratio increases with decreasing beach slope. The ratio is approximately 10% for a beach slope of 0.04 and approaches 40-50% for beach slopes less than 0.01. Therefore wind force should be considered in studying longshore currents during strong winds on gentle beaches and during offshore winds. In Chapter VII, wind to wave force ratios from the field experiment will be compared to the results in Table 3 and Table 4.

Table 3. RATIO OF WIND FORCE TO WAVE FORCE FOR A GENTLE BEACH SLOPE ($\tan \beta = 0.01$)

Wind Speed (ms^{-1})	Wind Direction (relative to normal incidence)									
	0°	10°	20°	30°	40°	50°	60°	70°	80°	90°
10	0.00	0.15	0.15	0.17	0.19	0.22	0.29	0.42	0.83	INF
20	0.00	0.23	0.24	0.26	0.29	0.35	0.44	0.65	1.28	INF
30	0.00	0.34	0.35	0.38	0.43	0.52	0.66	0.97	1.91	INF

- INF - ratio is infinite since there is no wave force
- waves are assumed to be locally generated and to approach the shoreline from the wind direction

Table 4. RATIO OF WIND FORCE TO WAVE FORCE FOR A STEEP BEACH SLOPE ($\tan \beta = 0.10$)

Wind Speed (ms^{-1})	Wind Direction (relative to normal incidence)									
	0°	10°	20°	30°	40°	50°	60°	70°	80°	90°
10	0.00	0.01	0.02	0.02	0.02	0.02	0.03	0.04	0.08	INF
20	0.00	0.02	0.02	0.03	0.03	0.03	0.04	0.07	0.13	INF
30	0.00	0.03	0.04	0.04	0.04	0.05	0.07	0.10	0.19	INF

- INF - ratio is infinite since there is no wave force
- waves are assumed to be locally generated and to approach the shoreline from the wind direction

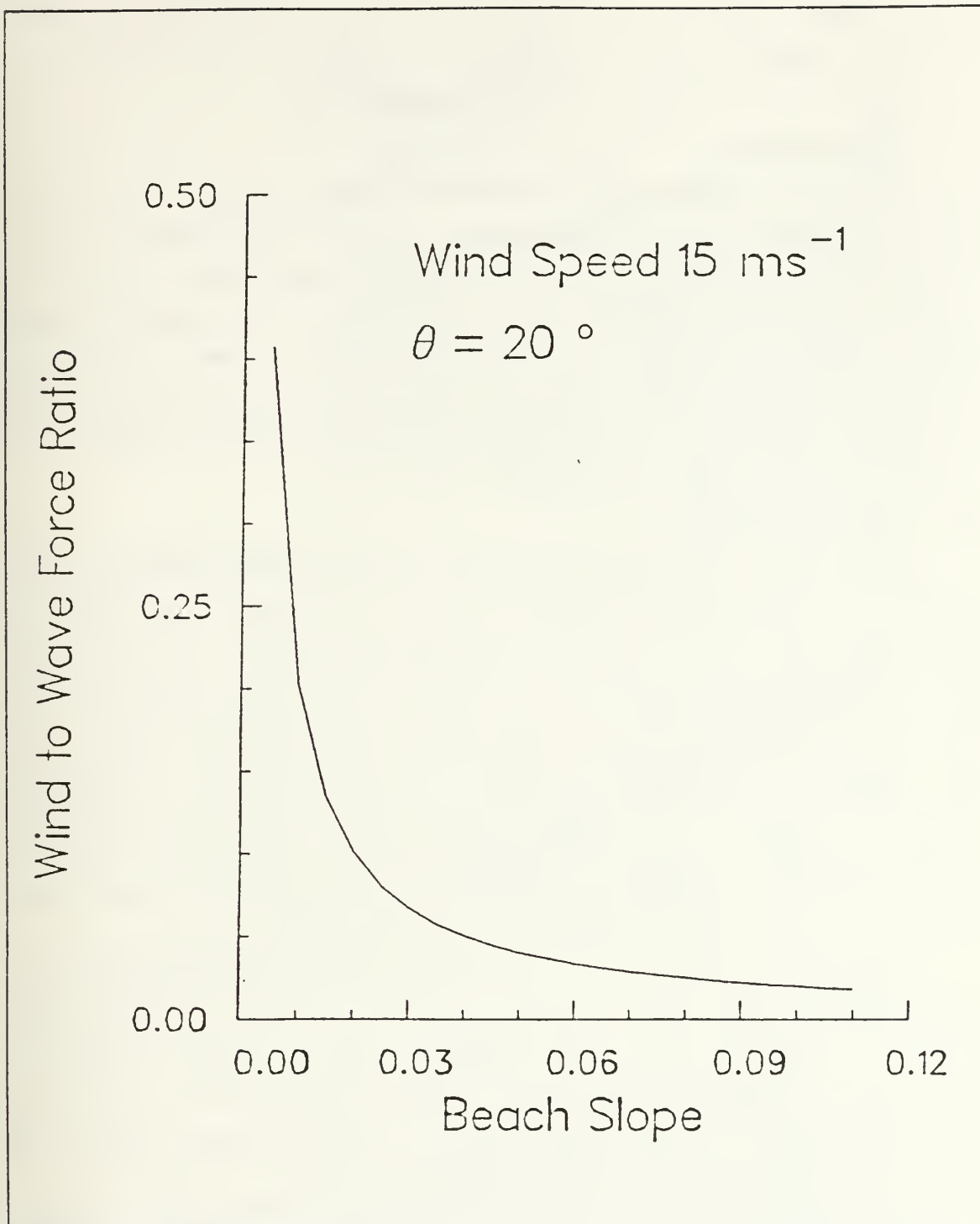


Figure 8. Wind to wave force ratio versus beach slope for a typical mid-latitude cold frontal passage. The wind and wave incident angle (θ) is relative to beach normal.

IV. FIELD EXPERIMENT

A. INTRODUCTION

To develop an improved understanding of coastal processes (currents, waves, sediment transport, and nearshore geomorphology) under a wide variety of conditions, a one month-long field experiment was held in the autumn of 1986 at the U.S. Army Corps of Engineers, Waterways Experiment Station's Coastal Engineering Research Center (CERC), Field Research Facility (FRF) at Duck, N.C. Duck is on the Atlantic Ocean side of the North Carolina Outer Banks and is located approximately 10 miles north of Kitty Hawk, N.C. This major field experiment was entitled SUPERDUCK and included nearly 20 scientific investigations.

B. SITE DESCRIPTION

The FRF site (Figure 9) is located along a 100-km unbroken stretch of shoreline of an extensive barrier island formation known as North Carolina's "Outer Banks." The barrier island upon which the FRF site is located is bordered by the Atlantic Ocean to the east and Currituck Sound to the west. Except for a few fishing piers, there are no major coastal structures or littoral barriers along the entire reach of shoreline. The site has a tidal range of 0.5 to 2.0 m and regular offshore bathymetry free of features which may affect wave climate. The beach is characterized by a mean foreshore slope of 1:10, a single longshore linear bar system which can become three-dimensional, and a mean slope of 1:100 offshore of the bar. Shoreline excursion due to tidal fluctuations is typically 10 m. Mean sediment grain size is approximately 0.5 mm.

FRF personnel support includes a staff of nine (scientists, technicians, divers, and heavy equipment and computer operators). Extensive equipment support includes a LARC-V amphibious vehicle, a Coastal Research Amphibious Buggy (CRAB), automated data processing (ADP) equipment, a heavy-duty forklift, four-wheel drive and all-terrain vehicles (ATV's), laboratories, electronic workshops, a maintenance garage, and high-resolution Zeiss Elta-2 electronic surveying systems.

Several planning workshops were held months prior to the experiment to synergize the efforts of all the principal investigators. The FRF staff and SUPERDUCK participants jointly installed more than 70 electronic sensors in the nearshore environment for the experiment. The overall set-up of the various instruments at the FRF site is illustrated in Figure 10. The longshore current meter array was approximately 500 m in

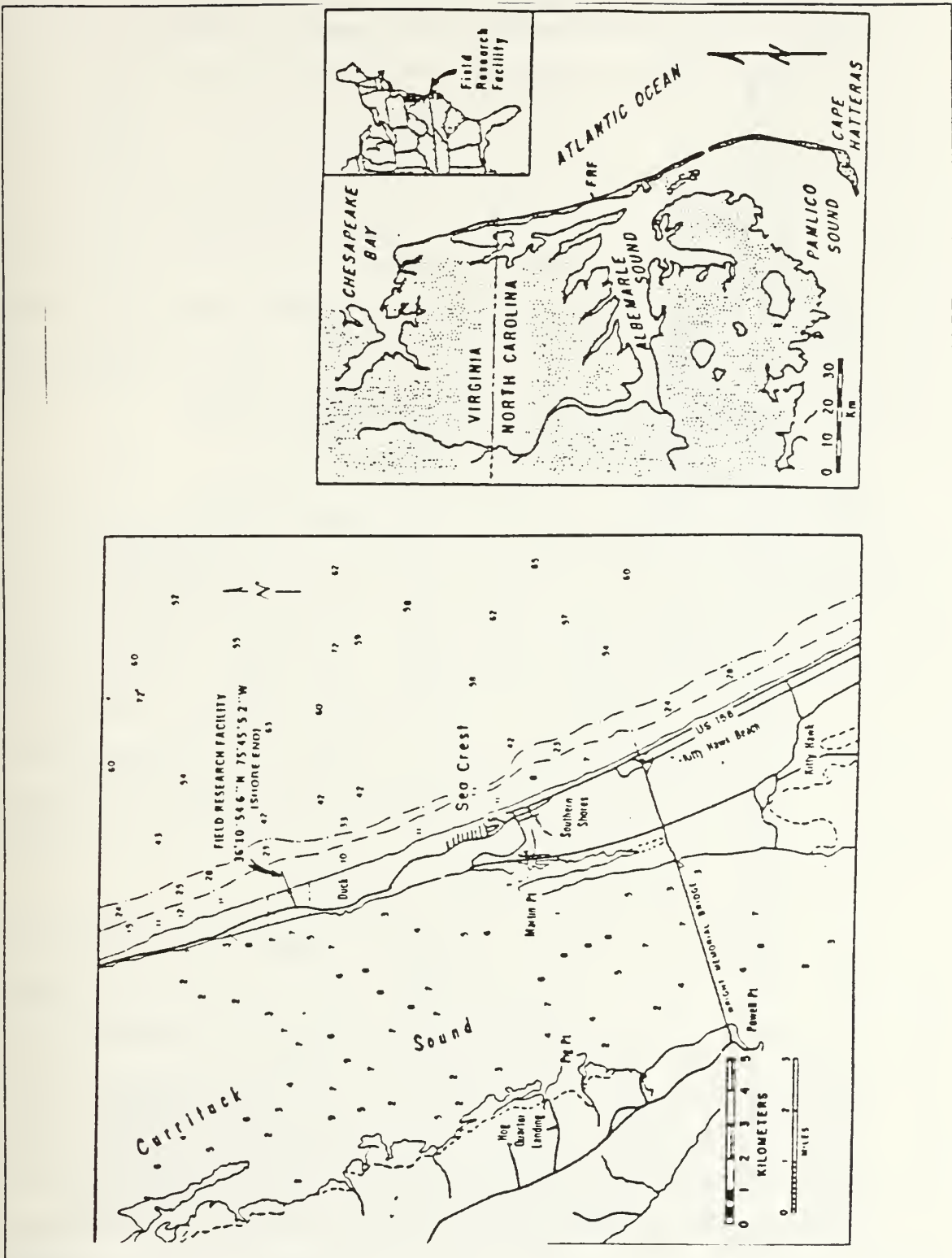


Figure 9. SUPERDUCK field experiment site.

length and 25 m offshore. Its primary purpose was for the investigation of infragravity waves, however its data will also be used in this research to investigate temporal and spatial variability of longshore momentum flux and to provide an extra data station for sled transects of the surf zone. Unfortunately, the cross-shore array of current meters and pressure sensors was not functional for the experiment. The third cross-shore sensors were sonar bottom profilers. A high-resolution linear pressure sensor array in 8 m depth provided offshore directional wave data. High resolution bathymetry data were collected on a nearly daily basis between profile lines 165 and 275 by laser positioning the CRAB with the Zeiss surveying system as it methodically traversed the area along the profile lines. Example products of the surveying effort are included in Figure 11 and Figure 12. A major difference between this and previous large-scale nearshore experiments was the extensive bathymetric data acquired using the CRAB.

C. EQUIPMENT DESIGN AND OPERATION

Only a brief description of the sled and its instrumentation is provided here. Martens and Thornton (1987) describe in detail the design, instrument calibration, and specification of the sled system. The all-aluminum sled (Figure 13) was constructed by the CERC Field Research Facility staff in Duck, N.C., based on a Naval Postgraduate School design. The sled foundation is two runners 3 m in length on which was placed a 3 m x 3 m aluminum sled frame with a 9 m aluminum sailboat mast. The frame was approximately one quarter of a meter above the sled runners. All the instrumentation was then attached to this frame. Significant additional weight was placed on the runners to provide stability and prevent dragging in the robust surf zone. The sled was designed with a low profile to minimize flow disturbance.

The differential pressure slope array concept was patterned after Bodge and Dean (1984) with some major modifications. Two-inch O.D. stainless steel threaded pipe and pipe fittings were assembled in the shape of a capital "H" to form two adjacent triangular slope arrays with a common vertex at the center (see Figure 13). The five differential pressure ports were located at the four ends of the "I" and one at the center. The pipe cavity was filled with a premium grade vacuum pump oil, similar to mineral oil, which had a low viscosity coefficient and was assumed incompressible. Four Sensym model LX06002D monolithic differential pressure transducers were installed at the ends of the "I", just inboard of the diaphragms which were exposed to the sea. These differential pressure transducers provide an output voltage proportional to the applied differential pressure with a response time of 0.1 seconds. The pressure at the center diaphragm was

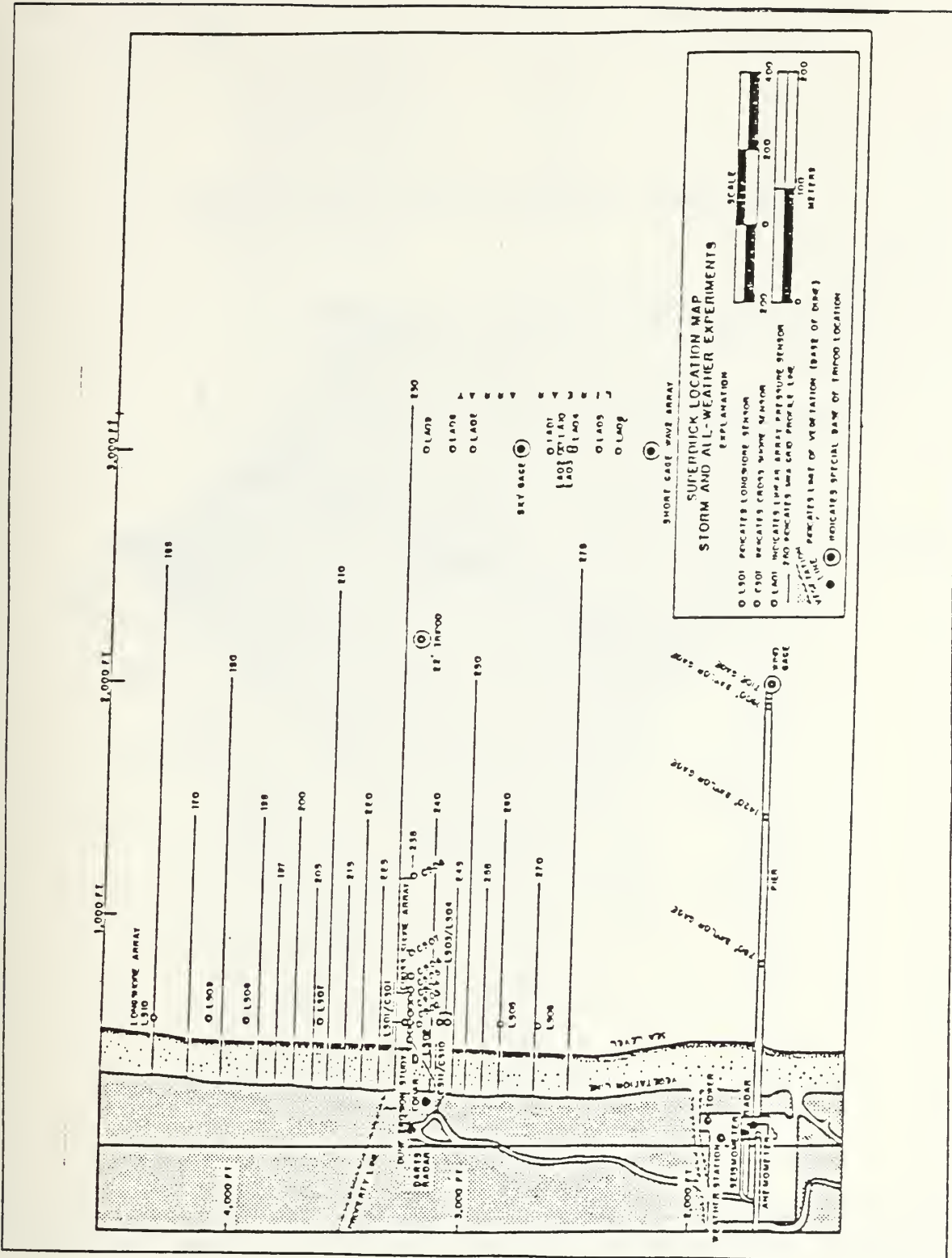


Figure 10. SUPERDUCK field experiment instrument locations.

SUPERDUCK BATHYMETRY 16 OCT 86

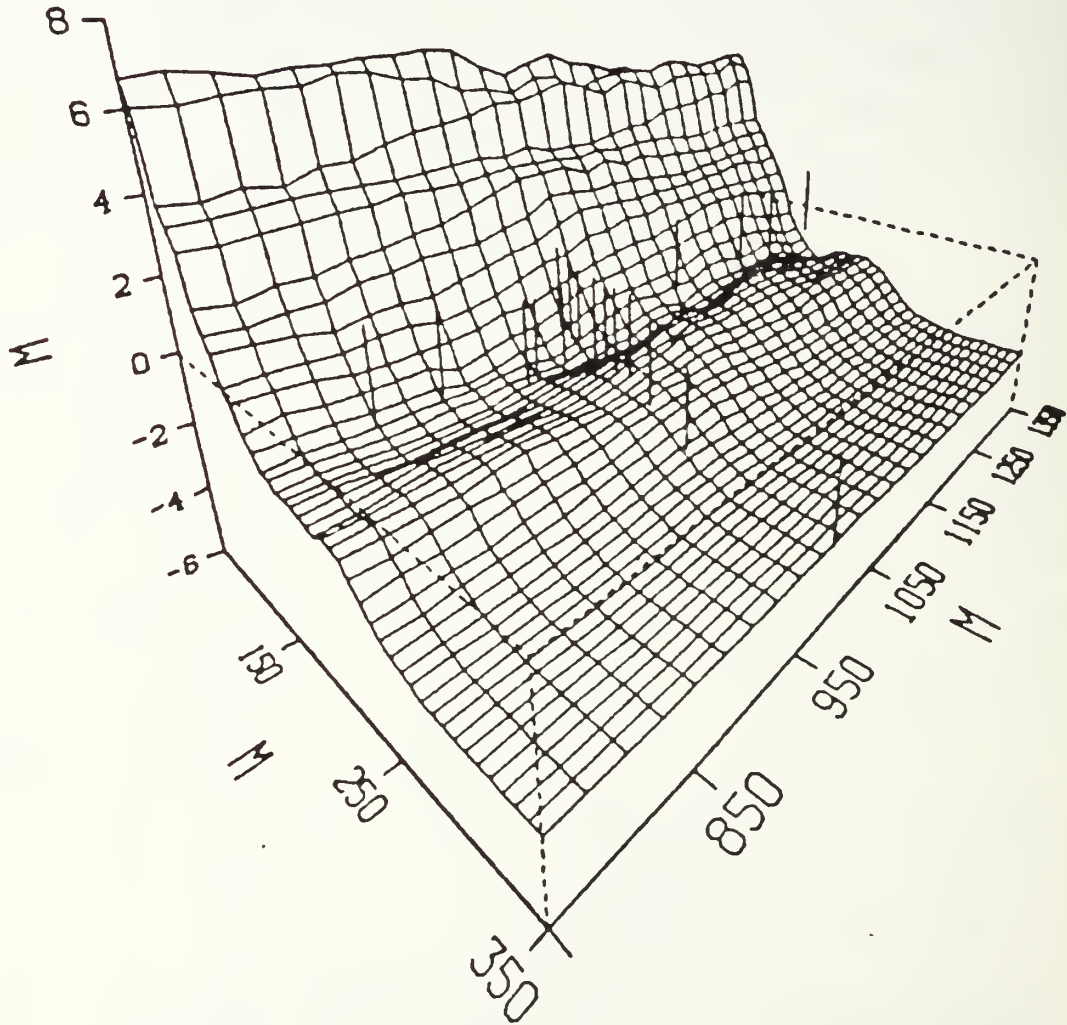


Figure 11. Three-dimensional bathymetry example, 16 October 1986. Short vertical lines represent locations of cross-shore and longshore instruments.

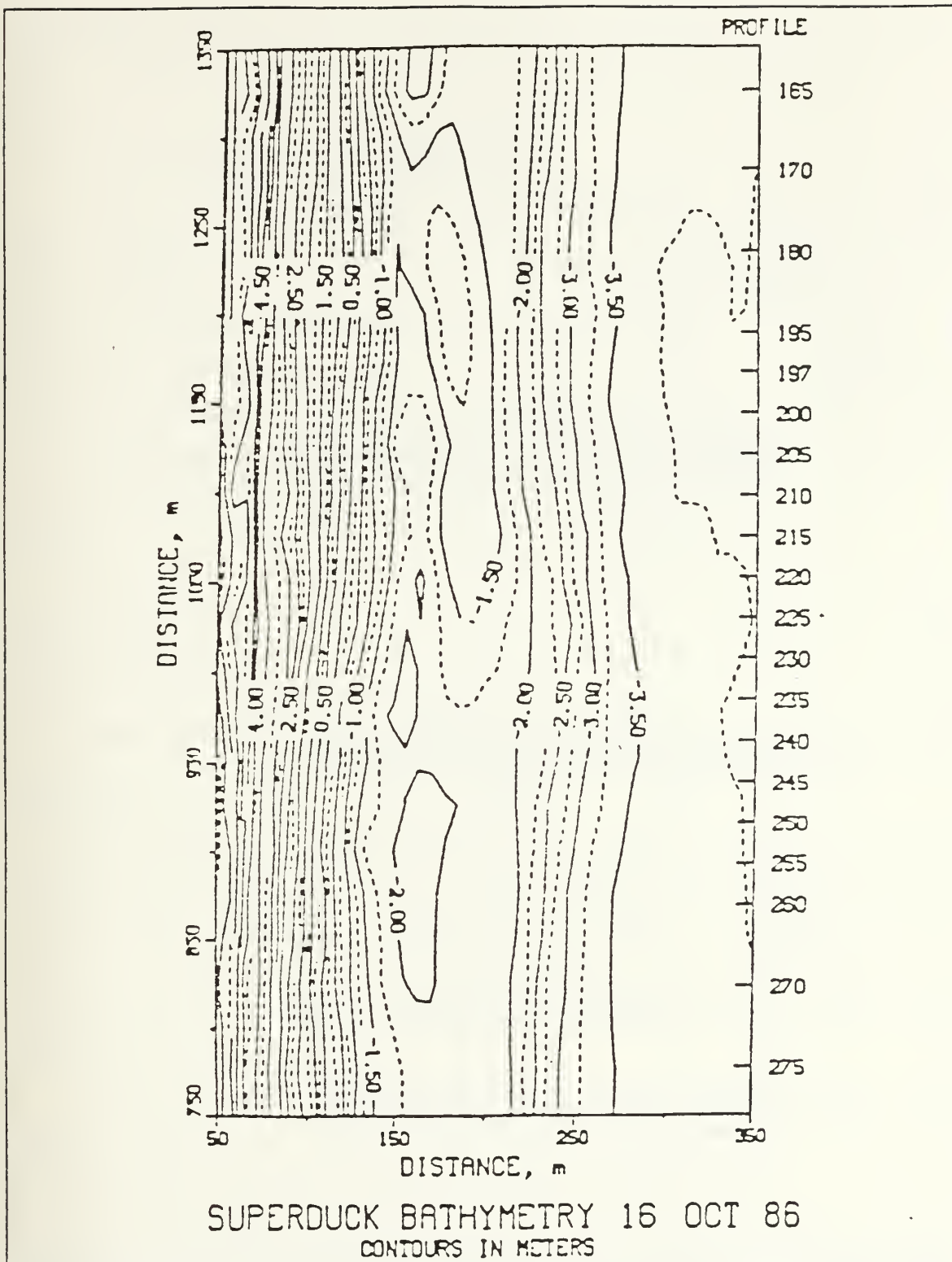


Figure 12. Two-dimensional bathymetry example, 16 October 1986.

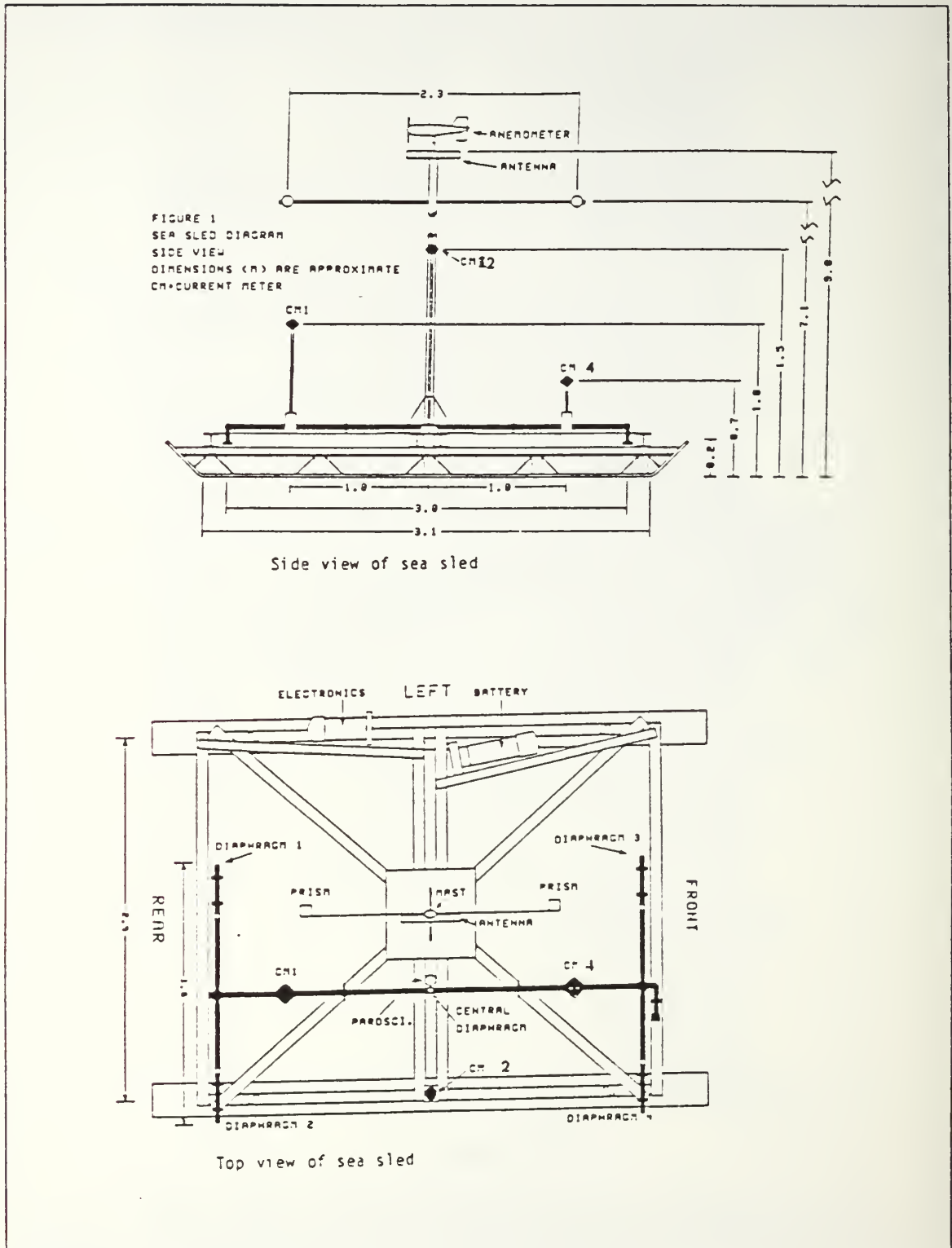


Figure 13. Side and top view of the SUPERDUCK sled.

hydraulically transmitted to the positive port of each differential pressure sensor, while the sea pressure at that location was sensed by the negative port of the sensor. A Paroscientific model 8020 digiquartz pressure sensor was installed adjacent to the center diaphragm to measure the absolute pressure.

Current velocities were measured using three Marsh-McBirney bi-directional electromagnetic current meters with spherical (4-cm diameter) probes mounted on the sled. These current meters are ideally suited for surf zone studies by providing accurate measurements in free stream turbulence as well as combined steady/oscillatory currents (Guza et al., 1986a). Both variable vertical stacking and slope array comparisons were considered in positioning the current meters on the sled frame. Two current meters were mounted at the centroids of the two triangular-shaped slope arrays at elevations 0.7 and 1.0 m above the bed, with the third current meter midway between at an elevation of 1.5 m. During sled deployment, the current meters were always positioned on the "up-current" side of the sled so as to avoid flow contamination by the sled mast.

The current meters' directional electrodes were aligned with the longitudinal axis of the sled frame by eye and are considered to be within $1 - 2^\circ$ of the true axis. During data analysis, a computational rotation is done for true alignment based on conservation of momentum flux outside the surf zone.

A single-point R.M. Young model 05103 wind monitor was mounted atop the mast to provide "in-situ" measurement of vector wind in the surf zone with simultaneous wave momentum measurements.

All equipment were battery-powered by 12 sealed lead-acid batteries housed in a watertight canister mounted on the sled. The analog data were PCM (pulse code modulated) encoded and then telemetered ashore by a system described by Lowe et al. (1972). The data were then decoded and recorded on 9-track magnetic tape. Data acquisition times for all the various SUPERDUCK experiments were referenced to a precise Eastern Standard Time (EST).

Visual observations of waves breaking on the sled mast were marked by an electrical trigger which registered a pulse on the data tapes. Although extremely tedious, this effort allows determination of the occurrence of wave dissipation events.

Precise orientation of the sled, with respect to true north and the SUPERDUCK experiment area, was obtained with the use of the FRF's Zeiss Elta-2 electronic surveying system. Two reflective prisms (5-cm diameter) were mounted at each end of a 2.4 m longitudinal mast spreader located approximately 7 m above the sled. From triangu-

lation. the relative positioning of these two prisms and their absolute positioning within the FRF coordinate system provided the required precise orientation (within 0.5°) of the current meters and slope array. Relative three-dimensional positions between various points on the sled and the prisms were obtained with separate Zeiss shootings prior to and after the sled's deployment in the SUPERDUCK experiment.

Prior to selecting an area of the surf zone to transect, the previous day's bathymetric profiles and contours were studied and changes in morphology noted. The geographic area with the highest degree of straight-and-parallel isobaths was selected for each day's operations. The runs were made during daylight and scheduled for 1-2 hours before and after a tidal change, so as to minimize the tidal effect and variation in mean shoreline location. This timing also coincided with the recording of all other SUPERDUCK data, which was accomplished within ± 2 hours of a tidal change on a 24-hour basis. The sled was initially towed offshore by the FRF's CRAB to a position just beyond the breaker zone for the first run of a surf zone transect. Subsequent runs were made at the point of maximum breaking, on top the nearshore bar, and in the nearshore trough. Each run was at least 35-minute in duration. The sled was brought inshore for each subsequent run of a transect by towing the sled with a chain tether attached to a four-wheel drive forklift located on the beach. Zeiss Elta-2 laser surveying shots of the sled's prisms were taken at the beginning and end of each run, with many runs having additional surveying shots during the run itself.

In addition to the sled's anemometer, simultaneous meteorological data of air temperature, sea surface temperature, atmospheric pressure, and wind velocity were recorded by other SUPERDUCK investigators at the end of the pier and near the FRF laboratory.

V. PRELIMINARY DATA ANALYSIS

Data analysis of the SUPERDUCK field experiment is addressed in the next four chapters. Preliminary data analysis is addressed in this chapter and includes data screening for data gaps and signal interference, instrument orientation, three-dimensional depiction of the mean current structure over the bar, and a discussion of homogeneity and stationarity for the experiment. Since surface wind stress is a major concern and few wind stress studies have been conducted in the surf zone, Chapter VI is entirely devoted to the parameterization of surf zone surface wind stress. The longshore momentum balance is addressed in Chapter VIII. The relative importance of each momentum term is calculated. Spatially-variable c_f 's are determined as residuals from the momentum balance. A longshore current model for planar beaches is modified to account for barred topography and its results are compared with observations in Chapter VIII.

A. INITIAL DATA SCREENING

The analog data were PCM decoded and then digitized at 8 Hz. Time series plots for all 16 channels of information were produced for the entire data collection period. These records were visually perused for data gaps and signal interference. Basic statistics (mean, variance, skewness and kurtosis) were calculated and formatted in tabular form. Temporal plots of two-minute means and variances were produced. This information was used to eliminate bad data collection periods and data channels. Data collection achieved a 98.5% successful collection rate with over 40 hours of data collected over a 10-day period. Nearly all of the eliminated data were identified at the beginning or end of a data run and therefore temporal continuity was maintained.

The wind direction portion of the R.M. Young wind monitor was not calibrated before its unexpected destruction by wave forcing on 18 October. Therefore the mean wind direction measured at the sled is unavailable. The mean wind direction measured at the end of the FRF pier (SethuRaman et al., 1987) was used for this research. Mean wind speed after 18 October was also taken from the end-of-pier data.

Occasionally, one or two current meters would be partially or totally above water during a sled data collection period, such as when the sled was atop the bar at low tide. These periods were identified from visual inspection of the time series, supplemented by field logbook entries. These data were not utilized in the radiation stress calculations.

B. SLED INTER-ORIENTATION.

A portable Zeiss laser ranging system was used to precisely measure the sled instrumentation positions relative to the sled. A hand-held reflective prism was placed at a designated measurement point on the sled (e.g., the right rear corner of the sled frame top) and that position designated as a three-dimensional reference point from which all other sled points of interest (prisms, current meter probes, slope array diaphragms, etc.) were measured. A complete laser measurement of the sled was conducted on 26 September 1986 and 20 October 1986. Sled modifications, such as instrument adjustment, mast replacement, etc., were noted in the field logbook so as to enable selection of the proper survey day for subsequent calculations. The Zeiss measurements were supplemented with engineer tape measurements.

The sled instruments were aligned to a three-dimensional local cartesian coordinate system referenced to the top of the sled frame by a rectangular coordinate rotation:

$$\begin{aligned}x_{\text{new}} &= x_{\text{old}} \cos \theta + y_{\text{old}} \sin \theta \\y_{\text{new}} &= -x_{\text{old}} \sin \theta + y_{\text{old}} \cos \theta\end{aligned}\tag{47}$$

where θ is the angle of rotation. A table of absolute three-dimensional distances between all points of interest was then generated. These distances were repeatedly used throughout the analysis.

During field operations, three-dimensional instrument coordinates, with respect to the FRF coordinate system were obtained from the sled prism three-dimensional coordinates by:

- relating the mast spreader, slope array, and current meter system longitudinal and vertical axes to the sled frame longitudinal and vertical axes,
- determining instrument pitch and yaw angles every 64 seconds from linear interpolation of the two-to-five survey fixes for a sled run collection period. All data were then adjusted every 64 seconds for the current sled pitch and yaw angles,
- adjusting current meter and anemometer heights above the bottom every 64 seconds for sled pitch and yaw angles, and
- correcting the distance between current meters for the sled's pitch and yaw angles.

Since all data were taken from a mobile sled rather than from fixed-bed instrumentation, it was imperative that the data were accurately translated into a coordinate system relative to the local bathymetric contours. Use of the Zeiss laser ranging system to accurately measure the sled points of interest, to fix the sled in the experiment area, and to provide comprehensive bathymetric data coverage, enabled this translation.

C. BEACH ANGLE ORIENTATION.

Location coordinates obtained from Zeiss-sighting of the sled's prisms were converted into sled pitch and yaw angles so as to correct the sensor data with respect to the horizontal and vertical and the FRF coordinate system. Pitch and yaw angles were calculated every 64 seconds from linear interpolation between the two most current Zeiss sightings to account for any sled movement during the data run. The instrument array orientation was then numerically rotated relative to the measured bathymetry. The selection of 64 seconds coincided with the ensemble averaging time for the spectral calculations.

Sled data were acquired from 11-18 October and 20-21 October 1986. Locations of sled data runs within the SUPERDUCK experiment site are illustrated in Figure 14. Incomplete survey sightings of the sled prisms due to salt incrustation on the prism lens and Zeiss operator error prevented determination of precise sled location on 13, 14 and 20 October. Therefore these three days of data were not used.

A complete bathymetric survey was not done on 11, 17 and 21 October due to high surf conditions or equipment availability. For sled collection days when no coincident bathymetry was surveyed, the previous or next day's bathymetry was appropriately selected based on minimizing any storm-induced morphological change (see Table 5).

A mean bathymetric contour direction was determined by applying a least-squares regression fit to the survey data offshore and located within approximately 100 - 150 m of the nearshore bar. This is the area of maximum bathymetric gradient with minimal slope farther offshore. The bathymetry inside the bar was more complex than offshore the bar, however the shoreward distance over which it could affect wave action was small ($O(30-50\text{ m})$). The most influential bathymetry was assumed to be that located on and offshore the bar.

The longshore length scale over which this regression fit was applied was weighted ($2/3 - 1/3$), with emphasis on the portion of the beach which favored the approaching waves (e.g., for waves approaching from the northeast, the northern offshore contours were favored by a factor of 2). The total distance assessed was varied from 100 to 250 m (or to maximum extent of precision bathymetry) with resultant mean orientation varying less than 0.5° between various distances considered. The mean orientation of the four "best-fit" straight lines (corresponding to 0.5 m contour intervals) was chosen as the mean bathymetric contour. The beach orientation angle was the angle between this mean contour and the coordinate system's y-axis. The beach orientation angle was

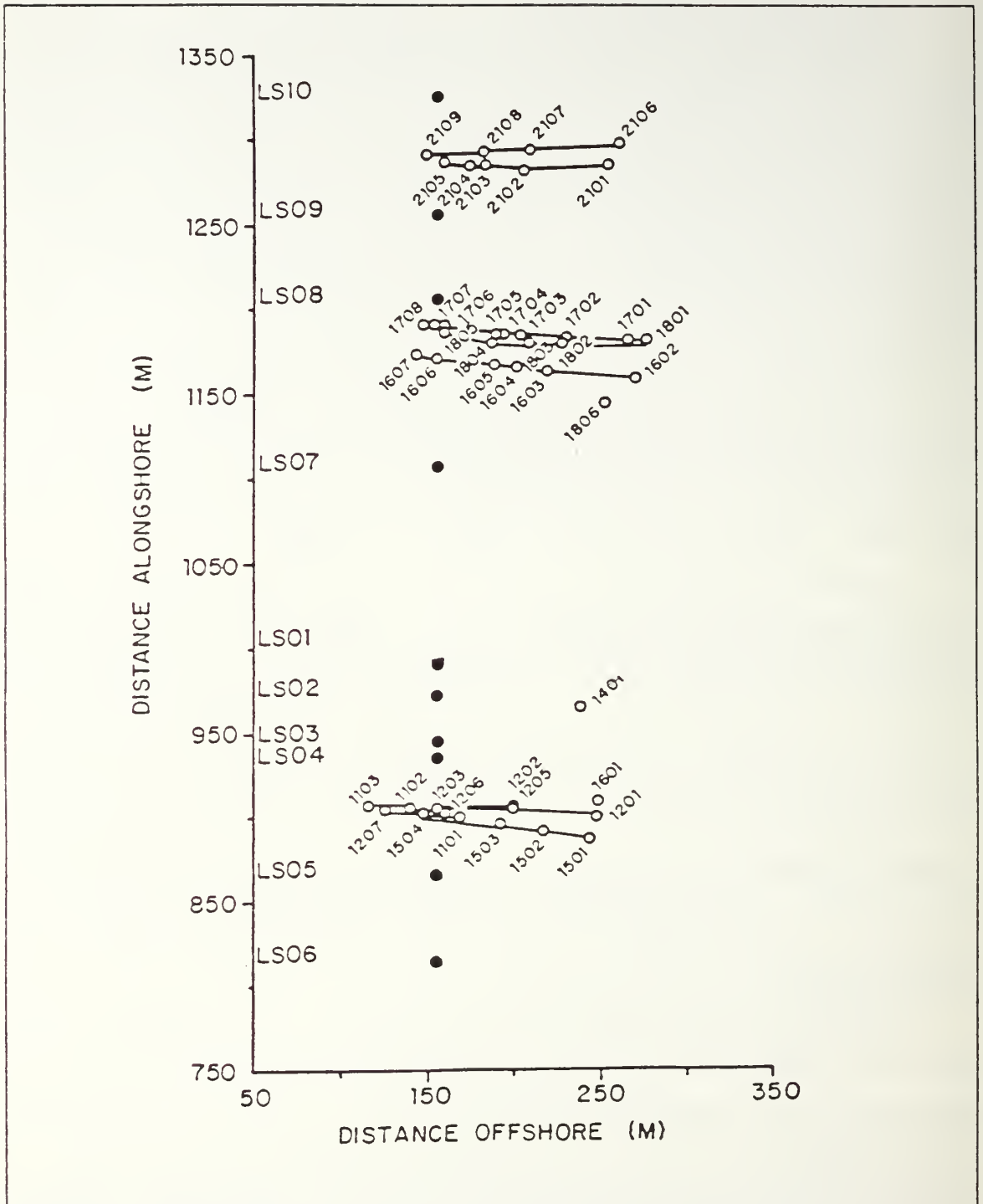


Figure 14. Sled data run locations. Open circles are sled run locations and closed circles are fixed-bed current meter locations.

then assigned as a constant for that transect and used in conjunction with instrument orientation which is described later.

Table 5. BATHYMETRY SELECTION AND BEACH ORIENTATION ANGLES

<u>Sled data day</u>	<u>Bathymetry day</u>	<u>Profile¹</u>	<u>Beach orientation angle (°)²</u>
11	12	250	0.5
12	12	250	0.5
15	15	255	4.0
16	16	197	-0.5
17	16	195	-0.5
18	18	195	1.5
21	22	170	0.8

¹ Profile locations are shown in Figure 10.
² Beach orientation angle is measured between the FRF coordinate system's y-axis and the mean bathymetric contour from on top and offshore of the bar. The angle was measured over a longshore length scale varying between 100-250 m.

A combined angle (θ_c) was used to convert from the yaw angle measured by the Zeiss to the correct rotation angle upon which to coordinate transform the u,v velocities. This combined angle was the sum of the sled yaw angle, the beach orientation angle, the angle between the current meter longitudinal axis and the sled centerline, and the angle between the mast spreader longitudinal axis and the sled centerline. This combined angle (θ_c) was used in equation (47), restated here with velocities substituted for coordinate locations, to perform the coordinate transformation:

$$\begin{aligned}
 u_{\text{new}} &= u_{\text{old}} \cos \theta_c + v_{\text{old}} \sin \theta_c \\
 v_{\text{new}} &= -u_{\text{old}} \sin \theta_c + v_{\text{old}} \cos \theta_c
 \end{aligned}
 \tag{48}$$

Fixed-bed current meter velocities were also converted to the FRF coordinate system using equation (48) where θ_c is field-measured orientation angles with respect to the FRF coordinate system.

D. CURRENT METER ORIENTATION PRIOR TO A TRANSECT.

Since the radiation stress gradient is conserved outside the surf zone, any difference in measured $S_{yx}(f)$ between the current meters on the sled is considered to be due to errors in current meter alignment with respect to each other and to the sled, current meter

calibration, or to imprecise orthogonal orientation of the dynamic measurements with respect to the assumed straight-and-parallel bathymetric contours. The contours outside the bar were nearly straight-and-parallel (see Figure 12 and Appendix B). Therefore, current meter alignment or gain was considered in error. Orientation of the current meters' axes with the sled's axes was considered to be within $1 - 2^\circ$.

To correct for the radiation stress difference between two current meters outside the surf zone, one current meter was assumed to be true in both gain and alignment. The other current meter was then rotated numerically using equation (48), or adjusted in gain, until the radiation stress gradient was minimized.

Two current meters and two adjustment criteria (gain and rotation) represent four initial parameters for adjustment:

- assume the front current meter is correct and adjust the rear current meter in gain (RGAIN) or rotation (RTWIST), or
- assume the rear current meter is correct and adjust the front current meter in gain (FGAIN) or rotation (FTWIST).

Because the sled instruments undergo significant stress in the surf zone, all sled transects commenced with an orientation run outside the surf zone to allow for daily reorientation. A numerical orientation prior to *each* transect's calculations was employed during data analysis. The resulting possible orientation adjustments for each transect and parameter (RGAIN, RTWIST, etc.) are shown in Table 6.

The adjustments and resulting total radiation stress (S_{yx}^T) were found to be linearly related, therefore an iterative method of linear interpolation, or "regula falsi" method (Gerald, 1978) was utilized to determine the orientation required to minimize S_{yx}^T between the current meters. Convergence to within a radiation stress gradient tolerance of 10^{-3} Jm^{-2} was generally obtained within six iterations. $S_{yx}(f)$ spectra with these adjustments were perused to ensure that the strict numerical definition of a conserved radiation stress gradient achieved a realistic and comparative spectral shape for the current meters.

The selection of orientation by gain or rotation does have constraints when dealing with bi-directional radiation stress spectra, which commonly occurred during SUPER-DUCK. Examples of typical bi-directional spectra are schematically illustrated in Figure 15. The spectra indicate swell with a 10-second mean period from the southeast, while wind waves with a 5-second period and significantly more energy approached from the northeast. Spectra from the front current meter are assumed correct and are depicted by a solid line, whereas the spectra from an incorrectly oriented or calibrated rear

current meter (and requiring gain or rotation to make its spectra coincide with the front current meter spectra) are depicted by a dashed line. In the first example, gain is the obvious correction whereas in the second example, rotation is the obvious correction.

All three current meters were calibrated in a flow tank before and after the experiment by different laboratories. The agreement in pre- and post-calibration was $\pm 3\%$ in gain and $0.01 - 0.04 \text{ ms}^{-1}$ in offset. This agreement is considered excellent for meters exposed to the robust surf zone. With this agreement, coupled with the subjective analyses of the different spectral shapes corresponding to different orientation combinations, and the field accuracy of current meter alignment ($\pm 2^\circ$), it was decided to utilize current meter rotation as the orientation criteria. Rear current meter rotation (RTWIST) was arbitrarily selected over front current meter rotation for the entire data analysis, except for Run 18-1 for which front gain was used. Resultant RTWIST angles are within the values of field accuracy alignment. Sensitivity to this rotation and the effect of other rotations (FTWIST only or both FTWIST and RTWIST) is addressed in the error analysis discussion in Chapter VII.

After completing this rotation for the rear current meter, the side current meter was rotated (STWIST) in a similar manner and its S_{yx}^T values served as a first-order comparison to the other two current meters values for S_{yx}^T . These orientation rotations were performed after the θ_c coordinate transformation were fixed for the calculations inside the surf zone for that particular transect. This post-calibration procedure provided a means of improving the accuracy of the current meter calibration and alignment. The procedure is essential to obtaining realistic physical results from the data and is a distinguishing feature of this research.

E. MEAN CURRENT OBSERVATIONS

1. Overview

Three-dimensional portrayal of the mean current structure is illustrated in Figure 16 and Appendix A (Figure 35 through Figure 40). All current vectors represent 34.1-minute means. The numbers indicate the data run location. The short dotted lines above each run location indicate the mean water level (MWL) measured by the sled's pressure sensor for that location and time. The different arrowheads delineate the height of measurement as illustrated in the three-dimensional box. MSL is indicated by the long dashed line. Only current meters which were completely submerged for the entire run duration are depicted. Thus some run locations have only one or two current vectors.

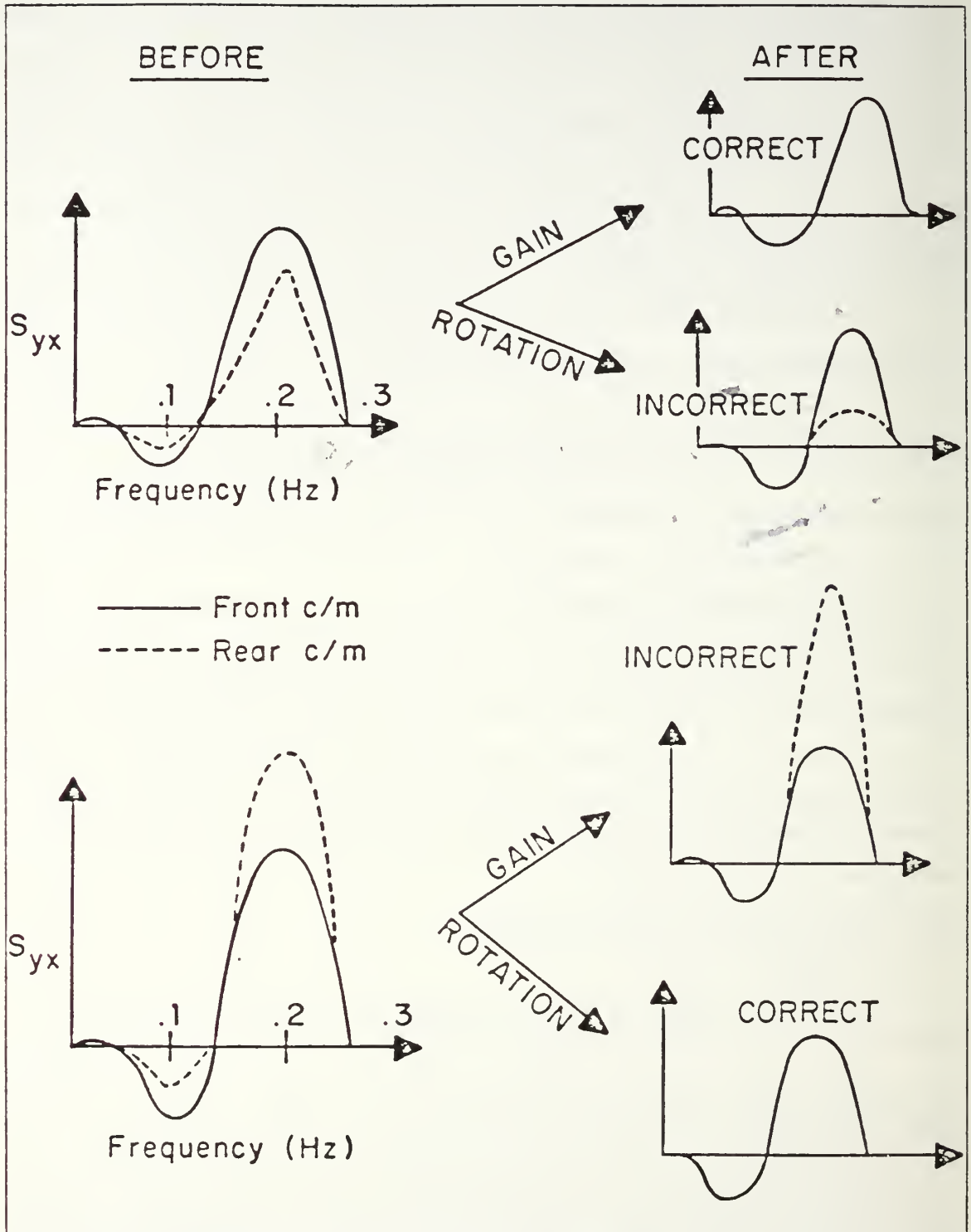


Figure 15. Constraints on current meter rotation or gain correction for bi-directional spectra outside the surf zone.

Table 6. INSTRUMENT ORIENTATION PARAMETERS. Rear and front current meter gains and rotations ("TWIST") required to conserve the radiation stress gradient outside the surf zone.

<u>Run</u>	<u>Rear Gain(%)</u>	<u>Front Gain (%)</u>	<u>Rear Twist (deg)</u>	<u>Front Twist (deg)</u>
12-1	-5.25	5.54	-0.81	0.80
15-1	1.04	-1.03	-0.29	0.27
16-2	4.57	4.38	-2.86	2.34
17-1	-0.58	0.58	0.12	-0.11
18-1	5.20	-4.94	-2.14	1.89
21-1	1.40	-1.44	0.02	-0.02
21-6	-	-	-0.41	0.40

- '-' indicates no iterative convergence or acceptable spectrum shape.
- 'Twist's', or current meter rotations, are in units of degrees.

The sled was first deployed on 11 October during the first of two SUPERDUCK storms. High surf (H_{mo} greater than 3 m) prevented sled deployment beyond the surf zone, therefore there was no instrument orientation run for that day. The high surf also prevented completion of a minigrid survey by the CRAB. Therefore the bathymetric profile, as well as the instrument orientation parameter was obtained from the 12 October data. The unrealistic c_f values later calculated for 11 October highlight the necessity for an instrument orientation prior to a transect. The 11 October data set was therefore deleted from further consideration.

The 12 October data revealed a meandering rip current. Two transects were completed with Runs 12-1 and 12-4 being the orientation runs outside the surf zone. Run 12-4's data were not used because of a Zeiss system malfunction. Therefore Run 12-1 is the only data run outside the surf zone in Figure 36. The strong offshore flow, $O(0.5 \text{ ms}^{-1})$, at all three levels above the bed was substantiated by comparison with current vectors from the longshore array. Although this rip current eliminates homogeneity for S_{yx}^T calculations, it provides a unique data set for a rip current study separate from this research.

October 15 is the first day with an established bar-trough system. Run 15-1 is the orientation run outside the surf zone. Strong flow, $O(1.0 \text{ ms}^{-1})$, is apparent inside

SUPERDUCK
16 Oct 86
Profile 197

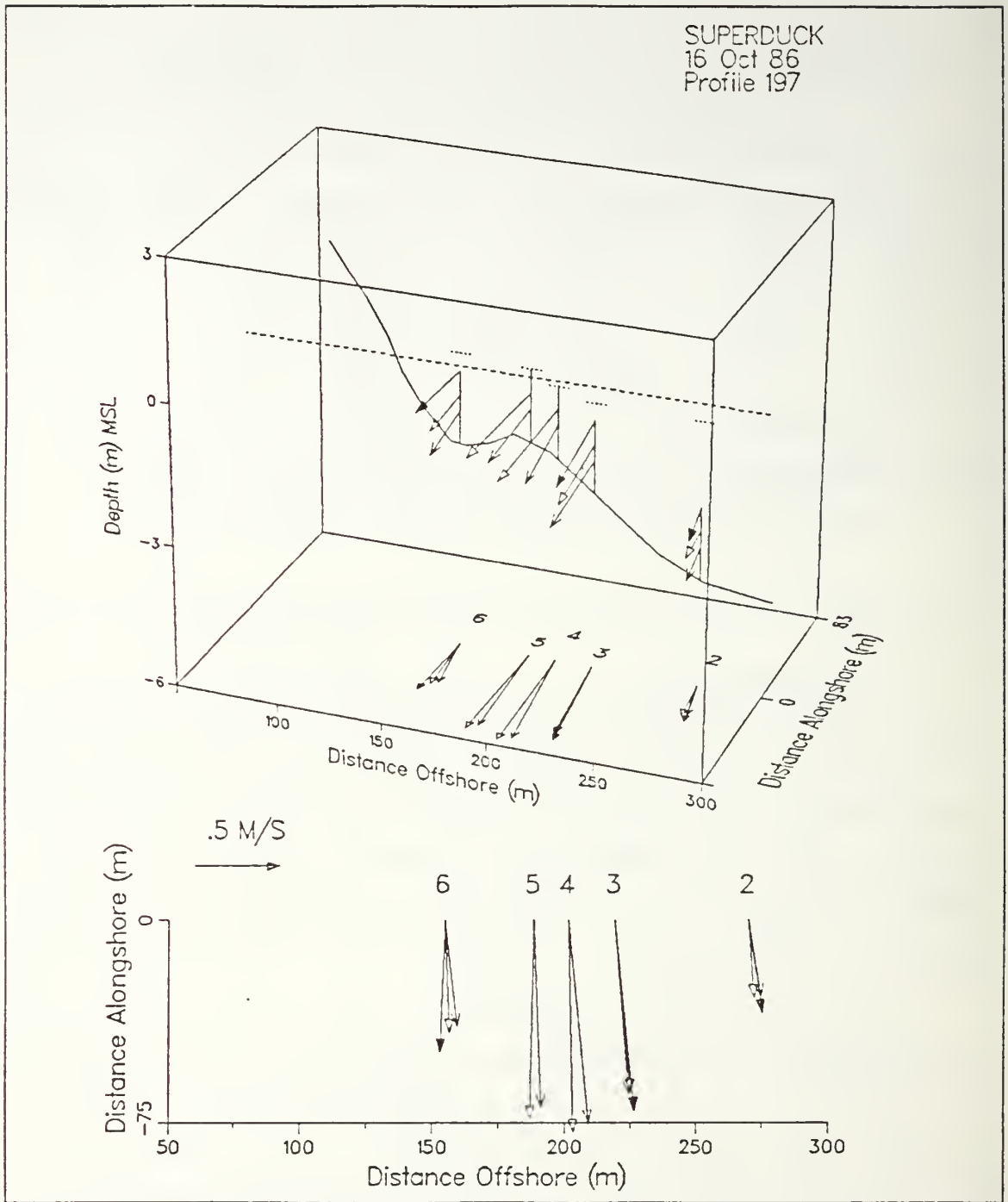


Figure 16. Mean current structure across the bar on 16 October 1986. Numbers represent data runs, short dotted lines are MWL's, and distance alongshore is arbitrary.

the surf zone with a 50% reduction in speed outside the surf zone. All speeds are nearly uniform in depth with slight speed reductions for sensor elevations closer to the bed. Multi-level current directions in the trough and outside the surf zone are co-linear. Angular deviation of currents with height (maximum 20°) are apparent at the location of maximum breaking, with the lower sensor elevations exhibiting a bias toward offshore flow near the bed.

October 16's data have the strongest velocities of all the sled data with speeds exceeding 1.0 ms^{-1} . Run 16-2 was the orientation run outside the surf zone. Current directions and speeds were nearly uniform with depth, with current speeds exhibiting a slight decrease closer to the bed. Strongest flows were on the offshore side of the bar.

Significantly weaker currents were measured on 17 October. Run 17-1 was the orientation run outside the surf zone. The three trough runs all produced negligible current. A combination of low tide and low wave heights [$H_{rms} O(0.2 \text{ ms}^{-1})$] on this day may have caused most waves to break on the bar and thus cause the negligible current in the trough. The onshore flows at Run 17-4 and 17-5 were due to the current meters' location in the upper water column of the shallow water.

Strong flows, $O(1.0 \text{ ms}^{-1})$, were again measured on 18 October. Runs 18-1 and 18-6 were orientation runs outside the surf zone for two separate transects. Run 18-6 was the start of a second transect which was abruptly terminated when the sled mast snapped in the high surf during Run 18-7. A nearly uniform horizontal velocity gradient ($\partial V/\partial x$) is observed with a maximum current located offshore and just before the bar crest. Vector uniformity is observed.

Two transects were conducted on 21 October. Runs 21-1 and 21-6 were orientation runs outside the surf zone. Unfortunately current velocities during both transects were too weak and variable in direction for meaningful analysis. Hence this data set was eliminated from further consideration, leaving only four (15-18 October) of the original nine transects for further analysis.

2. Discussion

Profiles of longshore currents across the barred beach generally showed significant spatial variability. Maximum flow is observed at the steepest offshore slope of the bar, generally just below the bar crest, while weaker currents are found outside the breaker zone and in the trough. A typical distribution of longshore currents across a barred beach is illustrated in Figure 16. Longshore currents are generated after wave breaking (Run 3 and 4) and are extended outside the surf zone, possibly by turbulent

momentum exchange. The vertical distribution of longshore and cross-shore velocities are compared to normalized water depth (Figure 17). Current measurements for one run are denoted by a continuous line connecting only those current meters which were entirely submerged for the entire run. Thus some shallow locations have only one or two current means illustrated. The plot of October 16 longshore velocities serves as a legend and has numbers beside the mean current symbols. The numbers represent the chronological order of runs in a transect, with the most offshore run being labeled as number 1.

The magnitude of the cross-shore flow is generally much less than the longshore flow and is of $O(0.2 \text{ ms}^{-1})$. The longshore flow velocities on three of the four data days are of $O(1.0 \text{ ms}^{-1})$. The cross-shore velocities exhibit a relative onshore flow in the upper third of the water column and relative offshore flow in the lower third of the water column. The lower mean currents after wave breaking tend to flow more offshore, thus exhibiting a limited "spiral" distribution with height and indicating the presence of an undertow flow (an offshore flow near the bed). The observations are in agreement with cross-shore theory (e.g., Svendsen et al., 1987). The longshore velocities indicate nearly depth uniform flow with a slight velocity increase with elevation. This depth uniform flow confirms the appropriateness of the depth-integration assumption for longshore flow. Longshore vertical current structure did not exhibit a logarithmic profile, therefore the profile method for the determination of bed shear stress coefficients is not applicable.

3. Stationarity and Homogeneity

Stationarity over the transect was investigated by examination of S_{yx}^T calculated from measurements outside the surf zone by a fixed-bed pressure and velocity ('puv') sensor designated "south tripod". The formulation for this calculation is discussed later in equations (78) and (79). Sequential 34.1-minute spectra and resulting S_{yx}^T were calculated for 15-18 October (Figure 18 and Appendix A (Figure 41 through Figure 43)). The short lines between the arrowheads at the top of the S_{yx}^T graphs represent sled run durations, with the numbers above the lines identifying the sled run number of that day. These comparisons are considered a *strict* indication of stationarity because of the sensitivity of S_{yx}^T to changes both in wave height and wave incidence angle.

The 'puv' data were collected by the FRF for four-hour periods, therefore these data were not completely synoptic with sled deployment times. The 'puv' data were digitized at 2 Hz. Spectral analysis was accomplished by Bartlett ensemble averaging which resulted in 31 degrees of freedom. Chi-squared confidence limits for 95% confi-

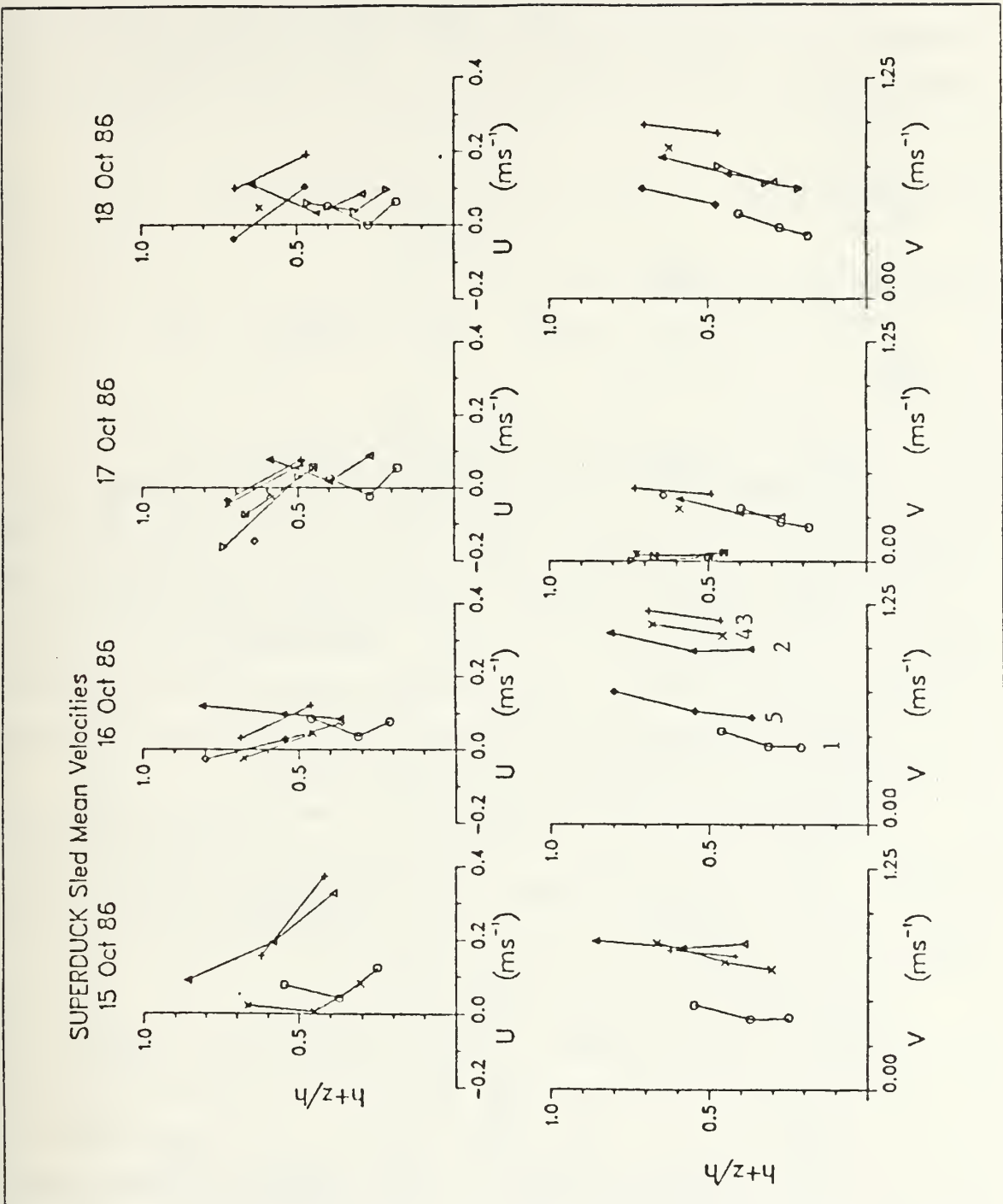


Figure 17. Mean cross-shore U and longshore velocity V profiles versus normalized water depth for 15-18 October. The 16 Oct V profile serves as a legend for the data symbols, where the numbers denote chronological order of runs in a transect with the most offshore run labeled as number 1.

dence yields a range for spectral estimates ($S_{yx}(f)$) between 0.66 and 1.81 of the spectral estimate calculated. Ninety-five percent confidence limits for the integrated or total radiation stress (S_{yx}^T , see equation 80) were based on the Fisher-Z transformation (Miller and Freund, 1985):

$$Z = \frac{1}{2} \ln \left[\frac{1+r}{1-r} \right] \quad (49)$$

where the correlation coefficient (r) is:

$$r = \frac{cov_{uv}}{\sigma_u \sigma_v} \quad (51)$$

and the covariance is calculated by the integrating the co-spectrum of u, v .

The October 15 runs inside the surf zone (15-2 through 15-4) appear to have a reasonably constant (within the bounds of the confidence limits) S_{yx}^T value with no more than a 10% variation about the mean. Both October 16 and 17 data sets have a constant S_{yx}^T with minimal variability. October 18 data also appears to have a reasonably constant S_{yx}^T , with the exception of Run 18-5 which occurred at the time of an S_{yx}^T increase. Fortunately, this run is within the trough, where flow conditions are not as rapidly affected by offshore change as are locations on the offshore side of the bar. Even with this S_{yx}^T increase, the variation is no more than 20% about the mean.

Tidal variation during an individual data run was approximately 5% of the mean water depth. Tidal variation over an entire transect ranged from 14% - 50% of the mean transect depth, with the longest transect duration having the largest tidal variation. The tidal range for each transect is illustrated by the short dotted lines in Figure 16 and Appendix A (Figure 35 through Figure 40).

Another test for stationarity is illustrated in Figure 19 where H_{mo} and wave incident angle (α) calculated from the 'puv' sensor are plotted from 0500 - 2000 E.S.T. for each day and compared with sled run times. H_{mo} values are denoted by an "x" and α values are denoted by an "o". Each short line at the top of the graphs represents the duration of a sled run, with the number above the line denoting the sled run number of that day. Comparison of Figure 19 with Figure 18 and Appendix A (Figure 41 through Figure 43) offers some insight into the nature of radiation stress. For example, the decrease in S_{yx}^T observed on 15 October from 1000 - 1200 was due to a slight reduction in wave height and a significant decrease in wave incident angle. In conclusion, no significant change in S_{yx}^T , H_{mo} , or α was observed during the times of sled deployment.

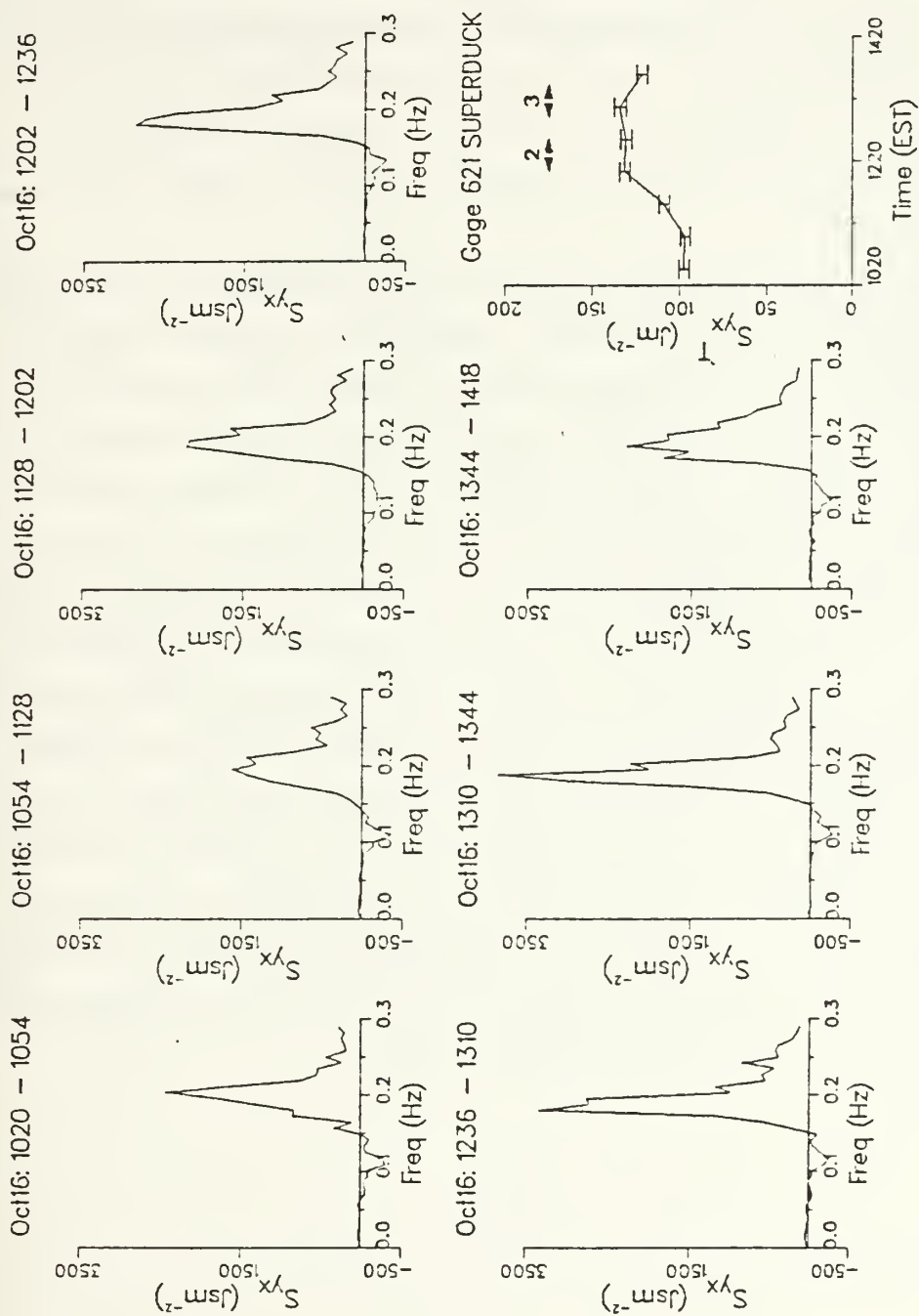


Figure 18. Offshore S_{yx} spectra and S_{yx}^T from 'puv' gage 621 for 16 October 1986. Numbers indicate data runs. Intervals are 95% confidence.

Stationarity requirements are therefore assumed satisfied. It should be noted that the stationarity being investigated here is measured over relatively long temporal scales (measured in hours) whereas the temporal term examined later in Chapter VII is measured over much shorter temporal scales (measured in minutes). In other words, the assumption of stationarity at this stage of the data analysis does not preclude contributions from the temporal term (e.g. due to edge waves) to the momentum balance.

Similarity of mean current vectors in the experiment area was considered a test for homogeneity inside the surf zone. Similarity was considered satisfied when all current directions were in the same quadrant with speeds $\pm 50\%$ of an overall mean for the same relative on-offshore position. This definition was chosen considering the bounds of instrument accuracy, current vertical variability, the number of instruments in the experiment area, and the variable elevations of the longshore array current meters. No visual evidence of rip currents was observed during 15-18 October. Two-dimensional plots of sled-determined current vectors were created for each transect, along with the fixed-bed array of mean current vectors, temporally centered for the sled transect. These comparisons were then overlaid on the coincident bathymetry (Appendix B). The bathymetry allows for isolation of cases where bathymetric forcing is dominant. Variable current direction is observed in the trough on 17 October. However this is not considered violation of homogeneity because of the extremely weak current speed in the trough on that day. Perusal of this data indicates the assumption of homogeneity for 15-18 October is reasonable. Data sets from 15-18 October are considered to meet the dual assumptions of homogeneity and stationarity.

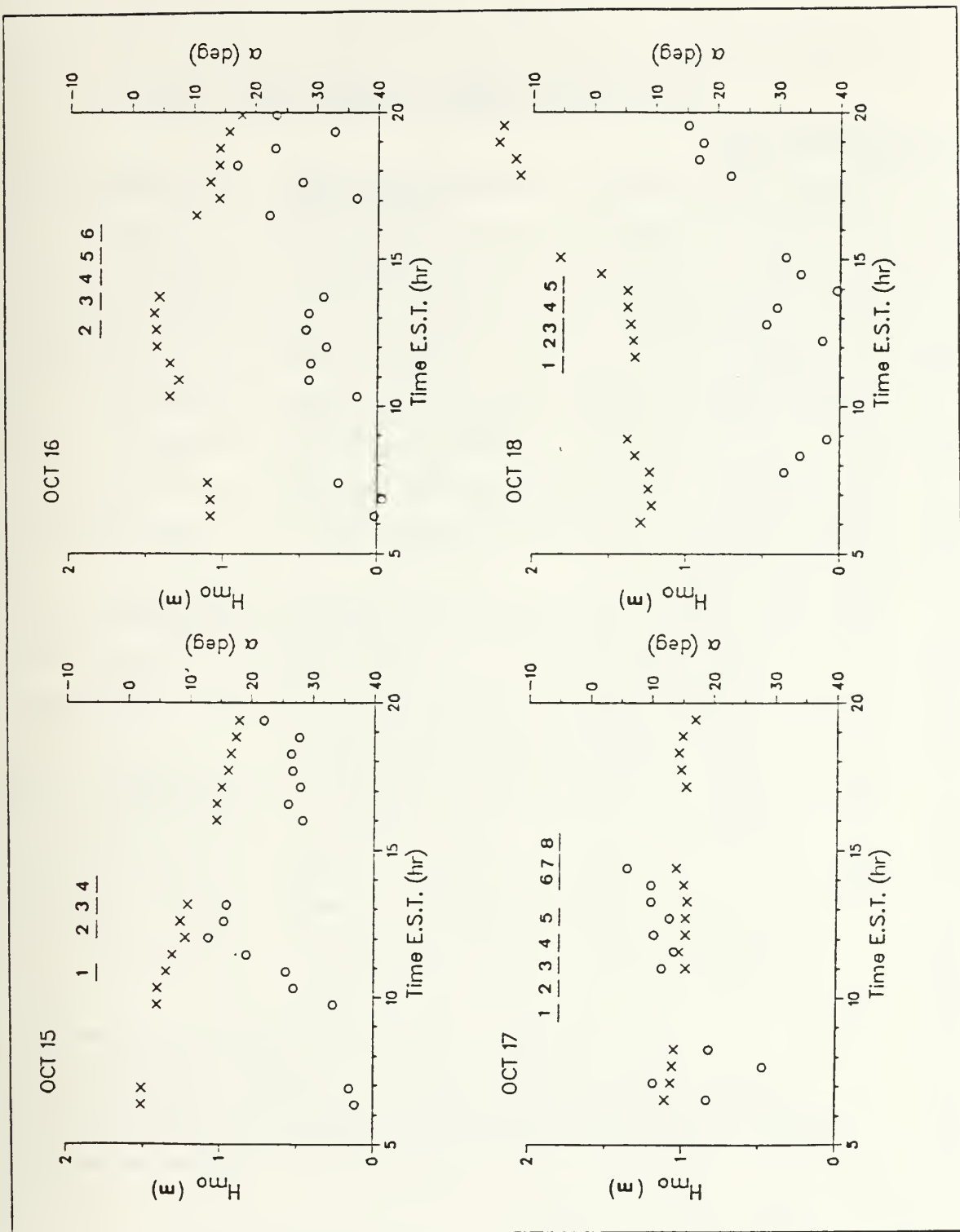


Figure 19. H_{m0} ('x') and wave incidence angle ('o') versus time for 15 - 18 October 1986. Numbers indicate data runs.

VI. SURFACE WIND STRESS (τ^y)

A. INTRODUCTION

The objective of this chapter is to determine representative surface wind stress for the *surf zone* based on atmospheric drag coefficients calculated from surface wind stress measured *outside the surf zone* and wind speeds measured by the sled anemometer *inside the surf zone*. Dr. S. SethuRaman and an investigative team from North Carolina State University calculated surface wind stress for the end of the FRF pier during SUPER-DUCK. Wind speeds were measured with a three-component Gill anemometer at a height of 18.7 m above mean sea level (MSL) and wind stress was calculated using the eddy correlation method. Although this wind stress measurement was outside the surf zone, it is a simultaneous and uncontaminated measurement over water and within 500 m of the sled transect areas.

A synopsis of the synoptic scale meteorological conditions during October 1986 is listed in Table 7. Sled deployments were on 11-12, 15-18, and 21 October. Predominant meteorological features were onshore winds and an unstable atmospheric boundary layer (as indicated by the air-sea temperature difference in Table 7).

The Gill anemometer has three polystyrene propellers which are rigidly mounted with their axes at 90° from each other. These propellers drive three d.c. generators whose output is directly proportional to wind speed. The anemometer has a threshold of 0.1 ms^{-1} , a distance constant of 0.8 m, and can be sampled at 100 Hz. Although additional wind measurements were acquired at 22 m and 13.7 m, the eddy correlation method is selected over the profile method for wind stress determination due to its increased accuracy. Air temperature (T_a) and relative humidity (RH) measurements were acquired by a YSI 44018 Thermilinear thermistor and a slow response relative humidity sensor (Model 207) manufactured by Campbell Scientific, respectively. Both instruments were mounted at 18.7 m above MSL. A YSI temperature probe measured sea temperature (T_s) at a depth of 0.6 m below MSL.

Wind stress determined by the eddy correlation method is computed by:

$$\tau = \rho_a \left[\overline{(u'w')^2} + \overline{(v'w')^2} \right]^{1/2} \quad (51)$$

Table 7. SUPERDUCK SYNOPTIC-SCALE METEOROLOGICAL DATA (OCTOBER 1986) (from SethuRaman et al., 1987).

Date	Wind Field	Brief Description	$T_a - T_s$	Clouds	Remarks
1	SW 3-7.5	High dominates	6.4	Clr	
2	Var. 3-7	High dominates	5.5	Cu,As S-B	Hazy
3	SE-SW 1-6	High dominates	1.7	Ac,As S-B	
4	SW 7-10	High dominates	7.9	Clr	
5	SW-NE 6-7	Frontal passage	3.3	Cu,Sc S-B	
6	NW-NE gust 13	Post-frontal region	-2.1	Cu,Ac S	Swell
7	NE-SE 3-5	High dominates	-3.5	Ac,Cu, B-S	
8	SE-SW	High dominates	2.1	Sc,As B-O	
9	NE-SE 1-5	Cold front approach	0.7	Cu,Sc S-B	Rain
10	NE 13 - 16*	Cold front passage	-2.3	St,Sc O	Rain
11	NE 11 - 16*	Post-frontal region	-0.8	St,Sc O-B	Swell
12	NE 6-10	High dominates	-0.5	Ac,As S	
13	SE 3-8	Cyclogenesis along shore	1.0	Cu,As B	Rain
14	SW 6-8	Cold front approach	1.4	TCu,St O	Rain
15	NE 7-11	Frontal passage	-6.8	St,Cu	Swell
16	NE-NW 7 - 13*	Post-frontal region	-3.3	St,Sc O-B	Swell
17	NE-NW 4-8	High dominates	-2.3	Cu,Ac S	
18	NW-NE 9 - 14*	High dominates	-3.7	Cu S-B	Swell
19	NE-NW 6 - 13*	High dominates	-2.9	Cu S-B	
20	NE 5-8	High dominates	-2.0	Clr	
21	NE-SE 1-3	High dominates	-1.3	Clr	
22	SW 3-5	High dominates	1.7	Clr	
23	SW 4-6	High dominates	2.5	Cs S-B	
24	NW-NE 3-9	High dominates	0.0	Ac,Cs S-B	
25	NE-E 7-10	Warm front section	0.0	Sc,Ac O	Rain
26	SE-SW 5-7	Cold front approach	4.1	St,Cu O	
27	SW-NE 3-5	Cold front passage	2.2	Sc,As B-O	Rain
28	NE-SE 2-8	High dominates	-0.6	Cu	
29	SW 1-5	Transition of 2 highs	0.7	Sc,Cs B-O	
30	SW-NE 4-7	Front sweeps through	-1.2	Sc,Cs B-O	
31	NE gust 12	High dominates	-0.8	Cu,Sc S-B	

Comments:

1. S: scattered, B: broken, Clr: clear, O: overcast
2. Cyclogenesis occurred in nearby region on 11th and 16th
3. Strong upper-level trough accompanied cold front during 14-18 Oct
4. * indicates high-energy cases of SUPERDUCK experiment
5. $T_a - T_s$ was measured at 1400 EST which was the approximate mid-time of the sled transects.

where u, v, w denote wind speed in the horizontal and vertical directions and the primes ($'$) denote deviations from the mean. Hourly means of wind stress data (SethuRaman et al., 1987) allow determination of an atmospheric shear velocity (u_*):

$$u_* = \left(\frac{\tau}{\rho_a} \right)^{\frac{1}{2}} \quad (52)$$

where τ is the surface wind stress.

Inherent in the u_* determination is the inclusion of atmospheric stability. The description of the turbulent regime of a temperature-stratified friction layer is based on the Monin-Obukhov similarity theory, which defines the stability-dependent vertical wind speed gradient as:

$$\frac{\partial u}{\partial z} = \frac{u_*}{\kappa z} \phi_m \left(\frac{z}{L} \right) \quad (53)$$

where z = height above the surface (m),
 L = Monin-Obukhov length,
 κ = von Karman's constant (0.4), and
 ϕ_m = a stability function.

The non-dimensional ratio z/L is a measure of atmospheric stability with negative values denoting unstable conditions and positive values denoting stable conditions. z/L is defined as:

$$\frac{z}{L} = \frac{g \kappa z T_v^*}{T_v u_*^2} \quad (54)$$

where T_v = virtual temperature (degrees Kelvin), and
 T_v^* = virtual temperature scaling parameter.

T_v is often considered to be the mean virtual potential temperature within the surface layer (Geernaert et al., 1987a) rather than its more strict definition of:

$$T_v = T_a (1 + .61q) \quad (55)$$

where q = specific humidity. In this research, T_a in degrees Kelvin was substituted for T_v .

Integrating equation (53) from the surface ($z = z_o$, where $u = 0$) to an arbitrary height ($z = z$, $u = u_z$), an expression for a stability-dependent logarithmic wind velocity profile is obtained:

$$U_z = \frac{u_*}{\kappa} \left(\ln \frac{z}{z_o} - \Psi_m \left(\frac{z}{L} \right) \right) \quad (56)$$

Determination of z/L requires an iterative process, since T_{v*} is also a function of stability. With all z/L 's initially set to zero, and the humidity roughness scale (z_{oq}) and temperature roughness scale (z_{ot}) set equal to 10^{-6} , an iterative approach (Appendix C) based on the stability flux profile relation of Businger et al. (1971) is utilized to determine z/L . Ψ_h and Ψ_q are assumed equal and formulated as (Large and Pond, 1981):

$$\Psi_h = \Psi_q \quad , \quad \left[\begin{array}{l} x = (1 - 16(\frac{z}{L}))^{\frac{1}{4}} \\ \Psi = 2 \ln \left[\frac{(1 + x^2)}{2} \right] \quad \frac{z}{L} < 0 \\ \Psi = -7(\frac{z}{L}) \quad \frac{z}{L} \geq 0 \end{array} \right] \quad (57)$$

The air at the air-sea boundary is assumed saturated.

The stability function, ϕ_m , is described by the Businger-Dyer formula for unstable stratifications (Businger et al., 1971) as:

$$\phi_m = (1 - 16 \frac{z}{L})^{-\frac{1}{4}} \quad (58)$$

The expression for Ψ_m is (Paulson, 1970):

$$\Psi_m = 2 \ln \left[\frac{1 + \phi_m^{-1}}{2} \right] + \ln \left[\frac{1 + \phi_m^{-2}}{2} \right] - 2 \tan^{-1} \phi_m^{-1} + \frac{\pi}{2} \quad (59)$$

which is an empirical representation of comprehensive observations over smooth terrain.

B. DETERMINATION OF AN ATMOSPHERIC DRAG COEFFICIENT FOR THE SURF ZONE

Atmospheric shear velocity and L are independent of height in the surface boundary layer (Panofsky and Dutton, 1984) and are assumed to apply for the sled transect locations in the surf zone located within approximately 500 m of the surface wind stress

measurements. Atmospheric shear velocity and L for the sled runs are linearly interpolated from the hourly pier data for the temporal midpoints of each sled run.

Boundary layer investigators universally convert drag coefficients to be applicable at 10 m height to allow intercomparison between different investigations. For equation (56) to be valid, a stability-dependent wind speed at 10 m (U_{10}) is required. U_{10} is obtained from equation (56) as:

$$U_{10} = u_{z_m} - \frac{u_*}{\kappa} \left[\ln\left(\frac{z_m}{10}\right) + \Psi_m\left(\frac{10}{L}\right) - \Psi_m\left(\frac{z_m}{L}\right) \right] \quad (60)$$

U_{10} is first calculated from the hourly pier data. Then two drag coefficients for a height of 10 m at the pier are determined -- the stability-dependent C_{d10} (from equation 11 with $U_{10} - U_o$ substituted for W) and the stability-independent or neutral drag coefficient, C_{dn10} (from equations 11, 52, and 56):

$$C_{d10} = \frac{\tau}{\rho_a (U_{10} - U_o)^2} \quad (61)$$

$$C_{dn10} = \left[C_d^{-\frac{1}{2}} + \left\{ \frac{\Psi_m\left(\frac{10}{L}\right)}{\kappa} \right\} \right]^{-2} \quad (62)$$

The surface boundary condition (U_o), represented by a mean current, was taken into account to determine the wind speed relative to the moving water surface. U_o is assumed zero for the end of the pier. U_o is represented by the mean surf zone current for the sled locations.

Wind, wave height, atmospheric stability, and initial pier C_d data versus time for the seven days of sled deployment are shown in Figure 20 and Appendix A (Figure 44 through Figure 46). Drag coefficients and pier and sled wind speeds are adjusted to 10 m elevation. Sled anemometer winds are represented by the first, mid, and last two-minute mean wind of the run. The clear arrowhead depicts the hourly mean wind vector for the pier wind and the solid arrowhead depicts a 34-minute mean wave direction vector for a location near the pier end. The point of the arrowhead indicates the time for which the vector is valid. Wind and wave directions are relative to the shoreline which is represented by the y-axis.

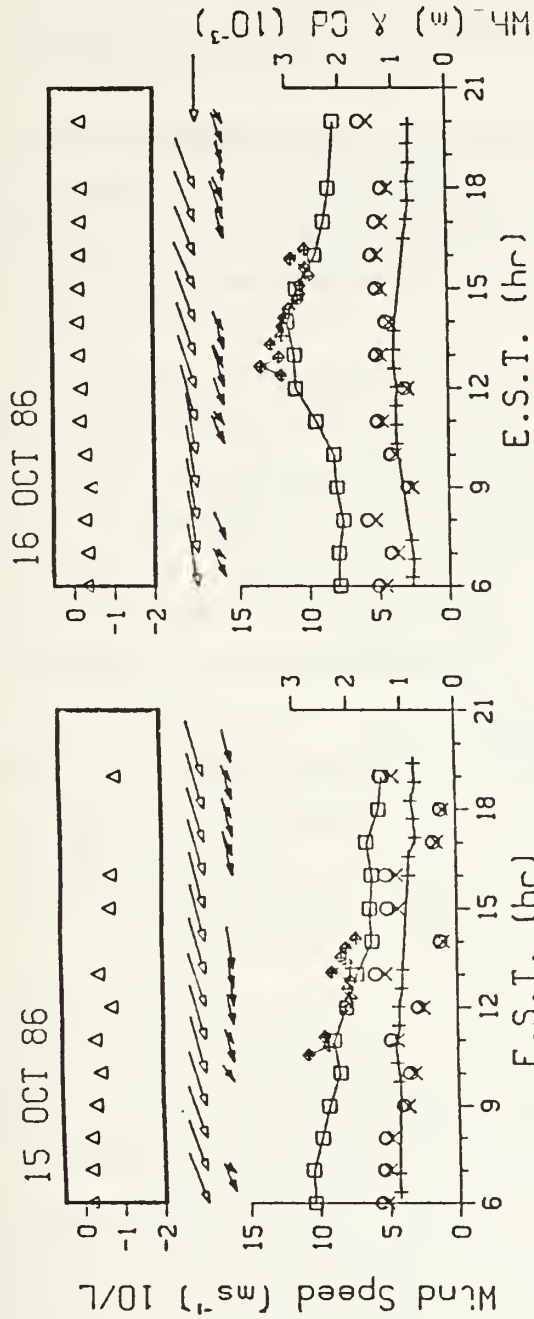


Figure 20. Wind speed, wave height, atmospheric stability, and initial C_d data for October 15-16, 1986. Beach is assumed parallel to the y-axis. Open arrowheads denote wind direction and closed arrowheads denote wave incident angle. Winds are adjusted to $z = 10$ m.

The absence of hourly 10 L (z/L stability indicator for $z = 10$ m) data and wind data indicates no boundary layer information was available. Absence of hourly 10 L data when a coincident wind speed is depicted indicates a 10 L value *more negative* than the limit plotted.

Boundary layer stability is a primary concern in interpreting the wind data. There were no stable atmospheric conditions during SUPERDUCK. C_{dn10} was plotted so as to remove the effect of stability in an effort to relate the drag coefficient variation to another physical parameter, such as wave height, wind direction, or wind speed. C_{dn10} is the standard drag parameter utilized for wind stress comparison between different investigators and serves as a basis for examining wave influence on wind drag. Neither wave height, wave direction, nor wind direction exert obvious influence on the drag coefficient as shown in Figure 20 and Appendix A (Figure 44 through Figure 46).

Increased instability places the atmosphere in a convective instability or local free convection regime where buoyancy forces become equal or greater in magnitude than mechanical mixing forces. Wyngaard and Cote (1971) conducted measurements of vertical velocity and temperature under unstable conditions and observed local free convection to occur at $z/L < -0.5$. Using the Businger et al. (1971) stability flux profile relation, Garrett (1977) showed that as instability increases, not only does C_d increase, but roughness becomes significantly more important. The Businger et al. (1971) iterative approach is inapplicable in a local free convection regime. Therefore an empirical approach is deemed more appropriate for surf zone C_d determination under local free convection.

Sled runs of $z/L < -0.5$ generally occurred during periods of low onshore wind speed. Therefore the drag coefficients in Figure 20 and Appendix A (Figure 44 through Figure 46) depicted for low wind speeds and very unstable conditions are inaccurate. Onshore winds of low speed and diabatic (unstable) conditions are representative of a sea breeze. A sea breeze is a local coastal wind caused by the temperature difference when the sea is colder than the adjacent land. It usually occurs on relatively calm and sunny days (Huschke, 1959). Review of surface weather analysis maps (Appendix D) and wind speed, wind direction, and stability (Table 7 and Table 9) indicate sea breeze conditions for most of the sled data run periods.

Measurements of surface wind stress above the swash zone under the effect of a sea breeze were made by simultaneous wind and temperature profiles over a shore transect near Fort Walton Beach, FL (Hsu, 1970). The sea breeze in the surface boundary layer

was determined to be in the atmospheric free-convection regime. A least-squares fit to the data (Figure 21) yields:

$$C_{d10} \times 10^3 = 10.06 - 1.30 (\bar{U}_{10} - U_o) \quad (63)$$

where \bar{U}_{10} is the mean wind speed at 10 m above the sea surface. It is noted that the drag coefficient under the sea breeze condition is higher than that under more stable conditions which is in agreement with e.g., Roll (1965).

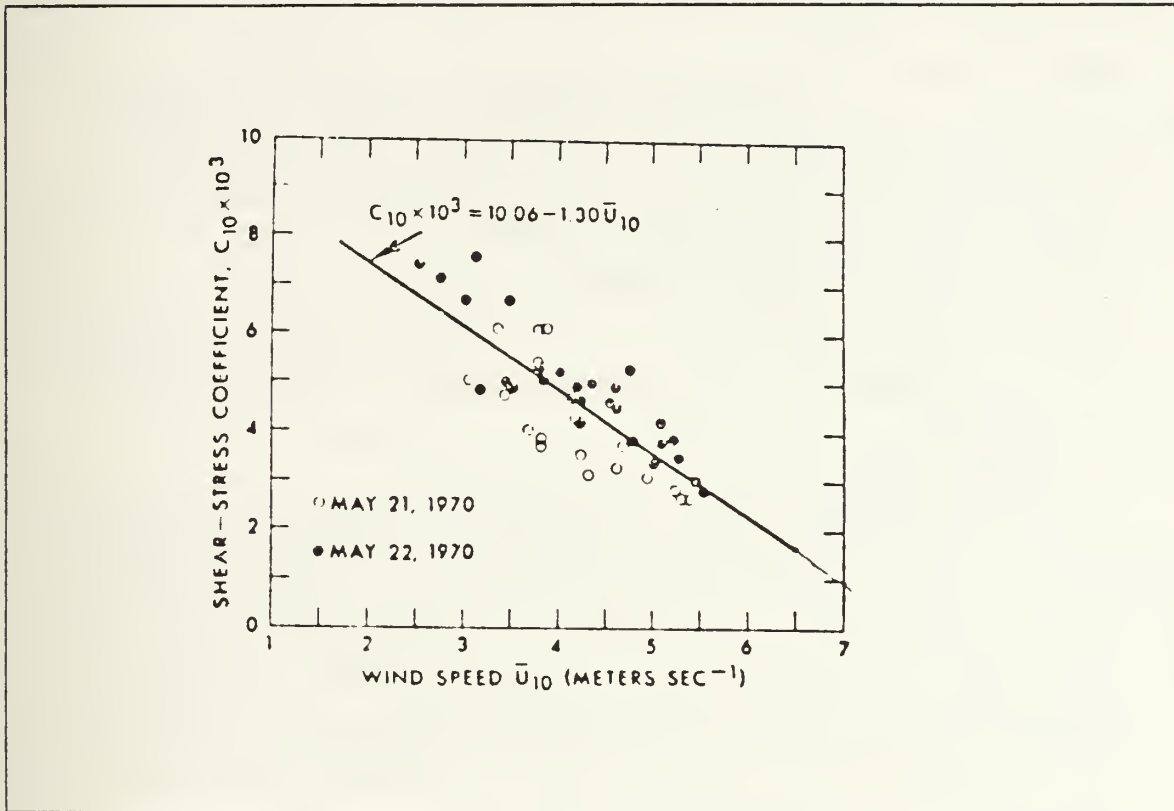


Figure 21. An empirically-derived stability-dependent drag coefficient obtained under a sea-breeze condition (from Hsu, 1970).

To determine appropriate drag coefficients for the sled transects based on the SUPERDUCK wind stress data, the following procedure is employed:

- When the sled's anemometer failed (Runs 18-1, 18-2, and all runs on 21 October), a linearly-interpolated hourly mean U_{10} from the pier is used as the sled U_{10} .
- A linearly-interpolated C_{d10} from the pier is assigned for the temporal mid-point of the sled run.
- When the actual $z.L$ was more negative than -1 or the wind speed was less than 6.5 ms^{-1} , C_{d10} is determined from the empirical relation of equation (63) where the

sled's U_{10} is determined from equation (60) and the z represents the run-varying height of the sled anemometer above mean water level for that particular run.

- When z/L was more negative than -1 and the wind speed greater than 6.5 ms^{-1} , C_{d10} is linearly interpolated between the value preceding and following the one in question. This is felt to be a better approximation than not using stability.

C. ADJUSTMENT OF C_d FOR THE SURF ZONE ENVIRONMENT

Since the surface wind stress was measured outside the surf zone, a C_d adjustment is required to more realistically reflect the surf zone environment. Early investigators of oceanic C_d 's sought a dependence on wind speed. Subsequent investigators (e.g., Hsu, 1974, 1986a; Byrne, 1982; Geernaert et al., 1986) began to search for a sea state dependence for C_d , since surface gravity waves are assumed to act as roughness elements (z_o) for the momentum transfer process. Most of these investigations were done for open ocean conditions and therefore are not directly applicable to the surf zone.

1. Uniqueness of surf zone air-sea interaction

The uniqueness of surf zone air-sea interaction as opposed to open ocean air-sea interaction can be summarized by three factors -- shoaling of the bottom, wave refraction, and wave breaking.

a. Shoaling effect

Momentum transfer is based on the relative wind speed difference between the absolute wind and wave speeds. During shoaling, there is a wave steepening and celerity decrease (relative wind increase) of surface gravity waves as they shoal. Geernaert et al. (1987b) state that C_d increases with decreasing values of the ratio c_o/u_* , where c_o is the phase speed of the dominant locally-generated gravity wave. Thus, larger than expected drag coefficients are observed over the sea during shoaling conditions (Smith, 1980; Geernaert et al., 1986).

b. Refraction

In most cases, the wave propagation direction is at some angle (up to 180°) to the predominant wind direction due to refraction of the waves in shoaling water. Over the open ocean, C_d is found to be larger if the wind is blowing at an angle different than the wave direction (Large and Pond, 1981; Smith, 1980). Geernaert et al. (1986) proposed wind stress enhancement in advance of a cold front due to surface gravity wave convergence. Swell generated behind the cold front would travel through the front and interact with waves generated ahead of the front and propagating parallel to the front. This interaction would result in a chaotic sea of larger wave amplitudes, steeper gravity

waves, and more wave breaking -- very similar to a robust surf zone. This enhancement was observed by Davidson et al. (1988a, 1988b) during the FASINEX 1986 experiment.

c. Wave Breaking

Moderate to high surf conditions undeniably result in increased surface roughness, which would result in increased drag coefficients. Although some work (Amarocho and DeVries, 1980; Melville, 1977) has quantified relations between breaking waves and increased drag coefficients, these investigations have dealt with the open ocean where the onset of breaking waves is produced by a dramatic increase in wind speed.

2. Surf Zone C_d Adjustment Formulation and Results

The wind stress data from the end of the FRF pier is assumed to include both the shoaling and refraction effects on C_d as one transitions from the open ocean to the surf zone. The increased C_d effect due to shoaling from the end of pier to the surf zone, as well as the additional refraction $O(15 - 25^\circ)$ maximum), is considered to be small compared to the breaking wave effect.

The approximate mean distance from the swash line to the end of the pier is 500 m. Each day at 0700 EST, the distance from the mean swash line to the outer extent of the surf zone was "stepped off" along the pier. These rough values for surf zone width on sled deployment days are listed in Table 8. The surf zone never extended to the end of the pier, although on 11 October, the farthest surf zone extent nearly did. With onshore winds, the increased roughness would not take effect until one was a measureable distance within the surf zone. Therefore, the increased roughness due to the breaking waves of the surf zone is not reflected in the end of the pier wind stress data.

The purpose of this research is not to explicitly characterize the C_d for the surf zone, but to intelligently select an appropriate C_d with which to address longshore surface wind stress as measured by a single anemometer in the surf zone. The increased surface roughness due to surf zone breaking waves may be *conservatively* likened to the chaotic seas observed by Davidson et al. (1988a, 1988b) in advance of storm fronts. From a composite of wind stress measurements taken from multiple chaotic sea cases found in advance of storm fronts, the drag coefficient was found to be increased by approximately 33% over that expected for non-chaotic seas and equal wind speed (Davidson et al., 1988a, 1988b). Therefore an increase of 33% in the drag coefficient (determined from equation 61) was deemed appropriate for all runs except those runs

Table 8. SUPERDUCK SURF ZONE WIDTH FOR SLED DEPLOYMENT DAYS (from Crowson et al., 1988).

<u>October</u>	<u>Surf zone width (m)</u>
11	500
12	320
15	120
16	100
17	80
18	80
21	100

occurring under strong diabatic conditions where equation (63) was utilized. Hsu's (1970) relationship is empirical and therefore the C_d values determined by equation (63) would already have the increased roughness considered. Drag coefficient values for each run and procedural step are listed in Table 9. All the values are of $O(10^{-3})$.

Surface wind stress is determined from equation (11) using the C_d 's listed in Table 9. Atmospheric density is assumed constant at 1.25 kgm^{-3} and θ is obtained from the end-of-pier wind direction. $U_{10} - U_o$ is substituted for W where U_{10} is the stability-dependent mean windspeed measured by the sled anemometer for the entire data run (approximately 34 minutes), corrected to an elevation of 10 m. U_o is the mean surf zone current measured by the sled current meters. The term $U_{10} - U_o$ is obtained from vectorial subtraction.

Table 9. ATMOSPHERIC DRAG COEFFICIENTS ($C_{D10} \times 10^3$) FOR EACH SLED DATA RUN

Sled Run	Sled $U_{10} - U_o$ (ms^{-1})	Pier $U_{10} - U_o$ (ms^{-1})	U_s (ms^{-1})	$\frac{10}{L}$	¹ Pier C_{d10}	² Sled C_{d10}	³ Sled C_{d10}
111	14.44	11.13	0.56	-0.025	2.49		3.31
112	13.69	11.33	0.57	-0.023	2.53		3.36
113	13.28	11.25	0.55	-0.023	2.41		3.21
121	10.70	7.28	0.30	-0.068	1.72		2.29
122	9.62	8.15	0.32	-0.048	1.54		2.05
123	9.14	7.86	0.29	-0.055	1.41		1.88
125	6.34	4.79	0.15	-0.256	1.07	1.82	
126	5.55	4.34	0.16	-0.230	1.48	2.85	
127	5.83	4.36	0.09	-0.640	0.49	2.48	
151	9.49	8.78	0.30	-0.337	1.18		1.57
152	8.00	7.76	0.24	-0.600	0.95		1.26
153	7.83	7.14	0.27	-0.448	1.44		1.92
154	7.57	6.33	0.14	-1.410	0.55		1.92
162	12.51	10.99	0.37	-0.128	1.15		1.53
163	11.14	11.30	0.39	-0.116	1.22		1.62
164	10.42	11.25	0.39	-0.123	1.22		1.62
165	9.76	10.72	0.39	-0.130	1.33		1.77
166	9.89	9.67	0.36	-0.158	1.40		1.86
171	6.25	6.37	0.20	-0.473	1.08	1.94	
172	7.21	4.77	0.20	-0.471	1.31		1.74
173	7.56	3.11	0.21	-0.476	1.35		1.80
174	6.50	5.27	0.21	-0.476	1.39		1.85
175	5.87	5.55	0.18	-0.464	1.10	2.43	
176	5.63	5.18	0.11	-1.414	0.49	2.74	
177	5.86	4.85	0.08	-2.505	0.30	2.44	
178	5.86	4.54	0.08	-2.664	0.33	2.44	
181	10.34	10.61	0.35	-0.163	1.11		1.48
182	10.39	10.87	0.40	-0.130	1.34		1.78
183	11.74	11.20	0.39	-0.140	1.17		1.56
184	12.17	11.42	0.40	-0.127	1.20		1.60
185	13.60	11.50	0.42	-0.111	1.32		1.76
186	13.94	11.80	0.43	-0.091	1.32		1.76
211	3.94	3.96	0.08	-2.147	0.46	4.94	
212	4.49	4.24	0.15	-0.728	1.20	4.22	
213	3.66	3.51	0.14	-0.690	2.10	5.30	
214	2.26	2.24	0.13	-0.775	3.38	7.12	
215	2.36	2.25	0.08	-2.068	1.25	6.99	
216	2.90	2.89	0.03	-14.286	0.12	6.29	
217	1.94	1.93	0.04	-6.645	0.49	7.54	
218	1.61	1.57	0.05	-2.939	1.38	7.97	
219	1.56	1.39	0.07	-1.678	3.69	8.05	

¹eqn. (61) ²eqn. (63) ³ 33% increase due to surf zone roughness

VII. LONGSHORE MOMENTUM BALANCE

The longshore momentum balance is calculated based on field measurements of wind, waves, and currents acquired across a barred beach. Spatially-dependent bed shear stress coefficients and the relative importance of the various terms in the momentum balance are calculated. Wind force to wave force ratios are calculated from the field data and compared to the results of the wind forcing model in Chapter III. This chapter concludes with an error analysis of these calculations.

The slope array did not perform as required for determination of the wave-induced longshore momentum flux (\tilde{S}_{yx}) in equation (1). Pre- and post-calibration values for the slope array differed as much as 10%. Assuming that breaking wave turbulence outside the surf zone is negligible, the gain required to match the slope array's radiation stress ($\tilde{S}_{yx}(f)$) to the current meter's radiation stress ($S_{yx}(f)$) was O(30 - 60%). Therefore, slope array data were judged in error and were not used in this analysis. Studies addressing turbulent momentum flux were suspended.

The slope array loss necessitates a rewriting of the longshore momentum balance equation as:

$$\frac{\partial M_y}{\partial t} + \frac{\partial S_{yx}^T}{\partial x} = -\tau_y^b + \tau_y^\eta \quad (64)$$

The turbulent momentum flux gradient is combined with the wave-induced momentum flux gradient to form a combined momentum flux gradient as measured by the current meters. The S_{yx}^T term implies integration over frequency (equation 80). Determination of surface wind stress is addressed in the Chapter VI. Calculation of the remaining terms in equation (64) will be addressed separately in this chapter.

A. TEMPORAL, OR ACCELERATION TERM ($\partial M_y / \partial t$)

The time-averaged depth-integrated mean momentum per unit area in the longshore direction (M_y) is composed of a steady (\overline{M}_y) and unsteady (M_y') flow component:

$$M_y = \overline{M}_y + M_y' = \rho V(\overline{\eta} + h) + \overline{\int_0^\eta \rho v' dz} \quad (65)$$

The steady component is calculated every 64 seconds with the term, $\bar{\eta} + h$, being taken as the mean water level (MWL) measured by the pressure sensor for that period of time. This resulted in thirty-two mean values of 64-second duration for M_y .

The unsteady flow contribution to the mean momentum, M_y' , is attributed to the mass flux of the wave motion:

$$M_y' = \overline{\int_0^\eta \rho v' dz} \tag{66}$$

where v' is only known at $z = 0$ from wave theory. By expanding in a Taylor series about $z = 0$ and retaining only the first order term, M_y' may be expressed independent of height in the crest-trough region:

$$M_y' = \overline{\int_0^\eta \rho v'(0) dz} = \overline{\rho v'(0) \eta} \tag{67}$$

Using linear theory and substituting for $v'(0)$ and η :

$$M_y' = \frac{1}{2} \rho g a^2 \frac{1}{C} \frac{k_l}{k} = \frac{E}{C} \frac{k_y}{k} \tag{68}$$

where a is wave amplitude. Rewriting equation (68) in terms of a finite frequency band, a significant wave incident angle ($\hat{\alpha}(f)$), total wave energy ($E(f)$), and wave celerity ($C(f)$) yields:

$$M_y' = \int_{f_1}^{f_2} \frac{E(f)}{C(f)} \sin \hat{\alpha}(f) df \tag{69}$$

where

$$C(f) = \frac{g}{\omega(f)} \tanh kh \tag{70}$$

Throughout this analysis, wave number (k) is calculated non-iteratively by the formulation of Wu and Thornton (1986).

Spectra of "significant wave angle" (Appendix F) are calculated as (Higgins et al., 1981):

$$\sin \hat{\alpha}(f) \cos \hat{\alpha}(f) = \frac{S_{yx}(f)}{[E(f) n(f)]} \quad (71)$$

The energy spectrum is calculated from velocity measurements. Time-averaged depth-integrated kinetic energy (KE) may be written as:

$$KE = 0.5 \rho \int_{-h}^{\eta} (u^2 + v^2 + w^2) dz \quad (72)$$

where w is the component of the flow velocity in the vertical direction. To the first order of approximation, there is equipartition of energy between potential energy and kinetic energy for linear progressive waves (Kinsman, 1965). The total energy, $E(f)$, is calculated as twice the kinetic energy:

$$E(f) = 2 |H_1(f)|^2 [G_u(f) + G_v(f)] \quad (73)$$

where

$$|H_1(f)|^2 = \frac{\rho [\sinh(2kh)]}{4k [\cosh^2 k(h + z_m)]} \quad (74)$$

and G_u and G_v are the one-sided spectral density functions for the horizontal velocity components in the x and y directions and z_m is the measurement depth. Calculations of equations (69) through (73) indicated that the time-varying momentum of the waves for this data set was one-to-two orders of magnitude less than the time-varying momentum of the steady flow. Therefore the temporal term may be simplified as:

$$\frac{\partial M_y}{\partial t} \approx \frac{\Delta M_y}{\Delta t} \quad (75)$$

where

$$M_y \approx \bar{M}_y = \rho V(\bar{\eta} + h) \quad (76)$$

and Δt = time step over which the finite difference is calculated, and $\bar{\eta} + h$ = MWL as sensed by the sled's pressure sensor.

A value of M_y is first determined for each ensemble of 64 seconds in the data run. Since the temporal scale of the longshore current is unknown, a range of ensembles

(comprised of 1 to 11 segments of 64-second duration) are defined using a running mean interval, $\Delta t'$. Then a finite difference is calculated from these larger ensembles for a specified Δt . Finally, a mean temporal term is calculated:

$$\frac{\overline{\Delta M_y}}{\Delta t} = \frac{1}{k} \sum_{j=1}^k \left[\frac{\Delta M_y}{\Delta t} \right]_j \quad (77)$$

for the k increments of $\Delta M_y/\Delta t$. This mean temporal term is assigned as the temporal term for the sled run. Calculations of the mean temporal term (equation 77) with and without a running mean, as well as variation of the time step (with subsequent change in the k increment), made negligible difference for this data. Therefore $\Delta t = 64$ seconds is used. The selection of $\Delta t'$ is discussed in paragraph D below.

B. RADIATION STRESS GRADIENT ($\partial S_{yx}^T / \partial x$)

Longshore momentum flux, as defined in equation (2), is calculated from current meter measurements and applying linear wave theory:

$$S_{yx}(f) = |H_2(f)|^2 C_{uv}(f) \quad (78)$$

where $|H_2(f)|^2$ is a linear transfer function:

$$|H_2(f)|^2 = \frac{\rho [\sinh(2kh) + 2kh]}{4k [\cosh^2 k(h + z_m)]} \quad (79)$$

and C_{uv} is the real part of the cross-spectrum of u' and v' . It is assumed in the application of the transfer function (equation 79) to the measured covariance that the vertical distribution of turbulence in the water column is the same as in the waves, and is described by the transfer function which is a function of depth and frequency (Figure 22).

The total radiation stress (S_{yx}^T), where total indicates frequency summation, is determined from:

$$S_{yx}^T = \sum_{f_1}^{f_2} S_{yx}(f) \Delta f \quad (80)$$

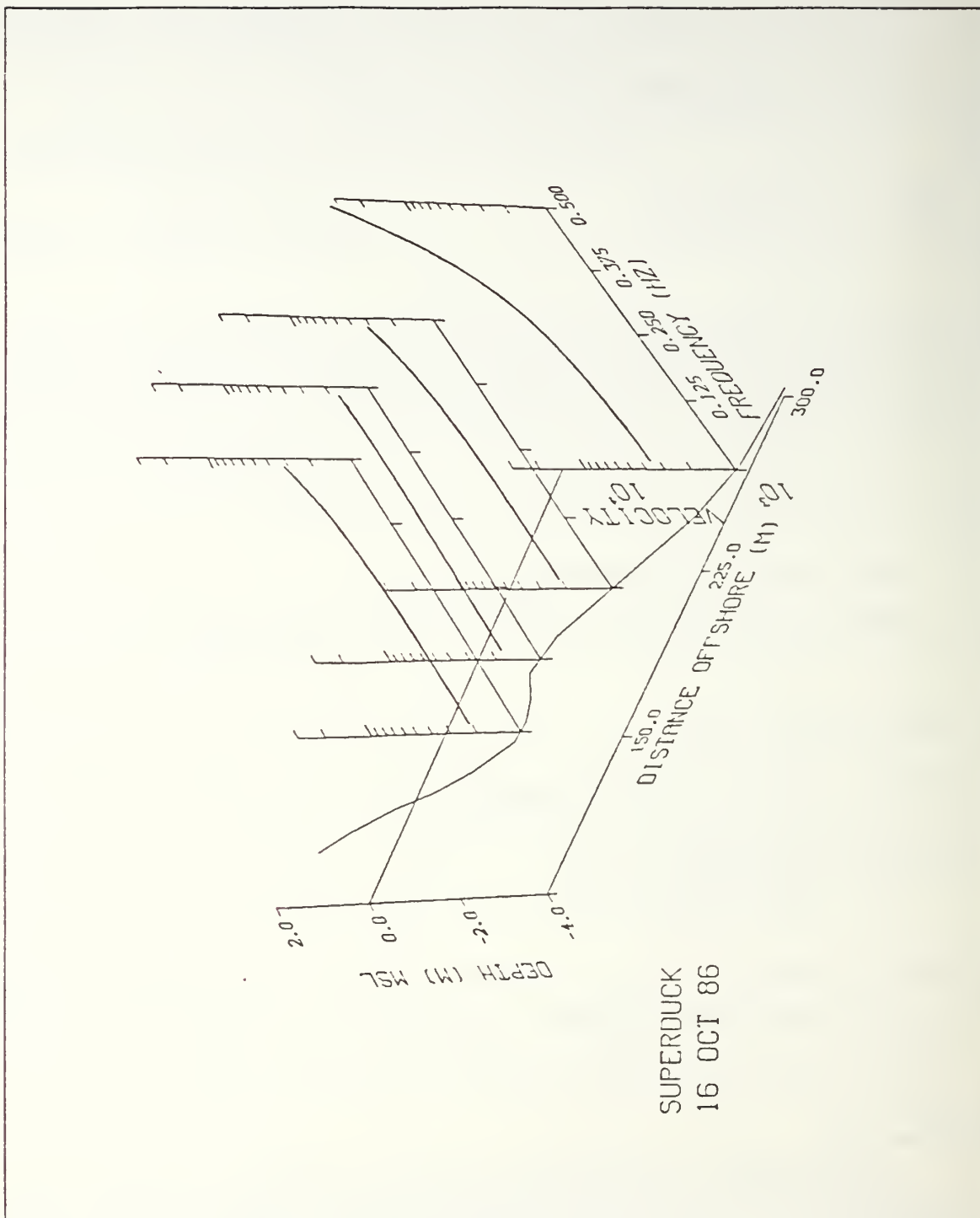


Figure 22. Linear wave theory transfer function used to calculate $S_{y_x}(f)$ from current velocity. showing decreasing frequency dependence with depth across a barred beach.

where f_1 and f_2 represent the lower and upper frequency limits of the sea-swell band under investigation and Δf represents the resolution of the spectral estimates. S_{yx}^T is the quantity required for the momentum balance of equation (64).

Analysis of the longshore component of momentum flux ($S_{yx}(f)$) was accomplished using Fast Fourier Transforms and ensemble averaging. Ensemble averaging requires segmentation of a time series into several shorter time series of equal length, and calculation of a sample spectrum for each of these sub-series. The mean of these spectra is a smoothed spectral estimate. The advantages of ensemble averaging are minimal computer storage and computational ease.

The data were initially demeaned and detrended. The 34.1 minute data runs were segmented into 32 sub-series of length 64 seconds. The $S_{yx}(f)$ used in equation (80) is the Bartlett smoothed spectral estimate (Jenkins and Watts, 1968) from 32 sample spectra. All spectral estimates (S_{yx} , η , etc.) have 63 ($\nu = 2m - 1$) degrees of freedom, a spectral resolution (Δf) of 0.015 Hz, and Chi-squared 95% confidence limits equal to 0.73 and 1.45 times the spectral estimate itself (Jenkins and Watts, 1968). Since sea and swell are of interest, lower and upper frequency limits are established at 0.06 and 0.44 Hz, respectively. These limits are used whenever frequency summation was required for any parameter.

Radiation stress spectra may be negative at one frequency while positive at another frequency, as in the case of sea and swell approaching from different quadrants. $S_{yx}(f)$ spectra transitioning from positive, through zero, to negative, and vice versa, may not be accommodated with a log-linear plot, therefore $S_{yx}(f)$ spectra are plotted on linear plots. Related spectra are also plotted in this manner for consistency.

The calculation of the *gradient* of radiation stress requires numerical differencing over an appropriate length scale:

$$\frac{\partial S_{yx}^T}{\partial x} \approx \frac{\Delta S_{yx}^T}{\Delta x} \quad (81)$$

The spatial step (Δx) was initially designated as the distance between the front and rear current meters after adjustment for sled yaw angle. A radiation stress gradient (equation 81) determined with this definition of Δx is labeled to have been determined by the "local" method. The Δx distance on the sled was approximately 2 m and the "local" finite differencing scheme is:

$$\frac{\partial S_{yx}^T}{\partial x} \approx \frac{(S_{yx}^T)_{\text{rear c m}} - (S_{yx}^T)_{\text{front c m}}}{\Delta x} \quad (82)$$

A second approach to the determination of the radiation stress gradient, called the "integrated" method, utilized the distance *between* sled run positions for Δx . This distance was O(20-40 m) and this finite differencing scheme is:

$$\frac{\partial S_{yx}^T}{\partial x} \approx \frac{1}{4} \left[\frac{(S_{yx}^T)_1 - (S_{yx}^T)_4}{\Delta x_{1-4}} + \frac{(S_{yx}^T)_1 - (S_{yx}^T)_3}{\Delta x_{1-3}} + \frac{(S_{yx}^T)_2 - (S_{yx}^T)_4}{\Delta x_{2-4}} + \frac{(S_{yx}^T)_2 - (S_{yx}^T)_3}{\Delta x_{2-3}} \right] \quad (83)$$

where the numbers 1 through 4 denote the two pair (front and rear) of current meter data available from two sled run positions (see Figure 23). The estimate of the S_{yx}^T gradient is based on four independent current meter locations covering slightly different transect segments and slightly different Δx 's. These segment and Δx differences are generally less than 10% of the distance between sled mast locations. It is therefore assumed that the four estimates represent four sample means of the true S_{yx}^T gradient between the two sled locations. From the Central Limit Theorem, the standard deviation of sample means is written as:

$$\sigma_{\bar{x}} = \frac{\sigma}{\sqrt{n}} \quad \text{or} \quad \sigma \frac{\Delta S_{yx}^T}{\Delta x} = \frac{\sigma \frac{\partial S_{yx}^T}{\partial x}}{\sqrt{n}} \quad (84)$$

where n is the number of sample means. Thus the standard deviation of the sample mean is reduced by 50% with the use of four sample means rather than one. This fact will be used in determining the measurement error for $\partial S_{yx}^T / \partial x$ in paragraph E. Selection of the "local" method versus the "integrated" method proved to be of significant importance.

C. SEA SURFACE ELEVATION (η)

Although not specifically required for the momentum balance, sea surface elevation spectra provided a useful reference against which to compare radiation stress spectra.

Sea surface elevation spectra ($G_\eta(f)$) are determined from linear wave theory using data from both the sled's pressure sensor and current meters:

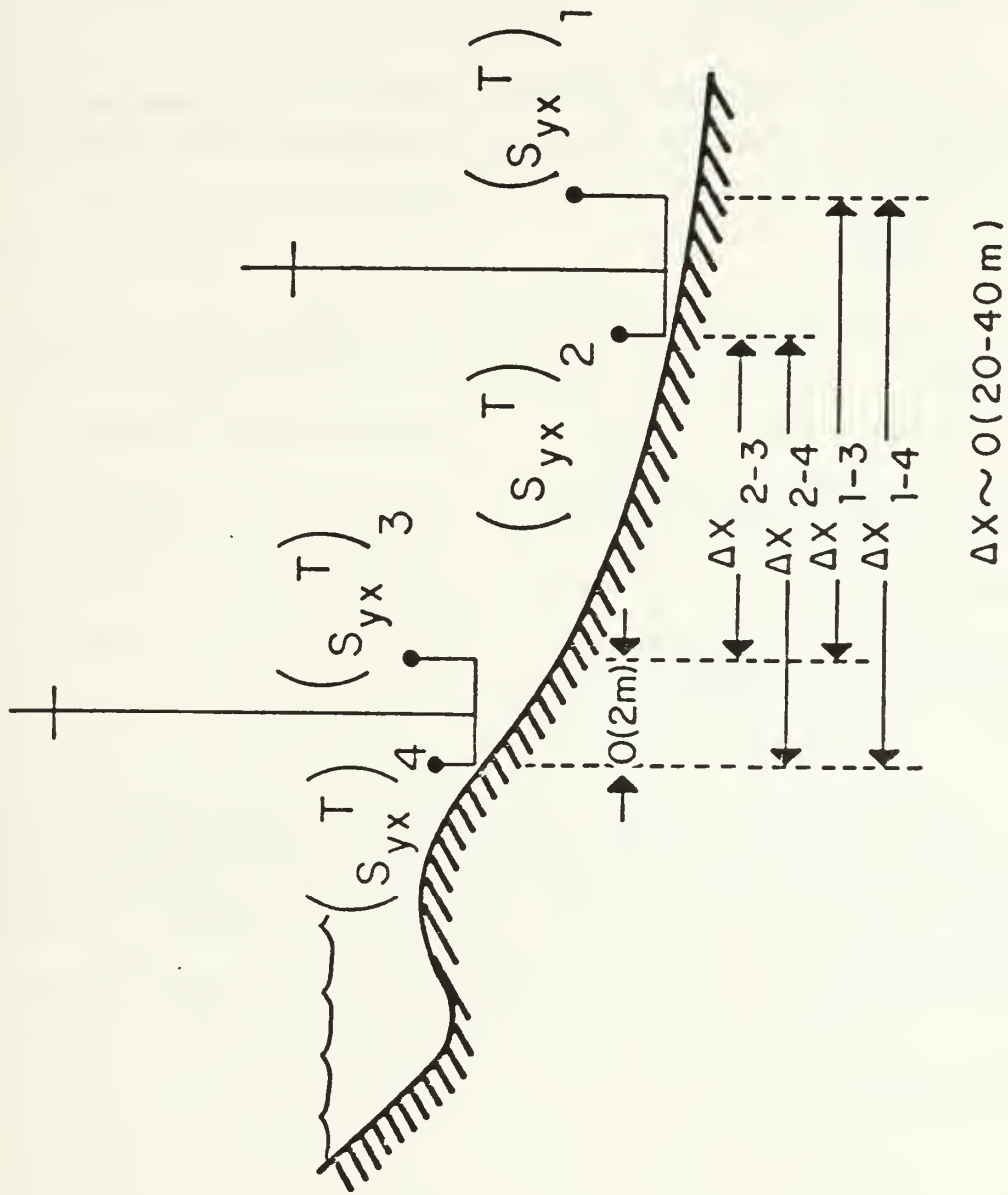


Figure 23. Finite differencing scheme for $\partial S_{yx}^T / \partial x$. from "integrated" method.

$$G_{\eta}(f) = |H_3(f)|^2 G_{p_h}(f) \quad (85)$$

where

$$|H_3(f)|^2 = \frac{\cosh^2(kh)}{\cosh^2[k(h + z_m)]} \quad (86)$$

and $G_{p_h}(f)$ is the one-sided energy density spectrum for the pressure head (p_h) measured by the pressure sensor. The pressure head is determined from the hydrostatic equation:

$$p_h = \frac{p - p_{atm}}{\rho g} \quad (87)$$

where p is the absolute pressure sensed by the pressure gage and p_{atm} is the atmospheric pressure.

The formulation for determining $G_{\eta}(f)$ from current meter velocities is:

$$G_{\eta}(f) = |H_4(f)|^2 [G_u(f) + G_v(f)] \quad (88)$$

where

$$|H_4(f)|^2 = \frac{\sinh(2kh)}{2gk \cosh^2[k(h + z_m)]} \quad (89)$$

$G_{\eta}(f)$ produced by these two formulations are in good agreement for the three vertically-stacked current meters and the pressure sensor, thereby providing confidence for the η spectra. Sea surface spectra produced in Appendix F are formulated from equation (85).

Wave height parameters are calculated from pressure-derived η spectra:

$$H_{rms} = (8 \sigma_{\eta}^2)^{\frac{1}{2}} \quad (90)$$

$$H_{mo} = 4 \sigma_{\eta} \quad (91)$$

where the total variance is expressed as:

$$\sigma_{\eta}^2 = \sum_{f_1}^{f_2} G_{\eta}(f) \Delta f \quad (92)$$

D. RESULTS OF THE MOMENTUM BALANCE

Field measurements of wind, waves, and currents are used to calculate the local longshore momentum balance at various locations across a barred beach. From the momentum balance, bed shear stress coefficients and the relative importance of the various terms comprising the balance are calculated. Mean values are determined relative to the bar. Wind force to wave force ratios are calculated from the field measurements and compared to the results of the wind forcing model in Chapter III.

1. Bed Shear Stress Coefficient

A spatially-dependent bed shear stress coefficient (c_f) may be determined from equations (18) and (64) as:

$$c_f = \frac{-\frac{\partial S_{yx}^T}{\partial x} + \tau_y^\eta - \frac{\partial M_y}{\partial t}}{\rho |u_t|v} \quad (93)$$

Resultant spatially-dependent bed shear stress coefficients are listed in Table 10 and illustrated in Figure 24. The column titled " $c_f(l)$ " are the c_f 's determined utilizing the "local" method for the radiation stress gradient. These coefficients are representative for the sled run position itself. The surface wind stress and temporal variability terms were 34.1-minute means taken only from the sled run being investigated in anticipation of gaining insight into the temporal variability of all terms in the longshore momentum balance. A running mean of 12.8 minutes was selected for determination of both the temporal term and the radiation stress based on radiation stress statistics of Freilich and Pawka (1987). They showed that, given n independent realizations of a time series of $u(t)$ and $v(t)$, that the Gaussian approximation for true S_{yx} statistics is valid for $n > 11$ independent realizations. An ensemble length of 64 seconds and a minimum number of ensembles (12) was selected for the analysis. Unfortunately, this procedure resulted in significant $c_f(l)$ variability. Utilization of a 34.1-minute mean $\partial S_{yx}^T / \partial x$ made negligible difference in resultant $c_f(l)$. Two possible reasons for the large $c_f(l)$ variability may be that the radiation stress is much more variable across the surf zone on a small spatial scale than previously imagined and the Δx is too small to resolve the difference between two large numbers (see equation (82) and paragraph 2 of the Error Analysis section in this chapter).

The column titled " $c_f(i)$ " are those c_f 's determined using the "integrated" method for the radiation stress gradient. These coefficients are representative for the portion of

the bathymetric profile *between* sled run positions. The wind stress and temporal variability terms are the 34.1-minute means from the two appropriate sled run means. The "beach" position along the transect is defined as the intersection of the bathymetric profile with the MWL as determined by the sled pressure sensor on the run closest to the beach. Extremely weak longshore currents inshore of run 17-6's location explain the variable $c_f(i)$'s. They are disregarded. The bed shear stress coefficients determined by the "integrated" method exhibit less variability than those from the "local" method and are all of $O(10^{-3})$. The "integrated" method is considered to be a reasonable method for the determination of the radiation stress gradient.

2. Relative Contributions of the Longshore Momentum Balance Terms

Relative contributions of wave forcing ($\partial S_{yx}^T / \partial x$), wind forcing (τ_y^η), and temporal variability of mean momentum ($\partial M_y / \partial t$) to the total momentum balance are determined by first defining their total contribution (TOT) as the cumulative sum of their absolute values:

$$\text{TOT} = \left| \frac{\partial S_{yx}^T}{\partial x} \right| + |\tau_y^\eta| + \left| \frac{\partial M_y}{\partial t} \right| \quad (94)$$

Their individual relative contributions (rc) are then determined by dividing by the total contribution:

$$\text{wave}_{rc} = \frac{\left| \frac{\partial S_{yx}^T}{\partial x} \right|}{\text{TOT}} \quad (95)$$

$$\text{wind}_{rc} = \frac{|\tau_y^\eta|}{\text{TOT}} \quad (96)$$

$$\left[\frac{\partial M_y}{\partial t} \right]_{rc} = \frac{\left| \frac{\partial M_y}{\partial t} \right|}{\text{TOT}} \quad (97)$$

Relative contributions from the wave, wind, and temporal terms, as formulated in equations (95) to (97) and utilizing the "integrated" method, are calculated. Results are presented in order of consecutive runs (Table 11) and by relative location along the transect with respect to the bar (Table 12). Relative locations are delineated as "off-shore" of the bar, "on the bar" and immediately before the bar, and in the "trough" re-

Table 10. SUPERDUCK BED SHEAR STRESS COEFFICIENTS (OCTOBER 15-18, 1986)

October 15, 1986			October 17, 1986		
Run	$c_f(l)$	$c_f(i)$	Run	$c_f(l)$	$c_f(i)$
15-1	*		17-1	0.002	
		0.006			0.003
15-2	0.008		17-2	0.003	
		0.002			0.005
15-3	*		17-3	0.004	
		*			0.003
15-4	0.012		17-4	0.026	
		0.001			0.005
Beach			17-5	0.099	
					0.003
			17-6	0.119	
October 16, 1986			October 18, 1986		
Run	$c_f(l)$	$c_f(i)$	Run	$c_f(l)$	$c_f(i)$
16-2	0.001		18-1	0.001	
		0.003			0.003
16-3	0.004		18-2	*	
		0.004			0.004
16-4	0.003		18-3	0.007	
		0.001			0.001
16-5	0.001		18-4	0.043	
		0.001			0.001
16-6	0.002		18-5	-.001	
		0.002			0.001
Beach			Beach		

- '*' indicates c_f value $< 5. \times 10^{-4}$
- $c_f(l)$ are determined by the "local" method
- $c_f(i)$ are determined by the "integrated" method
- relative contributions determined by the "integrated" method

gion. The mean wind stress remained nearly constant throughout each transect of the surf zone. However, the temporal term, as averaged over 34.1 minutes, was variable in sign and magnitude. The location of maximum wave breaking along the transect can be identified (Table 11) where wave forcing's relative contribution is maximum. Two peaks in wave forcing correspond to two breaking areas - waves breaking offshore of the

bar and waves reforming and then breaking on the nearshore beach face. The *relative* contribution of wind stress inside the surf zone generally increases in value as one proceeds onshore from the location of maximum breaking, due to the decrease in wave forcing. The relative contribution of wind stress can then decrease again inshore at the location where waves re-break on the nearshore. The relative contribution of the temporal term appears to be largest in the trough where wave forcing is reduced and possibly where the effect of longer period waves (e.g., surf beat or edge waves) is more pronounced.

The mean relative contributions for the wave, wind, and temporal terms (0.86, 0.08, and 0.06, respectively) are essentially identical for both "offshore" and "on the bar" (Table 12). However in the "trough", the mean relative contributions (0.64, 0.17, and 0.19, respectively) are significantly different. The relative importance of wave forcing is reduced by 25%, whereas the relative importance of surface wind stress is doubled, and the temporal term relative importance is tripled.

A comparison is made between the wind force to wave force ratios produced by the wind forcing model in Chapter III to those determined for the SUPERDUCK data. The wind to wave force ratios in Table 3 and Table 4 are based on a planar beach, therefore only the offshore side to the SUPERDUCK bar ($\tan\beta \approx 0.03$) is considered. The SUPERDUCK force ratios are obtained from ratios of the relative contributions of surface wind stress to radiation stress gradient in Table 12 for the "offshore" and "on the bar" categories. The wind force to wave force ratio for 15-18 October field data is 0.09. The mean wind speed was 9.6 ms^{-1} and the mean wave incident angle for the "offshore" region was 12° . Using linear interpolation in Table 3 and Table 4 results in a wind to wave force ratio of 0.12. Thus the field measurements are in good agreement with the results of the wind forcing model in Chapter III, with differences attributable to non-fully arisen seas and the presence of swell from a different direction than the wind waves.

Bed shear stress coefficients are calculated for cases without the surface wind stress and without both surface wind stress and the temporal term. The percentage change in c_f ranges from near zero to 100%, with a mean change of 10-30%. Thus under certain conditions for this data set, the surface wind stress and temporal terms can be of first order in the momentum balance.

A mean c_f based on relative position along the transect with respect to the bar is determined. Bed shear stress coefficients determined from the "integrated" method are

Table 11. RELATIVE CONTRIBUTIONS OF THE LONGSHORE MOMENTUM BALANCE TERMS FOR SUPERDUCK

Run	$\partial S_{yx}^T / \partial x$	τ_y^{η}	$\partial M_y / \partial t$
15-1	0.97	0.02	0.01
15-2	0.93	0.04	0.04
15-3	0.77	0.17	0.06
15-4	0.79	0.14	0.07
16-2	0.87	0.08	0.04
16-3	0.95	0.03	0.02
16-4	0.77	0.19	0.03
16-5	0.70	0.18	0.12
16-6	0.81	0.02	0.17
17-1	0.63	0.17	0.20
17-2	0.94	0.03	0.04
17-3	0.88	0.03	0.09
17-4	0.89	0.05	0.07
17-5	0.72	0.16	0.12
18-1	0.83	0.13	0.04
18-2	0.93	0.05	0.02
18-3	0.81	0.12	0.07
18-4	0.46	0.33	0.21
18-5	0.21	0.19	0.60

- Relative contributions determined by "integrated" method. Run number indicates offshore run of the required run pair.
- Runs 17-6 through 17-8 had negligible currents of variable direction. Their c_f results are disregarded.

Table 12. RELATIVE IMPORTANCE OF MOMENTUM BALANCE TERMS FOR LOCATIONS RELATIVE TO THE BAR

Offshore			
Run	$\partial S_{rx}^T / \partial x$	τ_f^T	$\partial M_r / \partial t$
15-1	0.97	0.02	0.01
16-3	0.95	0.03	0.02
16-2	0.87	0.08	0.04
17-1	0.63	0.17	0.20
17-2	0.94	0.03	0.04
18-1	0.83	0.13	0.04
18-2	0.93	0.05	0.02
Mean	0.87	0.07	0.05
On the Bar			
Run	$\partial S_{rx}^T / \partial x$	τ_f^T	$\partial M_r / \partial t$
15-2	0.93	0.04	0.04
16-4	0.77	0.19	0.03
17-4	0.89	0.05	0.07
17-3	0.88	0.03	0.09
18-3	0.81	0.12	0.07
Mean	0.86	0.09	0.06
Trough			
Run	$\partial S_{rx}^T / \partial x$	τ_f^T	$\partial M_r / \partial t$
15-4	0.79	0.14	0.07
15-3	0.77	0.17	0.06
16-5	0.70	0.18	0.12
16-6	0.81	0.02	0.17
17-5	0.72	0.16	0.12
18-4	0.46	0.33	0.21
18-5	0.21	0.19	0.60
Mean	0.64	0.17	0.19

assigned and a mean c_f determined for each of these relative locations (Table 13). The results indicate a decrease in mean c_f as one proceeds from offshore to onshore with mean c_f values equal to 0.004 ("offshore"), 0.002 ("on the bar"), and 0.001 (trough").

The shoreward decreasing c_f was initially thought to be the result of decreasing bed roughness. As previously stated, bed roughness is a function of both sand characteristics and bed form. Beaches generally exhibit a shoreward gradation of sand grain size from large to small. Waves tend to sort the sand with the largest sand residing in the most energetic area of the surf zone. This gradation would be commensurate with the maximum c_f found just inside the surf zone and a decreasing c_f further onshore. Unfortunately, field measurements of bed roughness were overlooked during the SUPERDUCK experiment and cannot be used to substantiate this hypothesis. Interviews with SUPERDUCK divers were conducted several months after the experiment, however their information about bed roughness was not specific enough to draw conclusions. An October 1982 sampling of sand grain size across the FRF beach showed shoreward increasing grain size (Birkemeier et al., 1985). It is reasonable to assume that grain size gradation would not change over a few years, therefore bed roughness is discarded as the reason for the c_f trend. Field and laboratory studies have shown that bed shear stress is enhanced when the near-bottom flow field is composed of mean current and oscillatory (i.e. wave) components (Grant and Madsen, 1979, 1982; Grant et al., 1984). Thus shoreward decreasing wave action would result in shoreward decreasing c_f .

Table 13. MEAN BED SHEAR COEFFICIENTS DETERMINED FOR LOCATIONS RELATIVE TO THE BAR

<u>Trough</u>		<u>On the Bar</u>		<u>Offshore</u>	
15-4	.001	15-2	.002	15-1	.006
15-3	<.001	16-4	.001	16-3	.004
16-5	.001	17-4	.005	16-2	.003
16-6	.002	17-3	.003	17-1	.003
17-5	.003	18-3	.001	17-2	.005
18-4	.001			18-1	.003
18-5	.001			18-2	.004
<hr/>		<hr/>		<hr/>	
Mean c_f =	.001		.002		.004

The variation in c_f due to varying $\Delta t'$ in the temporal term was examined by analyzing sample groups where $\Delta t'$ was specified as a running mean of (approximately)

1, 5, 10, 12, 14, 18, and 22 minutes. The mean variation in c_f due to varying $\Delta t'$ for the SUPERDUCK data was negligible.

E. ERROR ANALYSIS

An error analysis is conducted to assign appropriate error bounds on the resultant spatially-dependent c_f values. Approximated errors are the use of a linear wave theory transfer function to integrate the velocity covariance measurement over the water column and errors in stationarity due to tidal variation. Three sources of error which are specifically quantified are incident wave angle error, propagation of measurement error, and finite differencing error for the radiation stress gradient.

1. Incident Wave Angle Error

Radiation stress (equation 3) is sensitive to the incident wave angle (α). The determination of an accurate α is dependent on several other angles. The Zeiss electronic surveying system was required to measure the sled yaw angle. The Zeiss error (Table 14) is assumed negligible in the α determination. The adjustments (Chapter V) to translate the sled *instrument's* three-dimensional coordinates into the FRF coordinate system, and the measurements by the portable Zeiss system which made them possible, are considered to have negligible error. Three angular sources of error which cannot be neglected are beach angle orientation error, current meter orientation error, and current meter directional gain error.

a. Beach Angle Orientation Error

An analysis is conducted to assess sensitivity to beach angle orientation error. The beach angle orientation is calculated from a mean bathymetric contour determined in a least squares sense as described in Chapter V. For this analysis, monochromatic, linear, unidirectional wind waves are assumed for a straight-and-parallel planar beach. Using Snell's Law, the wave incident angle (α_2) at the inshore current meter may be determined given the wave incident angle (α_1) at the offshore current meter:

$$\alpha_2 = \sin^{-1} \left[\frac{\sin \alpha_1 C_2}{C_1} \right] \quad (98)$$

where wave celerity (C) is determined from equation (70). The radiation stress gradient (from equation 3) in the cross-shore direction may be stated as a finite difference between radiation stress calculated at the two on-offshore current meters where the sub-

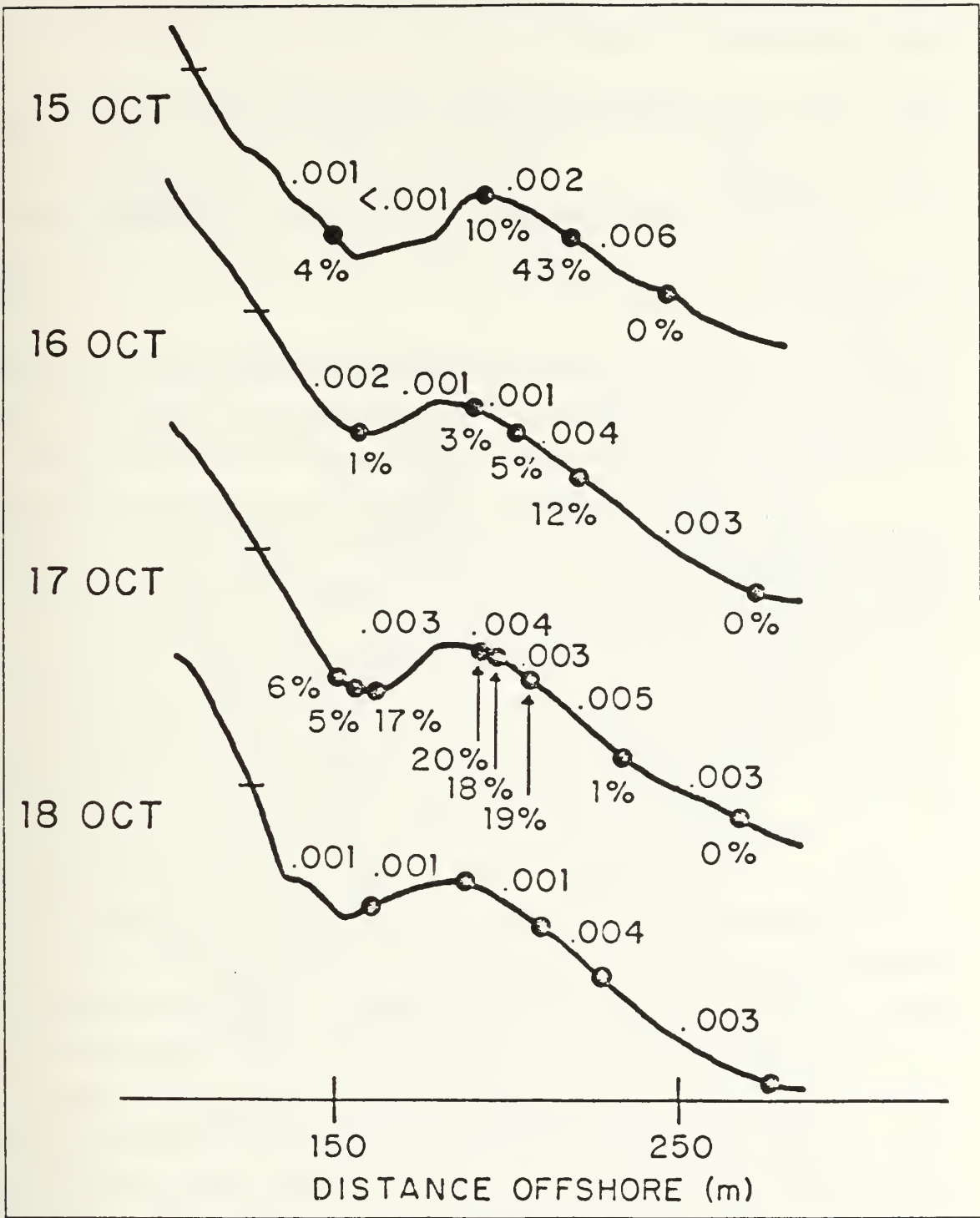


Figure 24. c_f and percent breaking wave (Q) values as a function of offshore distance (October 15-18, 1986). (c_f is above and Q is below the profile line).

script "rear" refers to the rear or offshore current meter and "front" to the front or inshore current meter of the sled:

$$\frac{\partial S_{yx}}{\partial x} \approx \frac{[E n \sin(\alpha \pm \Delta\alpha_e) \cos(\alpha \pm \Delta\alpha_e)]_{\text{rear}} - [E n \sin(\alpha \pm \Delta\alpha_e) \cos(\alpha \pm \Delta\alpha_e)]_{\text{front}}}{\Delta x} \quad (99)$$

where $\Delta\alpha_e$ is the beach angle orientation error. Total energy (E) is calculated from:

$$E = \frac{1}{8} \rho g H_{\text{rms}}^2 \quad (100)$$

Root-mean-square wave height (H_{rms}) for monochromatic shallow water waves can be related to depth (h) in the inner surf zone by equation (39). For SUPERDUCK, ratios of H_{rms} to h ranged from O(0.3) outside the surf zone to O(0.4) inside the surf zone.

The radiation stress gradient (equation 99) versus orientation error for representative depth, slope, and incident wave angles is illustrated in Figure 25. The three angles plotted for each depth are centered about a typical incident wave angle encountered during SUPERDUCK for that particular depth. For example, an incident wave angle of 25° , a depth of 3.5 m, and a beach orientation angle error of -5° , would result in an overestimation of the radiation stress gradient by 10%. On the other hand, a radiation stress gradient measured in a shallower depth with a reduced incident wave angle ($h = 1.5$ m, $\alpha = 15^\circ$) and the same error angle of -5° would result in an overestimation by 30%. Note that the overall governing parameter is incident wave angle. Therefore, for a fixed beach orientation angle error, the relative radiation stress error increases with decreasing wave angle, and hence with decreasing depth. For SUPERDUCK, errors in mean beach orientation angle are estimated to be less than $\pm 2^\circ$ and 1.0 m was the minimum depth in which data were acquired. Therefore radiation stress gradient errors for 3.5, 2.5, and 1.5 m depths would be $\pm 5\%$, $\pm 7-8\%$, and $\pm 10\%$, respectively. A 10% radiation stress error can be equated to approximately a 10% c_f error, as long as wind stress and temporal variability of mean momentum are small. As the magnitude of wind stress and temporal variability increase, the effect of a fixed radiation stress error on c_f becomes less. Varying beach slope from 0.01 to 0.10 or varying Δx from 2 m ("local" method) to 25 m ("integrated" method) had negligible effect on the relative radiation stress gradient error due to an incorrect beach orientation angle. Therefore c_f error due to inaccurate beach orientation angle is estimated to be less than 10%.

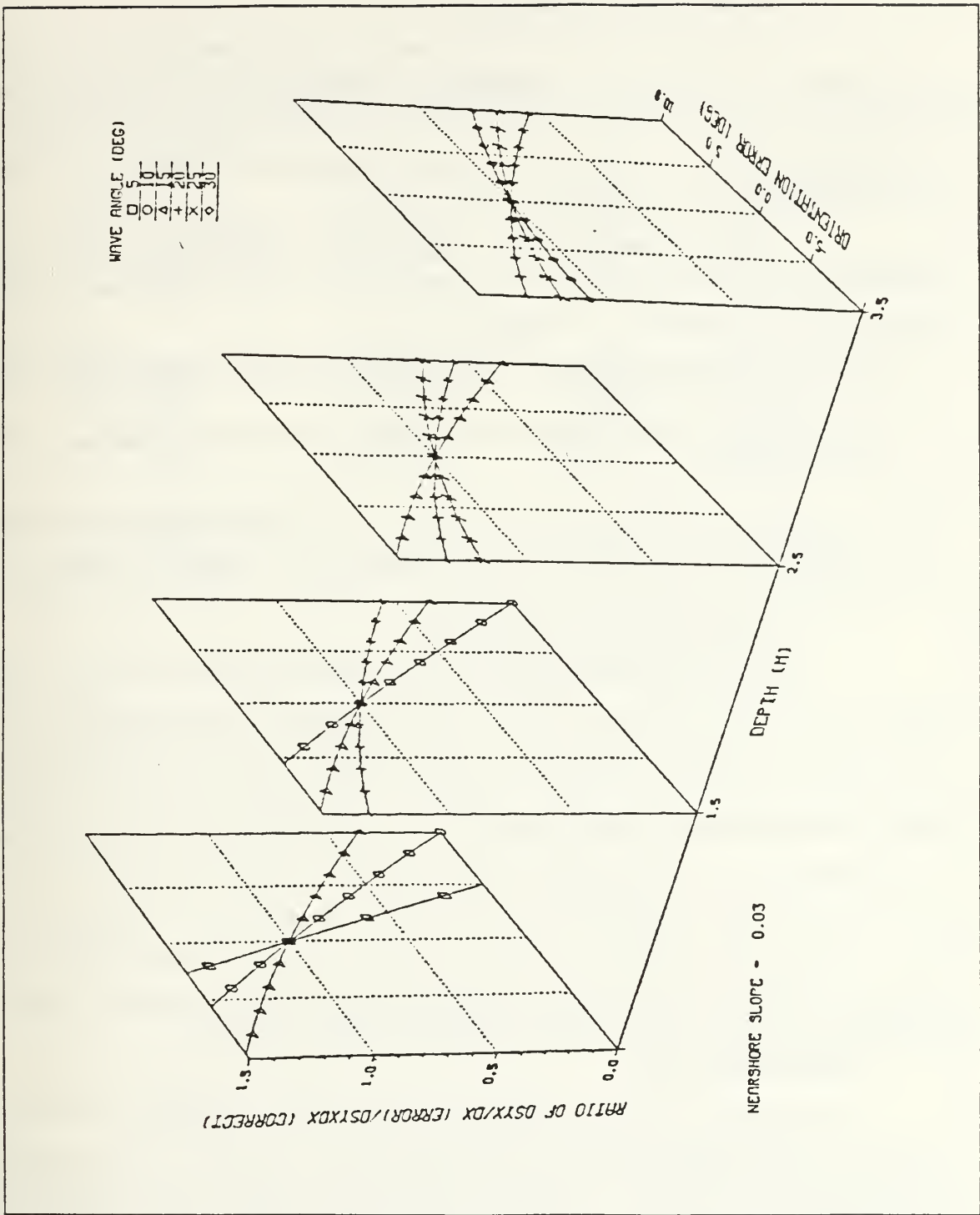


Figure 25. Sensitivity of $\partial S_{yx} / \partial x$ to beach angle orientation error for varying incident wave angles and depths and $\tan \beta = 0.03$.

b. Current Meter Orientation Error

Orientation of the current meters axes to the sled frame axes was considered to be within $1 - 2^\circ$ (Chapter V). Assuming conservation of the radiation stress gradient outside the surf zone, all current meters were individually oriented by a previously described selection process (Table 6). This numerical rotation is considered to have eliminated any current meter orientation error.

To assess the effect of other rotations which minimized the radiation stress gradient and which had realistic spectra shapes, rotation subsets within Table 6 combinations were also examined. For example,

- in run 16-2, rotating *both* current meters by a lesser amount instead of just the rear current meter by -2.86° , or
- in run 15-1, rotating the front current meter by 0.27° instead of the rear current meter by -0.29° ,

yielded no substantial difference in the magnitude of c_f along that transect. In other words, by using the concept of conservation of S_{yx} to initially orient the current meters, the resultant c_f 's were insensitive to the manner in which the orientation was done.

c. Current Meter Directional Gain Error

Current meter directional gain error is the error introduced by using a single gain and bias factor to calibrate current flows for all directions. The current meters were initially calibrated in a laboratory flow tank where gains and biases were determined for meter probe angles of 0° , 90° , 180° , and 270° . These angles correspond to the four sensor probes protruding from the current meter ball. Using the gain and bias factors for the u and v sensors determined for these four probe angles, the current meter was then checked against a controlled flow of $O(0.5 \text{ ms}^{-1})$ for meter probe angle increments of 15° . The standard deviations from the controlled flow for sled current meters 1, 2, and 4 were 0.012 , 0.012 , and 0.009 ms^{-1} , respectively. This error is included within the measurement error for current velocities addressed in the next section.

2. Measurement Error

To ascertain the effect of direct measurement error on the final determination of c_f , an error propagation analysis is conducted for both the "local" and "integrated" methods for c_f determination. Standard deviations (σ) of directly and indirectly measured variables used in equation (93) were estimated or determined from laboratory calibration results (Table 14).

The coefficient of variation (Barry, 1978), or fractional standard deviation (Young, 1962), is defined as:

Table 14. MEASUREMENT ACCURACY

parameter	σ	V_x (%)	typical value
water density	$\pm 2 \text{ kgm}^{-3}$	± 0.2	1022 kgm^{-3}
Zeiss vert control ¹	$\pm 0.03 \text{ m}$	± 1.5	2 m
Zeiss horiz control ¹	$\pm 0.03 \text{ m}$	± 0.075	40 m
c/m velocity	$\pm 0.05 \text{ ms}^{-1}$	± 5.0	u = 0.25 ms^{-1} v = $1. \text{ ms}^{-1}$
time	insignificant error		
wind stress	$\pm 0.04 \text{ Jm}^{-3}$	± 40.0	0.1 Jm^{-3}
MWL (Paro)	$\pm 0.0003 \text{ m}$	± 0.015	2 m
wind speed	$\pm 0.35 \text{ ms}^{-1}$	± 5.0	7 ms^{-1}
atmos. press.	$\pm 2 \text{ mb}$	± 0.2	1010.0 mb
atmos. temp.	$\pm 2^\circ\text{K}$	± 0.7	288°K
Indirect Measurement			
atmos. drag coeff.	$\pm 0.5 \times 10^{-3}$	$\pm 30.$	1.5×10^{-3}
atmos. density	$\pm 0.008 \text{ kgm}^{-3}$	± 0.6	1.25 kgm^{-3}

• where \pm refers to an approximate standard deviation.

¹ from Birkemeier and Mason (1984)

$$V_x = \frac{\sigma_x}{\bar{X}} \tag{101}$$

where \bar{X} is the arithmetic mean of replicate measurements of a variable. For the coefficient of variation determination (Table 14), the strict \bar{X} has been replaced by typical (order of magnitude) values, which are listed.

Calibration of the sled current meters was performed before and after the experiment by two different calibration laboratories. Pre-calibration gains and biases are listed in Table 15. Post-calibration gains varied by $\pm 3.0\%$ and $0.01 - 0.04 \text{ ms}^{-1}$ in bias or offset. A *conservative* estimate of measurement standard deviation for the current velocities is $\pm 5\%$ to include the unmeasured environmental source of error between field and laboratory conditions as well as the uncertainty ($\pm 3\%$) associated with using a single gain factor for all frequencies (Guza and Thornton, 1980) and directions.

The general rules of measurement error propagation can be stated for four arithmetic operators as (Barry, 1978):

$$\sigma_{\text{sum or diff}} = \pm \sqrt{\sigma_A^2 + \sigma_B^2 + \sigma_C^2 + \dots + \sigma_n^2} \quad (102)$$

$$\sigma_{\text{product}} = \pm ABC \dots n \sqrt{\left(\frac{\sigma_A}{A}\right)^2 + \left(\frac{\sigma_B}{B}\right)^2 + \left(\frac{\sigma_C}{C}\right)^2 + \dots + \left(\frac{\sigma_n}{n}\right)^2} \quad (103)$$

$$\sigma_{\text{quotient}} = \pm \frac{A}{B} \sqrt{\left(\frac{\sigma_A}{A}\right)^2 + \left(\frac{\sigma_B}{B}\right)^2} \quad (104)$$

$$\sigma_{\text{power}} = \pm nA^{n-1}\sigma_A \quad (105)$$

where the standard deviations σ_A, σ_B , etc., refer to the \pm error of the parameters (e.g., A, B) being analyzed (Young, 1962).

Table 15. SLED CURRENT METER CALIBRATION

<u>C/M</u> <u>Ser. #</u>	<u>Sled</u> <u>Lctn Hgt</u>	<u>Sled</u> <u>C/M #</u>	<u>PCM</u> <u>Channel</u>	<u>Vel</u>	<u>Gain</u>	<u>Bias</u>	<u>Correlation</u> <u>Coeff. (r²)</u>
S114	rear/mid	1	6	u	0.951	0.000	0.99944
			5	v	0.916	-0.008	0.99970
S762	front/lower	4	13	u	1.156	0.015	0.99899
			12	v	1.147	-0.012	0.99878
S354	side/upper	2	8	u	1.457	-0.030	0.99949
			7	v	1.457	0.017	0.99955

- current meters were Marsh-McBirney, Model 551
- calibrations by U.S.G.S, Gulf Coast Hydroscience Center, NSTL, MS
- formulation: velocity in ms⁻¹ = (gain x voltage) + bias

The wind stress measurement error has the largest V_x of all the parameters in Table 14. V_x can reach as high as 40%, depending on the manner and conditions under which the measurement was taken. Conditions during SUPERDUCK were conducive to accurate measurements of wind stress. These conditions were:

- over-water measurements taken during onshore winds,
- at the end of a 500 m pier,

- at a height of 18.7 m MSL which is 11.1 m above the pier deck,
- using the eddy correlation method, and
- using a Campbell CA27T Sonic Anemometer as backup for the Gill anemometer.

Standard deviation of atmospheric density (ρ_a) is estimated from equations (103), (104), and the equation of state for a perfect gas (Haltiner and Martin, 1957). Therefore, using a subjectively-determined and *conservative* value of $\pm 30\%$ for the wind stress measurement error, a C_d coefficient of variation of 30% is determined from equations (11) and (103).

Rewriting equation (93) as :

$$c_f = -\frac{\frac{\partial S_{yx}^T}{\partial x}}{\rho |u_t| v} + \frac{\tau_y^\eta}{\rho |u_t| v} - \frac{\frac{\partial M_y}{\partial t}}{\rho |u_t| v} \quad (106)$$

or

$$c_f = -A + B - C, \quad (107)$$

the measurement error in c_f , or the standard deviation of c_f , is the result of the additive σ 's of the three terms on the right-hand-side of equation (106), abbreviated as A, B, C in equation (107). Applying equations (102) to (104), results in standard deviations for the four terms in equation (107) as listed in Table 16.

Standard deviation determination of the radiation stress gradient (σ_A), requires σ of $(\partial S_{yx}^T / \partial x)$, which in turn requires σ of S_{yx}^T . S_{yx}^T or S_{yx} are calculated from equation (78) using the directly measured parameters u' , v' , ρ , and h . An upper bound for σ of S_{yx}^T can be formulated by approximating for shallow water waves:

$$S_{yx}^T = \rho h \int_{f_1}^{f_2} C_{uv} df = \approx \rho h cov_{uv} \leq \rho h \sigma_u \sigma_v \quad (108)$$

where cov_{uv} is the covariance of the u and v velocities and is bounded by (e.g. Davis, 1986):

$$cov_{u,v} \leq \sigma_u \sigma_v \quad (109)$$

Therefore $\sigma_{S_{yx}^T}$ can conservatively be approximated as:

$$\sigma_{S_{yx}^T} = \pm \bar{S}_{yx}^T \sqrt{\left(\frac{\sigma_u}{u}\right)^2 + \left(\frac{\sigma_v}{v}\right)^2 + \left(\frac{\sigma_\rho}{\rho}\right)^2 + \left(\frac{\sigma_h}{h}\right)^2} \quad (110)$$

σ_ρ and σ_h are negligible compared to σ_u and σ_v (Table 14) and may be neglected.

One may then write:

$$\sigma_{\Delta S_{yx}^T} = \pm \overline{\Delta S_{yx}^T} \sqrt{(\sigma_{S_{yx}^T}^T)_{rear}^2 + (\sigma_{S_{yx}^T}^T)_{front}^2} \quad (111)$$

$$\frac{\sigma_{\Delta S_{yx}^T}}{\Delta x} = \pm \frac{\overline{\Delta S_{yx}^T}}{\Delta x} \sqrt{\left(\frac{\sigma_{\Delta S_{yx}^T}}{\overline{\Delta S_{yx}^T}}\right)^2 + \left(\frac{\sigma_{\Delta x}}{\Delta x}\right)^2} \quad (112)$$

The standard deviation of Δx is much less than the standard deviation of ΔS_{yx}^T and therefore may be neglected. The standard deviation determined by equation (112) for the "integrated" method is reduced by a factor of one-half to account for that method's increased sample size (see equation 8-4). Standard deviation of the radiation stress gradient for each of the sled's data runs, using both the "local" and "integrated" methods for c_f determination, were calculated. The mean σ for radiation stress gradient of all four transects is listed in Table 16.

The standard deviation for the wind stress (τ_y^y) was determined from equations (11) and (103), and Table 14. Standard deviation of $\partial M_y / \partial t$ was determined by assuming:

$$\frac{\partial M_y}{\partial t} \approx \frac{\Delta M_y}{\Delta t} \approx \frac{\Delta(\rho D V)}{\Delta t} \quad (113)$$

since $M_y' \ll \bar{M}_y$, and then applying equations (102) through (104) and Table 14 values.

A typical mean c_f value of 0.003 was used in equation (101) to determine the c_f coefficient of variation in Table 16. Because of the relatively large incident wave angles and the measurement precision utilized in the SUPERDUCK experiment, propagation of measurement error resulted in reasonable c_f values for both methods (Table 16). The "integrated" method's σ_{c_f} was superior to the "local" method because of the larger relative error for the radiation stress gradient (equation 112) experienced when Δx is small. The integrated method's error bounds for the c_f range in Table 13 are $\pm 4-15\%$.

Table 16. ERROR PROPAGATION ANALYSIS

Term (eqn 107)	σ	V_x (%)	c_f Method
A	0.0015	24	local
	0.00013	10	integrated
B	0.00003	31	
C	0.00007	70	
c_f	0.0015	50	local
	0.00015	5	integrated

where term

$$A = \frac{\partial S_{yx}^T / \partial x}{\rho |u_t| v} \quad B = \frac{\tau_y^\eta}{\rho |u_t| v} \quad C = \frac{\partial M_y / \partial t}{\rho |u_t| v}$$

3. Finite Differencing Error

Thornton and Guza (1981) examined the error involved in representing an arbitrary continuous function by discrete measurement points. Using a Taylor series expansion for S_{yx} :

$$S_{yx}(x + \Delta x) = S_{yx}(x) + \Delta x \frac{\partial S_{yx}(x)}{\partial x} + \frac{(\Delta x)^2}{2!} \frac{\partial^2 S_{yx}(x)}{\Delta x^2} + \dots \quad (114)$$

and then solving for the true radiation stress gradient:

$$\frac{\partial S_{yx}}{\partial x} = \frac{\Delta S_{yx}}{\Delta x} - \frac{\Delta x}{2!} \frac{\partial^2 S_{yx}}{\partial x^2} - \frac{\Delta x^2}{3!} \frac{\partial^3 S_{yx}}{\partial x^3} - \dots \quad (115)$$

or

$$\frac{\partial S_{yx}}{\partial x} - \frac{\Delta S_{yx}}{\Delta x} = Error \quad (116)$$

where the sum of the second and infinite terms on the right-hand side of equation (115) is the error of the finite difference space approximation.

Relative error (R) may be defined as:

$$R = \frac{\text{Error}}{\frac{\partial S_{yx}}{\partial x}} \quad (117)$$

Solving for R where only the first error term in equation (115) is considered, S_{yx} for monochromatic shallow water linear waves inside the surf zone may be expressed as:

$$S_{yx} = E \sin \alpha \cos \alpha \approx AD^{5/2} \quad (118)$$

where

$$\begin{aligned} E &= \frac{1}{8} \rho g \gamma^2 D^2, \\ \gamma &= H_{rms}/h, \\ D &= \bar{\eta} + h, \text{ and} \\ A &= \text{complicated constant} \end{aligned}$$

Substituting equation (118) into (117):

$$R \approx \frac{3}{4} \Delta x \frac{\tan \beta}{h} \quad (119)$$

where $D \approx h$. (Thornton and Guza, 1981)

This approximation (equation 119) is adequate providing Δx and $\tan \beta$ are reasonably small. However, Δx and $\tan \beta$ are not always small in this application. Therefore R is redefined to include a sufficient number of terms on the right-hand side of equation (115) to allow convergence to within 5% of R. Resultant computations revealed that equation (119) was sufficiently accurate (within 5%) for most of the SUPERDUCK data. However, using the "integrated" method between the most inshore data run and the beach required additional iterations (up to five) to stabilize R.

The relative error in equation (117) is biased in one direction because the term of largest magnitude is written as:

$$\frac{\frac{\Delta x}{2!} \frac{\partial^2 S_{yx}}{\partial x^2}}{\frac{\partial S_{yx}}{\partial x}} \approx \frac{\left(\frac{\partial h}{\partial x}\right)^2}{\frac{\partial h}{\partial x}} = \text{slope} \quad (120)$$

and assuming negligible bottom curvature. Therefore the sign of R is fixed as the same sign as beach slope. The finite approximation for the radiation stress gradient may be written as:

$$\frac{\Delta S_{yx}}{\Delta x} = (1 + R) \frac{\partial S_{yx}}{\partial x} \quad (121)$$

where R represents the overestimation of $\partial S_{yx} / \partial x$ for positive slopes and the underestimation for negative slopes. Finite difference relative error for the four transects of this research are listed in Table 17 and Table 18. They are listed for both methods of c_f determination. The larger error for the "integrated" method value between the most inshore data run and the beach was due to the combined effect of increased Δx , decreased depth, and steeper slope, *all* which combine to increase R. The relative error is significantly reduced when using the "local" method due to its much smaller Δx . "Integrated" method's R ranges from -27% on the nearshore side of the bar to nearly 200% on the nearshore slope. However, except for the gross error on the nearshore slope, "integrated" method's relative error is less than 50%. This would cause c_f error due to finite differencing to be less than 50% (assuming negligible wind stress and steady state conditions in equation 93).

4. Combined Error

The various sources of error are now combined into a total, or combined, error relative to the bar. To establish a conservative combined error, finite differencing error is assigned a range of error rather than a bias and unquantified errors are estimated at $\pm 20\%$. Mean finite difference error for the trough does not include the gross error, O(200%), between the most inshore sled run position and the beach. Therefore the final c_f value for the trough does not reflect the nearshore slope.

The *maximum* combined error is determined by adding the four maximum possible errors listed in Table 19. However it is not reasonable to define maximum error in this manner since each of the four errors have a range of uncertainty associated with them and they are uncorrelated. It is very unlikely that the errors would all be a maximum and in the same direction at the same time (Barry, 1978). Hence, assuming the errors are independent of one another, the combined error is obtained from equation 102 and results in final momentum balance c_f values of 0.004 ± 0.0010 , for offshore the bar, 0.002 ± 0.0006 for on top and immediately before the bar, and 0.001 ± 0.0003 for the trough region.

Table 17. FINITE DIFFERENCE RELATIVE ERRORS

October 15 1986 Relative Error (R)				
<u>Sled Run</u>	<u>Δx (m)</u>	<u>$\tan \beta$</u>	<u>MWL (m)</u>	<u>R (%)</u>
15-1	1.99 27.99	0.0199 0.0238	2.80 2.29	1. 23.
15-2	1.99 24.24	0.0287 0.0241	1.78 1.72	2. 27.
15-3	1.99 44.65	-0.0031 -0.0127	1.67 1.99	0. -20.
15-4	1.99 42.03	0.0554 0.0549	2.30 1.15	4. 197.
Beach				
October 16 1986 Relative Error (R)				
16-2	1.99 50.52	0.0158 0.0290	3.33 2.61	1. 46.
16-3	1.99 17.69	0.0349 0.0341	1.89 1.70	3. 28.
16-4	1.99 12.99	0.0309 0.0198	1.51 1.52	3. 13.
16-5	1.99 33.49	0.0145 -0.0081	1.54 1.72	1. -12.
16-6	1.99 33.88	0.0029 0.0564	1.91 0.96	0. 196.
Beach				

Table 18. FINITE DIFFERENCE RELATIVE ERRORS

October 17 1986 Relative Error (R)				
<u>Sled Run</u>	<u>$\Delta x(m)$</u>	<u>$\tan \beta$</u>	<u>MWL (m)</u>	<u>R (%)</u>
17-1	1.99 34.60	0.0182 0.0224	3.85 3.22	1. 19.
17-2	1.99 26.80	0.0397 0.0364	2.59 2.01	2. 39.
17-3	1.99 9.54	0.0309 0.0265	1.43 1.31	3. 15.
17-4	1.99 4.09	0.0221 0.0232	1.19 1.14	3. 6.
17-5	1.99 31.56	0.0166 -0.0153	1.09 1.25	2. -27.
17-6	1.99 4.88	-0.0036 0.0109	1.40 1.48	0. 3.
17-7	1.99 6.27	0.0137 0.0276	1.55 1.49	1. 9.
17-8	1.99 20.06	0.0495 0.0716	1.43 0.72	5. 197.
Beach				
October 18 1986 Relative Error (R)				
18-1	1.99 48.33	0.0113 0.0259	3.80 3.09	0. 32.
18-2	1.99 18.85	0.0405 0.0369	2.38 1.94	3. 29.
18-3	1.99 21.60	0.0334 0.0258	1.49 1.31	3. 34.
18-4	1.99 27.67	0.0083 -0.0096	1.13 1.30	1. -15.
18-5	1.99 33.71	-0.0223 0.0438	1.48 0.74	-2. 196.
Beach				

Table 19. COMBINED ERROR RELATIVE TO THE BAR ON THE BED SHEAR STRESS COEFFICIENT AS DETERMINED FROM A MOMENTUM BALANCE

	Trough	On the Bar	Offshore
beach angle orientation error	$\pm 8\%$	$\pm 10\%$	$\pm 10\%$
measurement error	$\pm 5\%$	$\pm 5\%$	$\pm 5\%$
finite differencing error mean R $\frac{\Delta S_{yx}}{\Delta x}$ error = $1/(1+R)$	-19% 23%	19% -16%	31% -24%
unquantified errors (est.)	$\pm 20\%$	$\pm 20\%$	$\pm 20\%$
combined c_f error	$\pm 32\%$	$\pm 28\%$	$\pm 33\%$
final c_f	0.001 ± 0.0003	0.002 ± 0.0006	0.004 ± 0.0010

VIII. LONGSHORE CURRENT MODEL

A. INTRODUCTION

A first-order longshore current model for a barred beach is proposed. The model is based on balancing the wave-induced radiation stress gradient with longshore bed shear stress, turbulent momentum exchange, and longshore surface wind stress. Stationary wave conditions and straight and parallel bottom contours are assumed. The waves are described as random, but narrow-banded in frequency and direction. Model results are compared to field observations and bed shear stress coefficients are determined by model-fitting.

B. MODEL THEORY

There are no field-verified longshore current models for a barred beach. Therefore a model which has been field-verified for a planar beach was selected for this analysis. The model (Thornton and Guza, 1986; hereafter referred to as TG86) is based on a simple balance between the gradient of the wave-induced radiation stress, the bed shear stress, and the gradient of turbulence-induced radiation stress. The model's assumptions are stated in the previous paragraph. The longshore current model is based on a random wave height transformation model (Thornton and Guza, 1983; hereafter referred to as TG83). Modifications to the TG86 model are made based on the availability of additional data from SUPERDUCK and with the purpose of improving and broadening the model's applicability to barred beaches. These modifications are the inclusion of surface wind stress in the momentum balance, retention of incident wave angle dependency, and the use of a breaking wave height distribution based on a slope-dependent γ and an improved empirical expression for the breaking wave percentage as a function of H , h , and γ . Whereas TG86 found turbulent momentum exchange to be unimportant for their planar beach topography, turbulent momentum exchange is shown to be required in order to model current velocities in the trough region of a barred beach. The TG86 longshore current model is briefly summarized below with modifications described later.

1. Wave Height Transformation

This portion of the model is an extension of work by Battjes and Janssen (1978). The wave height transformation is conceptualized as an energy flux balance given by:

$$\frac{\hat{c}(EC_g \cos \hat{\alpha})}{\hat{c}x} = \langle \varepsilon_b \rangle \quad (122)$$

where $C_g \cos \hat{\alpha}$ is the shoreward component of wave group velocity, $\hat{\alpha}$ is the mean incident wave angle of the narrow-banded waves, and $\langle \varepsilon_b \rangle$ is the ensemble-averaged dissipation due to wave breaking. Analysis of SUPERDUCK data, as well as results from TG83, indicated that the ensemble-averaged dissipation due to bottom friction $\langle \varepsilon_f \rangle$ is negligible compared with $\langle \varepsilon_b \rangle$, and therefore $\langle \varepsilon_f \rangle$ is omitted in equation (122).

Based on analysis of field data from Torrey Pines Beach, CA, the Rayleigh wave height probability density function (pdf), $p(H)$, was shown to qualitatively describe the measured wave heights across that planar beach. The Rayleigh pdf is described by:

$$p(H) = \frac{2H}{H_{rms}^2} \exp \left[-\left(\frac{H}{H_{rms}} \right)^2 \right] \quad (123)$$

where H is wave height. The Rayleigh distribution describes all waves.

Only the breaking waves are dissipative, resulting in changes in the momentum flux, i.e. wave forcing. Therefore a distribution describing the breaking waves alone is required. Wave height probability density functions were calculated from field measurements taken at Ft. Ord's Soldiers Beach, Monterey, CA. These pdf's were used to more realistically model random wave height transformation across the surf zone.

Within the surf zone, breaking wave height distribution $[p_b(H)]$ is approximated by weighting the Rayleigh pdf:

$$p_b(H) = W(H) p(H) \quad (124)$$

where the weighting function $W(H) \leq 1$. It is noted the breaking wave distribution is not a pdf, but that the area of $p_b(H)$ gives the percentage of the waves that are breaking. A simple form of $W(H)$ which approximates the fraction of waves that break from off-shore to saturation conditions is:

$$W(H) = \left[\frac{H_{rms}}{\gamma h} \right]^4 \quad (125)$$

where

$$\gamma = \frac{H_{rms}}{h} \quad (126)$$

for saturated wave breaking conditions. Based on the Ft. Ord data, a modification to equation (125) which more heavily weights the larger waves is given by:

$$W(H) = \left[\frac{H_{rms}}{\gamma h} \right]^2 \left[1 - \exp \left[- \left[\frac{H}{\gamma h} \right]^2 \right] \right] \leq 1 \quad (127)$$

Wave breaking dissipation is modeled as a simple periodic bore:

$$\varepsilon_b = \frac{\bar{f}}{4} \rho g \frac{(BH)^3}{h} \quad (128)$$

where B is a breaker coefficient of $O(1)$ and \bar{f} is the mean wave frequency which is the peak frequency for narrow-band wave spectra. The B coefficient accounts for differences in various breaker types and is a function of the proportion of foam region on the breaker face (Figure 26). The peak frequency in the SUPERDUCK S_{yx} spectra is used for \bar{f} .

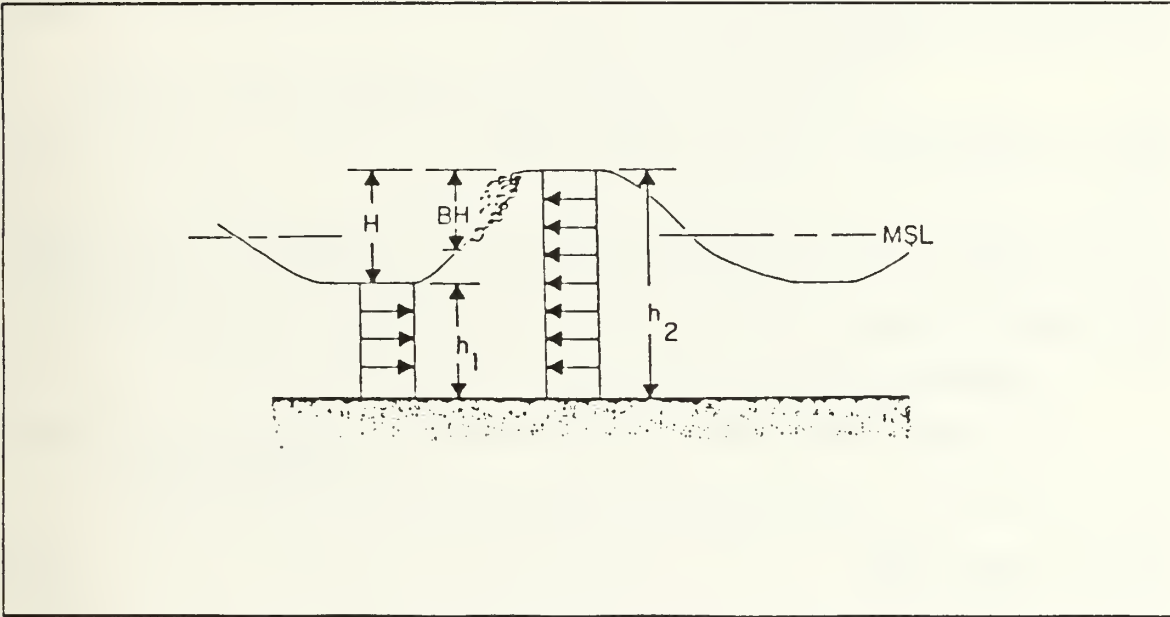


Figure 26. Periodic bore used to describe spilling breakers. (from Thornton and Guza, 1983).

The ensemble-averaged dissipation due to wave breaking is calculated by multiplying the dissipation for a single broken wave of height H by the probability of wave breaking at each height $[p_b(H)]$, and integrating over all H :

$$\langle \varepsilon_b \rangle = \frac{B^3}{4} \rho g \frac{\bar{f}}{h} \int_0^\infty H^3 p_b(H) dH \quad (129)$$

By substituting from equations (124) and (127) and evaluating the definite integral, equation (129) may be written as:

$$\langle \varepsilon_b \rangle = \frac{3\sqrt{\pi}}{16} \rho g B^3 \bar{f} \frac{H_{rms}^5}{\gamma^2 h^3} \left[1 - \frac{1}{(1 + (H_{rms}/\gamma h)^2)^{5/2}} \right] \quad (130)$$

Energy flux (EC_g from equation 122), is approximated using linear theory for C_g at frequency \bar{f} , and energy is calculated based on the Rayleigh pdf:

$$E = \frac{1}{8} \rho g \int_0^\infty H^2 p(H) dH = \frac{1}{8} \rho g H_{rms}^2 \quad (131)$$

Substituting equations (130) and (131) into (122) yields a first-order differential equation for the linear wave height transformation model:

$$\frac{\partial}{\partial x} \left(\frac{1}{8} \rho g H_{rms}^2 C_g \cos \alpha \right) = \frac{3}{10} \sqrt{\pi} \rho g \frac{B^3}{\gamma^4 h^5} \bar{f} H_{rms}^7 \quad (132)$$

A spatially-dependent wave height [$H_{rms}(x)$] can then be determined for an arbitrary bottom profile across the surf zone by numerical integration, given an initial value of H_{rms} . The H_{rms} profile is used as input for the longshore current calculation.

2. Longshore Current

The longshore current distribution across the surf zone is based on conservation of momentum. Rewriting equation (3), wave-induced radiation stress may be written:

$$\tilde{S}_{yx} = EC_g \cos \alpha \frac{\sin \hat{\alpha}}{C} \quad (133)$$

where

$$\frac{\sin \hat{\alpha}}{C} = \text{constant} = \frac{\sin \hat{\alpha}_o}{C_o} \quad (134)$$

by Snell's Law of linear wave refraction. The subscript "o" refers to any arbitrary location. Therefore the wave-induced radiation stress gradient may be written as

$$\frac{\hat{c}}{\hat{c}x} \tilde{S}_{yx} = \frac{\sin \alpha_o}{C_o} \frac{\hat{c}}{\hat{c}x} (EC_g \cos \hat{\alpha}) = \frac{\sin \hat{\alpha}_o}{C_o} \langle \varepsilon_b \rangle \quad (135)$$

where $\langle \varepsilon_b \rangle$ is substituted from equation (122). Assuming steady state conditions and negligible wind stress, the longshore momentum balance is written as:

$$\frac{\sin \hat{\alpha}_o}{C_o} \langle \varepsilon_b \rangle = -\tau_y^b - \frac{\hat{c}}{\hat{c}x} S_{yx}'' \quad (136)$$

TG86 used equation (136) and model-fitting to solve for the horizontal profile of longshore current across a planar beach. They obtained a hierarchy of solutions by choosing combinations of linear or non-linear bed shear stress, with and without turbulent momentum exchange. Turbulent momentum exchange was found not to be important for their planar beach topography. They concluded that a non-linear bed shear stress without turbulent momentum exchange was their preferred choice for general applications, based on its fit to their data. A mean c_f for their four days of data was 0.006 ± 0.0007 .

C. MODIFICATION OF MODEL BASED ON FIELD DATA

Modifications to the TG86 longshore current model are the inclusion of surface wind stress, incident wave angle dependency, and use of a breaking wave weighting function based on a slope-dependent γ and an improved empirical expression for breaking wave percentage as a function of H , h , and γ . The use of turbulent momentum exchange is found to be important for modeling longshore current velocities in the trough. The inclusion of surface wind stress and incident wave angle dependency are covered in the Model Results section. The other modifications are addressed next.

1. A Slope Dependent γ

Since the TG83 model was developed for planar beaches, γ was assigned a constant value of 0.42 (equation 39) and is the ratio H_{rms}/h for saturated wave breaking conditions. However, Sallenger and Holman (1985) found γ to be a function of beach slope based on data from several field experiments. They determined an empirical relation for a slope-dependent γ based on their data:

$$\gamma = 3.2 \tan \beta + 0.30 \quad (137)$$

The ratio H_{rms}/h is compared to beach slope (Figure 27) for both the SUPER-DUCK data and the data used by Sallenger and Holman (1985). The solid line in

Figure 27 is Sallenger and Holman's (1985) empirical relation for γ . Most of the SUPERDUCK data has the same magnitude of scatter as previous data sets about the solid line, with even negative slopes (found on the inshore side of the bar) in general agreement. The exception is for SUPERDUCK data sets located in the trough and on the foreshore slope (Runs 11-3, 15-4, 17-6, 17-7, 17-8, 21-4). They have a significantly lower value of H_{rms}/h and are indicative of non-saturated breaking wave conditions. Obviously a slope-dependent γ relationship is required for a barred beach. Based on Figure 27 and the general fit of the SUPERDUCK data, equation (137) is used for the SUPERDUCK analysis.

2. Breaking Wave Weighting Function

The weighting function, $W(H)$, used in TG83 was based on only four data runs for a single transect of a beach with a tidal plateau. To improve on the formulation of $W(H)$, breaking wave pdf's are calculated for the SUPERDUCK data. Time series of pressure head, $[p_h(t)]$, are linearly transformed into $\eta(t)$ time series by first calculating the complex Fourier spectra of $p_h(t)$, then multiplying by a linear transform function $[H(f)]$, band pass filtering between 0.03 - 1.00 Hz, and finally applying an inverse Fourier transform to the $\eta(f)$ function.

The transfer function $H(f)$ (from equation 38) is held constant at the 0.5 Hz value for the interval 0.5 Hz to 1.0 Hz so as to include the additional higher frequency variance for the H_{rms} calculations, but not to overly bias them with the exponentially increasing $H(f)$ values. Filtering is accomplished by zeroing out the Fourier amplitude coefficients of the undesired frequencies before applying the inverse Fourier transform. The entire 34.1 min record is transformed at one time. As an example, the initial three minutes of Run 15-2's $p_h(t)$ time series is compared with its transformed $\eta(t)$ series in Figure 28. The transfer function $H(f)$ and the $G_\eta(f)$ spectra determined from the entire $\eta(t)$ series are also included. Wave periods and heights are determined from the $\eta(t)$ time series by the down-crossing method. Root-mean-square wave height is determined statistically from the calculated $\eta(t)$ time series as:

$$H_{rms} = \left[\frac{1}{N} \sum_{i=1}^N H_i^2 \right]^{1/2} \quad (138)$$

The statistical H_{rms} from the $\eta(t)$ series are compared with the energy-based H_{rms} (equation 90) determined from both the $G_\eta(f)$ spectra discussed in Chapter VII and the $G_\eta(f)$ spectra calculated from the $\eta(t)$ record (Figure 28). Root-mean-square wave

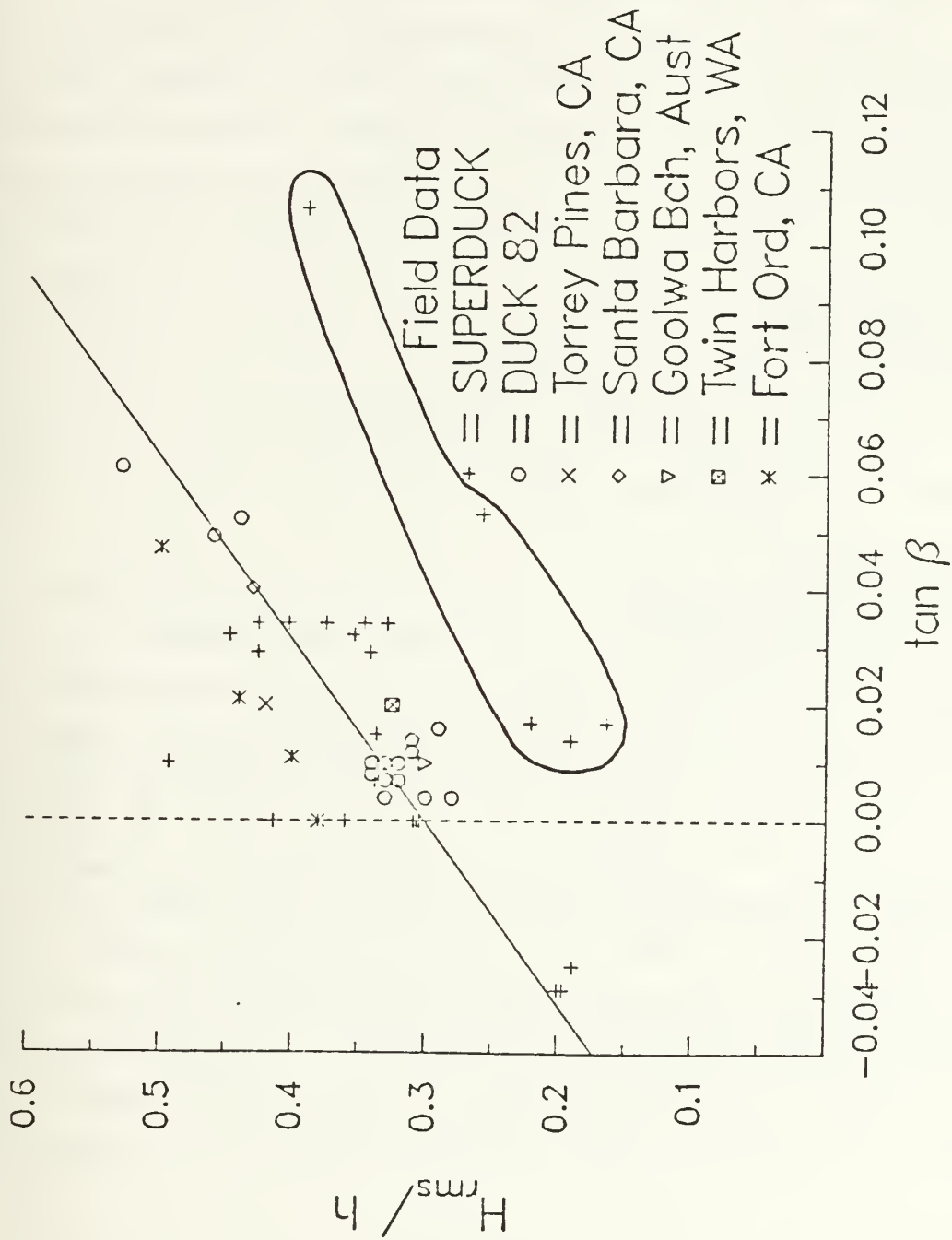


Figure 27. Ratio H_{rms}/h versus beach slope for various data sets. Circled data represent trough and foreshore slope locations.

height from all three sources compared favorably [within (10%)], with the difference indicating a measure of non-linearity in the surface elevation record.

As discussed in Chapter IV, visual observations of wave dissipation (i.e., wave breaking) at the sled were electronically marked on the data set records. These marks are then superimposed on the calculated $\eta(t)$ time series to identify which waves were breaking during each 34.1 min data run. From this procedure, wave heights and periods for all waves, and a subset for just breaking waves, are obtained. Pdf's of all waves and breaking waves for 15-17 October are illustrated in Figure 29 and Appendix A (Figure 47 through Figure 49). Since the data were measured sequentially and not simultaneously, wave heights are normalized by the mean offshore wave height to account for any variability in the incident wave conditions. The pdf's are normalized to the mean offshore wave height measured by a WAVERIDER buoy located 6 km offshore. Equipment malfunction precluded breaking wave identification on other days of the experiment.

Breaking wave data from SUPERDUCK, as well as the four data runs from Ft. Ord (TG83), are compared in Figure 30. The ordinate is the fraction of waves which are breaking (Q) and the abscissa is the ratio, $H_{rms}/\gamma h$, where γ is slope-dependent and calculated from equation (137). Thus for saturated conditions, both the ordinate and abscissa are equal to unity. The breaking wave fraction is obtained by dividing the number of waves identified as breaking by the total number of waves. The total number of waves in a data run was approximately 400. The Ft. Ord data are indicated by an 'x', SUPERDUCK data acquired in the trough are solid circles, and all other SUPERDUCK data are indicated by open circles. Three breaking wave weighting functions are illustrated. The dotted line is the TG83 weighting function (equation 127). The chain-dot line is from a theoretical expression (Battjes and Janssen, 1978; Battjes and Stive, 1985) where the cumulative probability distribution of all wave heights (breaking or non-breaking) is the Rayleigh distribution, but abruptly terminated at the breaking wave height:

$$Q = \left[\frac{H_{rms}}{\gamma h} \right] \ln Q + 1 \quad (139)$$

Neither of these two functions provide a reasonable fit to the data. However, a function which substantially improves the fit to the data is:

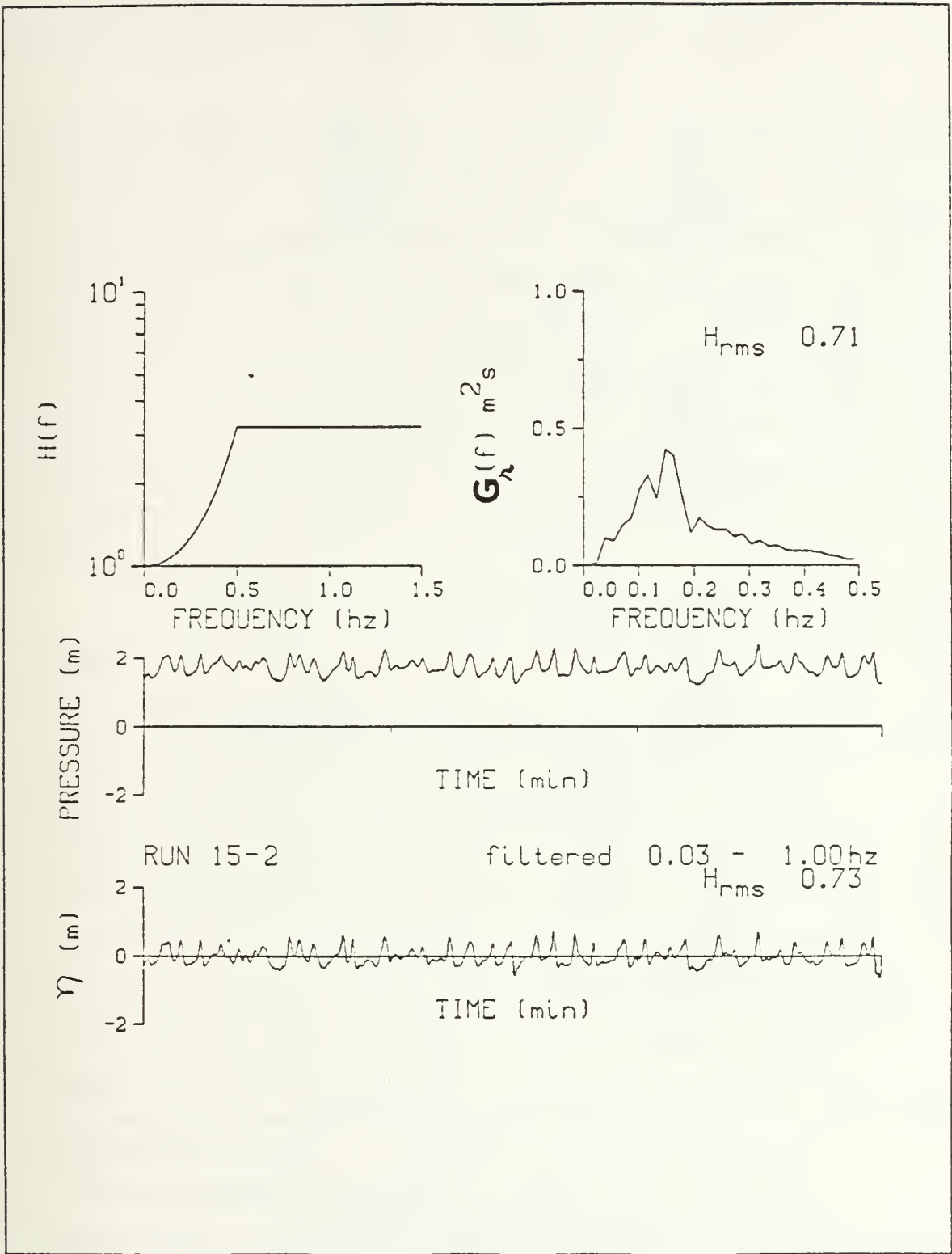


Figure 28. Example $p_h(t)$ and $\eta(t)$ time series with corresponding $G_\eta(f)$ spectra.

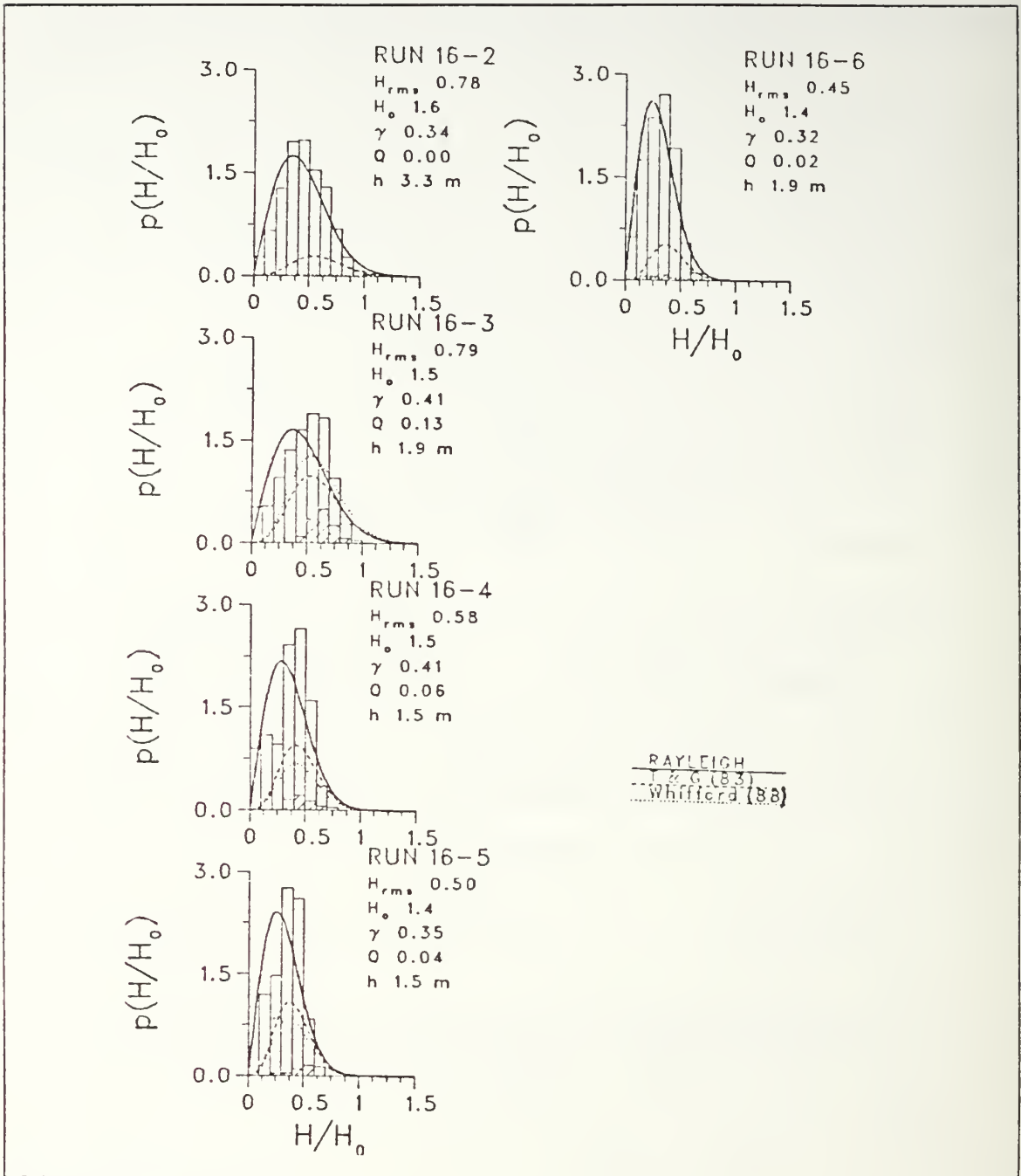


Figure 29. Wave height and breaking wave height distributions (hatched area) normalized to offshore H_{rms} for 16 October. The Rayleigh distribution is the solid line and empirical breaking wave distributions given by equations (127) and (140) are the dotted and dashed lines, respectively.

$$Q = W(H) = \left[1 + \tanh \left[8 \left[\frac{H_{rms}}{\gamma h} - 0.99 \right] \right] \right] \left[1 - \exp \left[- \left[\frac{H}{\gamma h} \right]^2 \right] \right] \quad (140)$$

and is delineated by a dashed line. This function (equation 140) has no physical justification but is merely an empirical expression derived to better fit the non-trough data. It is noted that none of the three functions fit both the trough and non-trough data. The right half of the right-hand side of equation (140) is taken from equation (127) and is used to more heavily weight the larger waves towards breaking. Observations show that the largest waves at a particular location are more likely to break (TG83). This skewing of the pdf is substantiated by the breaking wave observations (hatched areas) seen in the pdf figures. Very little wave breaking occurs until $H_{rms}/\gamma h$ reaches 0.8, then the percentage of breaking waves increases rapidly. The addition of the SUPERDUCK data suggests a more rapid increase in the breaking wave percentage within a smaller $H_{rms}/\gamma h$ band -- almost to the point of describing a "step" function indicative of all waves breaking at a fixed *breaker point*.

The ratio $H_{rms}/\gamma h$ in Figure 30 has a certain amount of error associated with it. The error in γ is the result of an imperfect fit to the data in Figure 27. Tidal fluctuations also affect the h term. Thus there are runs which have $H_{rms}/\gamma h$ ratios greater than one, yet were unsaturated.

It is also noted that during field identification of the breaking waves, breaking wave percentages were visually estimated to be often in the range between 60-90%. Yet subsequent data analysis reveals the percentages to be much lower. This may perhaps be similar to the phenomena associated with visually estimating wave heights from ships, where it has long been recognized that the human eye perceives an average of the highest 1/3 wave heights and not the true mean wave height. This lead to the designation of ship wave height observations as "significant wave heights" and not mean wave heights. In a similar manner, SUPERDUCK visual observations of breaking wave percentages were overestimates. Thus visual observations of saturated wave conditions from other experiments may need to be reviewed.

D. MODEL RESULTS

1. Wave Height Transformation

As input to the wave transformation model, H_{rms} and \bar{f} measured during the orientation runs outside the surf zone (Runs 15-1, 16-2, 17-1, 18-1) are used as initial conditions. Mean wave frequency is assigned as the frequency of the spectral peak in

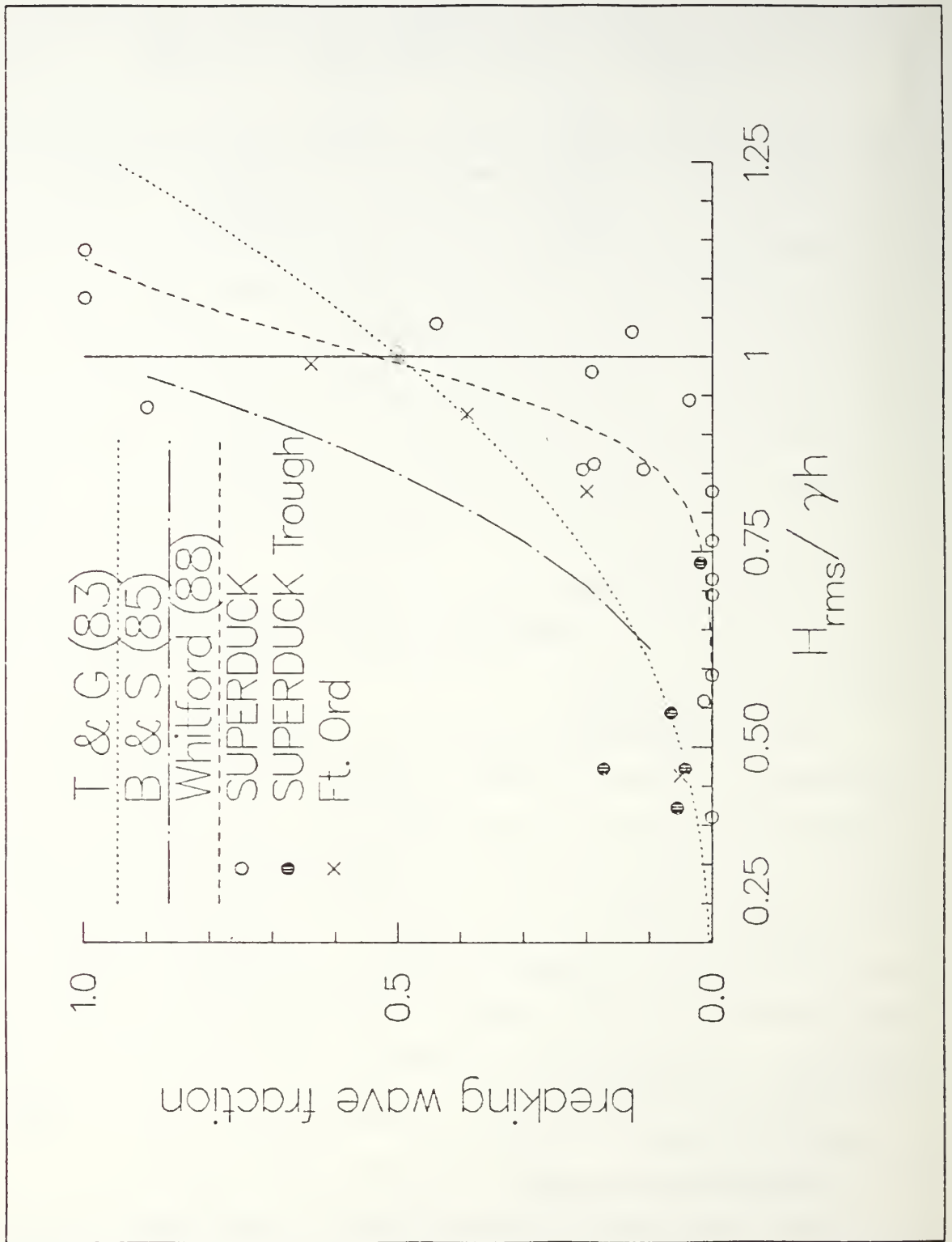


Figure 30. Breaking wave fraction (Q) versus the ratio $H_{rms}/\gamma h$.

sea surface elevation. Mean incident wave angle is then assigned as the angle for \bar{f} from the significant wave spectra for that day. TG83 and TG86 assumed small wave incident angles and set the $\cos \hat{\alpha}$ term in equation (122) to unity. Because of the large incident wave angles during SUPERDUCK, incident wave angle dependency is retained throughout the analysis by inclusion of the $\cos \hat{\alpha}$ term. A forward stepping scheme is used to evaluate equation (122):

$$(EC_g \cos \hat{\alpha})_2 = (EC_g \cos \hat{\alpha})_1 + (\langle \varepsilon_b \rangle)_1 \Delta x \quad (141)$$

All variables in equation (141) are known except B, which is determined by model-fitting the calculated H_{rms} to the field-measured H_{rms} . Model-fitting is accomplished by minimizing the least square error between observed and modeled data. Results of the model-fitting are shown in Figure 31 and Appendix A (Figure 50 through Figure 52). Field H_{rms} is represented by an "x" for each of the sled runs and is determined from pressure sensor measurements. The spatial step size, Δx , was varied from 0.5 m to 10.0 m with negligible effect on the H_{rms} profile. Therefore $\Delta x = 5.0$ m was arbitrarily selected to allow suitable cross-shore definition along with reduced computational time.

A constant B coefficient of O(1) is determined by a least square fit for all four days (Table 20). Field and modeled H_{rms} show good agreement except for the trough area on 15 and 16 October. Root-mean-square wave height is undermodeled by about 35% for these exceptions. Spatially-variable B coefficients were also determined which gave exact fits to the field data. However their drastic spatial changes in B appeared unrealistic since the breaker type was observed to be similar for most of the transect, except on the very nearshore slope inshore of the last sled runs. A constant B coefficient for a transect was deemed appropriate.

2. Longshore Current Model Results

Longshore current is modeled by including surface wind stress in the momentum balance equation of equation (136):

$$\frac{\sin \alpha_o}{C_o} \langle \varepsilon_b \rangle = -\tau_y^b + \tau_y^{\eta} - \frac{\hat{c}}{\partial x} S_{yx}'' \quad (142)$$

and using various combinations of the following approaches:

- linear or non-linear formulation of τ_y^b ,
- with and without turbulent mixing,
- spatially-variable or constant c_f and N.

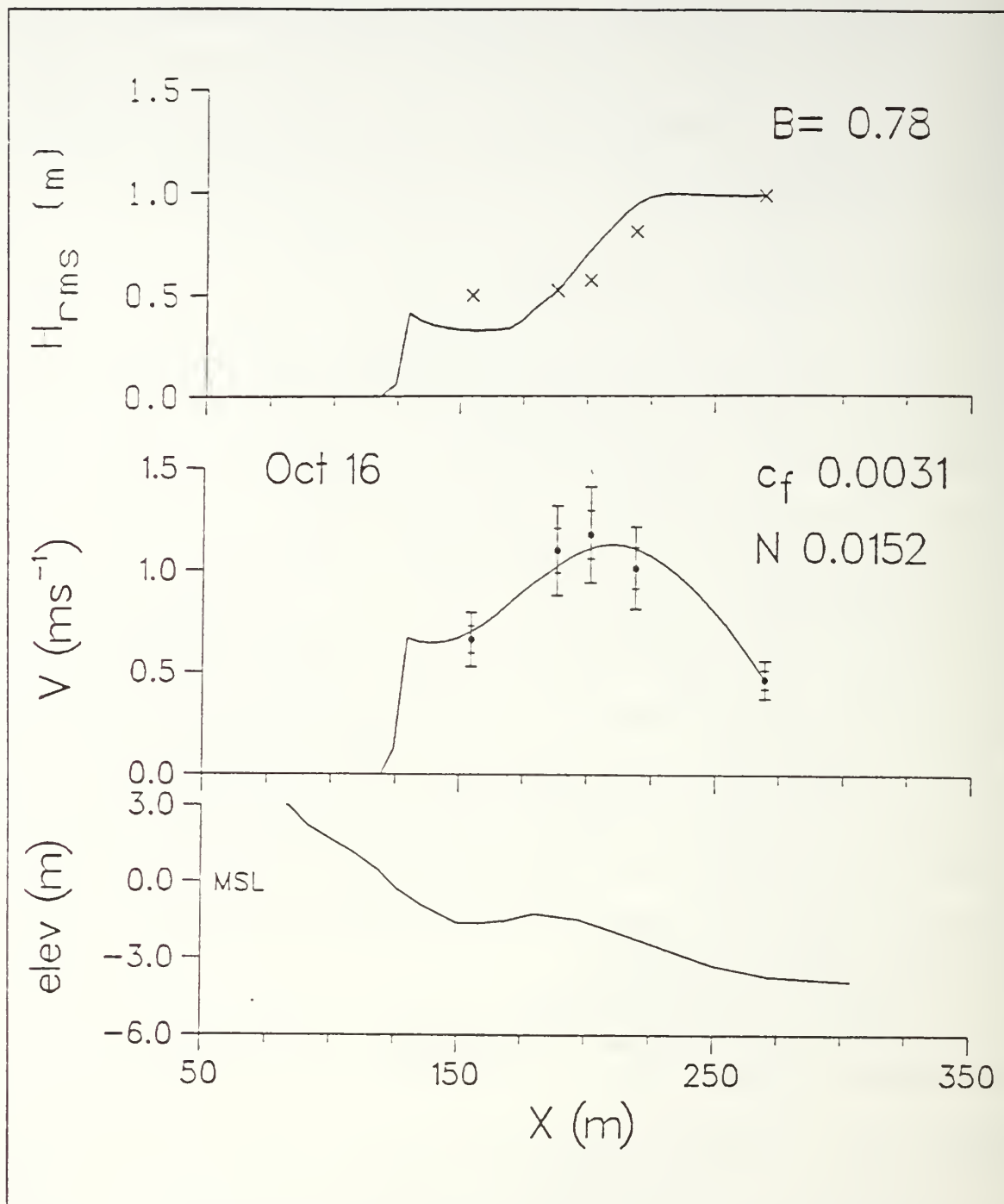


Figure 31. Model-generated H_{rms} and V compared with field observations versus distance for invariant c_f and B and including turbulent momentum exchange, 16 October. Model results are solid lines and field observations are "x"'s. Elevation is referenced to MSL.

In all cases, the spatially-invariant B coefficients listed in Table 20 are used. As with the B coefficient determination, c_f and N are model-fitted by a least square error criteria.

A spatially-invariant c_f with a non-linear (and presumably more realistic) τ_y^b and without turbulent mixing results in poor agreement between modeled and field-measured longshore current velocities (Figure 32 and Appendix A, Figure 53). Although the general shape of the observed longshore current profile is modeled, there are large discrepancies between observed and modeled current velocities, especially in the trough regions. Current velocities in the trough region are in error by as much as a factor of 7. Order of magnitude for c_f is similar to the momentum balance determination of c_f (Chapter VII) for all 4 transects.

Allowing c_f to vary spatially provides some improvement in the model-fit. However major discrepancies still occur on the nearshore slope where a steep increase in velocity is modeled along with significant underestimation of velocity in the trough. The spatially-variant c_f solution is dismissed because of these discrepancies.

Although TG86 determined turbulent momentum exchange to be unimportant for their planar beach data, turbulent momentum exchange is investigated for this analysis as a possible mechanism to transfer momentum across the bar and into the more placid trough region where wave breaking is reduced. Turbulent momentum exchange is expressed as the last term in equation (142) and is approximated using an eddy viscosity formulation:

$$S_{yx}'' = \overline{\int_{-h}^{\eta} \rho u'' v'' dz} = -\rho \xi D \frac{dV}{dx} \quad (143)$$

where D is total depth and the eddy viscosity coefficient (ξ) is parameterized by a dimensionless and adjustable coefficient (N) from equation (21). A first approach for the inclusion of turbulent momentum exchange was to determine the minimum least square error for spatially-invariant c_f and N across a reasonable range of c_f and N values. Bed shear stress coefficients were varied from 0.0005 to 0.0200 and N was varied from 0.000 to 0.016. A three-dimensional depiction of their solution surface is illustrated in Figure 33 for a typical data run. Minimum least square error is represented by a peak in the solution surface closest to the top of the three-dimensional box. Note that there are many combinations of c_f and N that minimize the least square error to nearly the same degree. Thus too many degrees of freedom result in multiple mathematical solutions with a corresponding loss of insight for the physics involved.

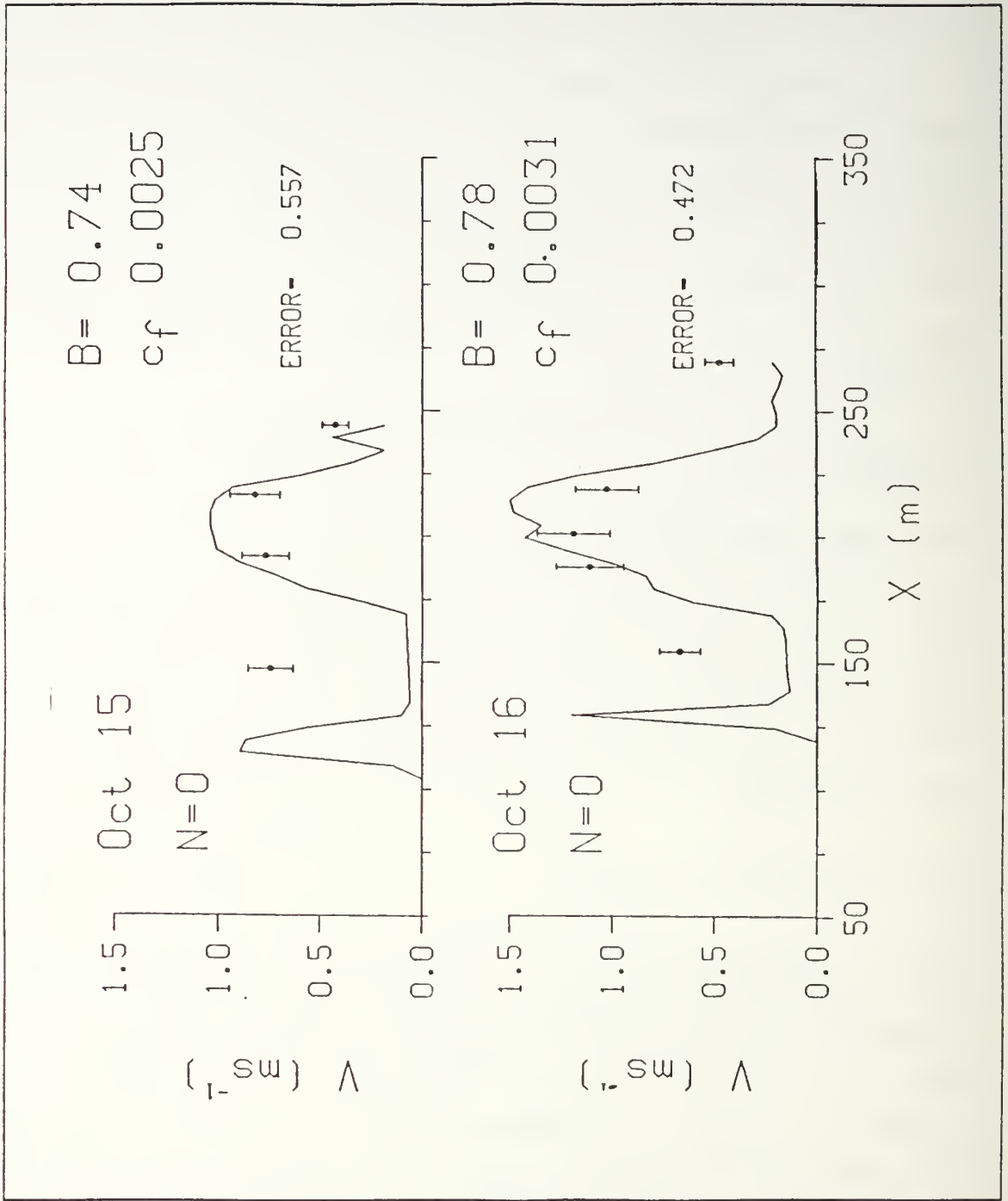


Figure 32. Model-generated V compared to field observations versus offshore distance for constant c_f no turbulent momentum exchange, 15-16 October. Model results are solid line and field observations are "x"s. Error is mean least square error.

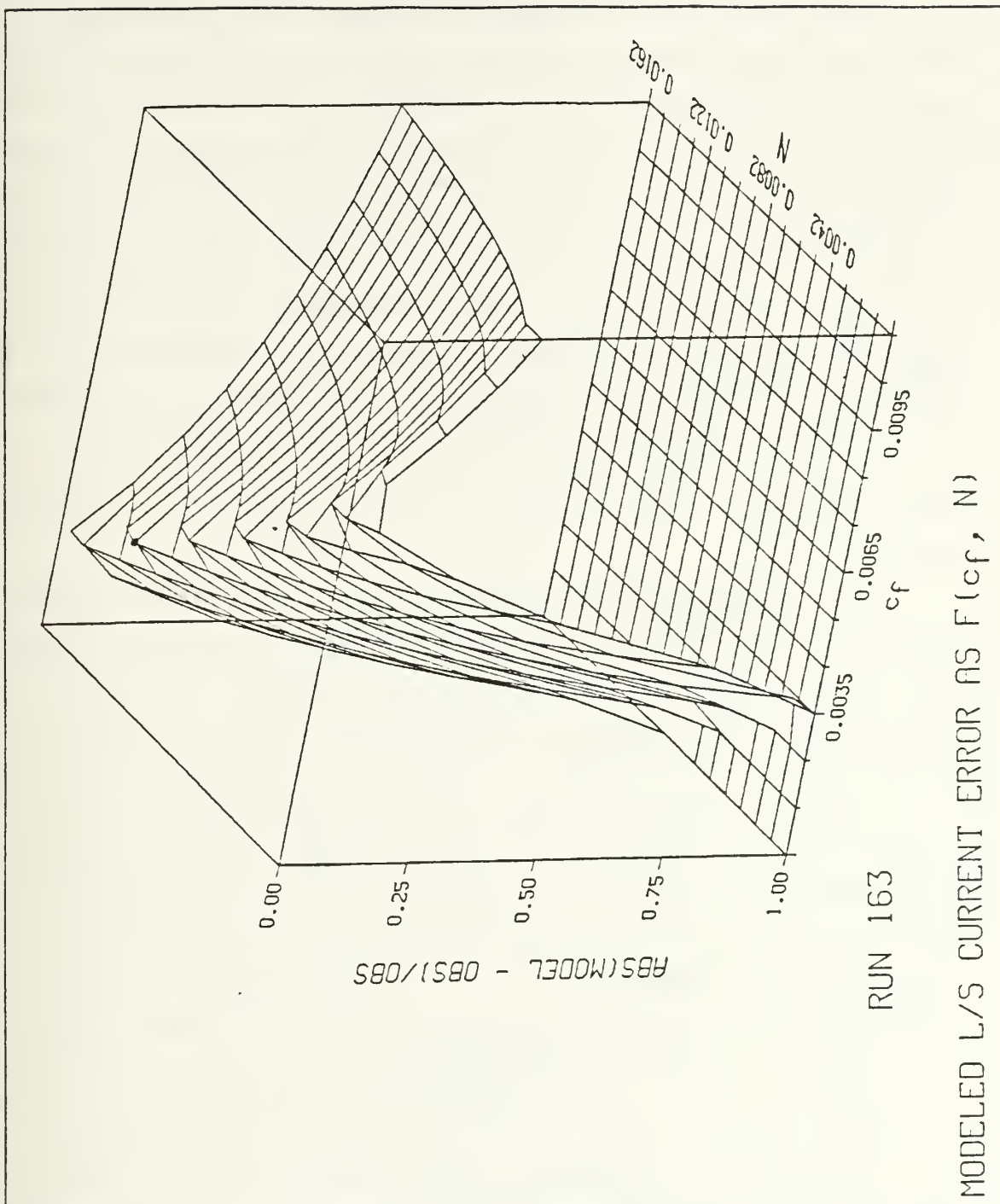


Figure 33. Example of a least square error solution surface for model-fitted longshore current for various c_f and N combinations. Results show an almost constant ridge for optimal c_f and N indicating a non-unique solution.

The spatially-invariant c_f approach is therefore considered a baseline upon which to use turbulent momentum exchange to improve the model results. The procedures are to first determine an invariant c_f , and then to vary N until the least square error is minimized. This results in a substantial improvement in model results over previous approaches. The 18 October data run required an additional c_f iteration after a value of N was determined. The model result prior to this additional iteration is represented by a dashed line in Figure 52. With longshore momentum being transferred over the bar and into the trough, the previous velocity underestimation in the trough has been significantly reduced. Velocities are modeled within 20% of measured values, with the exception of the trough region on 17 October. This case is unique and is addressed below. Interval bars in Figure 31 and Appendix A (Figure 50 through Figure 52) represent 10% and 20% of the observed value and are provided solely as a visual aid for interpreting the data. Mean least square error ranges between 7-15% for all four transects.

Current velocities in the trough (Runs 17-6, 17-7, and 17-8) on 17 October are much lower (and actually of opposite direction to the longshore current offshore the bar) than on the other three days. Guza et al. (1986) showed that it is S_{yx}^T , and not the structure of $S_{yx}(f)$, that is important for longshore current response. It is therefore possible that the low current velocities in the trough on 17 October are the result of bi-directional wave forcing where breaking swell and sea are driving longshore currents in opposing directions and cancelling each other out. Radiation stress spectra (Appendix F) show weak wave forcing for the trough region on 17 October. Radiation stress spectra for runs 17-1 and 17-2 show sea and swell approaching from different directions with relatively large incident angles (18° and -9° , respectively). The cross-over wave period separating swell from sea is 6.7 seconds. A scatter plot of breaking wave heights versus breaking wave periods for a trough run (17-6) shows that approximately half of the breaking waves consisted of swell and half consisted of sea (Figure 34). A scatter plot for Run 17-4 (located offshore the bar) does not show as much breaking wave activity for the swell. Thus the minimum combined velocity in the trough on 17 October and the poor model results for that particular day and location are possibly a result of opposing longshore currents.

3. Bed Shear Stress Coefficients

Spatially-invariant c_f 's are determined from model-fitting using a non-linear formulation of τ_y^b (TGS6) and turbulent momentum exchange (Table 20). The ratio of

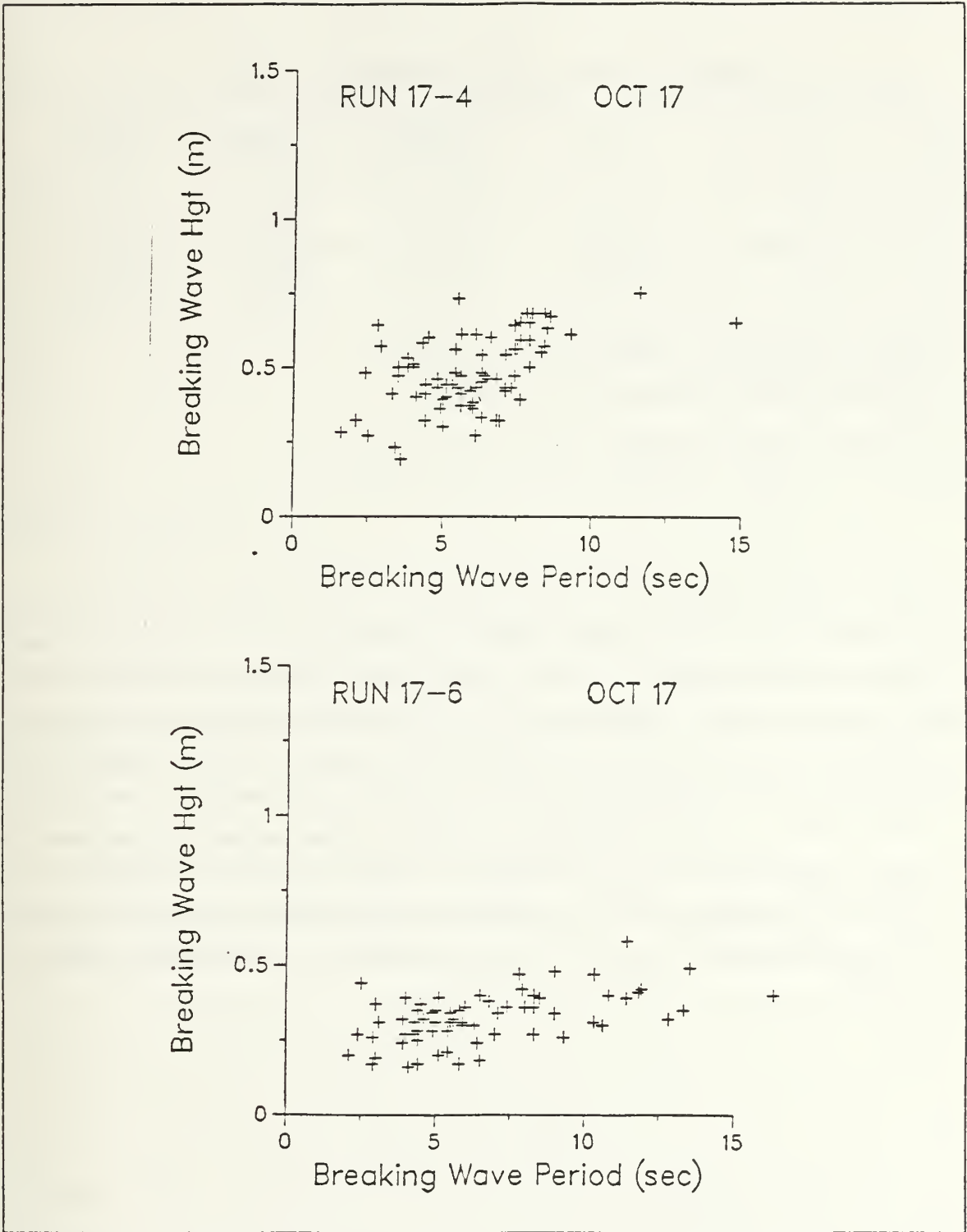


Figure 34. Scatter diagram of breaking wave periods and heights for 17 October. Run 17-4 is offshore the bar and 17-6 is in the trough.

Table 20. MODEL-FITTING RESULTS FOR B, c_f AND N

	<u>15 Oct</u>	<u>16 Oct</u>	<u>17 Oct</u>	<u>18 Oct</u>
B	0.74	0.78	1.10	1.06
N	0.006	0.015	0.004	0.016
Error	0.146	0.071	0.078	0.114
c_f^1	0.003	0.003	0.009	0.003
c_f^2	0.003	0.002	0.004	0.002

Error is mean least square error for the transect

¹transect mean c_f determined by model-fitting

²transect mean c_f determined by momentum balance

wind force to wave force for the SUPERDUCK data was 0.09 (see Chapter VII), therefore the inclusion of surface wind stress in this model did not have significant impact on the magnitude of c_f from model-fitting for this particular data set. However, as discussed earlier, the inclusion of surface wind stress under certain wind, wave, and beach slope conditions can have significant impact. Bed shear stress coefficient values for 15-18 October are 0.003, 0.003, 0.009, and 0.003, respectively. N coefficient values are 0.006, 0.015, 0.004, and 0.016, respectively. These c_f values are in good agreement (see Table 20) with the mean c_f 's determined for each day by the momentum balance method. This agreement is encouraging and lends credibility to the c_f results considering the complex physics being addressed and the different and independent methods employed.

IX. SUMMARY AND CONCLUSIONS

Previous investigators of longshore currents have used many simplifying assumptions which often preclude meaningful and realistic results. The assumptions of a planar beach, a steady and depth uniform flow, invariant bed shear stress, and negligible wind stress are quantitatively examined by measuring the relative importance of each term in a local longshore momentum balance based on measurements acquired during a field experiment at a barred beach. Wind and wave forcing of longshore currents is investigated with a numerical model and from field measurements. Measurements of pressure, current velocities at three levels, wind speed, and sea surface slope were acquired from an instrumented sled positioned at various locations across a transect of a barred beach. Unfortunately the slope measurements were found during data analysis to be unreliable and were disregarded.

Three-dimensional depictions of the current structure over a nearshore bar are developed. The cross-shore velocities [$O(0.2\text{ms}^{-1})$] indicate a relative onshore flow in the upper third of the water column and a relative offshore flow in the lower third of the water column, irrespective of bar location and in agreement with cross-shore theory. The longshore velocities [$O(1.0\text{ms}^{-1})$] indicate nearly depth uniform flow with a slight velocity increase with elevation. This depth uniform flow confirms the appropriateness of the depth-integration aspect of radiation stress for a barred beach. The longshore vertical current structure did not exhibit a logarithmic profile.

A numerical model is developed to compare wind and wave forcing for varying wind conditions and beach slope. The finite-depth TMA spectral wave model is used as input for the energy spectrum. Waves are assumed to be locally generated and fully arisen. Wind force is proportional to surf zone width and therefore inversely proportional to beach slope. Wave force is independent of surf zone width and beach slope. Wind force is found to increase more rapidly than wave force for an increase in wind speed or an increase in the wind and wave incident angle relative to beach normal. Ratios of wind to wave force are calculated. For a given wind direction, a wind speed increase of 10ms^{-1} results in a 50% increase in this ratio. In other words, wind force becomes increasingly significant relative to wave force, as wind speed and incident wind direction increase. For obliquely onshore winds and a steep beach slope ($\tan \beta = 0.10$), wind force is generally less than 10% of the wave force and thus may be considered negligible. For ob-

liquely onshore winds and a gentle beach slope ($\tan \beta = 0.01$), wind force can be significant, with wind to wave force ratios ranging from 15% to 100% for winds between 10-30 ms^{-1} and wind and wave directions from 10 – 70°. Thus under certain wind and wave conditions, wind force can be a first order term in the longshore momentum balance. For offshore winds, longshore currents are *totally* wind-driven. In summary, the model shows that wind force should be considered as a forcing term for longshore currents and that it is inappropriate to assume that wind force can be omitted.

There are no field studies addressing surface wind stress for robust surf zones (H_{mo} greater than 0.5 m). Surf zone atmospheric drag coefficients are determined from surface wind stress measurements acquired immediately outside the surf zone and wind speed measurements acquired by the sled anemometer inside the surf zone. Stability-dependent drag coefficients are calculated using the Businger et al. (1971) iterative approach. A conservative increase of 33% for C_d was made to account for the significantly increased surface roughness of the surf zone due to breaking waves based on the results of Davidson et al. (1988) which indicate an increased C_d for chaotic seas. During periods of atmospheric convective instability and reduced surface roughness (low wave heights), Hsu's (1970) empirical relationship for C_d is used. Resultant C_d 's range from 1.5×10^{-3} to 3.4×10^{-3} for non-convective instability and from 4.6×10^{-3} to 8.25×10^{-3} for convective instability. These C_d magnitudes are consistent with previous field measurements of C_d over the open ocean as well as the theoretical C_d values of Geernaert et al. (1987) for shallow water depths.

All terms in the longshore momentum balance are calculated from field measurements of pressure, current velocity, and wind speed. The sled was initially positioned *beyond* the surf zone for a complete data run. This additional data run allowed a daily numerical calibration of the current meters during data analysis based on conservation of $\partial S_{yx} / \partial x$ outside the surf zone. This procedure is essential for obtaining realistic physical results and is a distinguishing feature of the research. Longshore momentum due to unsteady flow was determined to be less than 10% of the longshore momentum due to steady flow for this data set. Relative contributions of the radiation stress gradient ($\partial S_{yx} / \partial x$), temporal term ($\partial M_y / \partial t$), and surface wind stress (τ_y^x) to the longshore momentum balance were calculated and analyzed by location relative to the bar. Mean relative contributions for the wave, wind, and temporal terms were 0.86, 0.08, and 0.06, respectively, for both offshore and on top the bar. However in the trough, the mean relative contributions were significantly different (0.64, 0.17, and 0.19, respectively). For

the trough region, the relative importance of wave forcing is reduced by 25%, whereas the relative importance of surface wind stress is doubled and the temporal term relative importance is tripled. All three terms are of first order in the trough. Although surface wind stress was nearly constant across the surf zone, the relative contribution of surface wind stress increases shoreward from the location of maximum breaking due to the decrease in wave forcing. The relative contribution of the temporal term appears to be largest in the trough, possibly due to the presence of surf beat or edge waves. Wind to wave force ratios calculated from the field data (0.09) are in agreement with those determined from the model (0.12) for the same wind conditions.

Spatially-dependent bed shear stress coefficients are determined *between* sled run locations. The spatial step size (Δx of the radiation stress gradient) is determined by error analysis to be too small when assigned the 2 m distance between the current meters on the sled. It had originally been planned that the slope array, which did not work properly, would have provided the necessary precision to measure the radiation stress gradient over the 2 m distance. Reasonable c_f results are calculated when the spatial step size is increased to the distance between run positions O(20 - 40 m). Resultant c_f 's range from less than 0.001 to 0.006. Spatially-variable mean c_f 's are found with values of 0.004 ± 0.0010 for offshore the bar, 0.002 ± 0.0006 for on top the bar, and 0.001 ± 0.0003 for the trough (excluding the nearshore slope). A trend for a shoreward decreasing c_f is noted, possibly due to the shoreward decrease in wave action. A mean c_f for the nearshore slope is not specified since error analysis shows that a significant overestimation of c_f can occur for the nearshore slope due to the combined effect of decreased depth and steeper slope upon the finite difference approximation. The percentage change in c_f due to neglecting surface wind stress of the temporal term in the momentum balance ranges from near zero to 100%, with a mean change between 10-30%. Thus for this data set and under certain conditions, the surface wind stress term and the temporal term can be of first order in the momentum balance.

Longshore current velocities at a barred beach are modeled to within $\pm 20\%$ of the observed values at SUPERDUCK by modifying the Thornton and Guza (1986) model to include wind stress, wave incident angle dependency, slope-dependent γ , and an improved breaking wave weighting function. Mean least square error between modeled and observed current velocity ranges from 7-15%. The inclusion of turbulent momentum exchange to transport momentum into the more placid trough region is required and is physically reasonable. Spatially-invariant c_f values determined by model-fitting

for 15-18 October are 0.003, 0.003, 0.009, and 0.003, respectively. These c_f values agree well with mean c_f values determined for each day by the momentum balance method. This agreement is encouraging and lends credibility to the c_f results considering the complex physics being addressed and the different and independent methods employed.

APPENDIX A. DATA ANALYSIS FIGURES FOR DAYS OTHER THAN
OCTOBER 16, 1986

SUPERDUCK
11 Oct 86
Profile 250

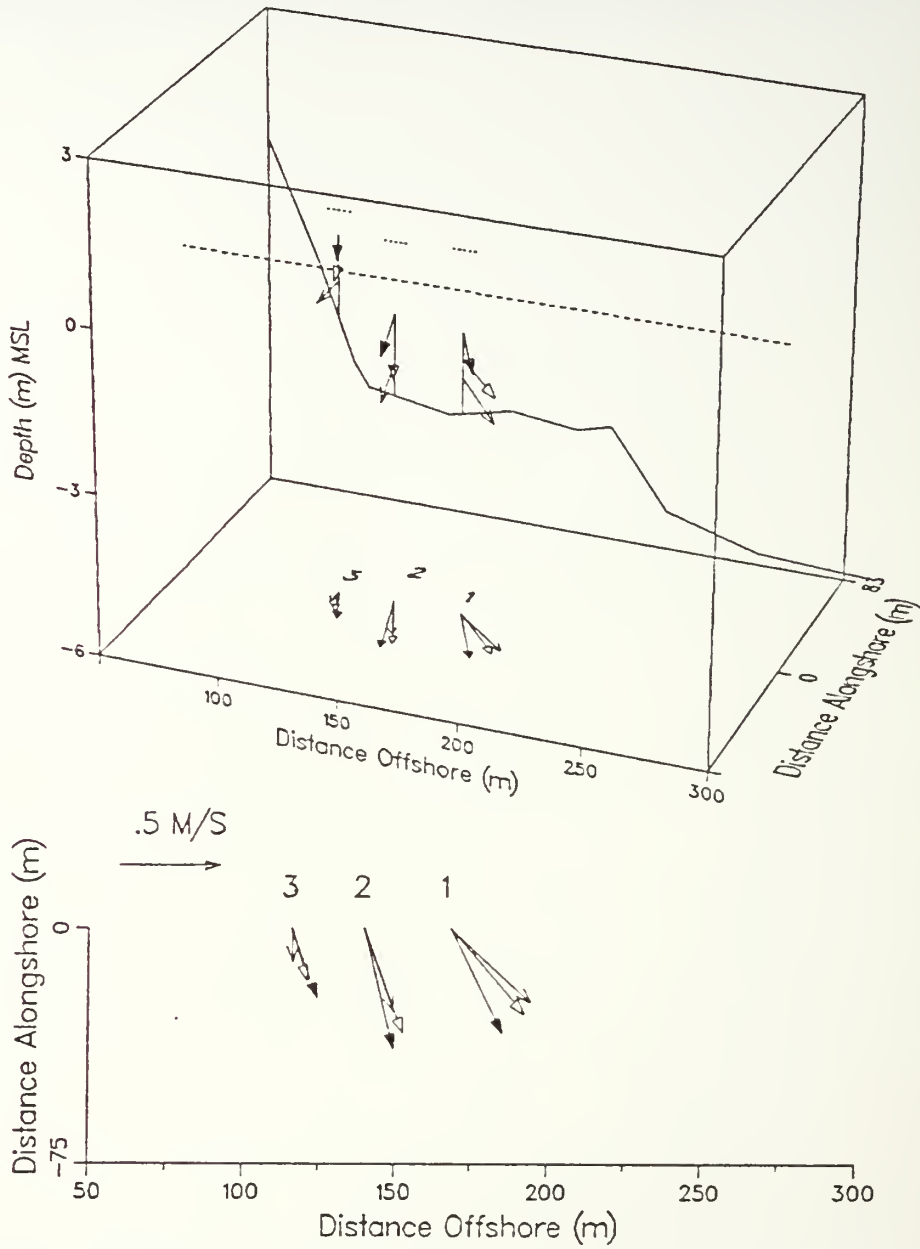


Figure 35. Mean current structure on 11 October 1986. Numbers represent data runs, short dotted lines are MWL's, and distance alongshore is arbitrary.

SUPERDUCK
 12 Oct 86
 Profile 250

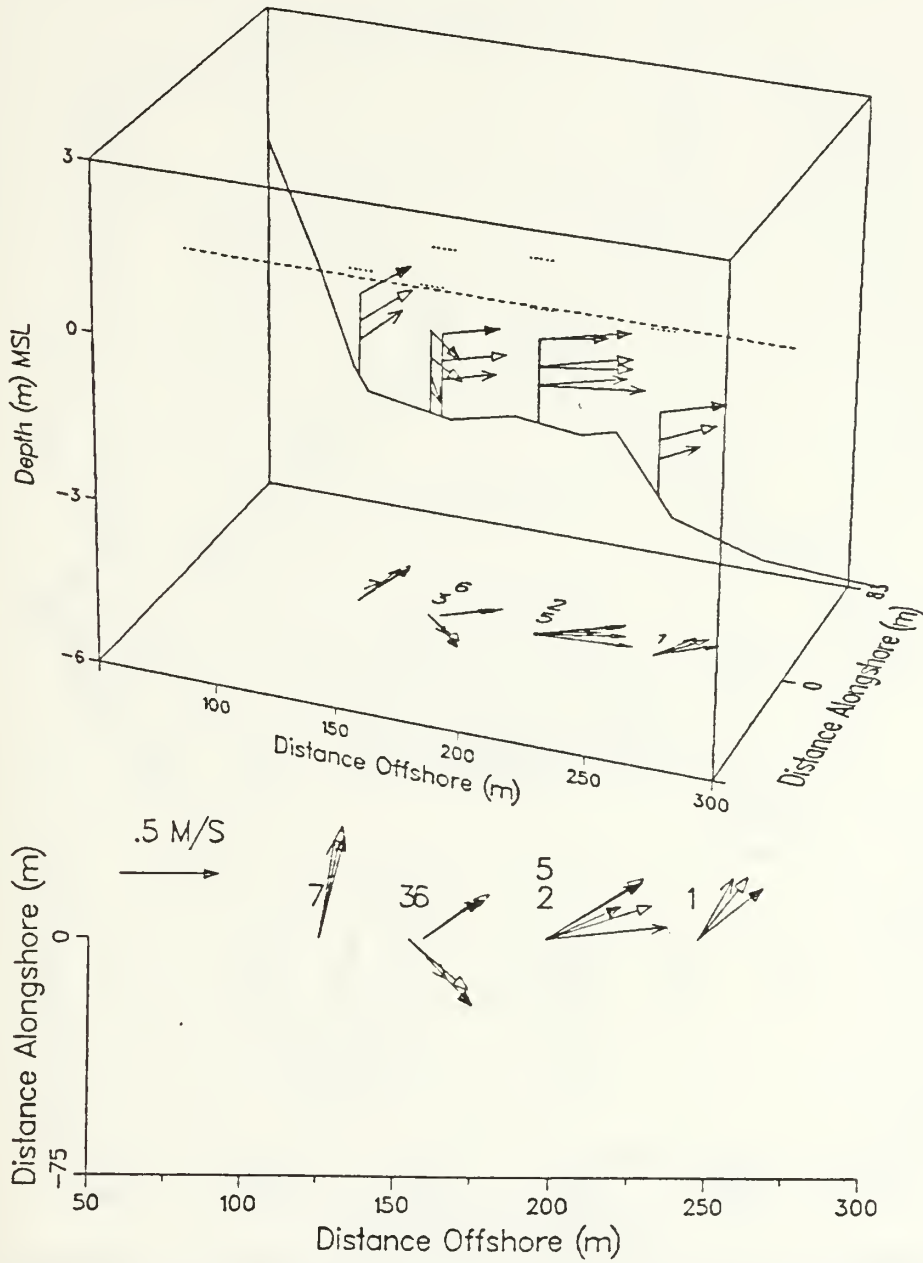


Figure 36. Mean current structure on 12 October 1986. Numbers represent data runs, short dotted lines are MWL's, and distance alongshore is arbitrary.

SUPERDUCK
15 Oct 86
Profile 255

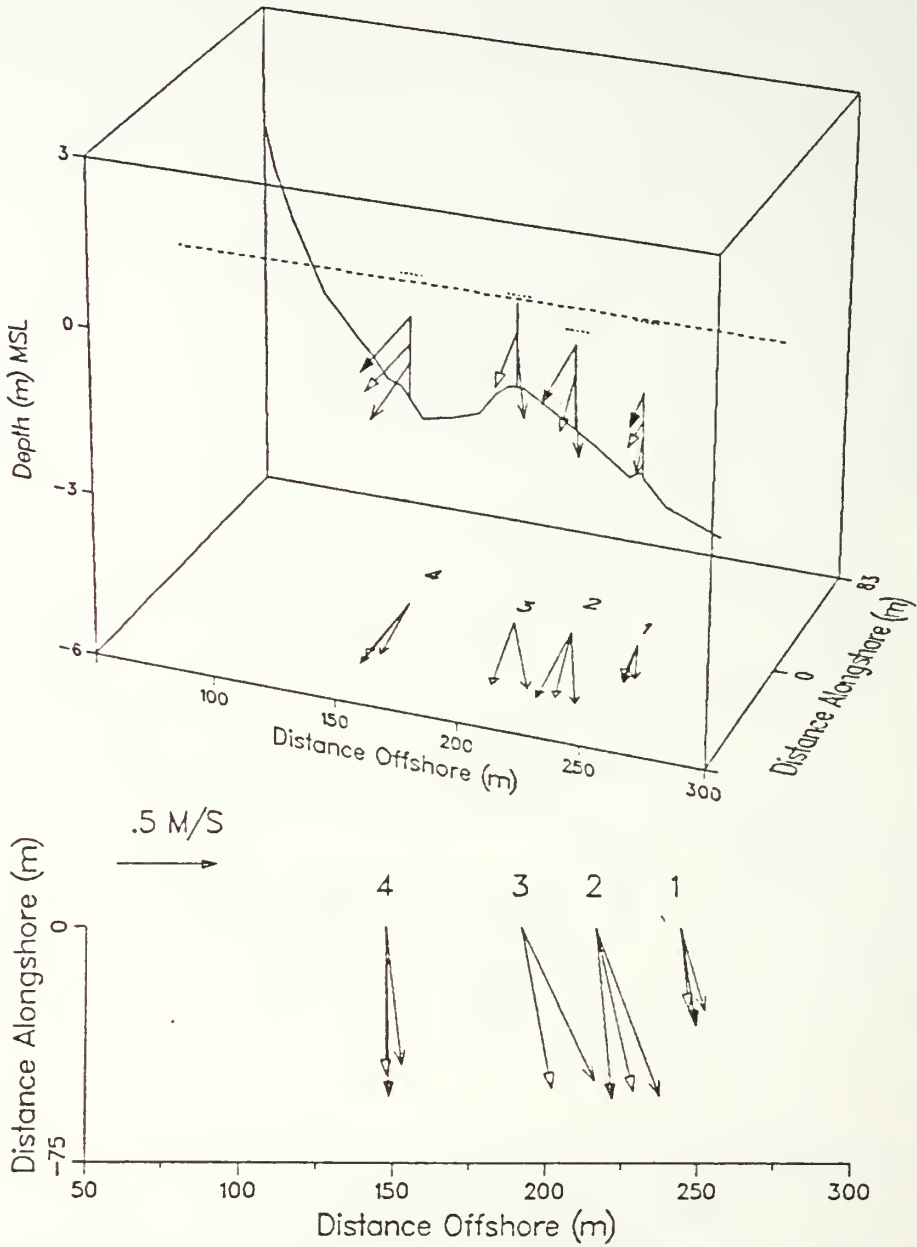


Figure 37. Mean current structure on 15 October 1986. Numbers represent data runs, short dotted lines are MWL's, and distance alongshore is arbitrary.

SUPERDUCK
 17 Oct 86
 Profile 195

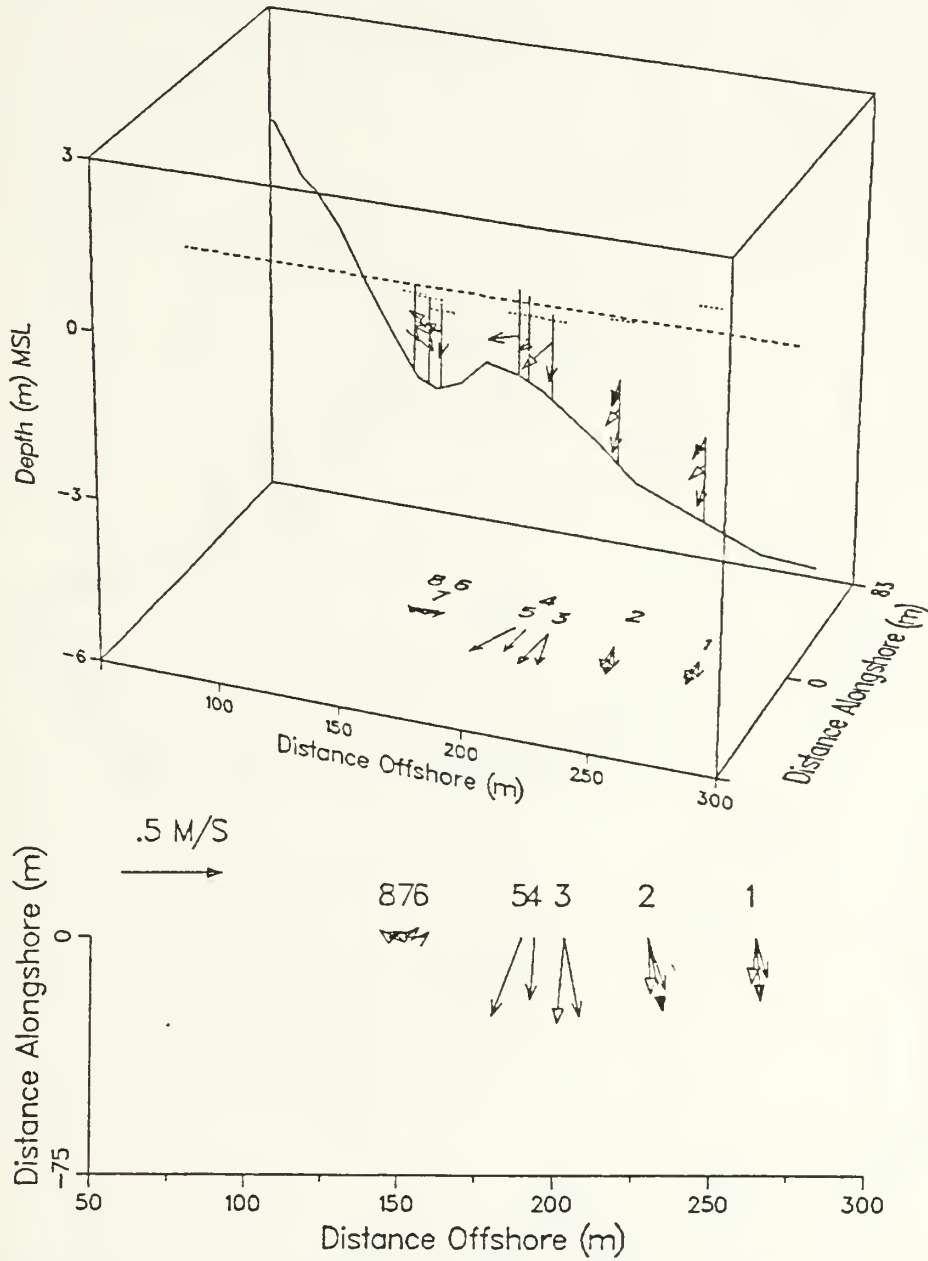


Figure 38. Mean current structure on 17 October 1986. Numbers represent data runs, short dotted lines are MWL's, and distance alongshore is arbitrary.

SUPERDUCK
18 Oct 86
Profile 195

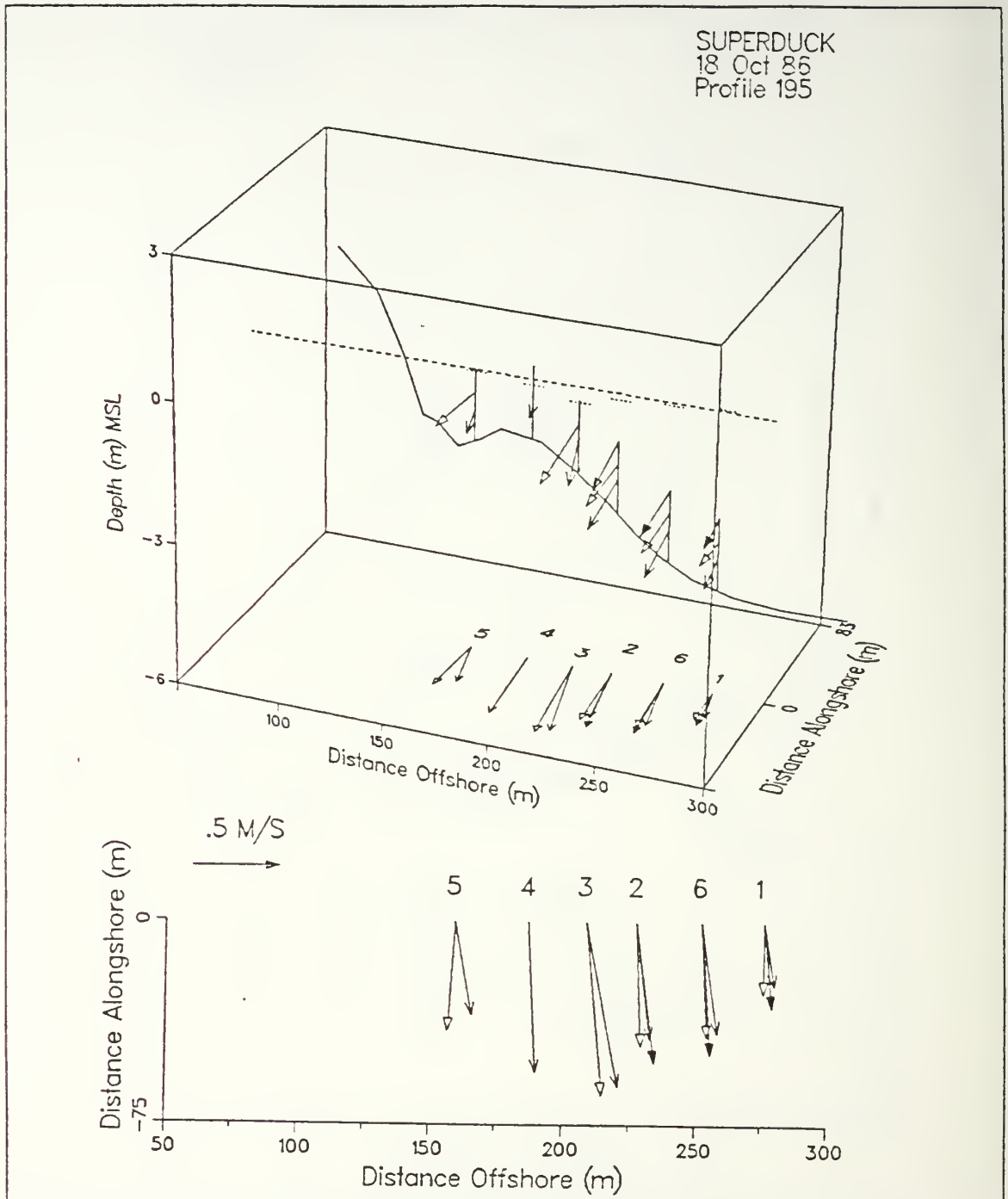


Figure 39. Mean current structure on 18 October 1986. Numbers represent data runs, short dotted lines are MWL's, and distance alongshore is arbitrary.

SUPERDUCK
 21 Oct 86
 Profile 170

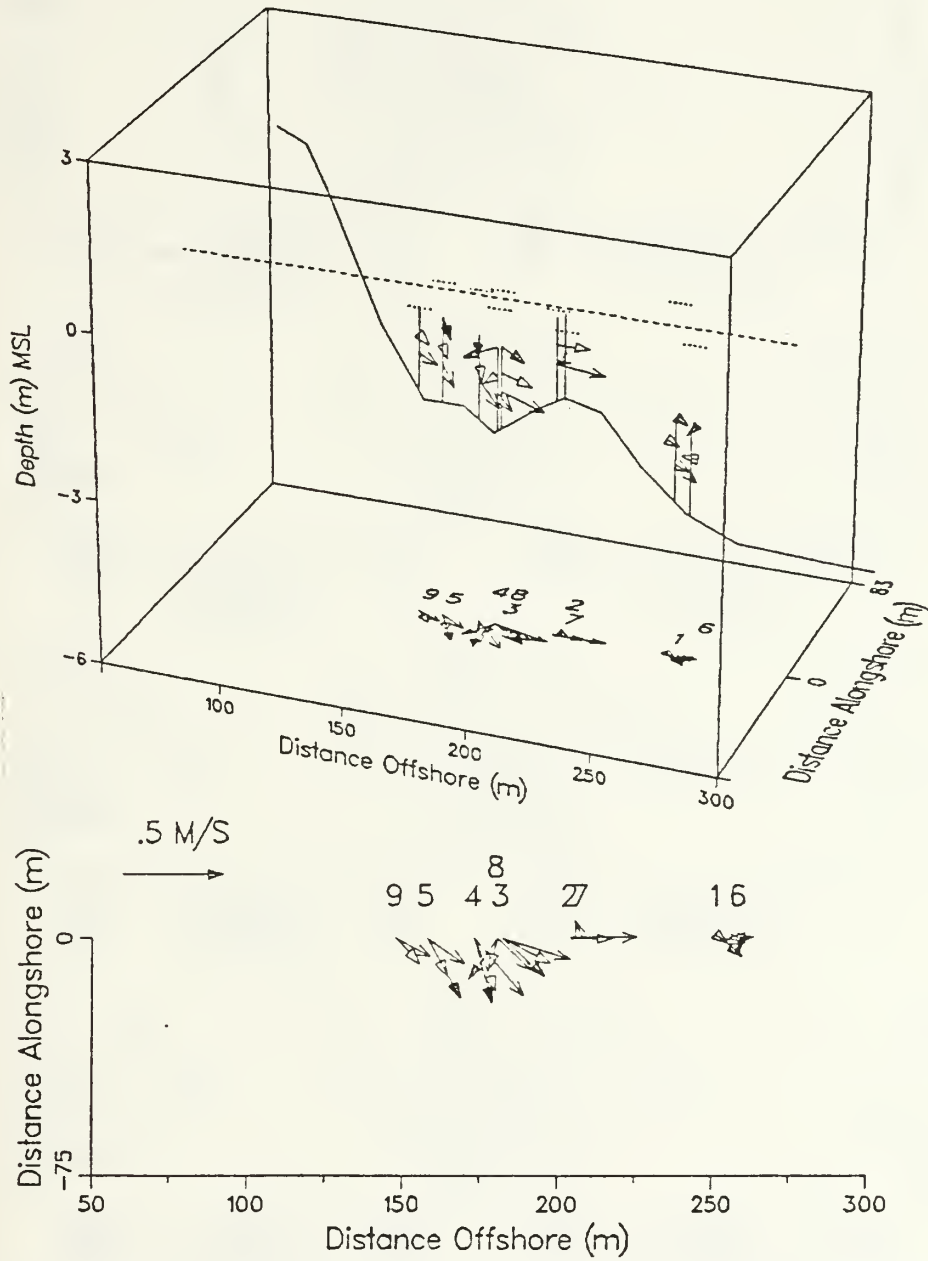


Figure 40. Mean current structure on 21 October 1986. Numbers represent data runs, short dotted lines are MWL's, and distance alongshore is arbitrary.

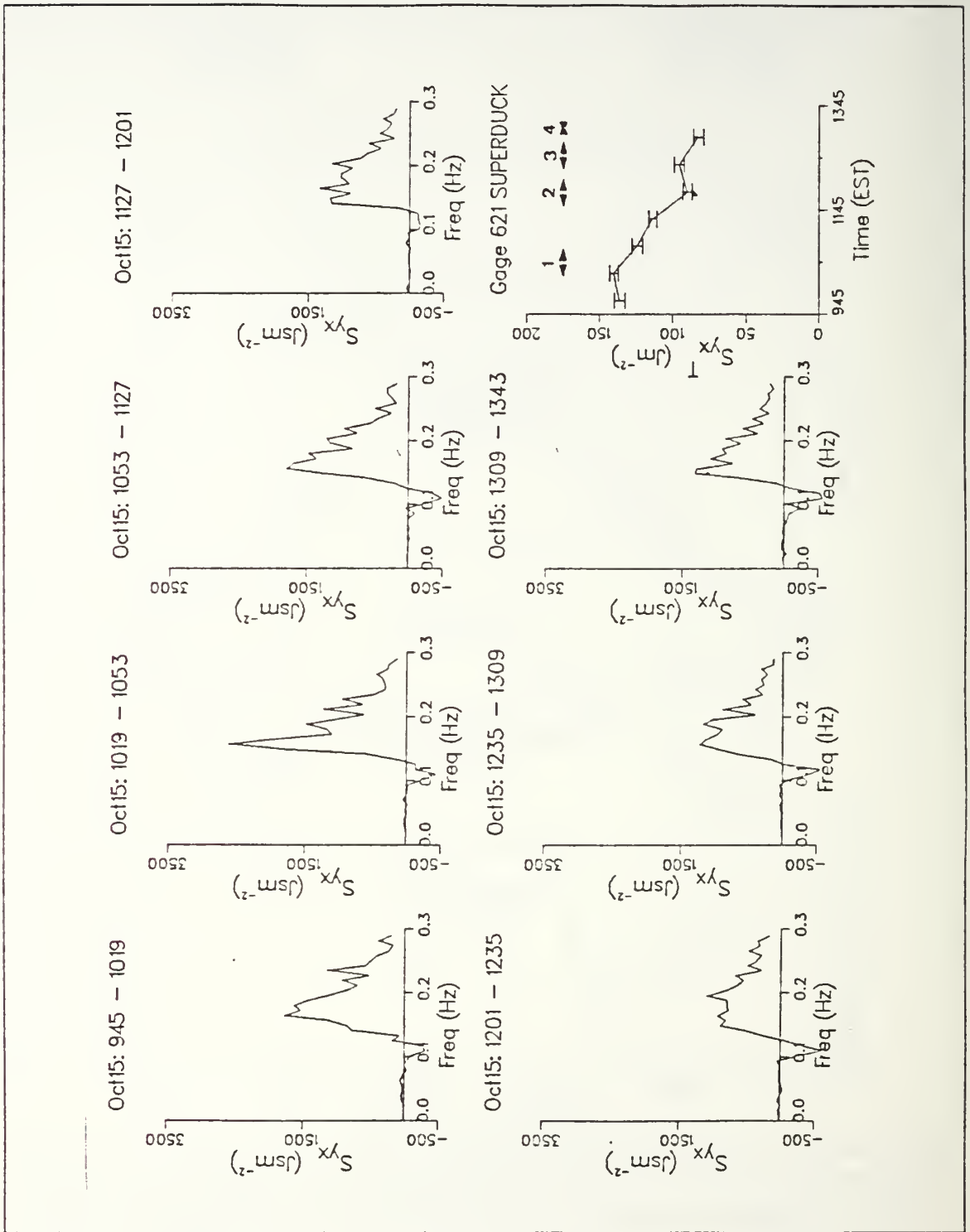


Figure 41. Offshore S_{yx} spectra and S_{yx}^I from 'puv' gage 621 for 15 October 1986. Numbers indicate data runs. Intervals are 95% confidence.

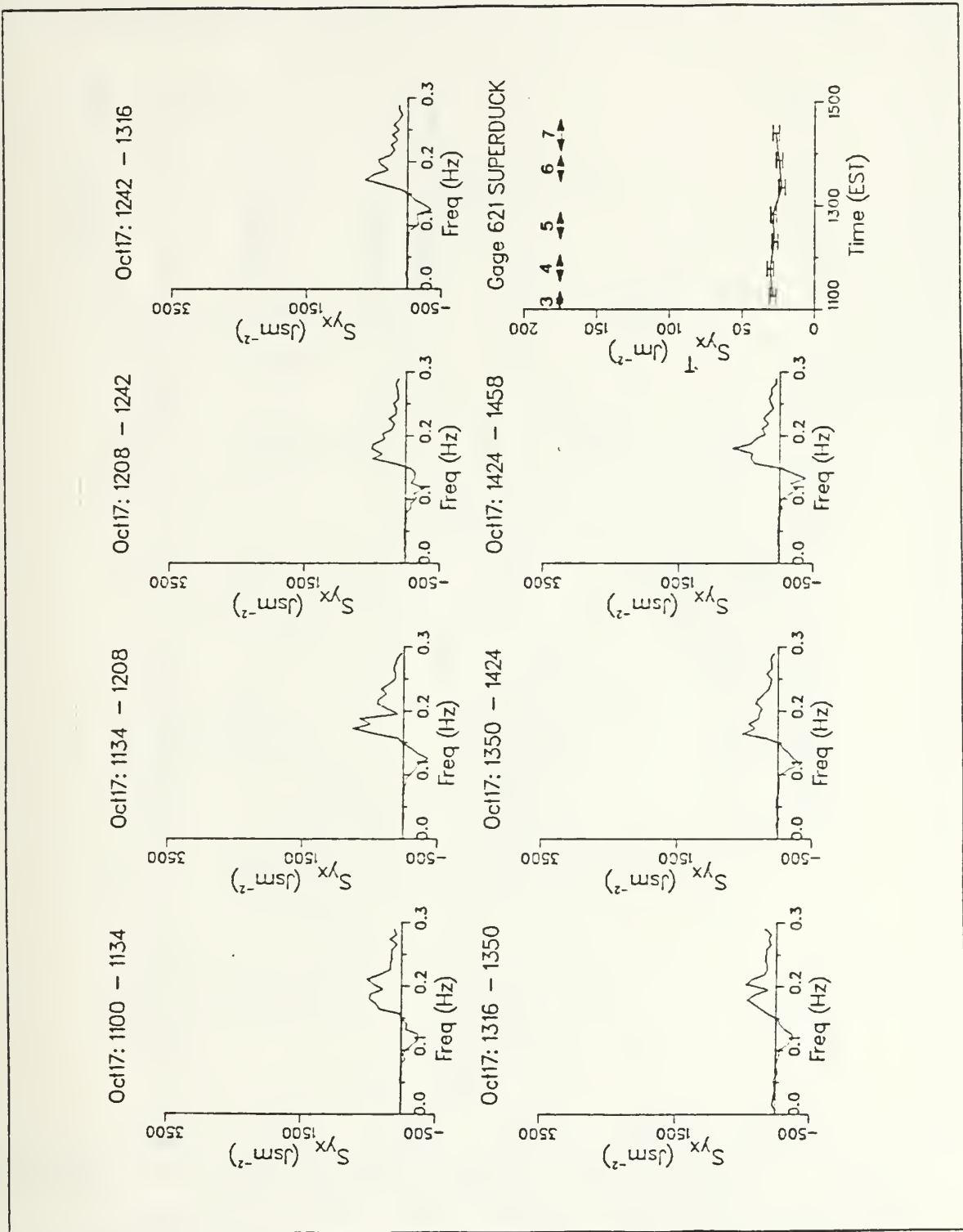


Figure 42. Offshore S_{yx} spectra and S_{yx}^T from 'puv' gage 621 for 17 October 1986. Numbers indicate data runs. Intervals are 95% confidence.

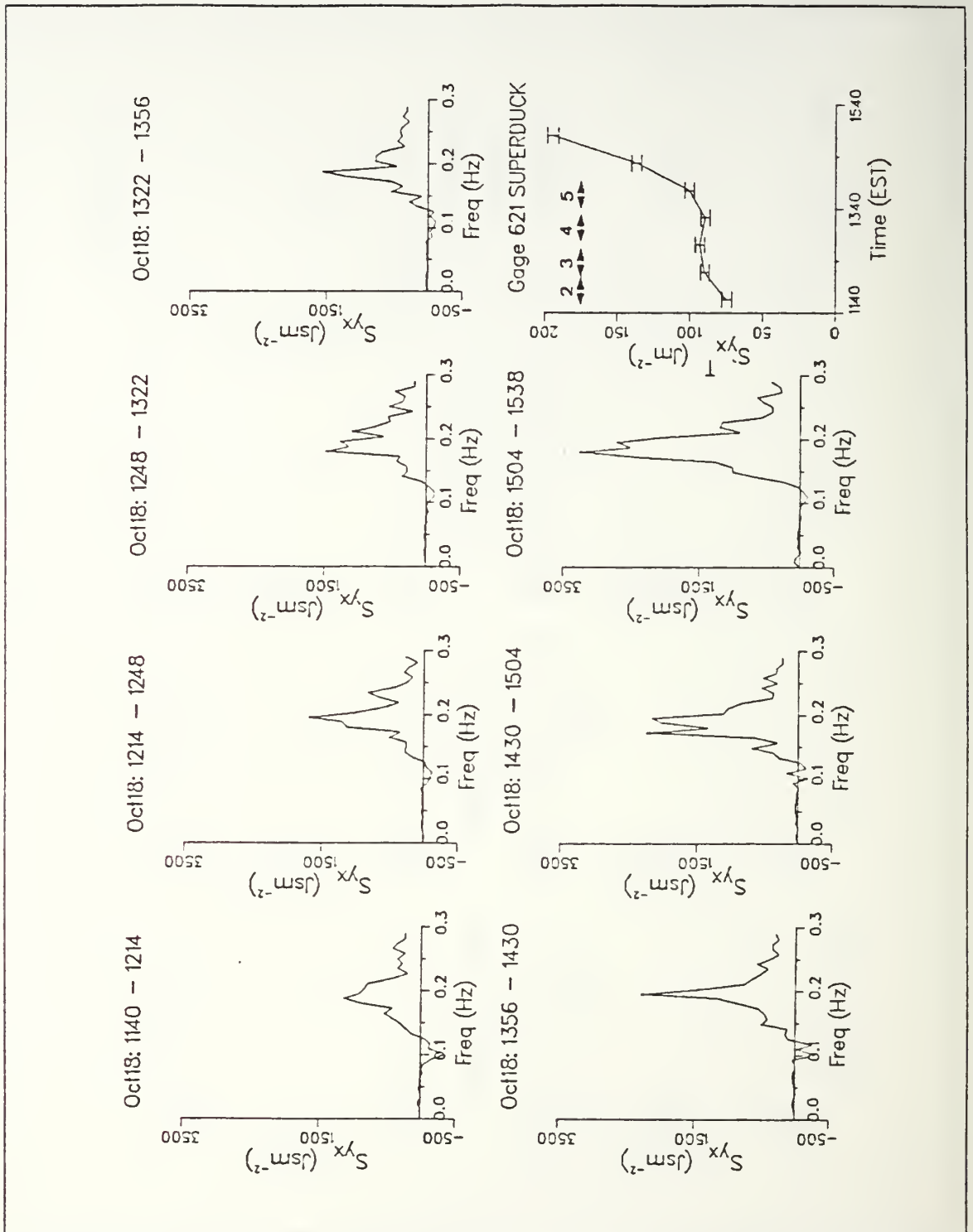


Figure 43. Offshore S_{yx} spectra and S_{yx}^I from 'puv' gage 621 for 18 October 1986. Numbers indicate data runs. Intervals are 95% confidence.

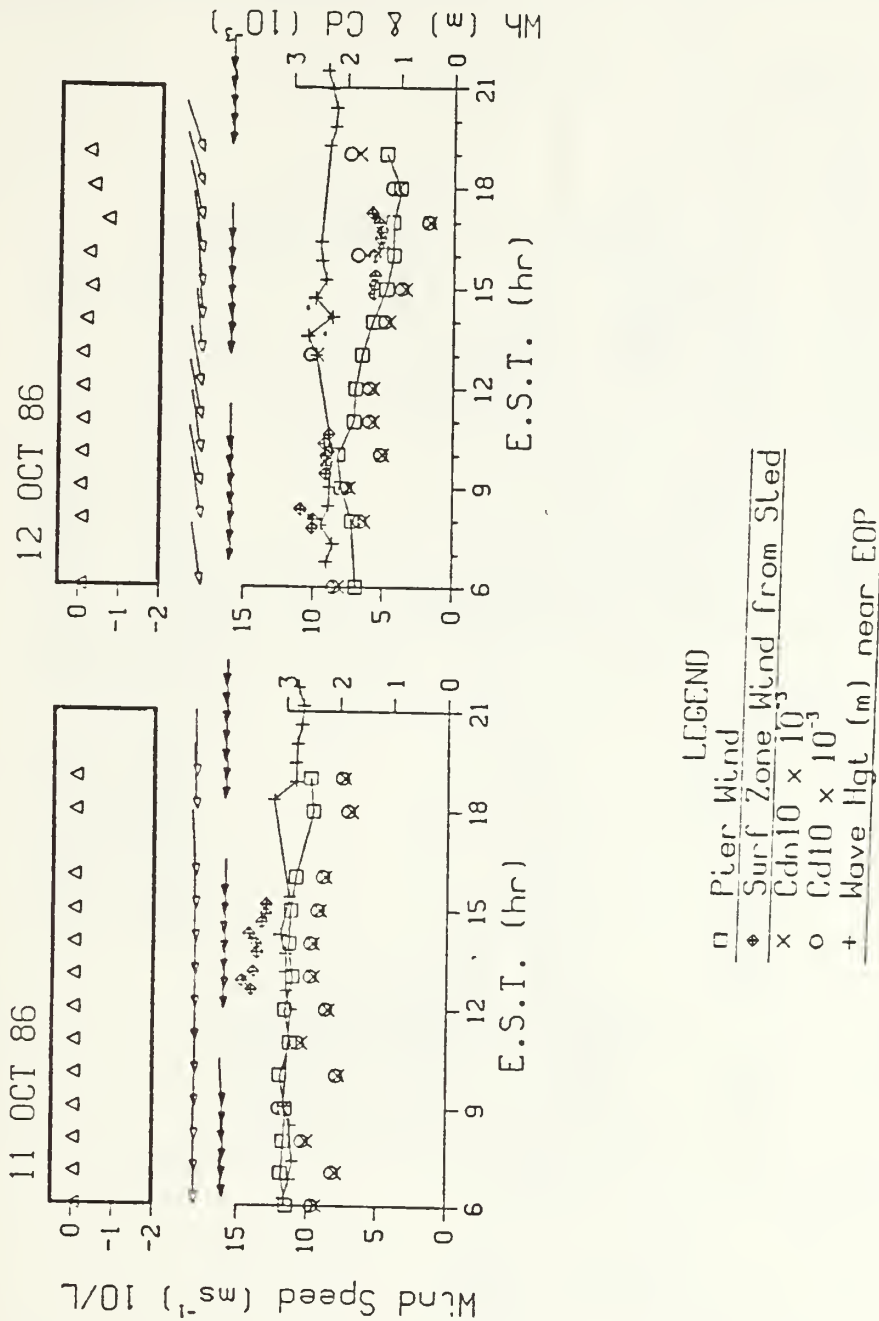


Figure 44. Wind speed, wave height, atmospheric stability, and initial C_2 data for October 11-12, 1986. Beach is assumed parallel to the y-axis. Open arrowheads denote wind direction and closed arrowheads denote wave incident angle. Winds are adjusted to $z = 10$ m.

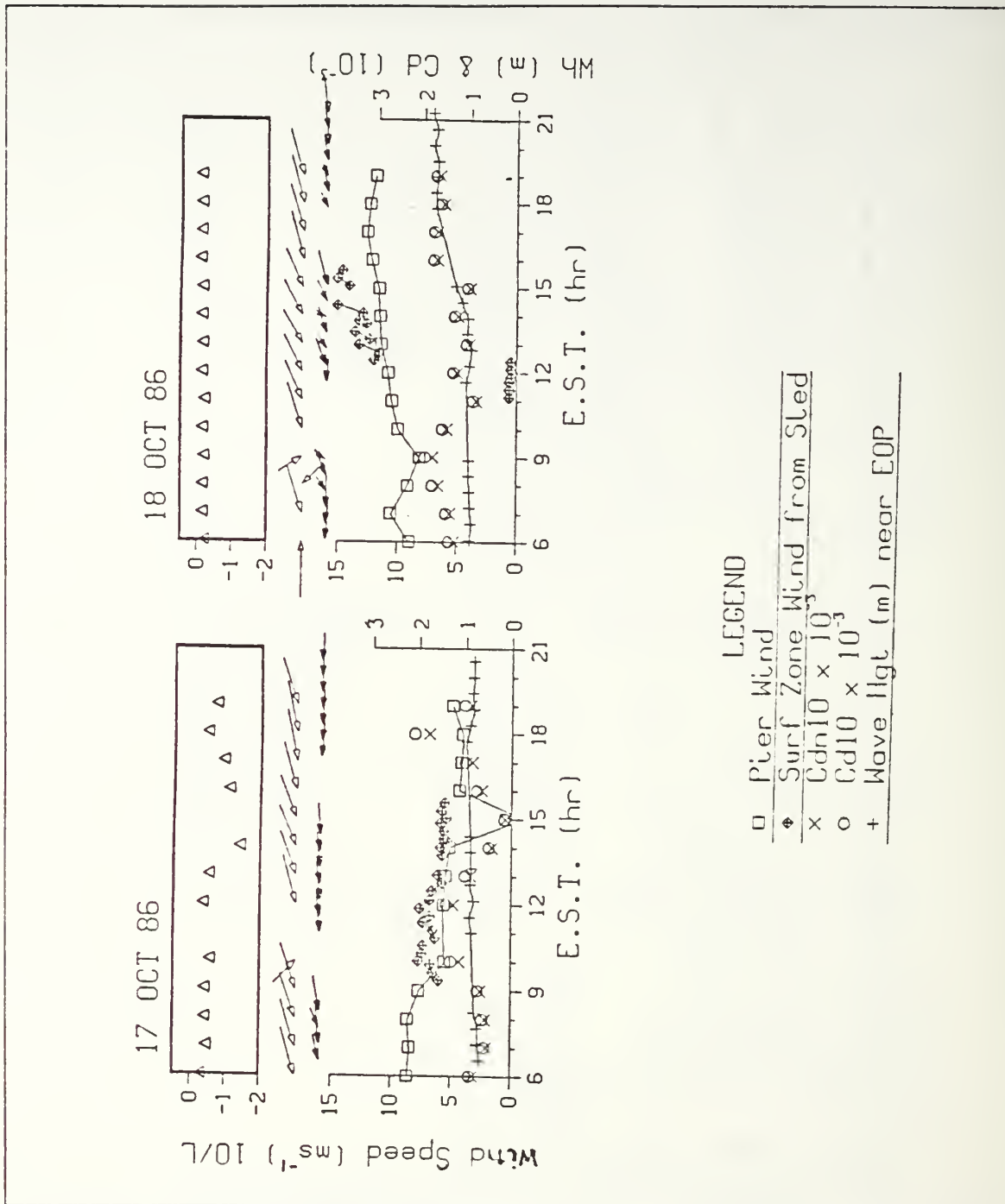
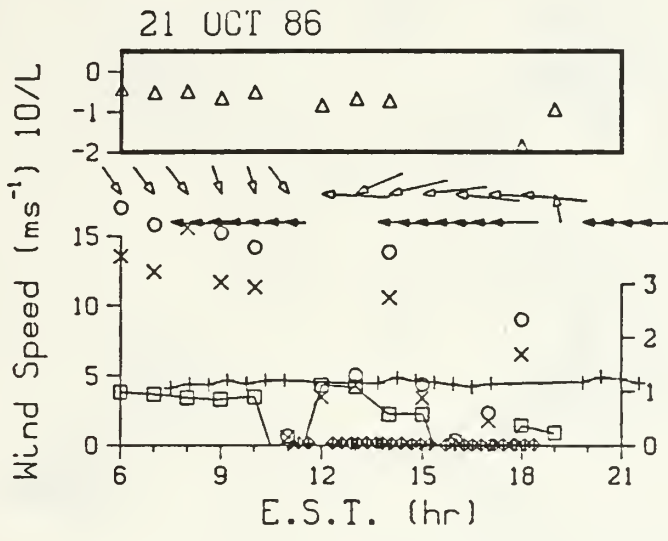


Figure 45. Wind speed, wave height, atmospheric stability, and initial C_d data for October 17-18, 1986. Beach is assumed parallel to the y-axis. Open arrowheads denote wind direction and closed arrowheads denote wave incident angle. Winds are adjusted to $z = 10$ m.



- LEGEND
- Pier Wind
 - ◆ Surf Zone Wind from Sled
 - × $Cd_{10} \times 10^{-3}$
 - $Cd_{10} \times 10^{-3}$
 - + Wave Hgt (m) near EOP

Figure 46. Wind speed, wave height, atmospheric stability, and initial C_d data for October 21, 1986. Beach is assumed parallel to the y-axis. Open arrowheads denote wind direction and closed arrowheads denote wave incident angle. Winds are adjusted to $z = 10$ m.

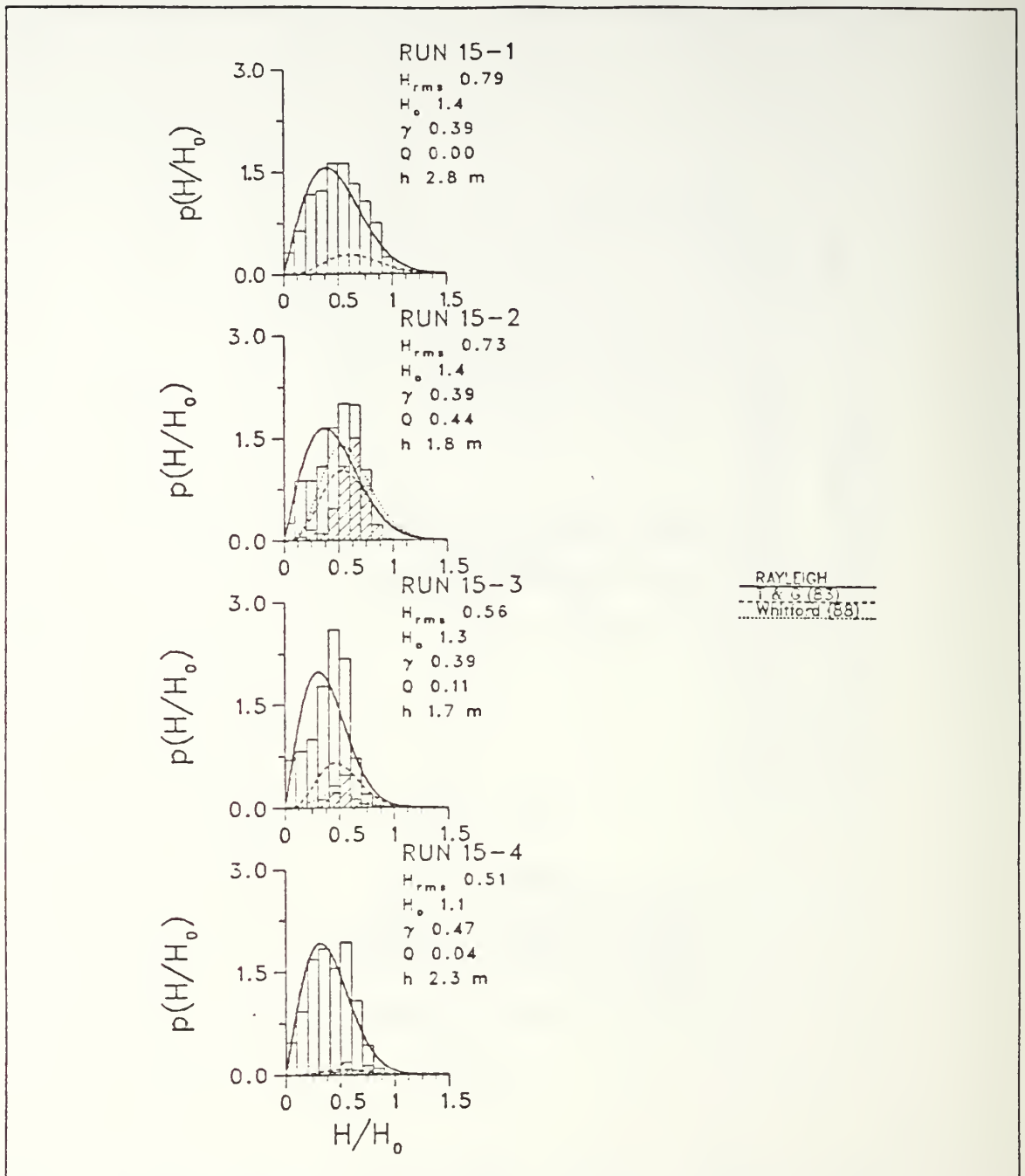


Figure 47. Wave height and breaking wave height distributions (hatched area) normalized to offshore H_{rms} for 15 October.. The Rayleigh distribution is the solid line and empirical breaking wave distributions given by equations (127) and (140) are the dashed and dotted lines, respectively.

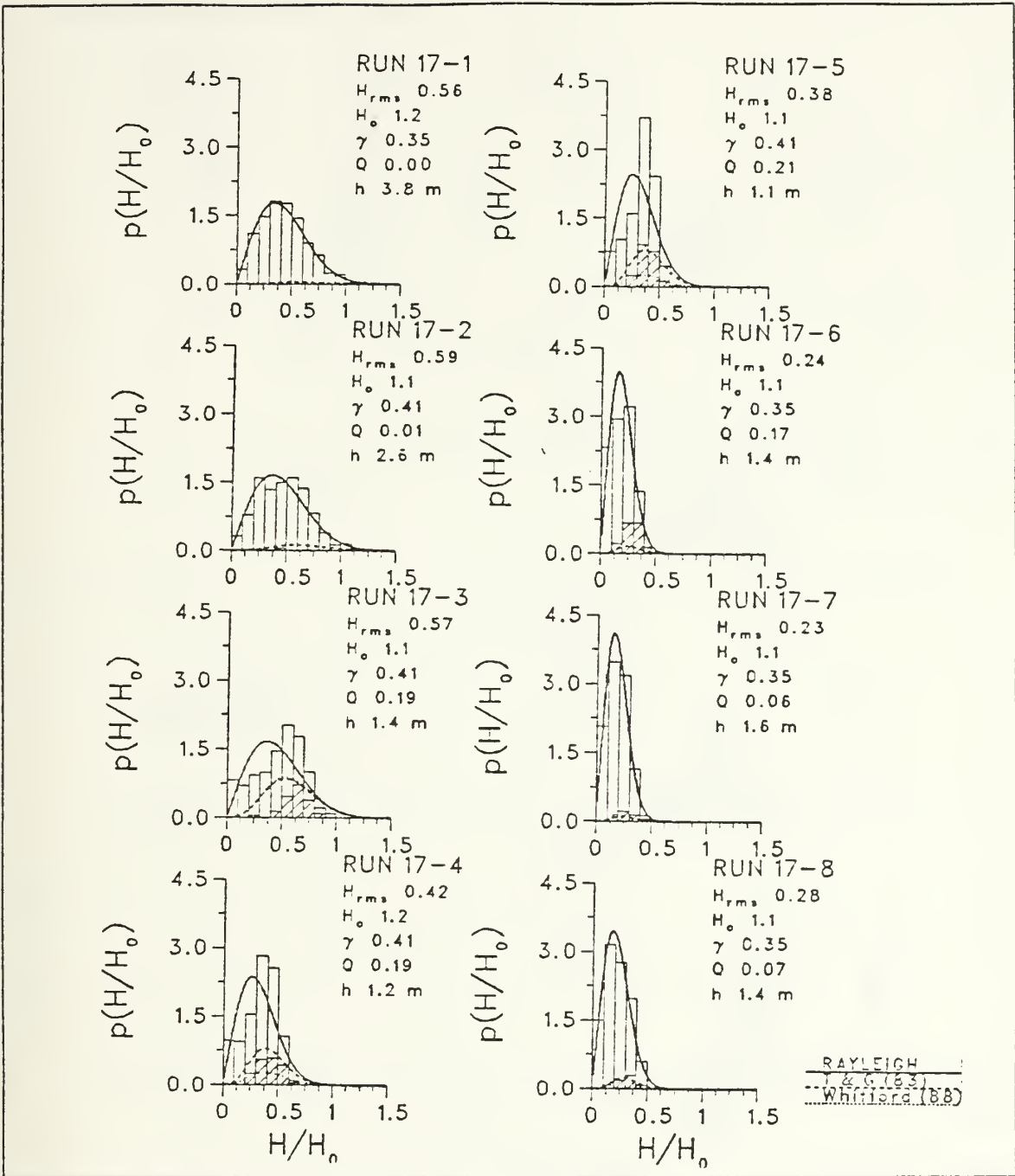


Figure 48. Wave height and breaking wave height distributions (hatched area) normalized to offshore H_{rms} for 17 October. The Rayleigh distribution is the solid line and empirical breaking wave distributions given by equations (127) and (140) are the dashed and dotted lines, respectively.

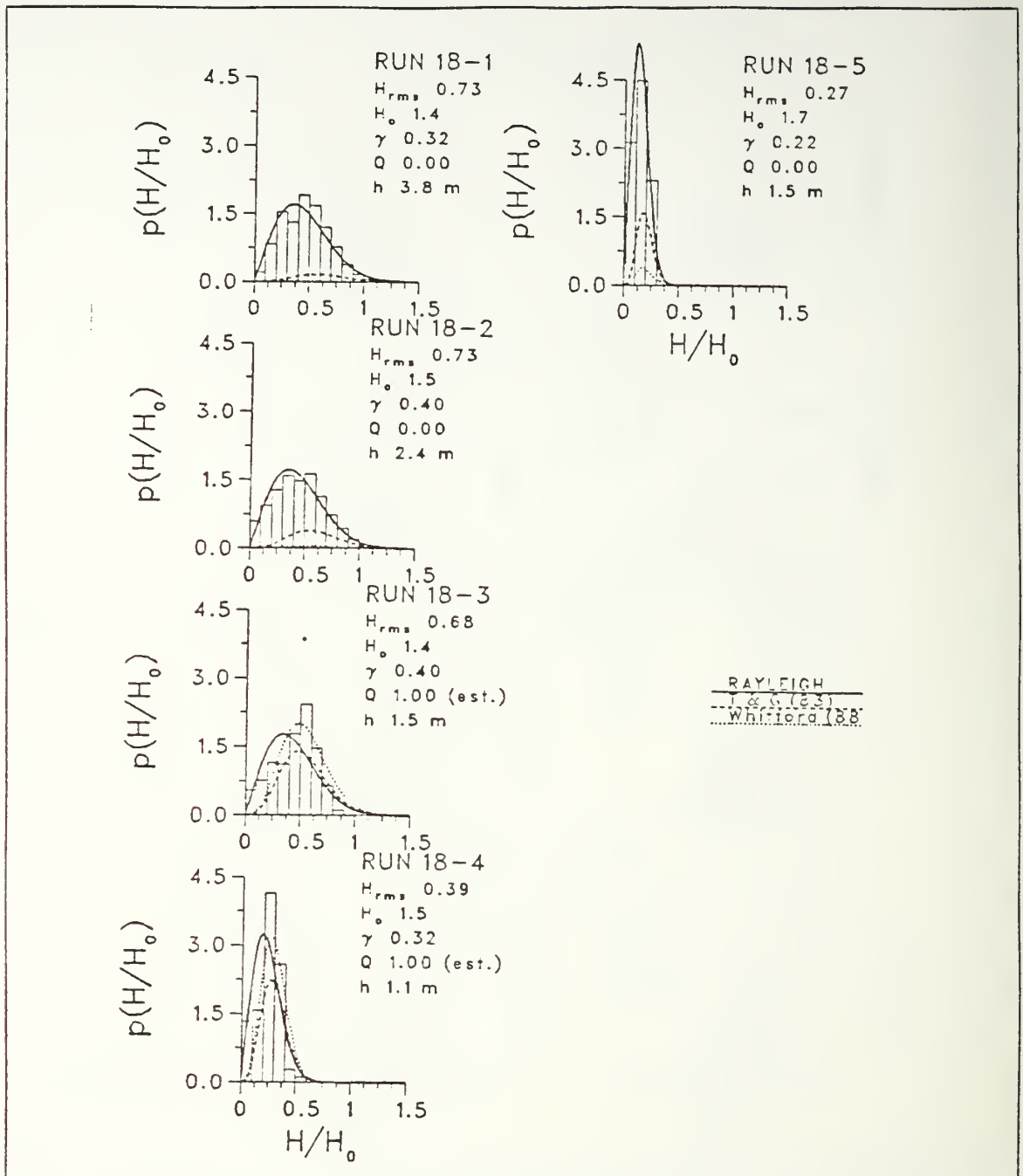


Figure 49. Wave height and breaking wave height distributions (hatched area) normalized to offshore H_{rms} for 18 October. The Rayleigh distribution is the solid line and empirical breaking wave distributions given by equations (127) and (140) are the dashed and dotted lines, respectively.

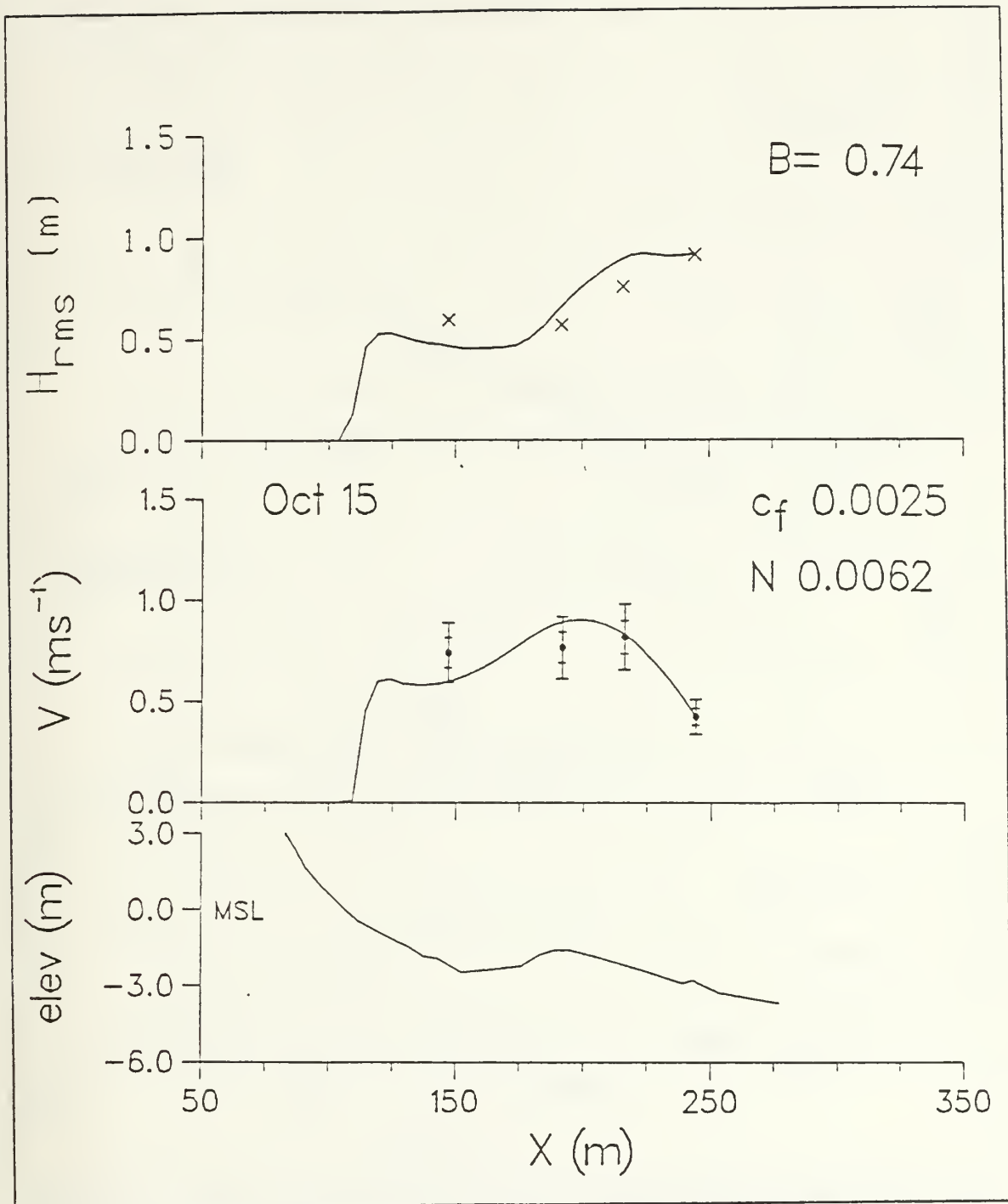


Figure 50. Model-generated H_{rms} and V compared with field observations versus distance for invariant c_f and B and including turbulent momentum exchange, 15 October. Model results are solid lines and field observations are "x"'s. Elevation is referenced to MSL.

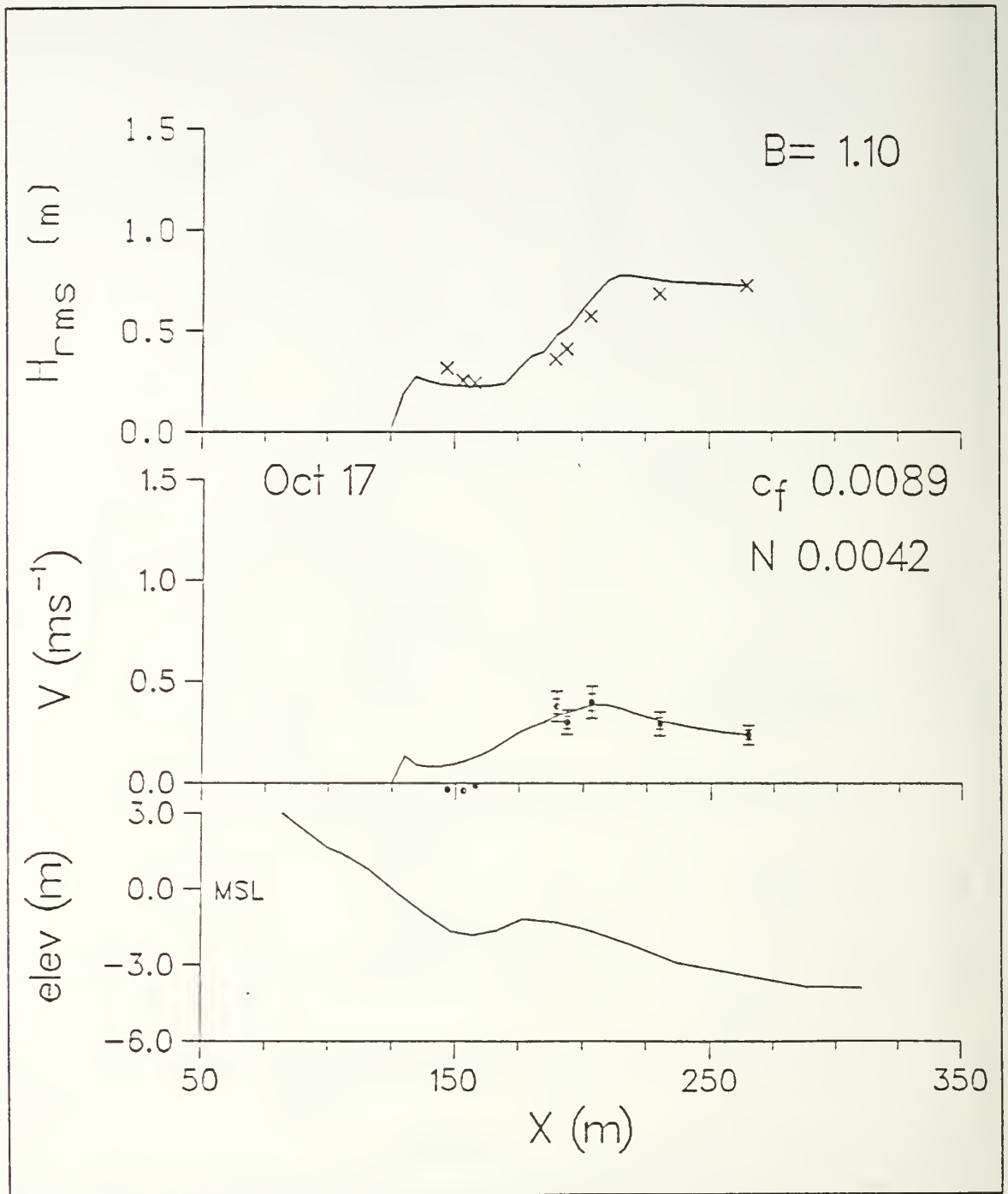


Figure 51. Model-generated H_{rms} and V compared with field observations versus distance for invariant c_f and B and including turbulent momentum exchange, 17 October. Model results are solid lines and field observations are "x"s. Elevation is referenced to MSL.

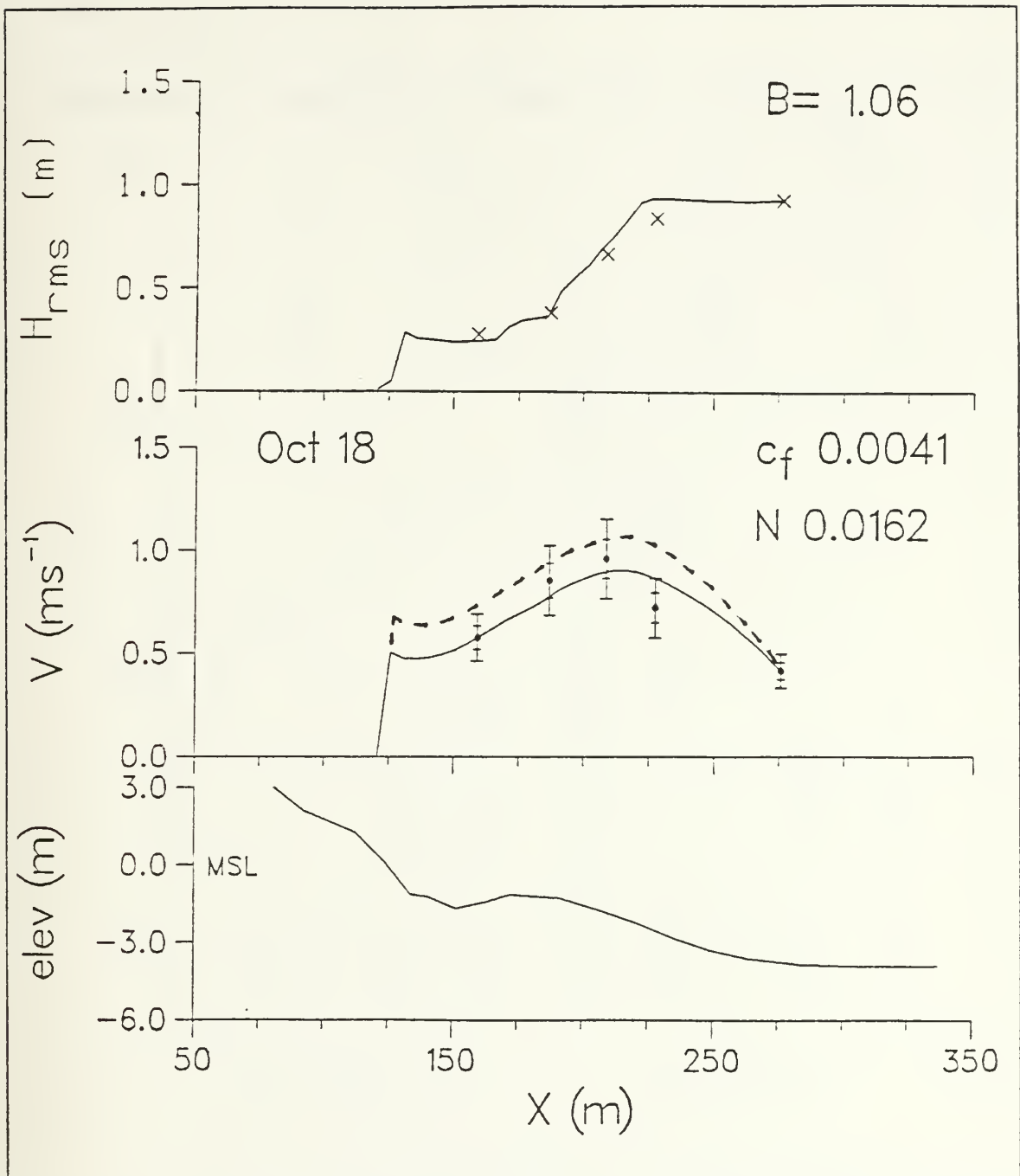


Figure 52. Model-generated H_{rms} and V compared with field observations versus distance for invariant c_f and B and including turbulent momentum exchange, 18 October. Model results are solid lines and field observations are "x"s. Elevation is referenced to MSL. Model result prior to the last c_f iteration is represented by the dashed line.

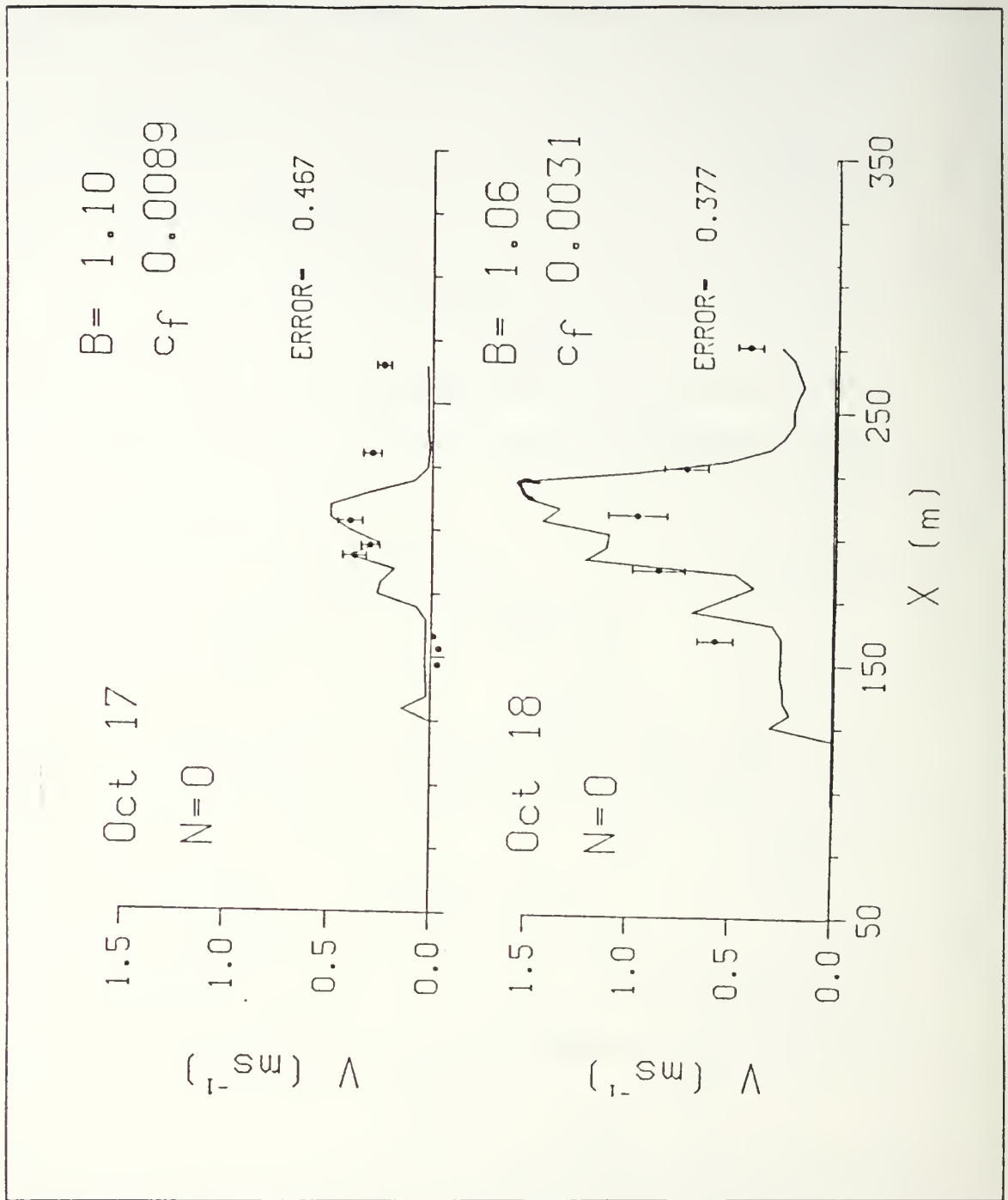


Figure 53. Model-generated V compared to field observations versus offshore distance for constant c_f and no turbulent momentum exchange, 17-18 October. Model results are solid line and field observations are "x"s. Error is mean least square error.

APPENDIX B. CURRENT VECTORS OVERLAYED ON BATHYMETRY

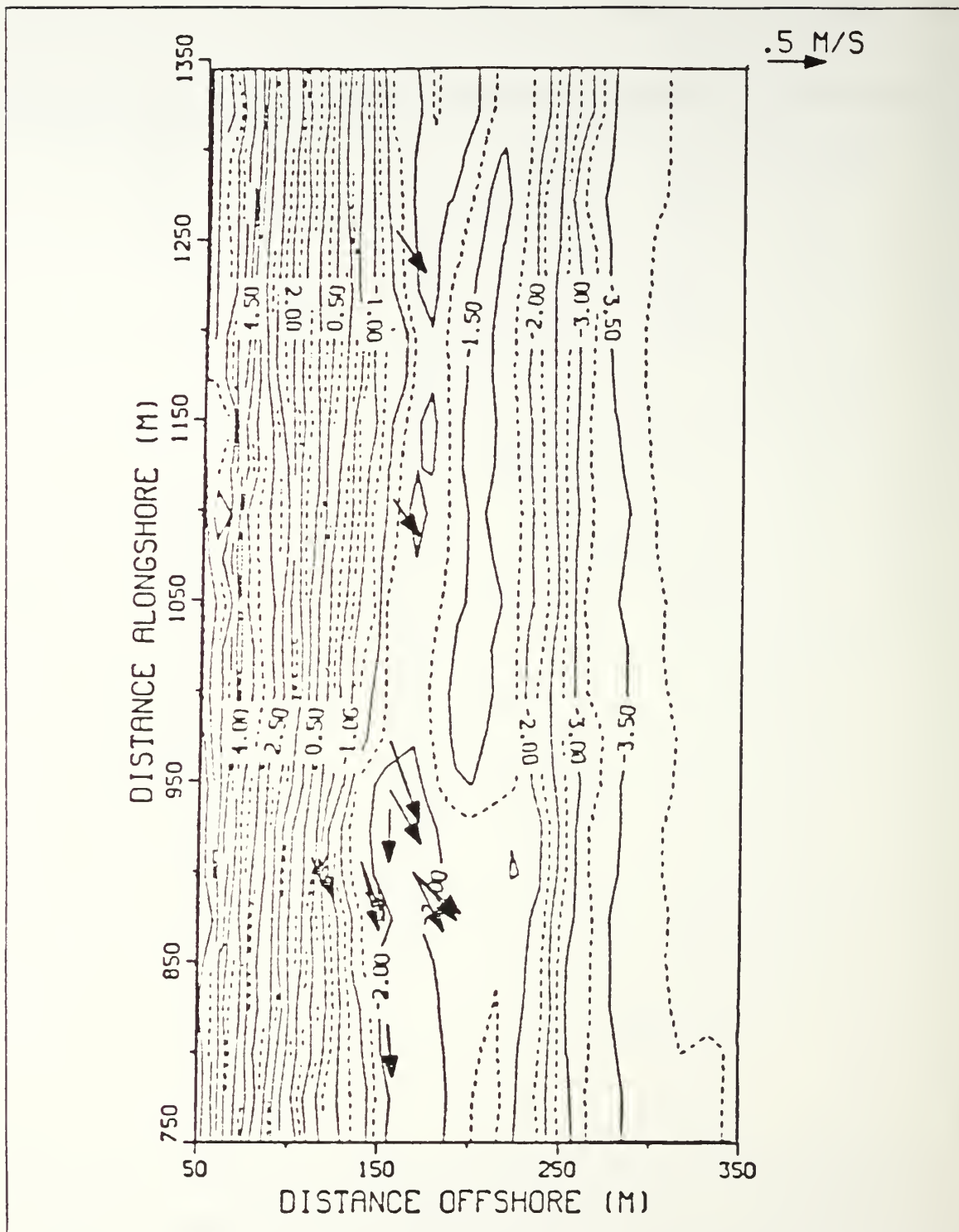


Figure 54. Sled and alongshore array mean current vectors for 11 October 1986 overlaid on bathymetry. Velocity scale is at upper right.

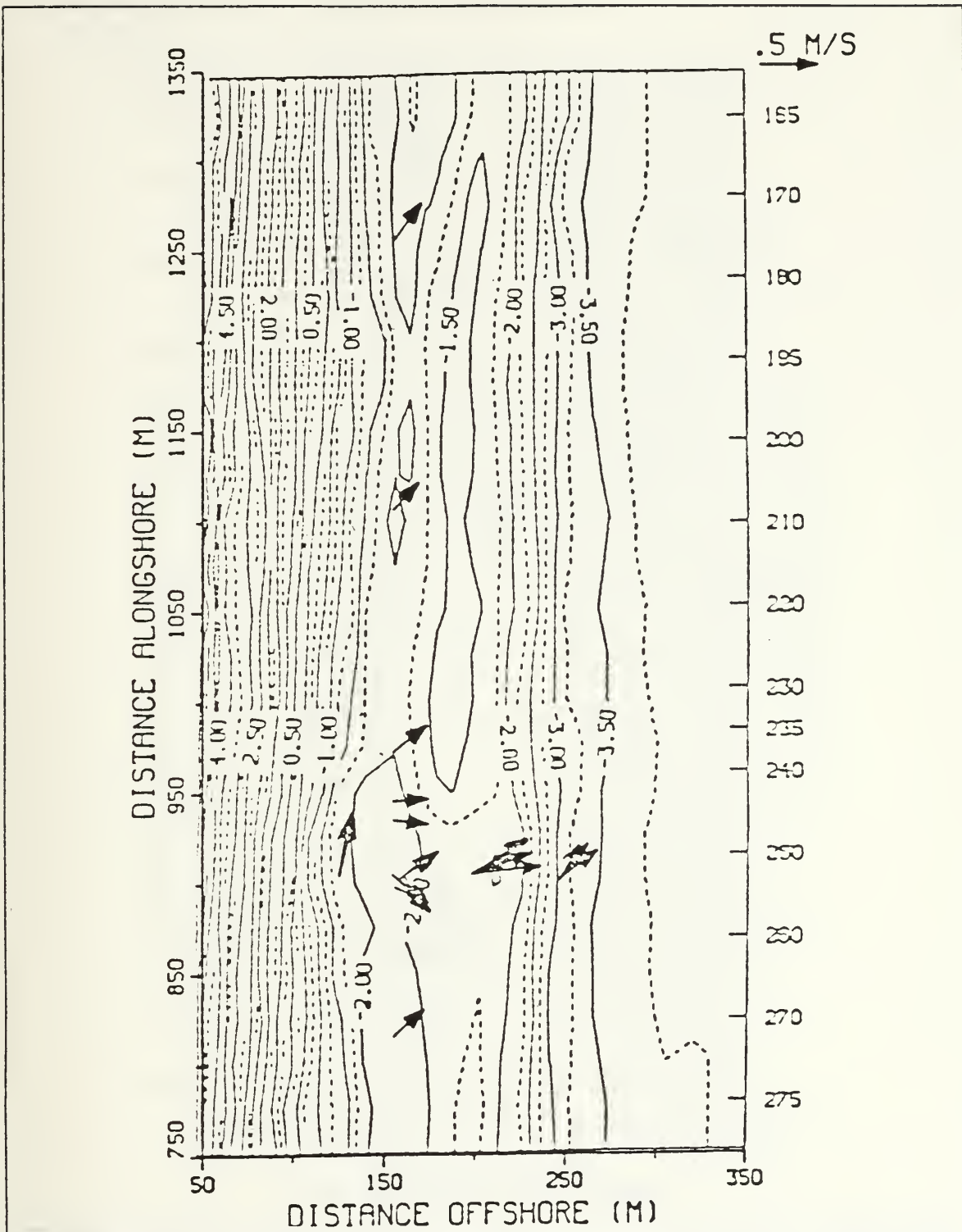


Figure 55. Sled and alongshore array mean current vectors for 12 October 1986 overlaid on bathymetry. Velocity scale is at upper right.

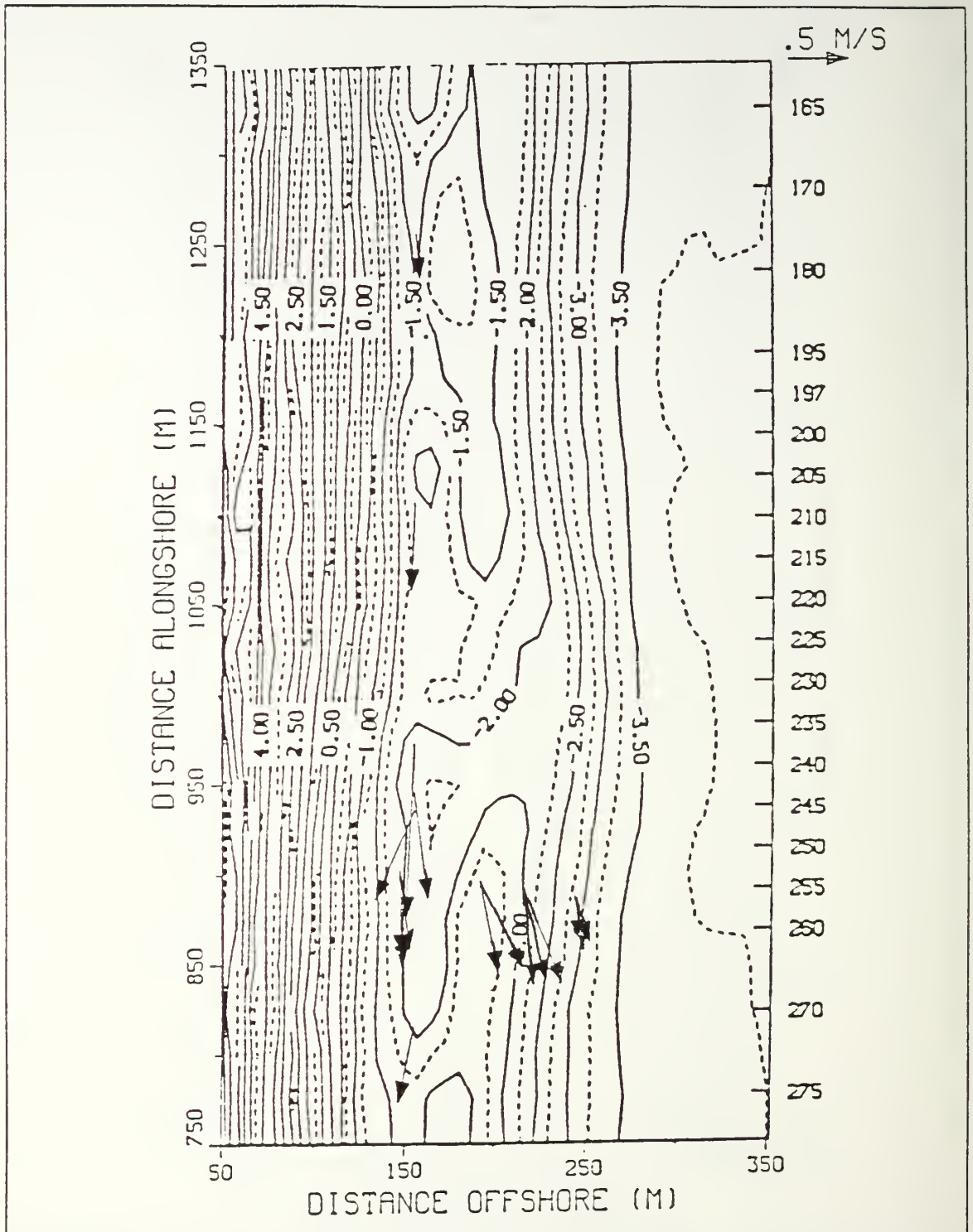


Figure 56. Sled and alongshore array mean current vectors for 15 October 1986 overlaid on bathymetry. Velocity scale is at upper right.

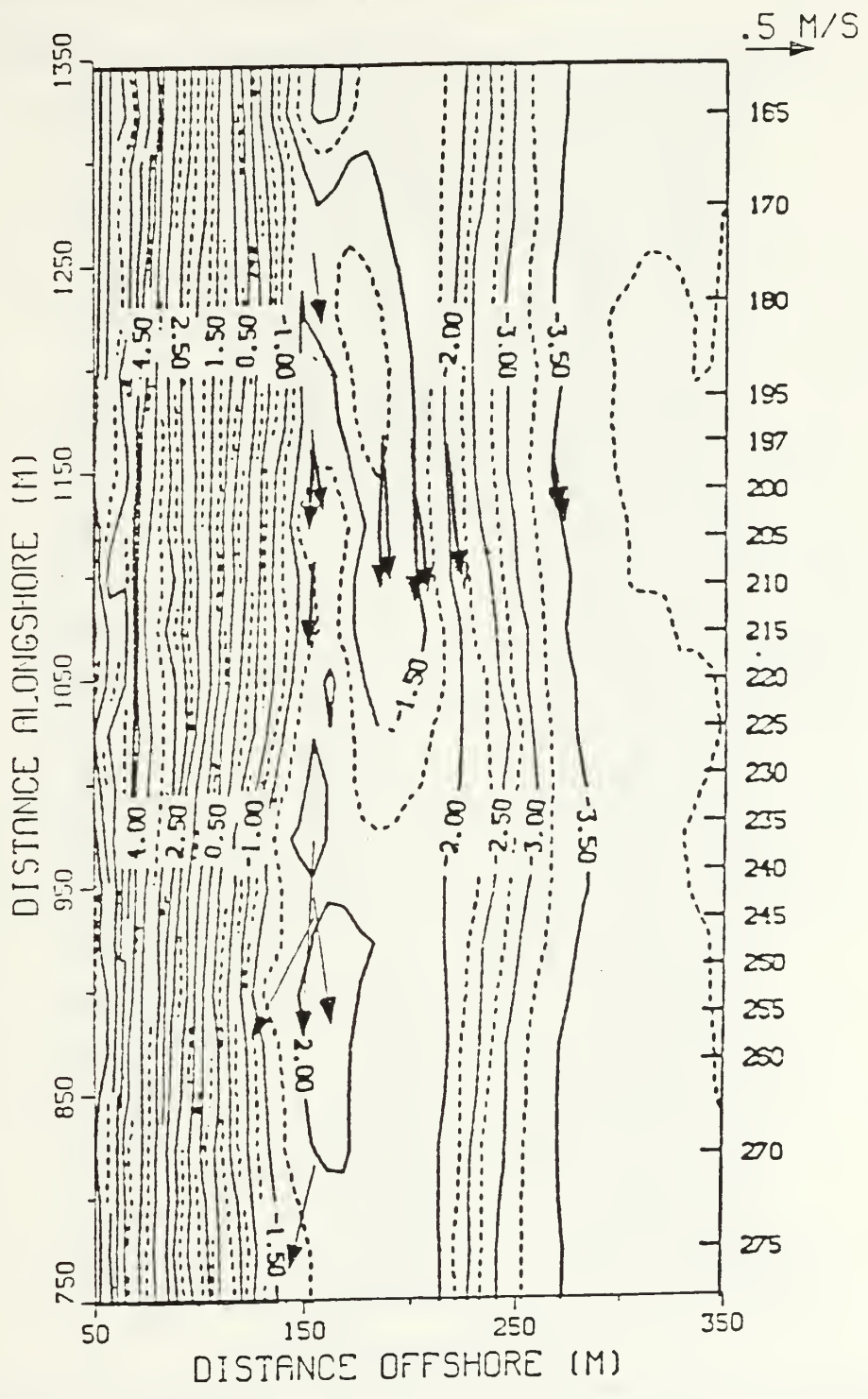


Figure 57. Sled and alongshore array mean current vectors for 16 October 1986 overlaid on bathymetry. Velocity scale is at upper right.

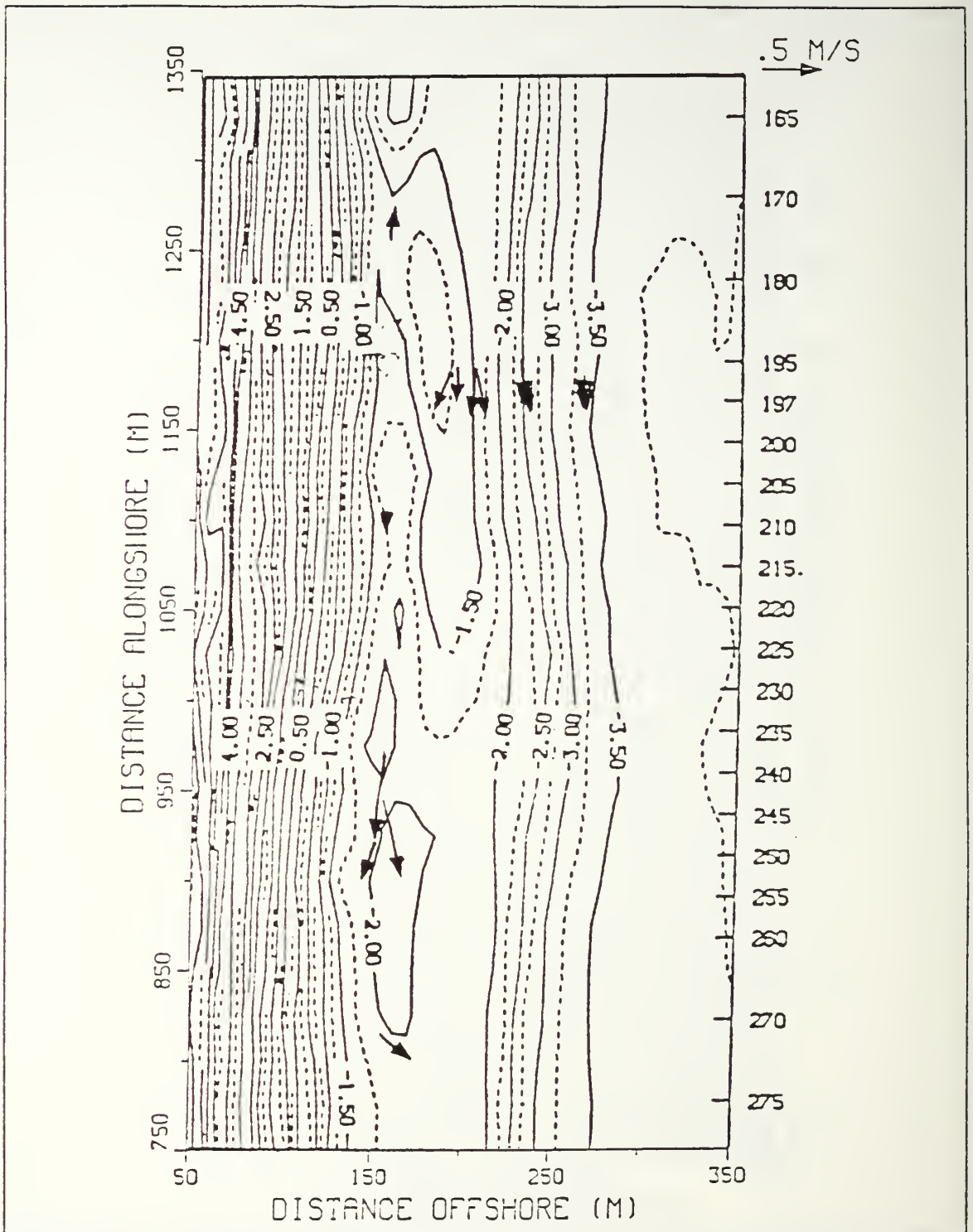


Figure 58. Sled and alongshore array mean current vectors for 17 October 1986 overlaid on bathymetry. Velocity scale is at upper right.

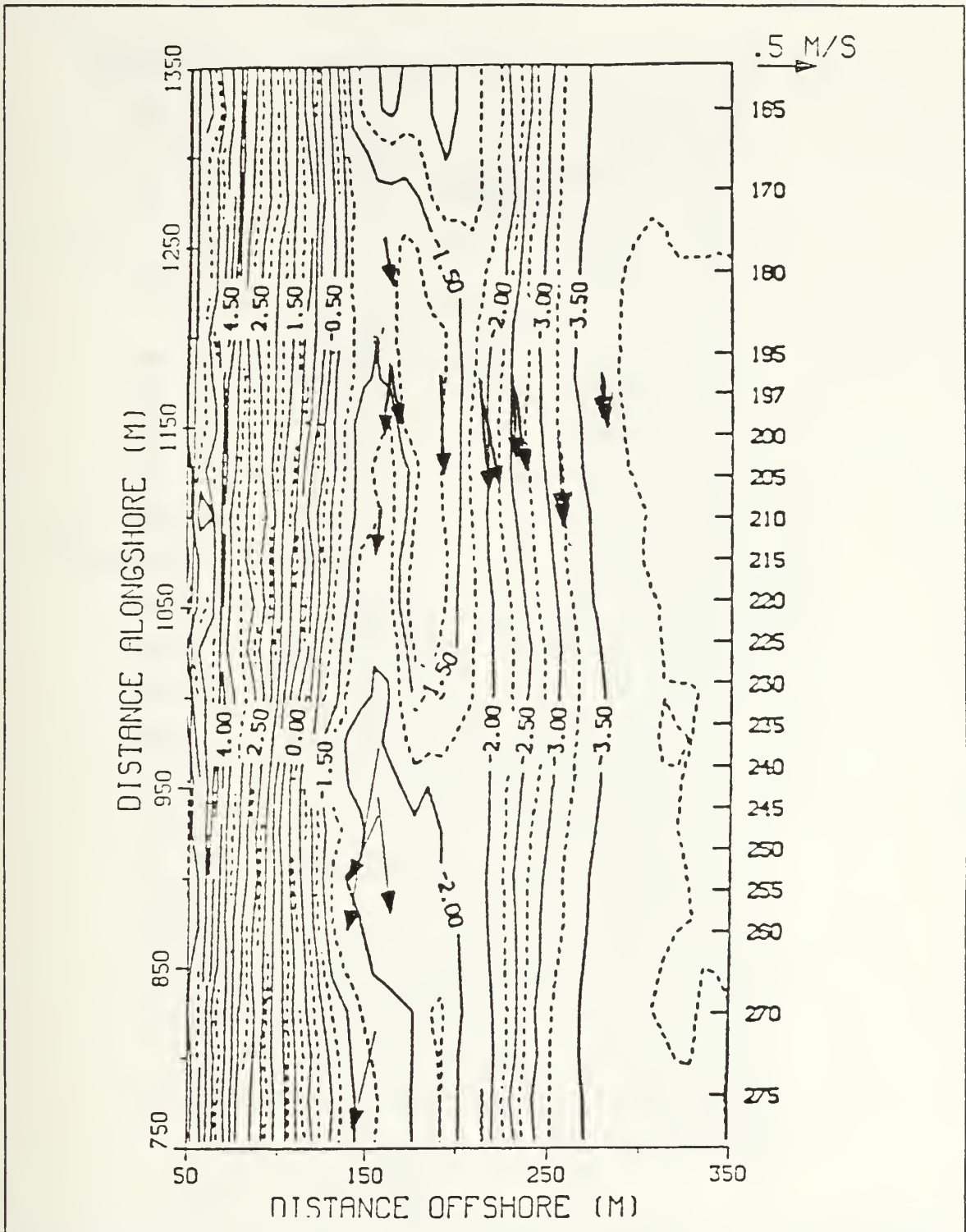


Figure 59. Sled and alongshore array mean current vectors for 18 October 1986 overlaid on bathymetry. Velocity scale is at upper right.

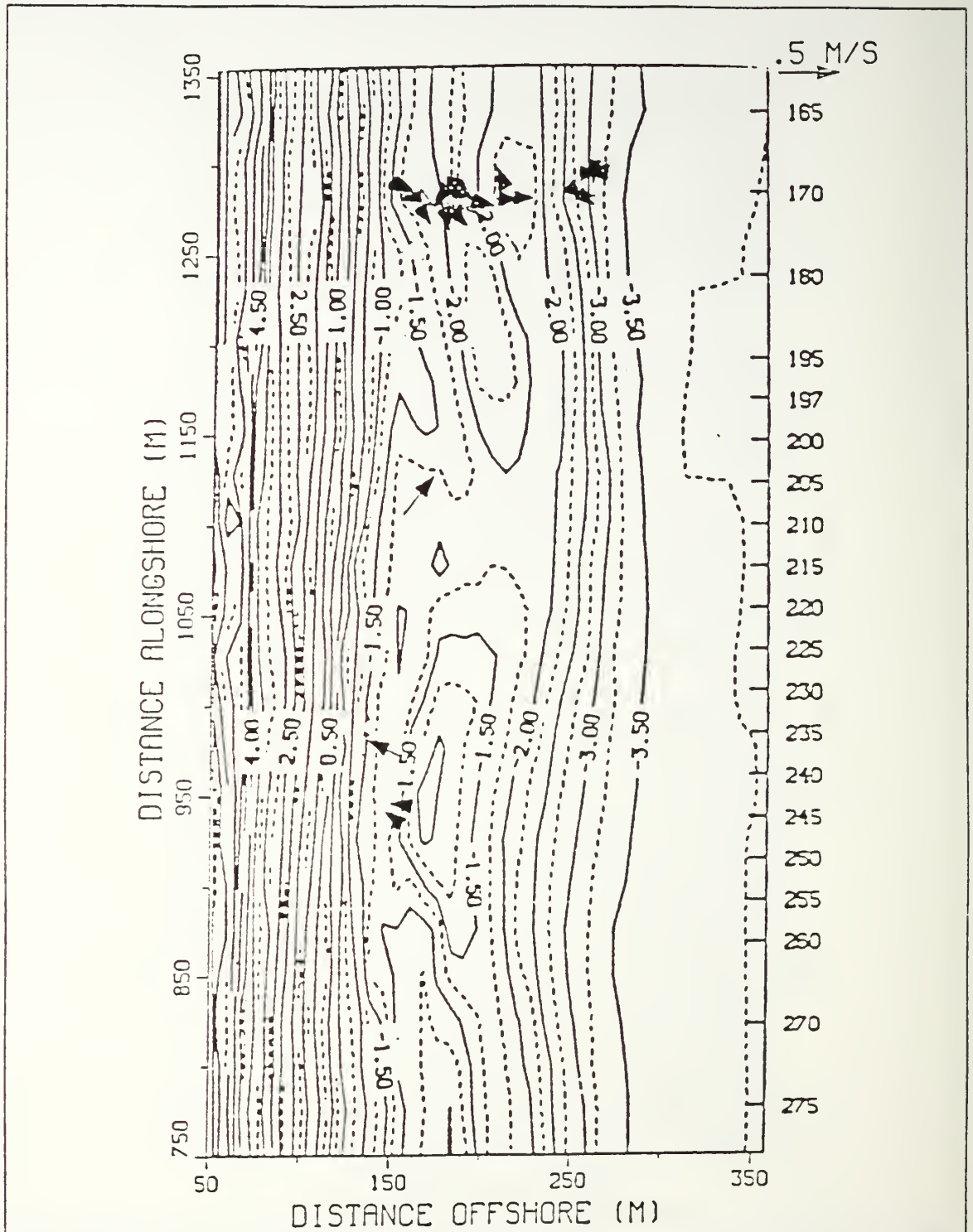


Figure 60. Sled and alongshore array mean current vectors for 21 October 1986 overlaid on bathymetry. Velocity scale is at upper right.

APPENDIX C. ATMOSPHERIC STABILITY DETERMINATION

The following set of equations represent an iterative procedure to determine z, L based on the stability flux profile relation of Businger et al. (1971).

Initial equations:

$$T_{dew} = T_{air} + 35(\ln(.01RH)) \quad (C1)$$

$$\Delta T = T_{air} - T_{surface} - .0098Z_T \quad (C2)$$

$$T_{Kel} = T_{air} + 273.15 \quad (C3)$$

Assign all $\frac{z}{L}$'s = 0

Determine T^* from iteration:

$$T^* = \frac{\Delta T \kappa}{\ln\left(\frac{z_m}{z_{oT}}\right) - \Psi_h\left(\frac{z}{L}\right)_T} \quad (C4)$$

$$\Psi_h = \Psi_q \left[\begin{array}{l} x = \left(1 - 16\left(\frac{z}{L}\right)\right)^{\frac{1}{4}} \\ \Psi = 2 \ln\left[\frac{(1+x^2)}{2}\right] \quad \frac{z}{L} < 0 \\ \Psi = -7\left(\frac{z}{L}\right) \quad \frac{z}{L} \geq 0 \end{array} \right] \quad (C5)$$

$$Q = Q_s(T_{dew} + 273.15)(.01 RH) \quad (C6)$$

$$Q_o = Q_s(T_{sea} + 273.15) \quad (C7)$$

$$Q_s = .62510^n \quad n = 23.84 - \frac{2948.}{T_{Kel}} - 5.03 \log(T_{Kel}) \quad (C8)$$

$$Q^* = \frac{(Q - Q_o)\kappa}{\ln\left(\frac{z_q}{z_{oq}}\right) - \Psi_h\left(\frac{z}{L}\right)_q} \quad (C9)$$

$$T_v^* = T^* + 6.1 \times 10^{-4}(T_{air} Q^*) \quad (C10)$$

$$\frac{z}{L} = \frac{g \kappa z T_v^*}{T_{Kel} u_*^2} \quad (C11)$$

$$\left(\frac{z}{L}\right)_T = \frac{g \kappa z_T T_v^*}{T_{Kel} u_*^2} \quad (C12)$$

$$\left(\frac{z}{L}\right)_q = \frac{g \kappa z_q T_v^*}{T_{Kel} u_*^2} \quad (C13)$$

Continue iterations from equation (C4) until $\left(\frac{z}{L}\right)$ converges.

Definitions:

z_T = temperature measurement height (m),

z_q = humidity measurement height (m),

RH = relative humidity (%),

T_d = dewpoint temperature (degrees C)

z_{0T} = temperature roughness length (2×10^{-6})

z_{0q} = humidity roughness length (2×10^{-6})

Ψ_h = integral diabatic term for temperature

Ψ_q = integral diabatic term for humidity

Q = specific humidity (g kg)

APPENDIX D. SURFACE WEATHER MAPS

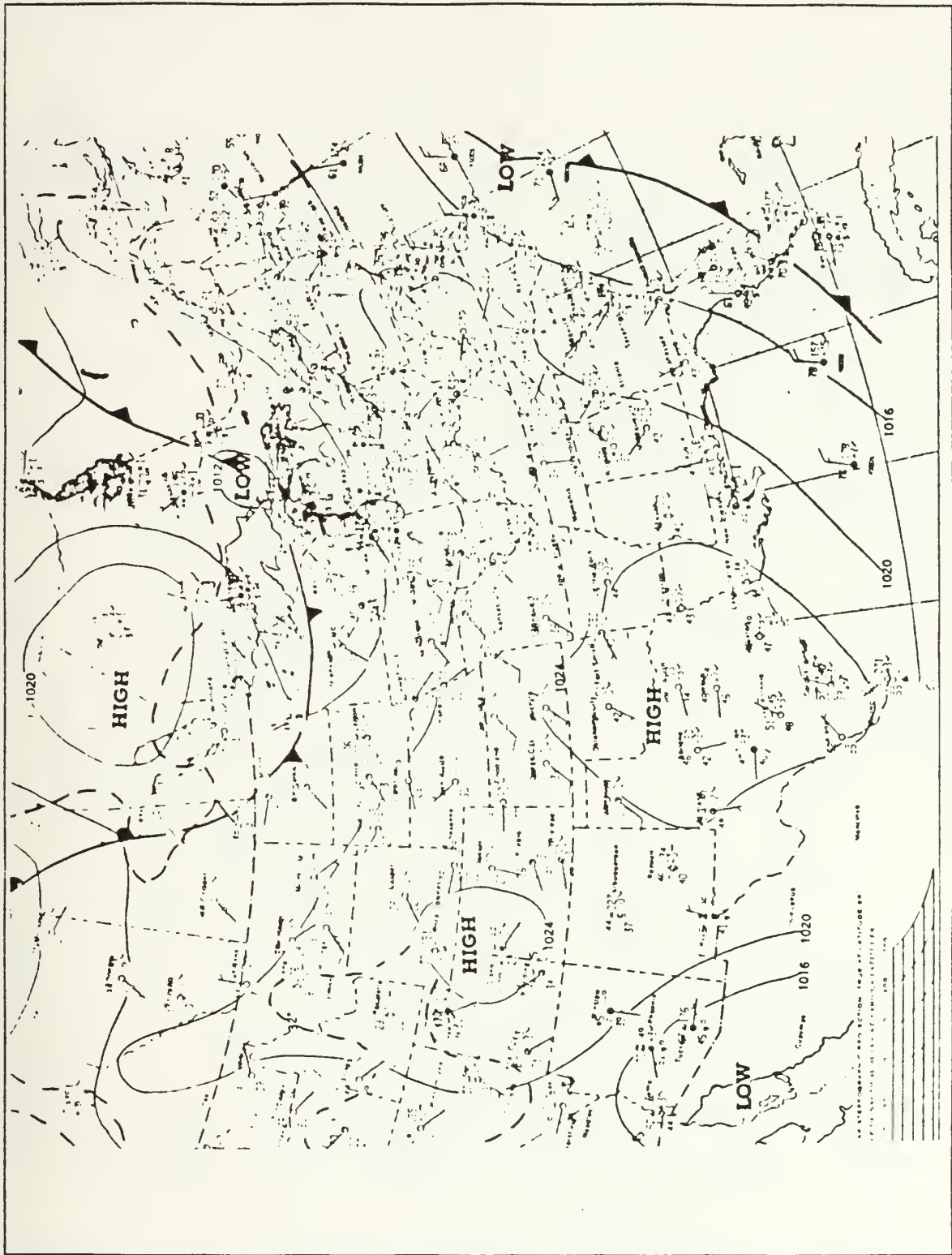


Figure 62. Surface weather analysis for 0700 E.S.T. 16 October 1986.

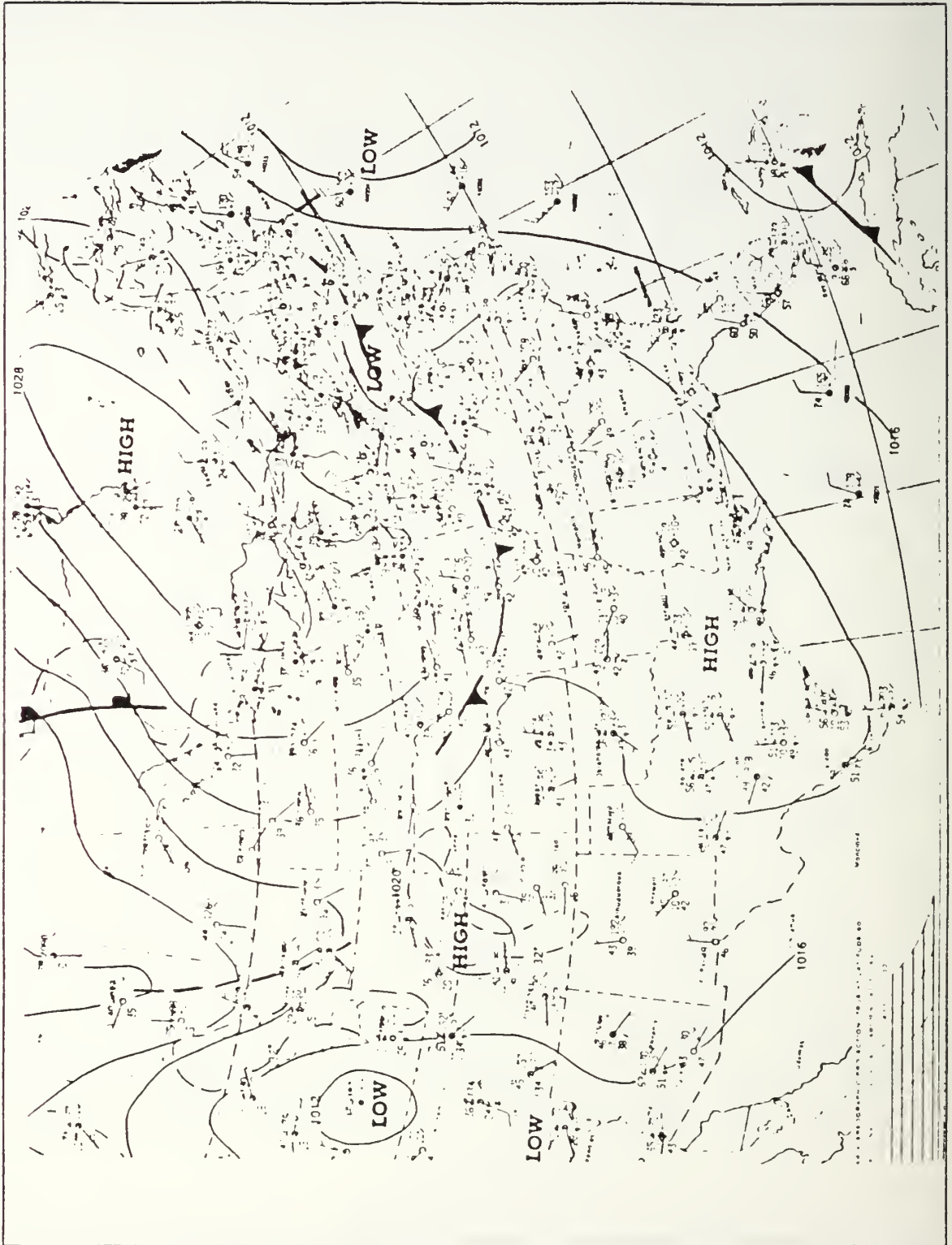


Figure 63. Surface weather analysis for 0700 E.S.T. 17 October 1986.

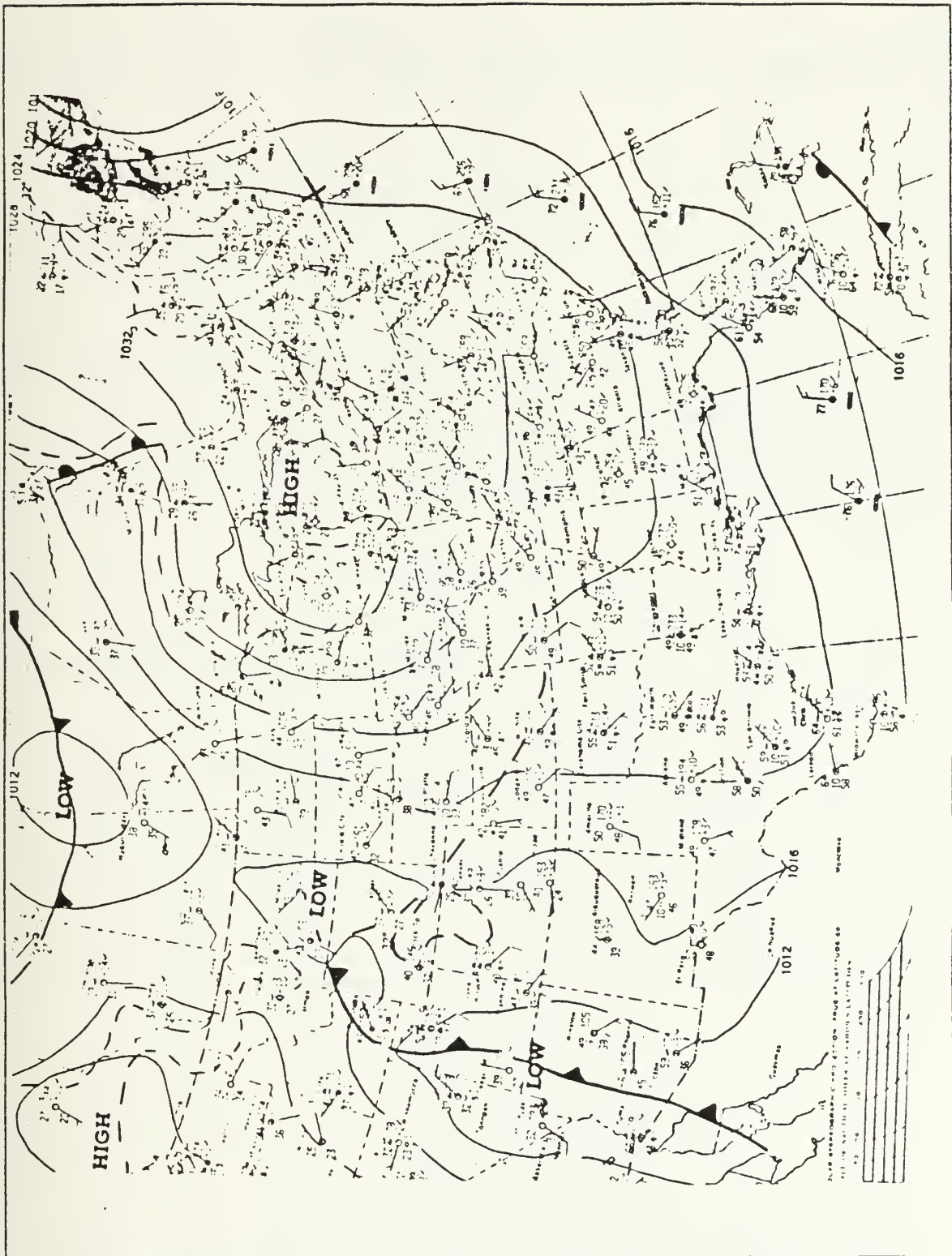


Figure 64. Surface weather analysis for 0700 E.S.T. 18 October 1986.

APPENDIX E. ANALYSIS PARAMETERS FOR ALL SLED DATA RUNS

Run	start time (hhmmss)	h (m)	H_{rms} (m)	f_m (Hz)	S_{yx}^T (Jm^{-2})	EMW (deg)	z_{anem} (m)	$\tan \beta$
11-1	123504	2.99	0.92	0.0938	24.33	1.4	5.92	.000
11-2	134359	2.80	0.85	0.0938	18.86	1.2	6.11	.000
11-3	143700	1.95	0.76	0.0938	18.51	1.5	6.95	.106
12-1	074600	2.97	1.12	0.0938	-134.39	-5.1	5.95	.059
12-2	092453	2.03	0.73	0.0938	13.23	1.2	6.88	.000
12-3	100300	2.29	0.64	0.0781	-14.03	-1.6	6.64	.000
12-5	145000	2.93	1.21	0.0781	-56.10	-1.8	6.00	.000
12-6	155700	3.03	0.93	0.0781	-28.95	-1.6	5.89	.000
12-7	164200	1.94	0.82	0.0781	13.61	0.9	6.97	.106
15-1	103257	2.79	0.92	0.1563	150.03	9.1	6.13	.029
15-2	120000	1.78	0.76	0.1563	60.60	5.2	7.15	.029
15-3	124700	1.67	0.57	0.1563	16.76	2.5	7.25	.029
15-4	133100	2.30	0.59	0.2031	33.45	5.0	6.62	.053
16-2	122200	3.33	0.98	0.1875	250.54	14.7	5.60	.012
16-3	131821	1.89	0.80	0.1875	151.02	12.1	7.03	.034
16-4	140600	1.51	0.57	0.1875	57.20	8.9	7.41	.034
16-5	144900	1.54	0.52	0.1875	47.99	9.0	7.39	.015
16-6	153600	1.91	0.49	0.1875	25.94	5.4	7.01	.005
17-1	092040	3.85	0.72	0.1719	61.53	6.3	5.08	.017
17-2	100036	2.59	0.69	0.1719	52.84	5.7	6.32	.034
17-3	104900	1.43	0.57	0.1094	24.14	3.4	7.50	.034
17-4	113500	1.18	0.41	0.1094	27.96	7.8	7.74	.034
17-5	122857	1.09	0.36	0.1094	70.37	31.4	7.83	.034
17-6	134336	1.41	0.24	0.0938	1.45	1.1	7.52	.017
17-7	141749	1.55	0.26	0.1094	3.99	2.9	7.38	.017
17-8	150024	1.43	0.32	0.1094	2.60	1.2	7.45	.017

18-1	110730	3.80	0.93	0.2031	175.62	11.8	5.12	.007
18-2	115000	2.38	0.84	0.1250	124.59	8.6	6.54	.032
18-3	122555	1.49	0.67	0.1094	49.62	5.3	7.44	.032
18-4	130900	1.13	0.38	0.1094	99.69	45.0	7.80	.007
18-5	134937	1.48	0.28	0.0469	3.71	2.2	7.45	-.025
21-1	110319	3.55	0.76	0.0938	-6.82	-0.6	5.31	.021
21-2	121953	1.65	0.68	0.0938	2.38	2.4	7.22	.000
21-3	130448	2.51	0.49	0.0938	-17.72	-3.4	6.35	-.029
21-4	134800	2.33	0.45	0.0938	2.08	0.5	6.54	.014
21-5	144000	2.17	0.38	0.0938	11.54	3.7	6.71	.014
21-6	154200	3.05	0.76	0.0938	4.20	0.3	5.82	.021
21-7	163059	1.20	0.59	0.0938	0.28	0.0	7.64	.010
21-8	171000	2.22	0.45	0.0938	6.13	1.5	6.65	-.029
21-9	174900	1.51	0.48	0.0781	-7.72	-1.6	7.35	.089

- start time is referenced to Eastern Standard Time
- H_{rms} is measured from variance of the pressure sensor
- z_{anem} is the height of the anemometer above the mean water level as measured by the pressure sensor for that run
- x,y coordinates are referenced to the FRF coordinate system
- f_m is the peak freq in the sea sfc elevation spectrum
- 'EMW' is the "equivalent monochromatic wave" incident angle (Thornton and Guza, 1986)
- S_{yx}^T is the mean S_{yx}^T for the submerged current meters on that run
- f_m is the peak frequency of the sea surface elevation spectra

Run	sled x coord (m)	sled y coord (m)	P_{aim} ($10^2 Pa$)	θ ($^{\circ} TN$)	W_{10} (ms^{-1})	boa (deg)	# submerged c/m's
11-1	168.44	899.90	1023.6	067.	13.37	0.5	3
11-2	139.66	905.65	1023.8	066.	12.84	0.5	3
11-3	116.11	907.30	1023.9	065.	12.72	0.5	3
12-1	247.15	900.44	1024.1	049.	10.00	0.5	3
12-2	198.94	904.57	1023.8	047.	8.82	0.5	3
12-3	154.69	904.92	1023.7	047.	8.71	0.5	3
12-5	198.55	904.42	1023.6	052.	5.66	0.5	3
12-6	159.41	902.77	1023.5	047.	5.04	0.5	3
12-7	125.21	904.17	1023.6	041.	5.43	0.5	3
15-1	244.01	887.14	1017.3	037.	9.37	4.0	3
15-2	216.02	891.67	1017.2	037.	8.11	4.0	3
15-3	191.78	895.64	1017.2	039.	7.81	4.0	2
15-4	147.13	901.89	1017.3	040.	7.80	4.0	3
16-2	269.28	1157.39	1016.8	030.	12.28	-0.5	3
16-3	218.76	1162.25	1016.9	027.	11.43	-0.5	3
16-4	201.06	1165.24	1017.0	025.	10.90	-0.5	2
16-5	188.07	1166.64	1017.1	026.	10.22	-0.5	2
16-6	154.58	1170.37	1017.3	026.	10.04	-0.5	3
17-1	264.71	1179.83	1019.1	001.	6.23	-0.5	3
17-2	230.10	1182.31	1019.2	276.	7.24	-0.5	3
17-3	203.30	1184.07	1019.3	150.	7.06	-0.5	2
17-4	193.76	1184.49	1019.4	037.	6.55	-0.5	1
17-5	189.67	1184.39	1019.5	033.	5.89	-0.5	1
17-6	158.10	1188.54	1019.9	025.	5.53	-0.5	2
17-7	153.23	1189.60	1020.1	026.	5.80	-0.5	2
17-8	146.96	1190.44	1020.2	029.	5.80	-0.5	2
18-1	275.56	1179.98	1026.8	023.	inop	1.5	3
18-2	227.23	1178.08	1027.1	021.	inop	1.5	3
18-3	208.39	1177.67	1027.2	018.	12.13	1.5	2
18-4	186.79	1179.03	1027.4	017.	12.59	1.5	1
18-5	159.11	1185.79	1027.4	018.	13.75	1.5	2

21-1	252.89	1282.94	1023.1	353.	inop	0.8	3
21-2	204.39	1280.80	1022.5	044.	inop	0.8	2
21-3	182.12	1283.45	1022.6	035.	inop	0.8	3
21-4	173.04	1283.81	1022.7	041.	inop	0.8	3
21-5	157.84	1285.67	1022.7	056.	inop	0.8	3
21-6	259.15	1295.27	1022.8	083.	inop	0.8	3
21-7	207.88	1292.45	1022.8	089.	inop	0.8	1
21-8	180.63	1291.45	1022.8	079.	inop	0.8	2
21-9	147.96	1290.75	1022.9	083.	inop	0.8	2

- sled x,y coordinates are referenced to the FRF coordinate system
- 'boa' is beach orientation angle
- MKS conversion for pressure: 1 mb = 100 Pa

Run	$\hat{\alpha}(f_m)$ (°)	H_o (m)	f_m of S_{rx} (Hz)	Q	H_{rms} (m)
111	-1.2		.0156		
112	-1.7		.0781		
113	1.0		.0781		
121	-4.3		.0781		
122	-0.4		.1250		
123	-4.3		.0781		
125	-1.2		.0781		
126	0.0		.0781		
127	1.8		.0625		
151	10.2	1.43	.1563	0.00	0.79
152	6.5	1.40	.1719	0.44	0.73
153	5.8	1.30	.1563	0.11	0.56
154	8.9	1.14	.1719	0.04	0.51
162	19.0	1.59	.1875	0.00	0.78
163	14.9	1.53	.1875	0.13	0.79

164	12.0	1.46	.1875	0.06	0.58
165	18.9	1.41	.1875	0.04	0.50
166	9.5	1.35	.1875	0.02	0.45
171	7.6	1.16	.1875	0.00	0.56
172	8.8	1.14	.1875	0.01	0.59
173	-2.8	1.11	.1719	0.19	0.57
174	1.8	1.15	.1719	0.19	0.42
175	-2.1	1.09	.1250	0.21	0.38
176	0.2	1.09	.0938	0.17	0.24
177	-1.9	1.11	.0781	0.06	0.23
178	0.2	1.11	.0781	0.07	0.28
181	22.2	1.44	.1875	0.00	0.73
182	-1.6	1.46	.1875	0.00	0.73
183	-1.4	1.40	.1719	1.00	0.68
184	14.1	1.48	.1094	1.00	0.39
185	-0.7	1.67	.2500	0.00	0.27
211	-3.6		.0938		
212	4.5		.0938		
213	-3.6		.0781		
214	-1.2		.0156		
215	9.7		.0625		
216	-2.6		.1094		
217	3.7		.0938		
218	6.6		.0938		
219	-1.6		.0156		

- $\hat{\alpha}(f_m)$ is the mean $\hat{\alpha}$ of the rear and front current meter (if they were both submerged) and is obtained from the significant wave angle spectra for peak frequency in sea surface elevation spectra (see equation 71).
- H_o is determined from SUPERDUCK gage 630.
- f_m of S_{yx} is the peak frequency from the rear current meter S_{yx} spectra
- H_{rms} is determined from the η time series using equation 138
- Q is the fraction of all waves which are breaking.

**APPENDIX F. RADIATION STRESS, SEA SURFACE ELEVATION,
SIGNIFICANT WAVE ANGLE, AND CURRENT VELOCITY SPECTRA**

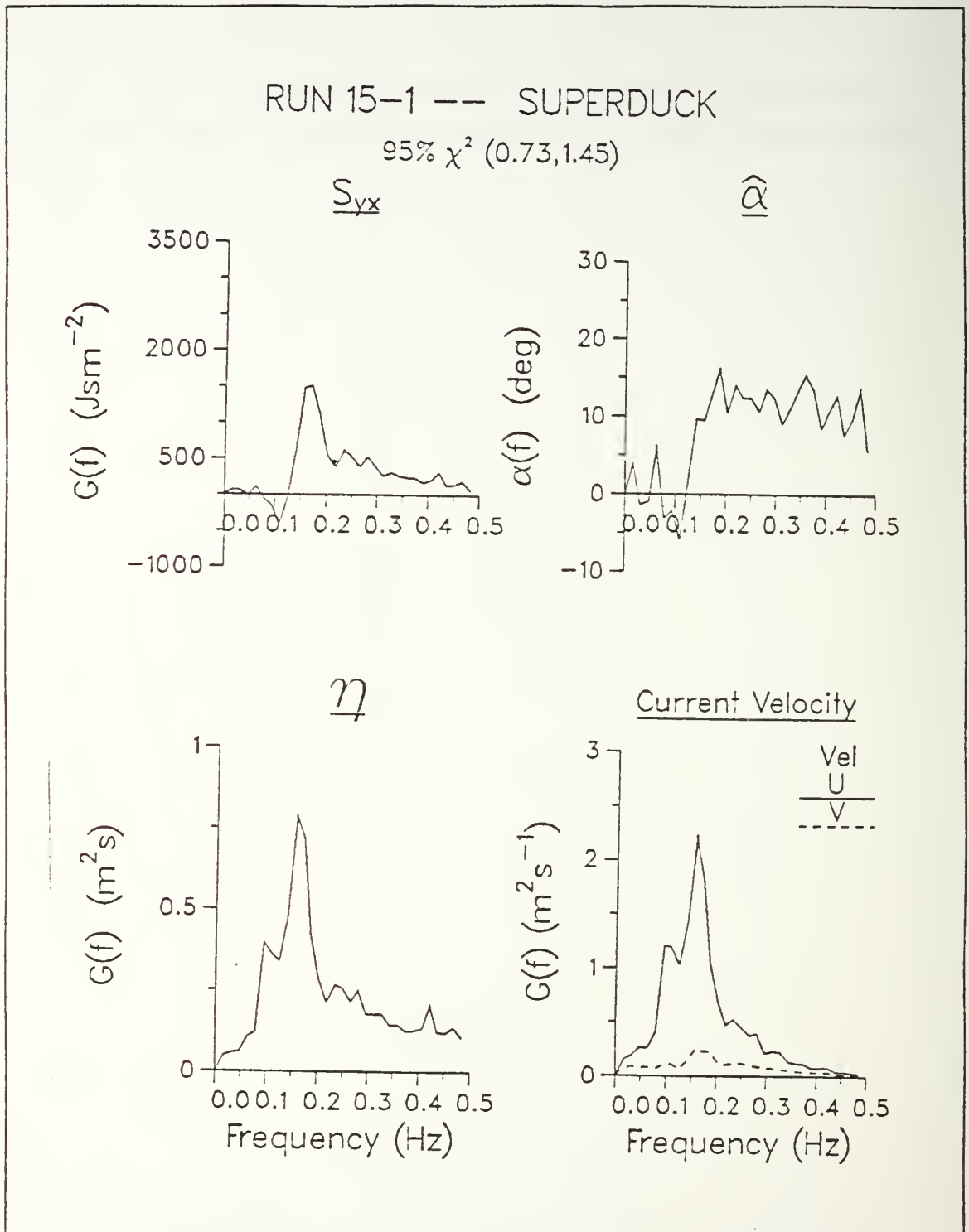


Figure 65. Radiation stress (S_{yx}), sea surface elevation (η), significant wave angle ($\hat{\alpha}$), and current velocity spectra for sled run 15-1.

RUN 15-2 -- SUPERDUCK

95% χ^2 (0.73, 1.45)

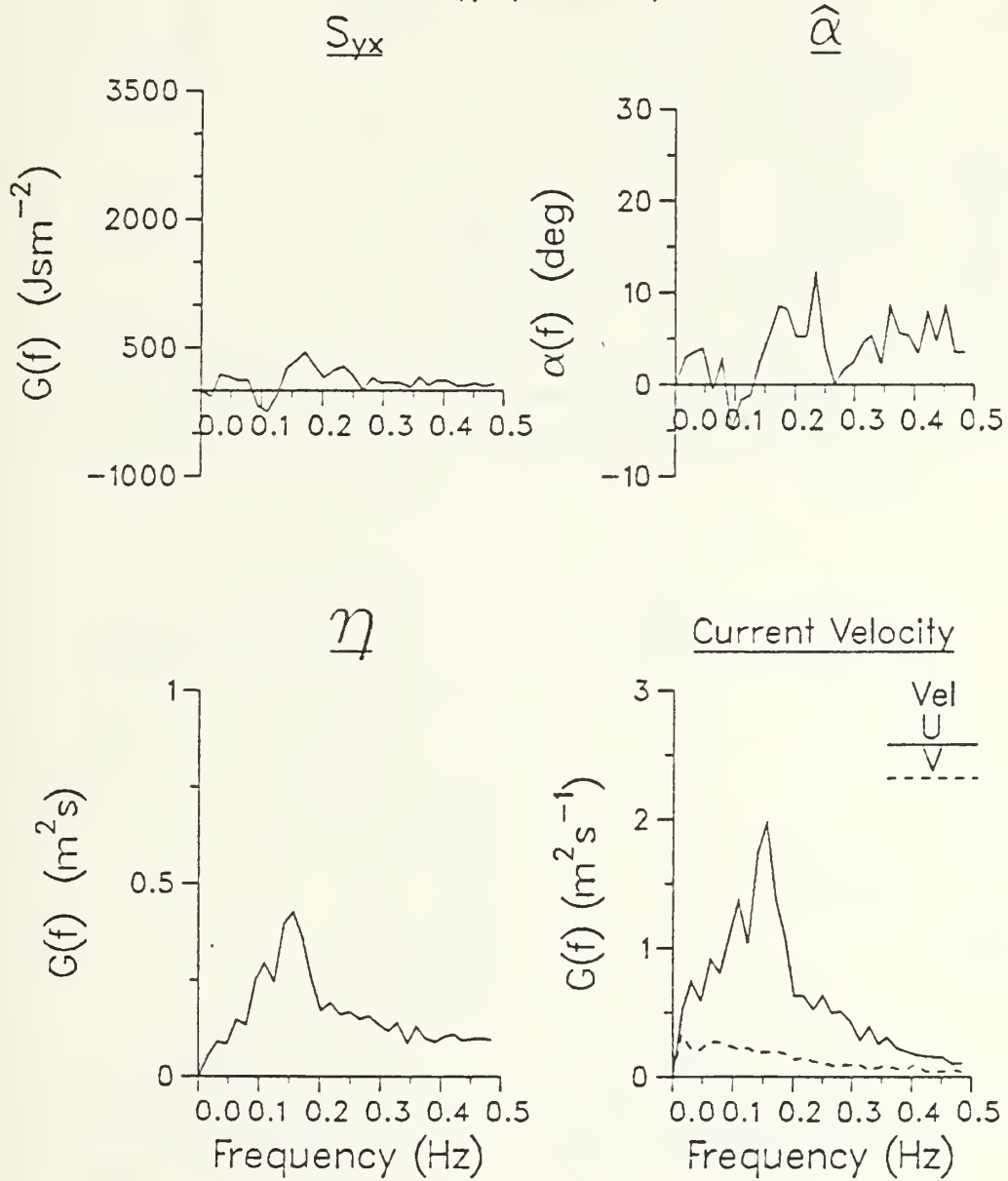


Figure 66. Radiation stress (S_{yx}), sea surface elevation (η), significant wave angle ($\hat{\alpha}$), and current velocity spectra for sled run 15-2.

RUN 15-3 -- SUPERDUCK

95% χ^2 (0.73, 1.45)

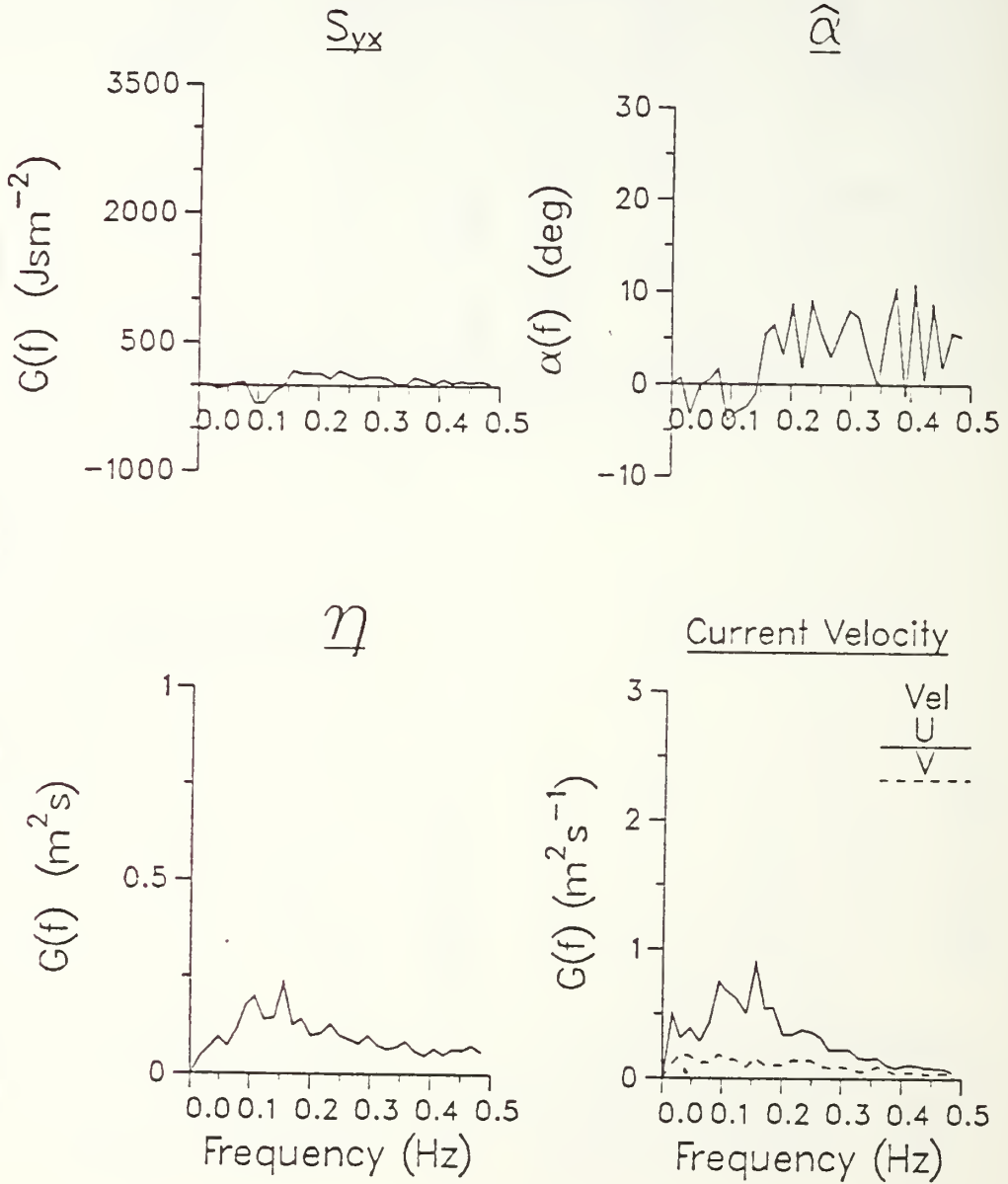


Figure 67. Radiation stress (S_{yx}), sea surface elevation (η), significant wave angle ($\hat{\alpha}$), and current velocity spectra for sled run 15-3.

RUN 15-4 -- SUPERDUCK

95% χ^2 (0.73, 1.45)

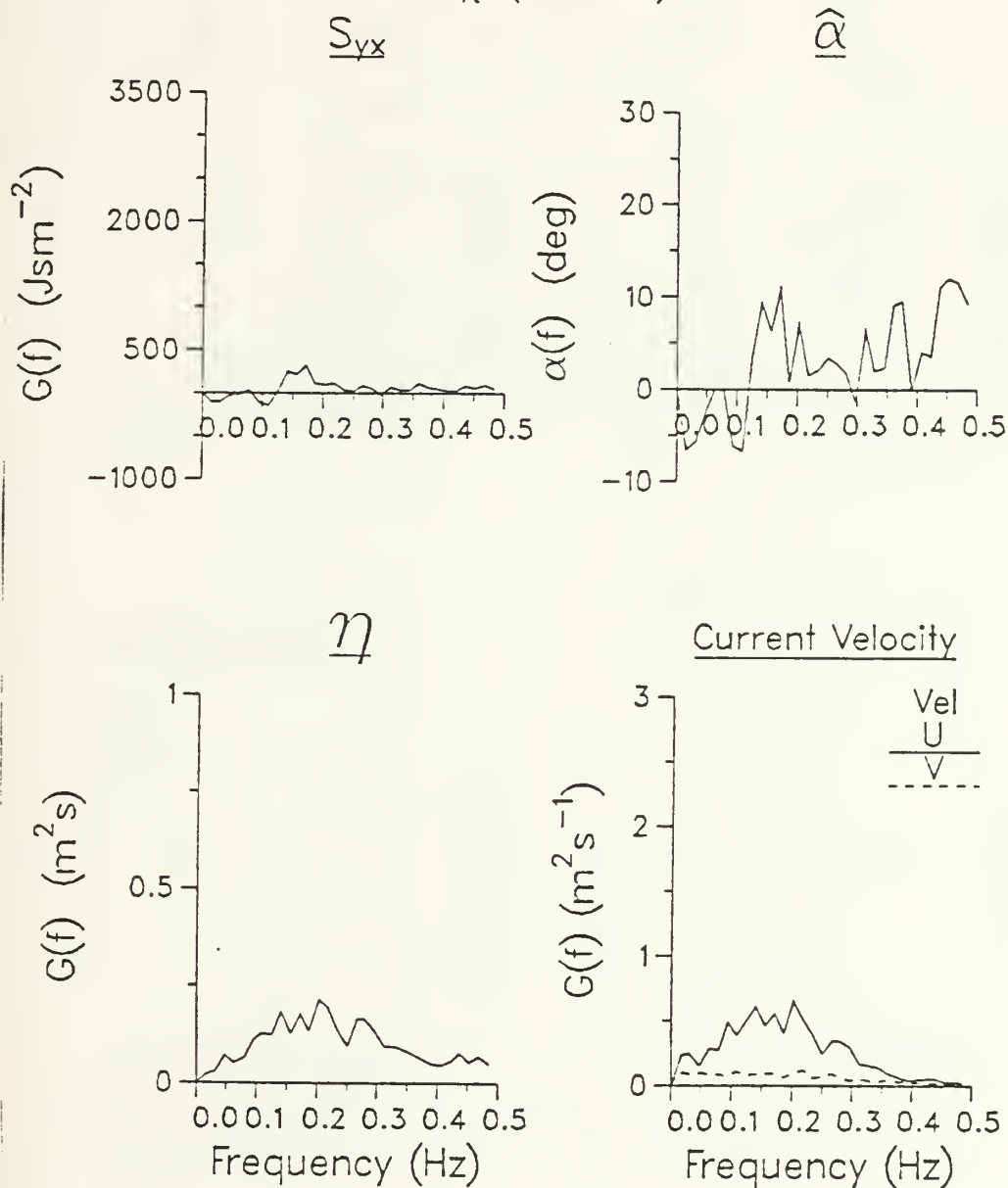


Figure 68. Radiation stress (S_{yx}), sea surface elevation (η), significant wave angle ($\hat{\alpha}$), and current velocity spectra for sled run 15-4.

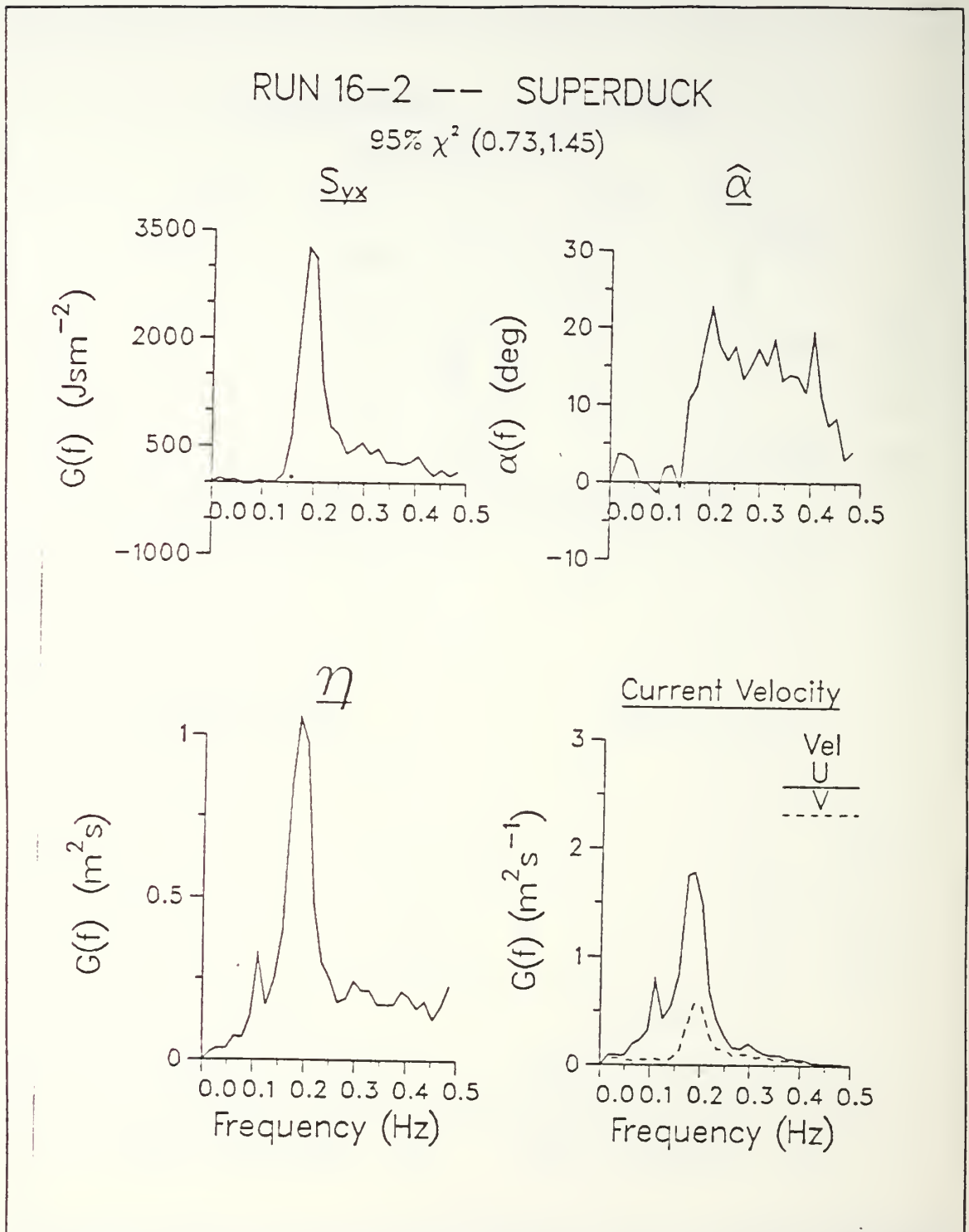


Figure 69. Radiation stress (S_{yx}), sea surface elevation (η), significant wave angle ($\hat{\alpha}$), and current velocity spectra for sled run 16-2.

RUN 16-3 -- SUPERDUCK

95% χ^2 (0.73, 1.45)

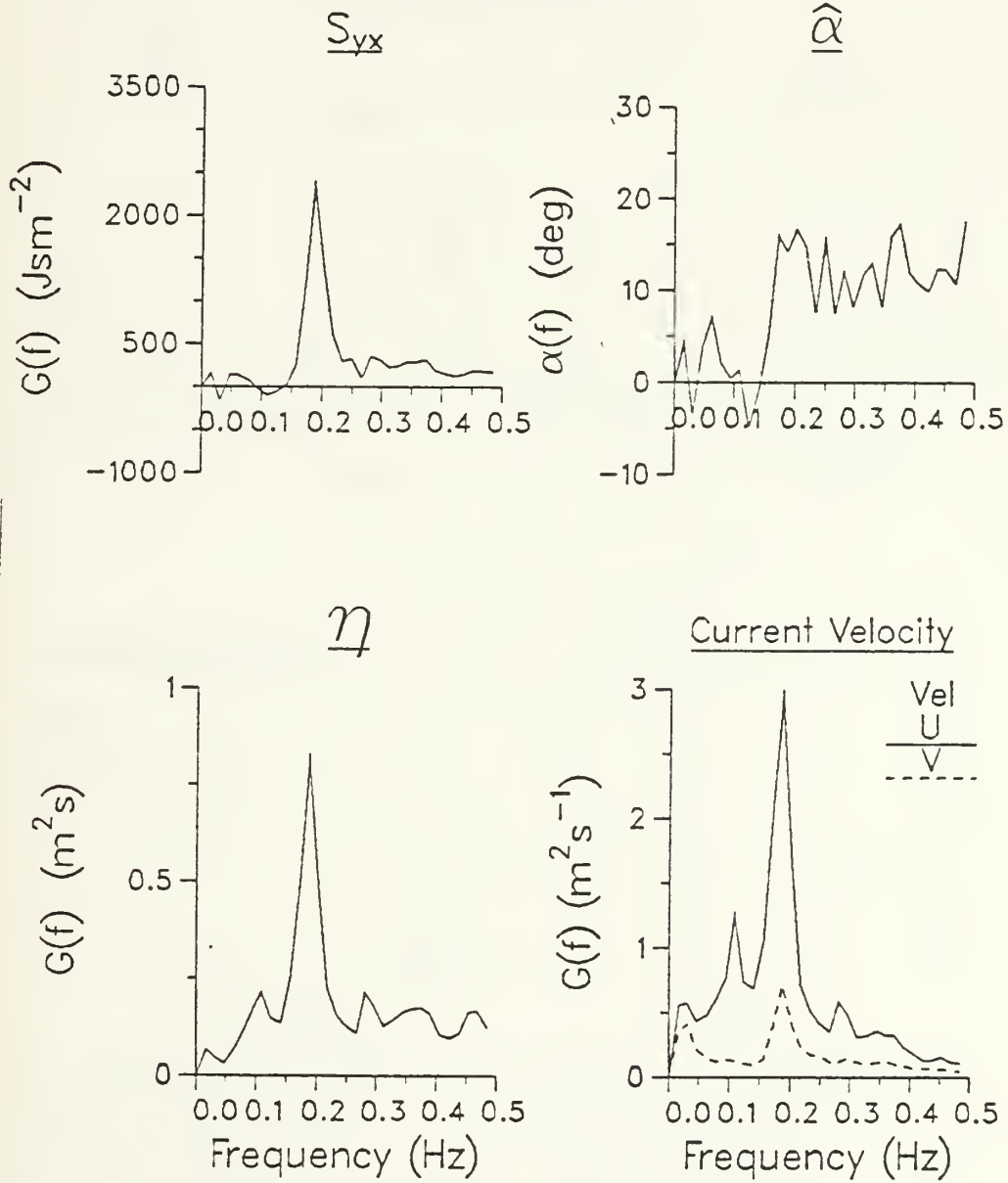


Figure 70. Radiation stress (S_{yx}), sea surface elevation (η), significant wave angle ($\hat{\alpha}$), and current velocity spectra for sled run 16-3.

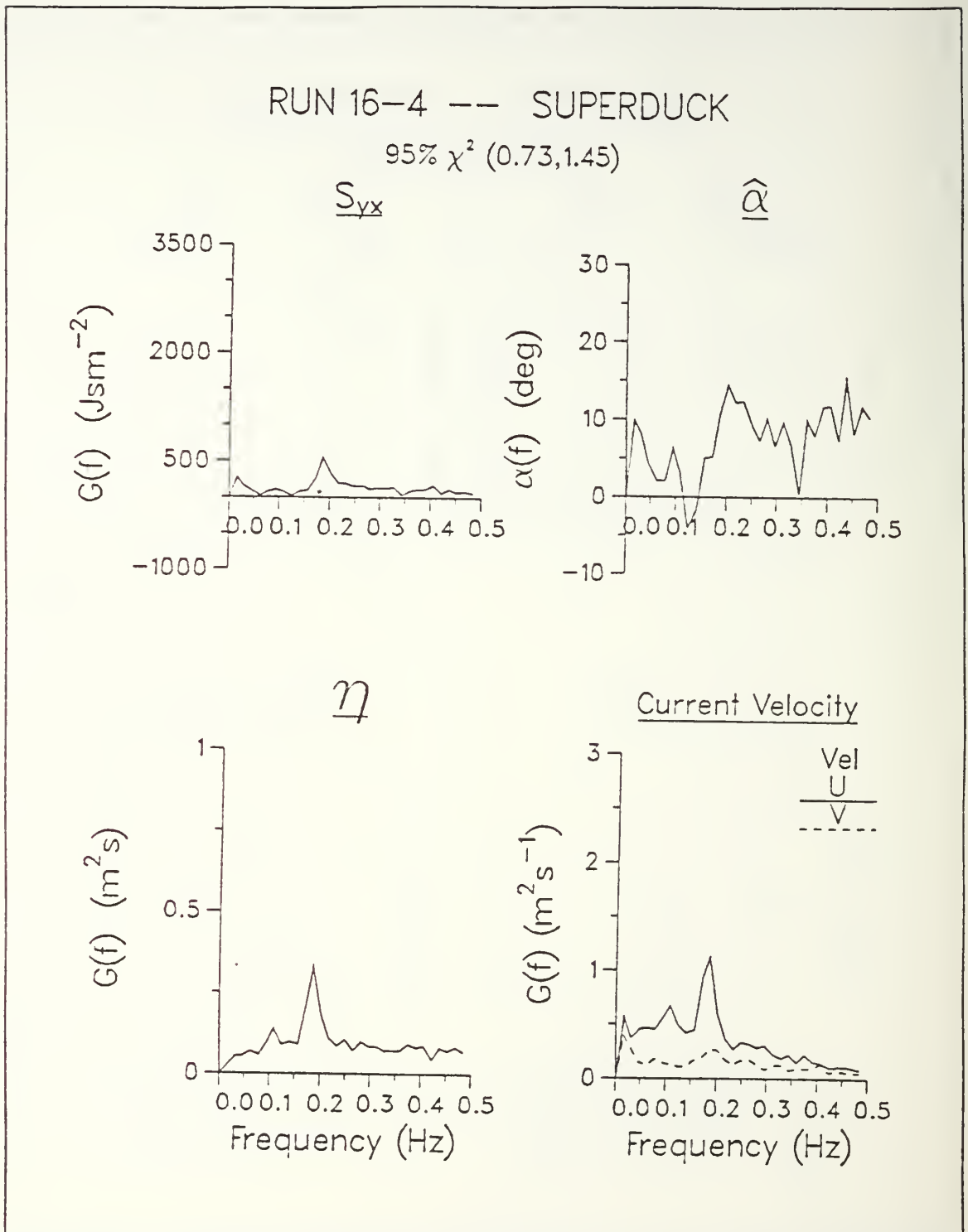


Figure 71. Radiation stress (S_{yx}), sea surface elevation (η), significant wave angle ($\hat{\alpha}$), and current velocity spectra for sled run 16-4.

RUN 16-5 -- SUPERDUCK

95% χ^2 (0.73, 1.45)

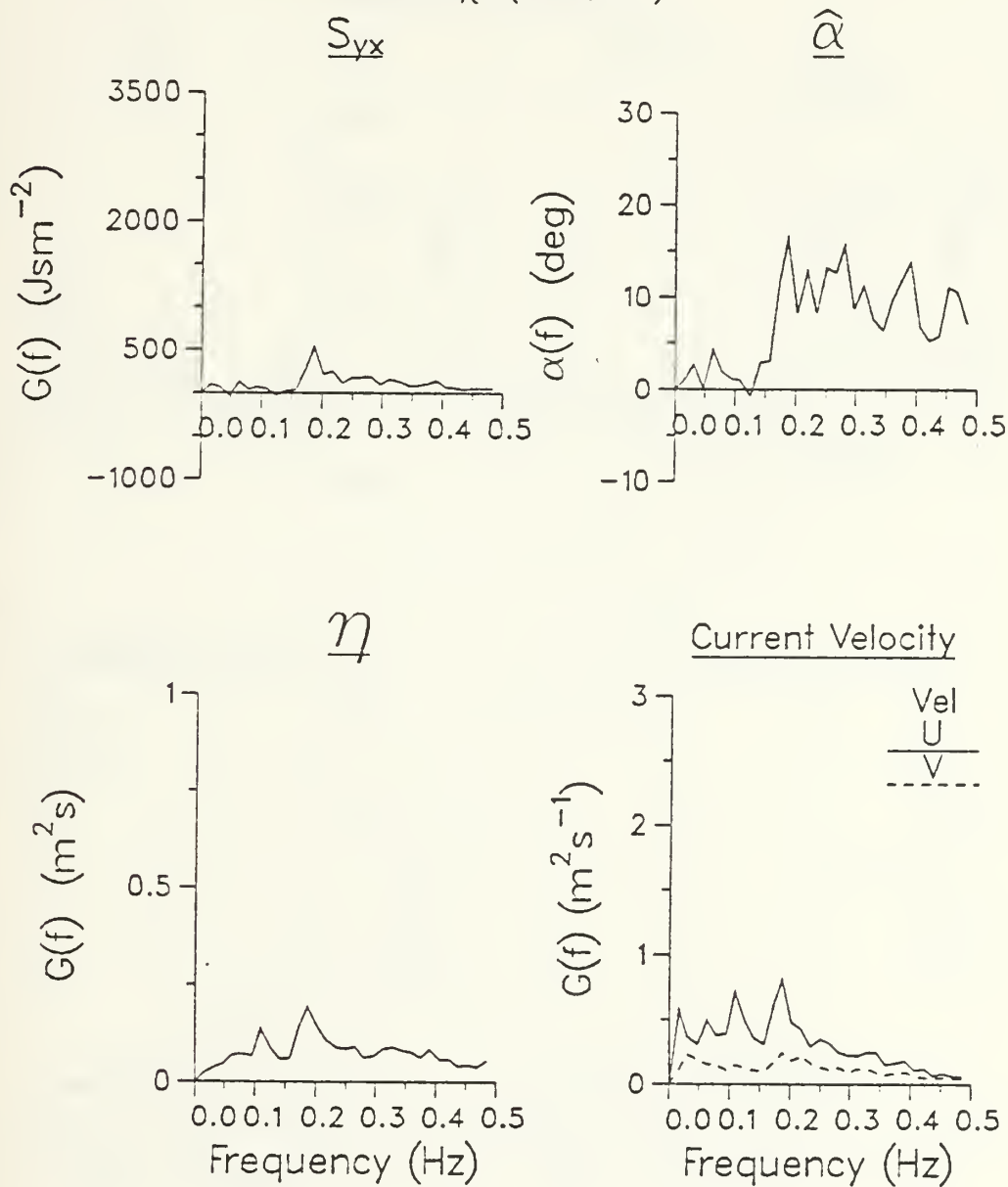


Figure 72. Radiation stress (S_{yx}), sea surface elevation (η), significant wave angle ($\hat{\alpha}$), and current velocity spectra for sled run 16-5.

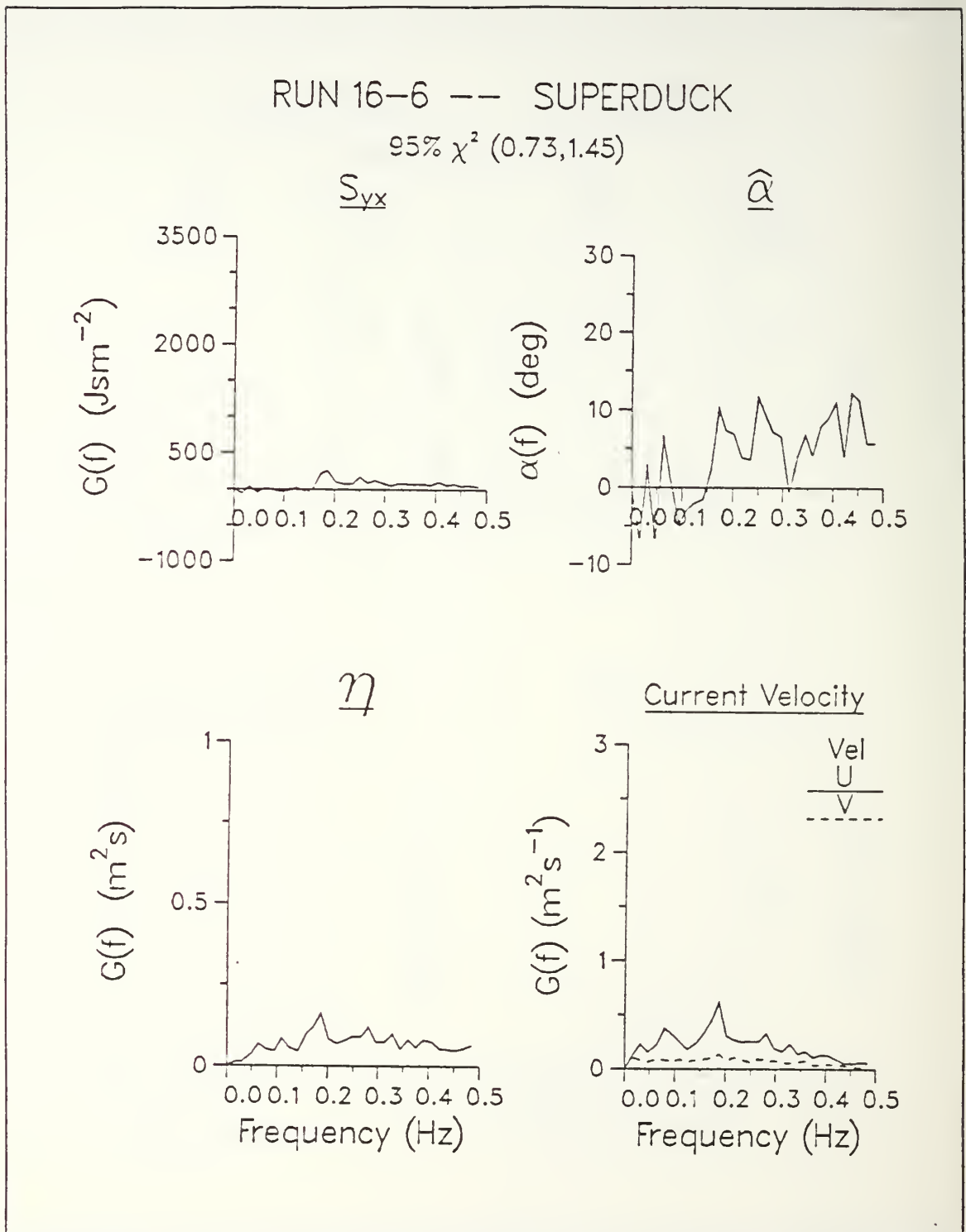


Figure 73. Radiation stress (S_{yx}), sea surface elevation (η), significant wave angle ($\hat{\alpha}$), and current velocity spectra for sled run 16-6.

RUN 17-1 --- SUPERDUCK

95% χ^2 (0.73, 1.45)

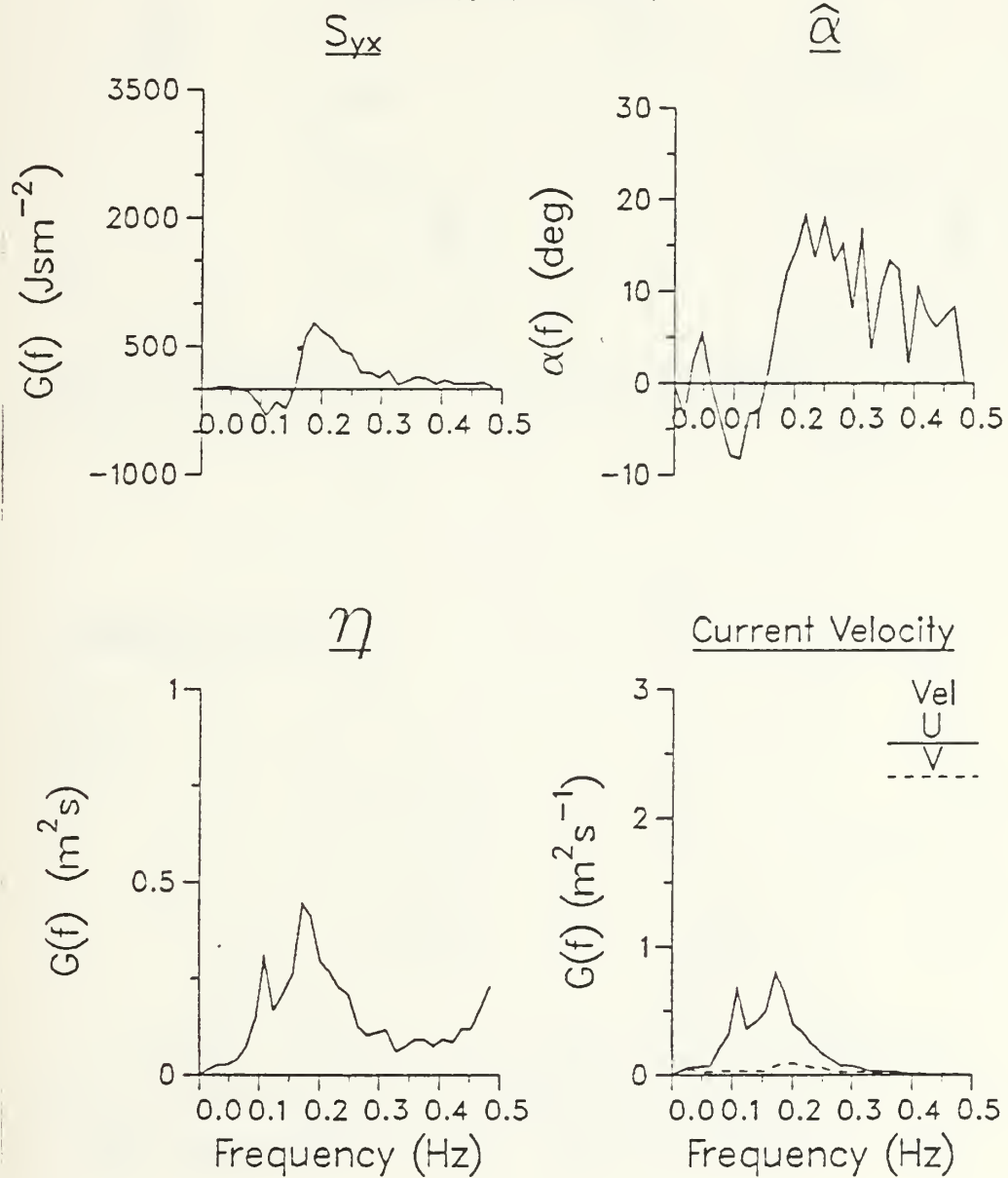


Figure 74. Radiation stress (S_{yx}), sea surface elevation (η), significant wave angle ($\hat{\alpha}$), and current velocity spectra for sled run 17-1.

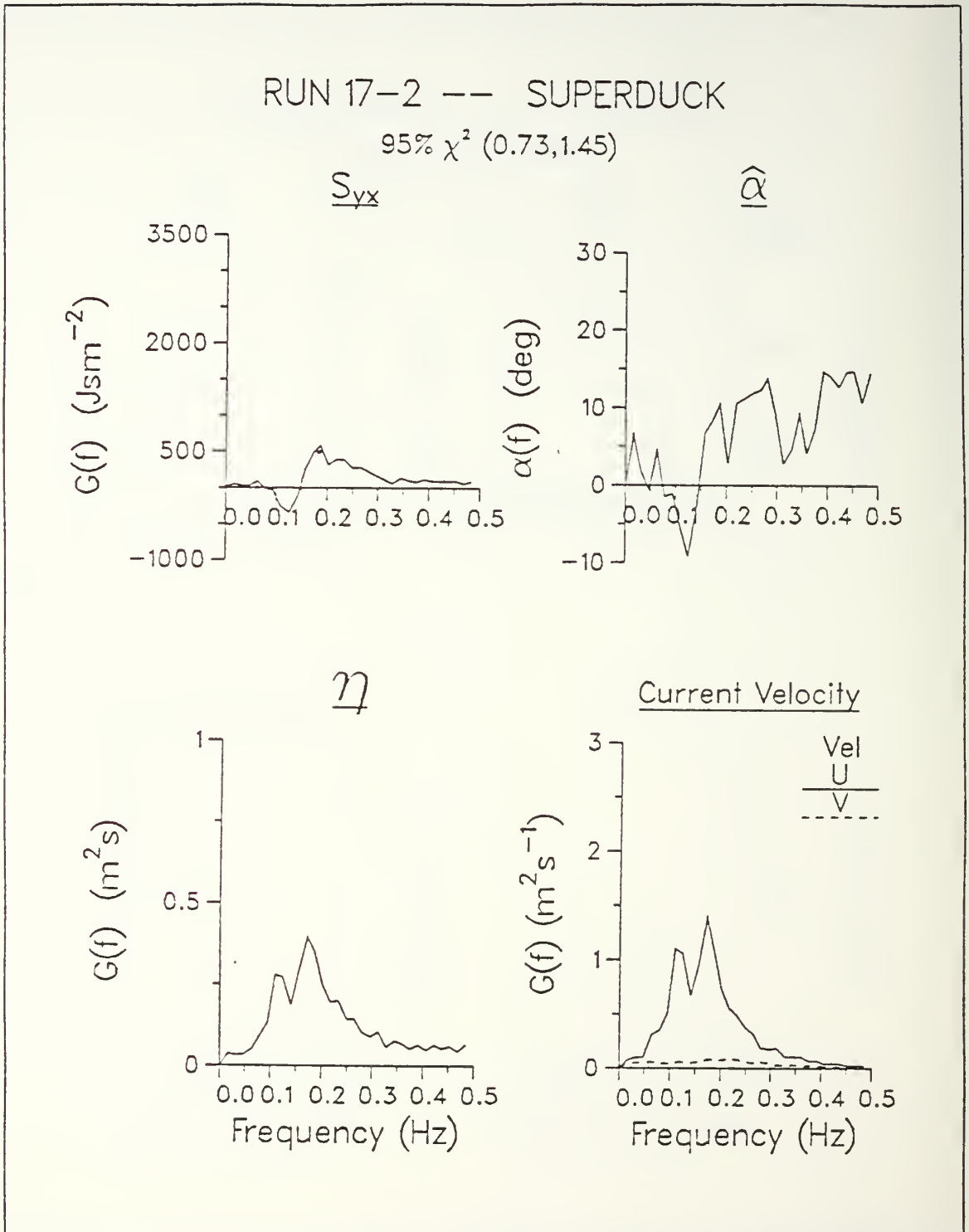


Figure 75. Radiation stress (S_{yx}), sea surface elevation (η), significant wave angle ($\hat{\alpha}$), and current velocity spectra for sled run 17-2.

RUN 17-3 --- SUPERDUCK

95% χ^2 (0.73, 1.45)

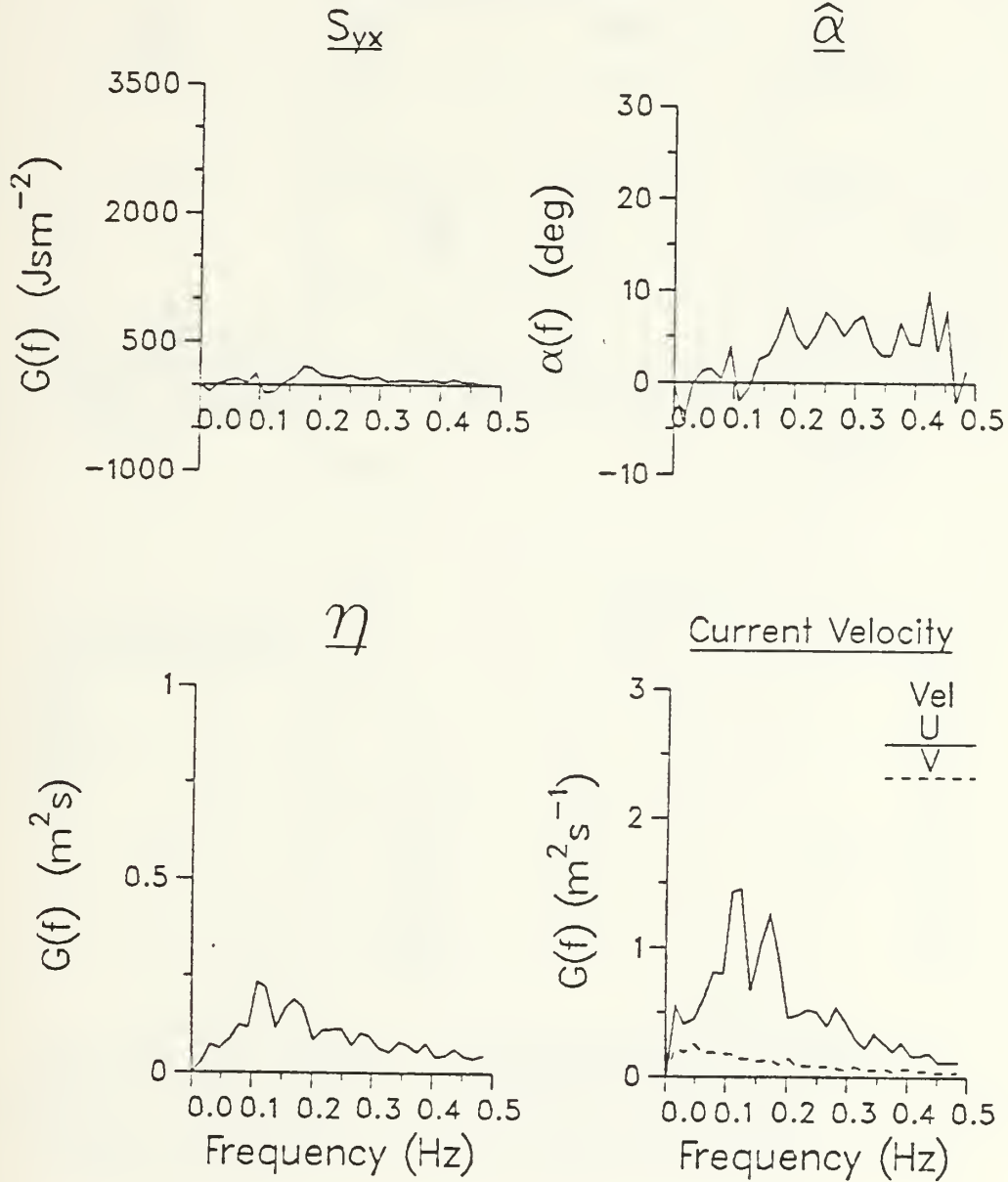


Figure 76. Radiation stress (S_{yx}), sea surface elevation (η), significant wave angle ($\hat{\alpha}$), and current velocity spectra for sled run 17-3.

RUN 17-4 -- SUPERDUCK

95% χ^2 (0.73, 1.45)

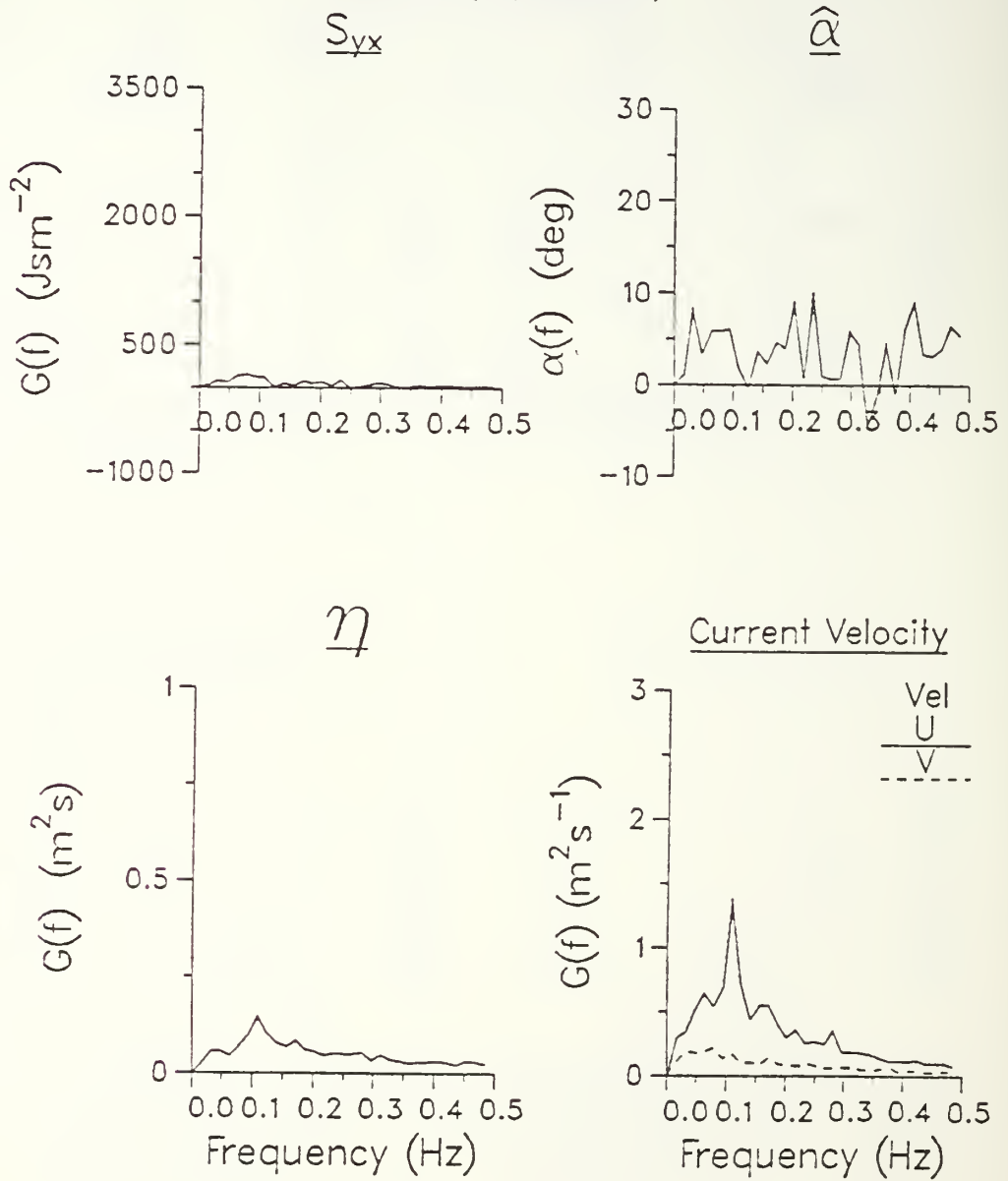


Figure 77. Radiation stress (S_{yx}), sea surface elevation (η), significant wave angle ($\hat{\alpha}$), and current velocity spectra for sled run 17-4.

RUN 17-5 -- SUPERDUCK

95% χ^2 (0.73, 1.45)

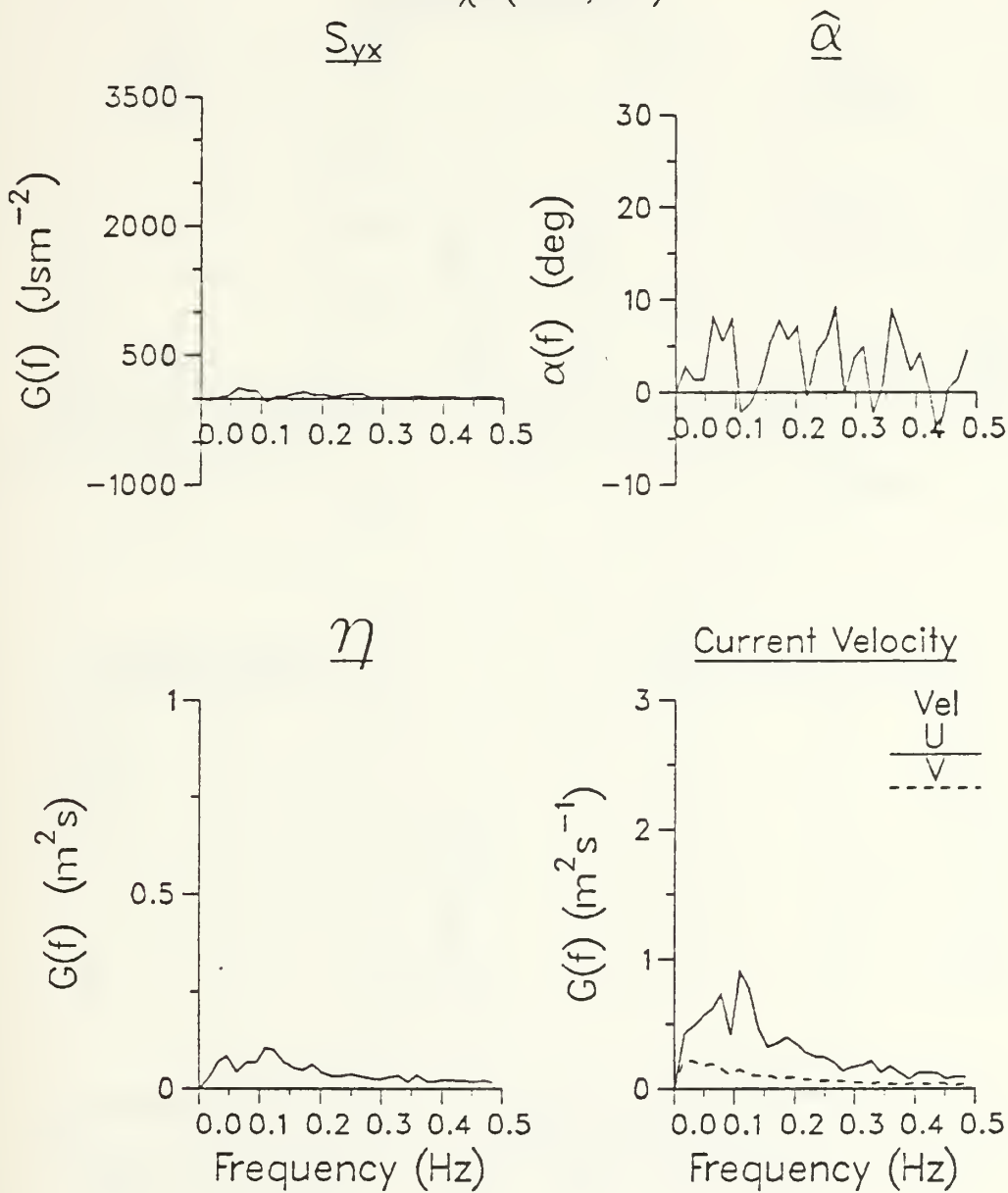


Figure 78. Radiation stress ($S_{y,x}$), sea surface elevation (η), significant wave angle ($\hat{\alpha}$), and current velocity spectra for sled run 17-5.

RUN 17-6 -- SUPERDUCK

95% χ^2 (0.73, 1.45)

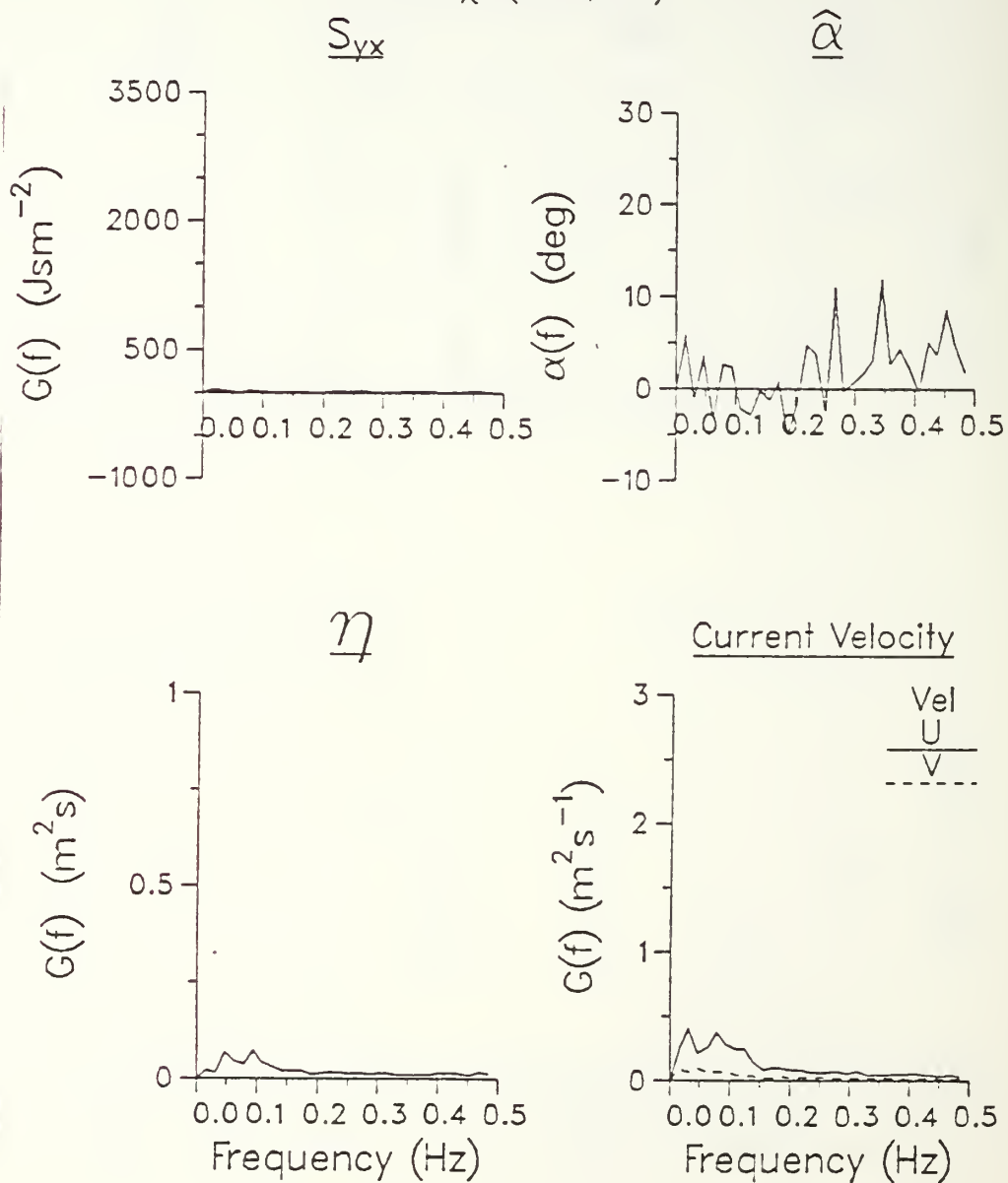


Figure 79. Radiation stress ($S_{j,x}$), sea surface elevation (η), significant wave angle ($\hat{\alpha}$), and current velocity spectra for sled run 17-6.

RUN 17-7 -- SUPERDUCK

95% χ^2 (0.73, 1.45)

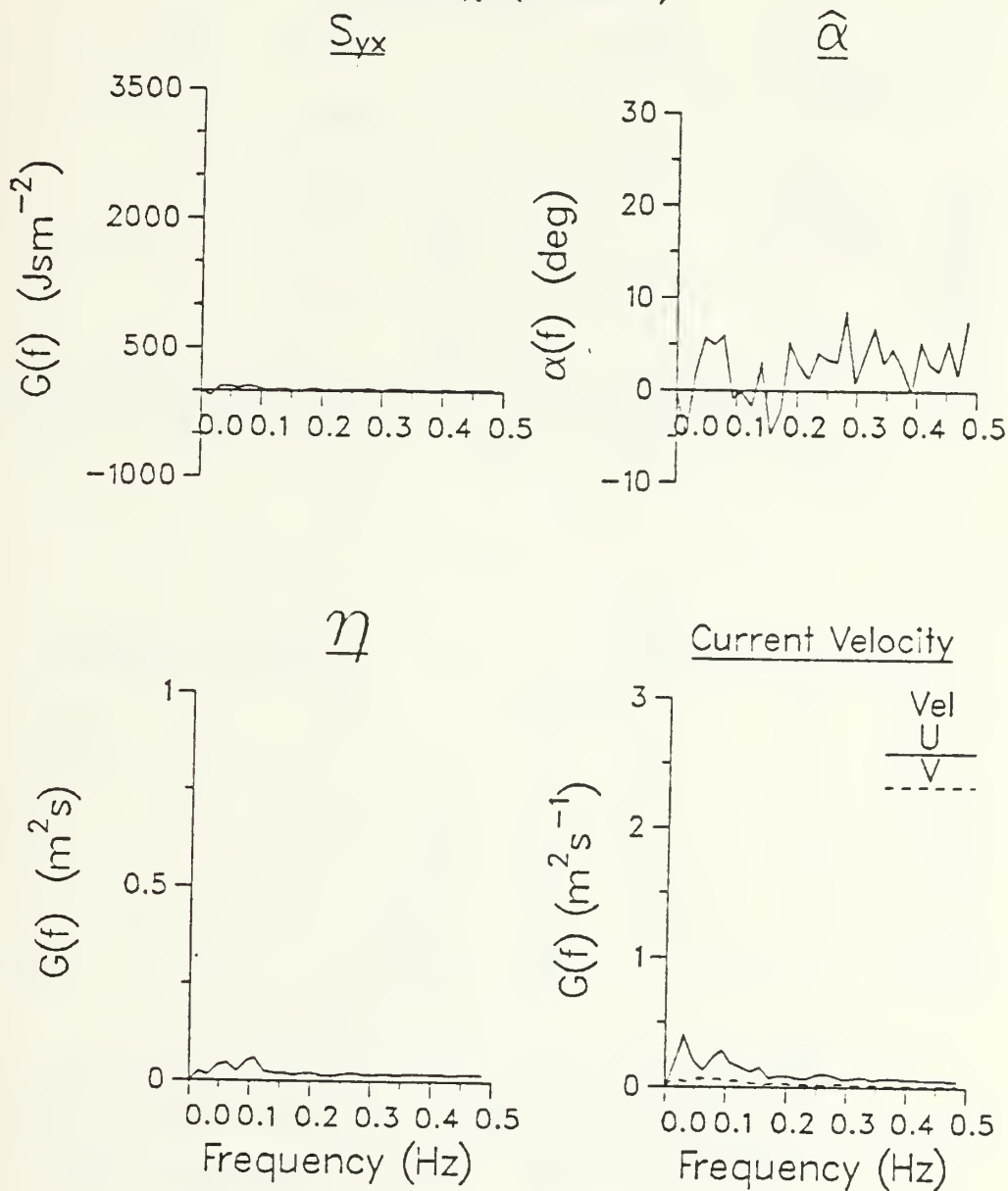


Figure 80. Radiation stress (S_{yx}), sea surface elevation (η), significant wave angle ($\hat{\alpha}$), and current velocity spectra for sled run 17-7.

RUN 17-8 -- SUPERDUCK

95% χ^2 (0.73, 1.45)

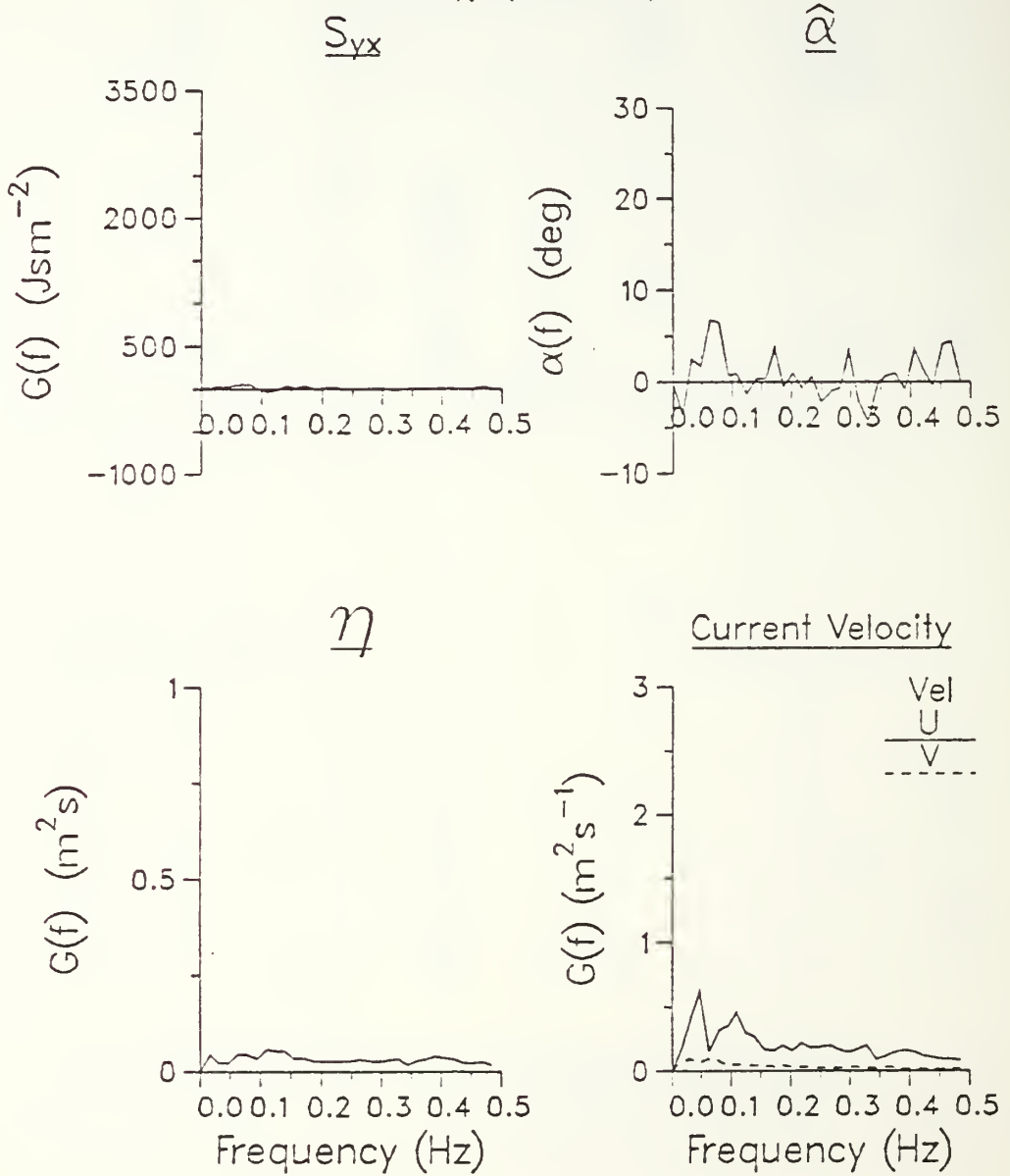


Figure 81. Radiation stress (S_{yx}), sea surface elevation (η), significant wave angle ($\hat{\alpha}$), and current velocity spectra for sled run 17-8.

RUN 18-1 --- SUPERDUCK

95% χ^2 (0.73, 1.45)

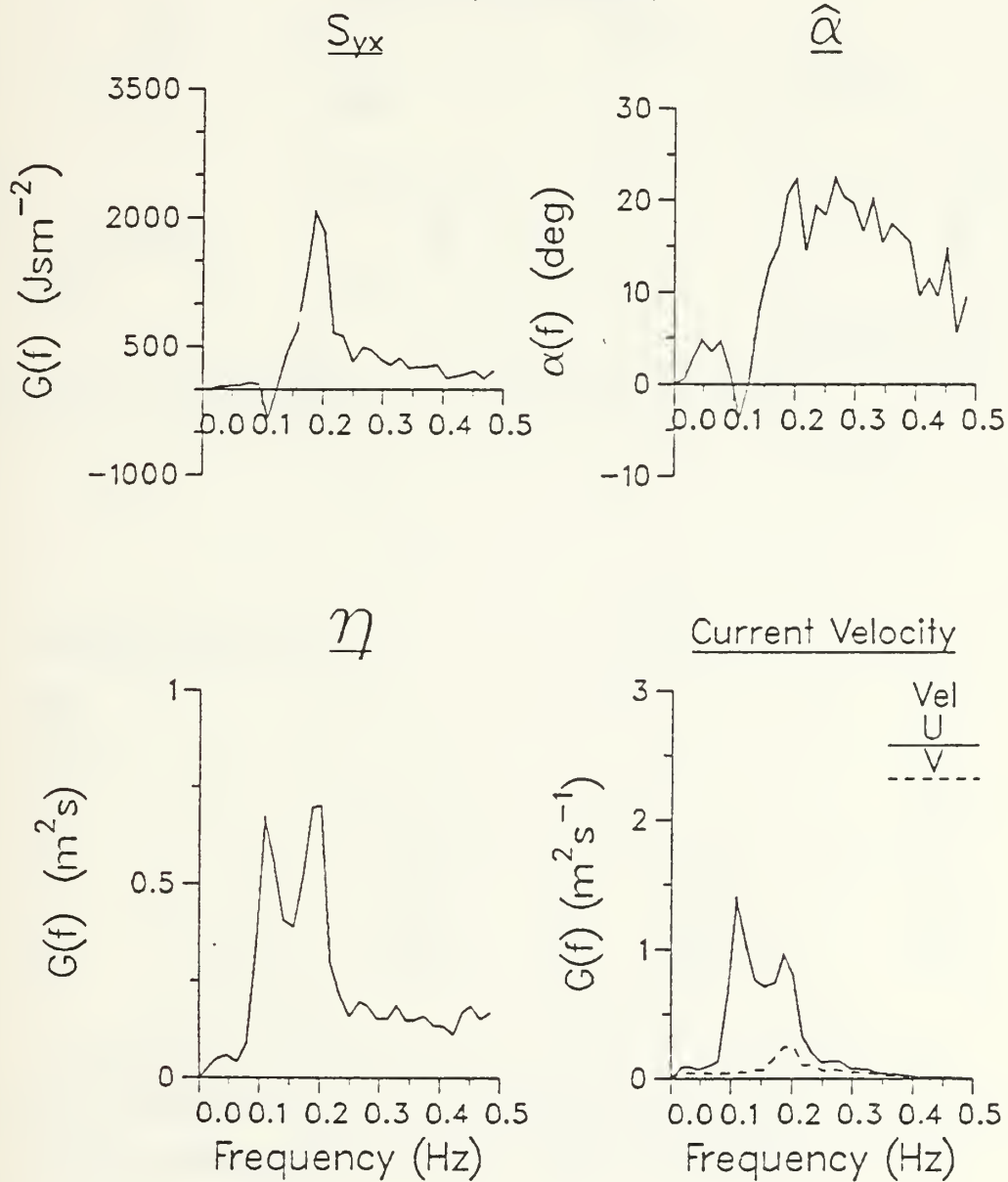


Figure 82. Radiation stress (S_{yx}), sea surface elevation (η), significant wave angle ($\hat{\alpha}$), and current velocity spectra for sled run 18-1.

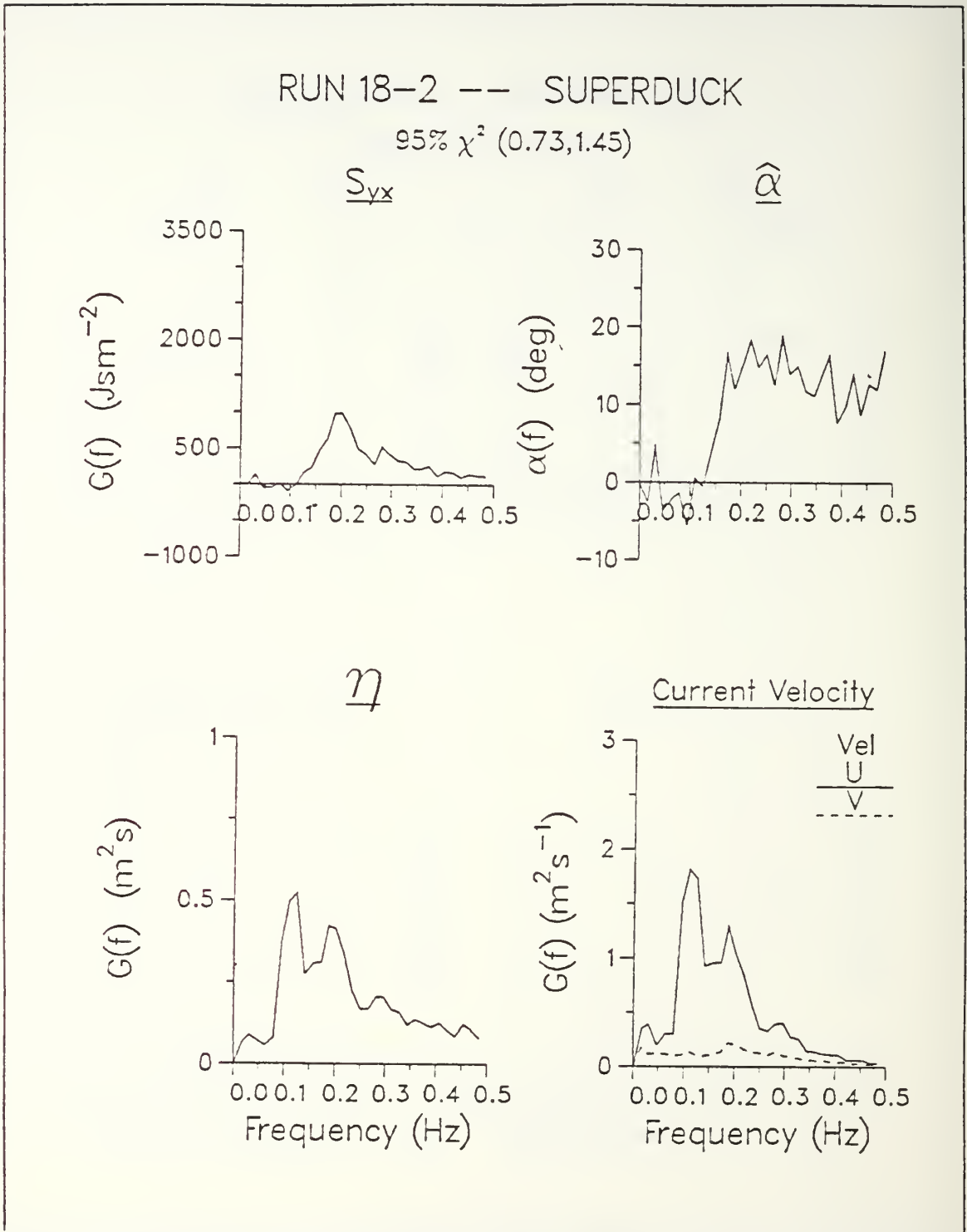


Figure 83. Radiation stress (S_{yx}), sea surface elevation (η), significant wave angle ($\hat{\alpha}$), and current velocity spectra for sled run 18-2.

RUN 18-3 --- SUPERDUCK

95% χ^2 (0.73, 1.45)

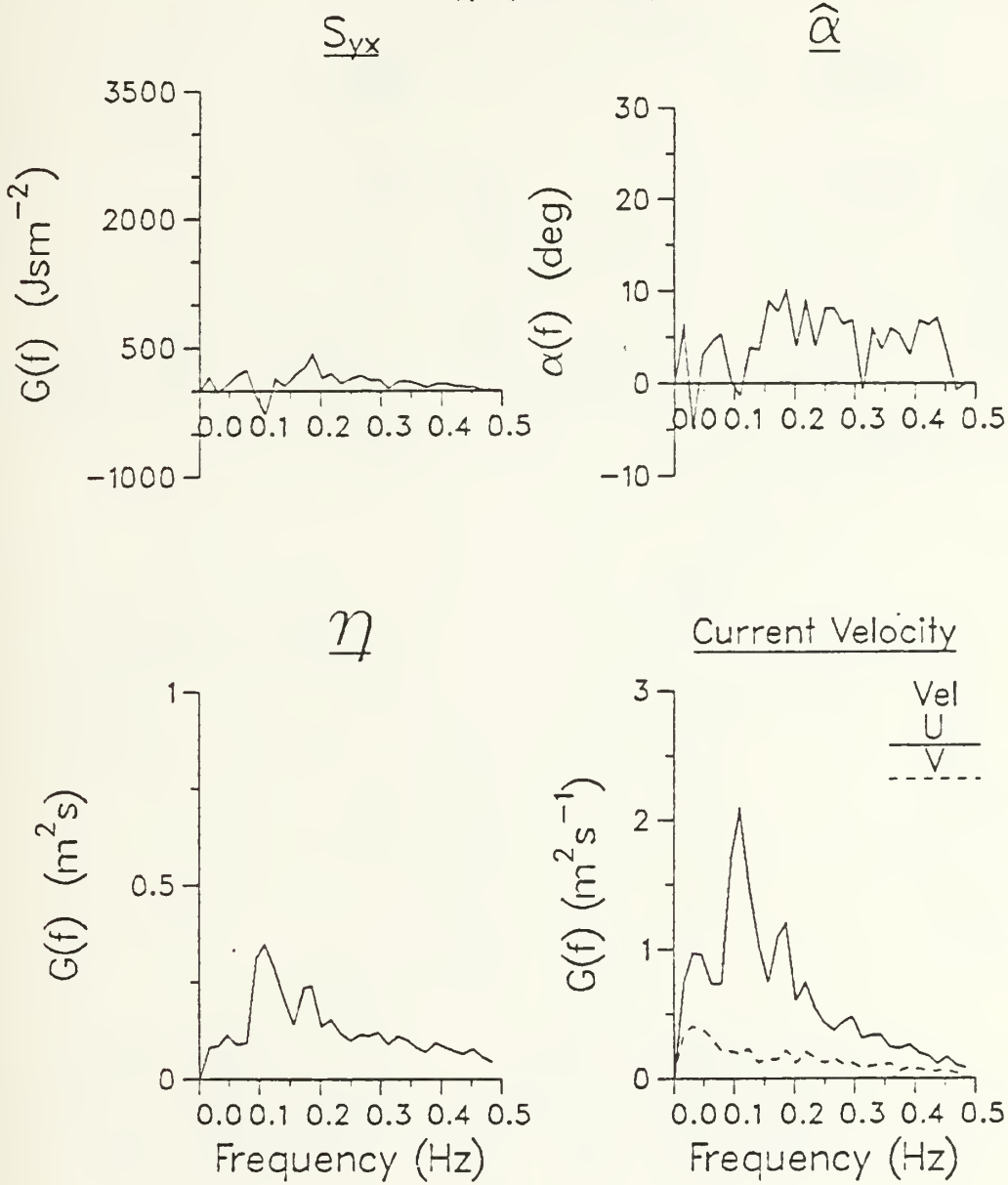


Figure 84. Radiation stress (S_{yx}), sea surface elevation (η), significant wave angle ($\hat{\alpha}$), and current velocity spectra for sled run 18-3.

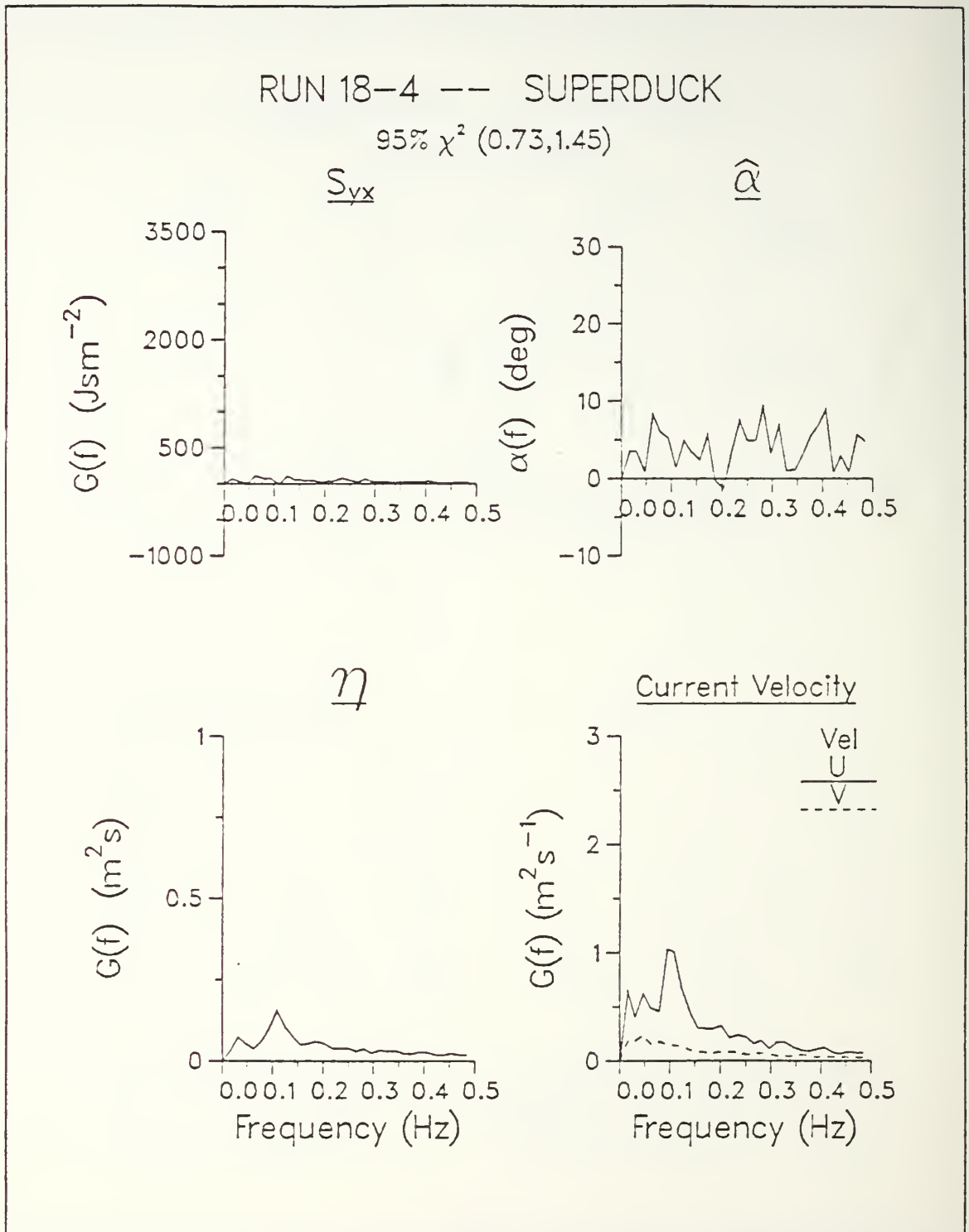


Figure 85. Radiation stress (S_{yx}), sea surface elevation (η), significant wave angle ($\hat{\alpha}$), and current velocity spectra for sled run 18-4.

RUN 18-5 --- SUPERDUCK

95% χ^2 (0.73, 1.45)

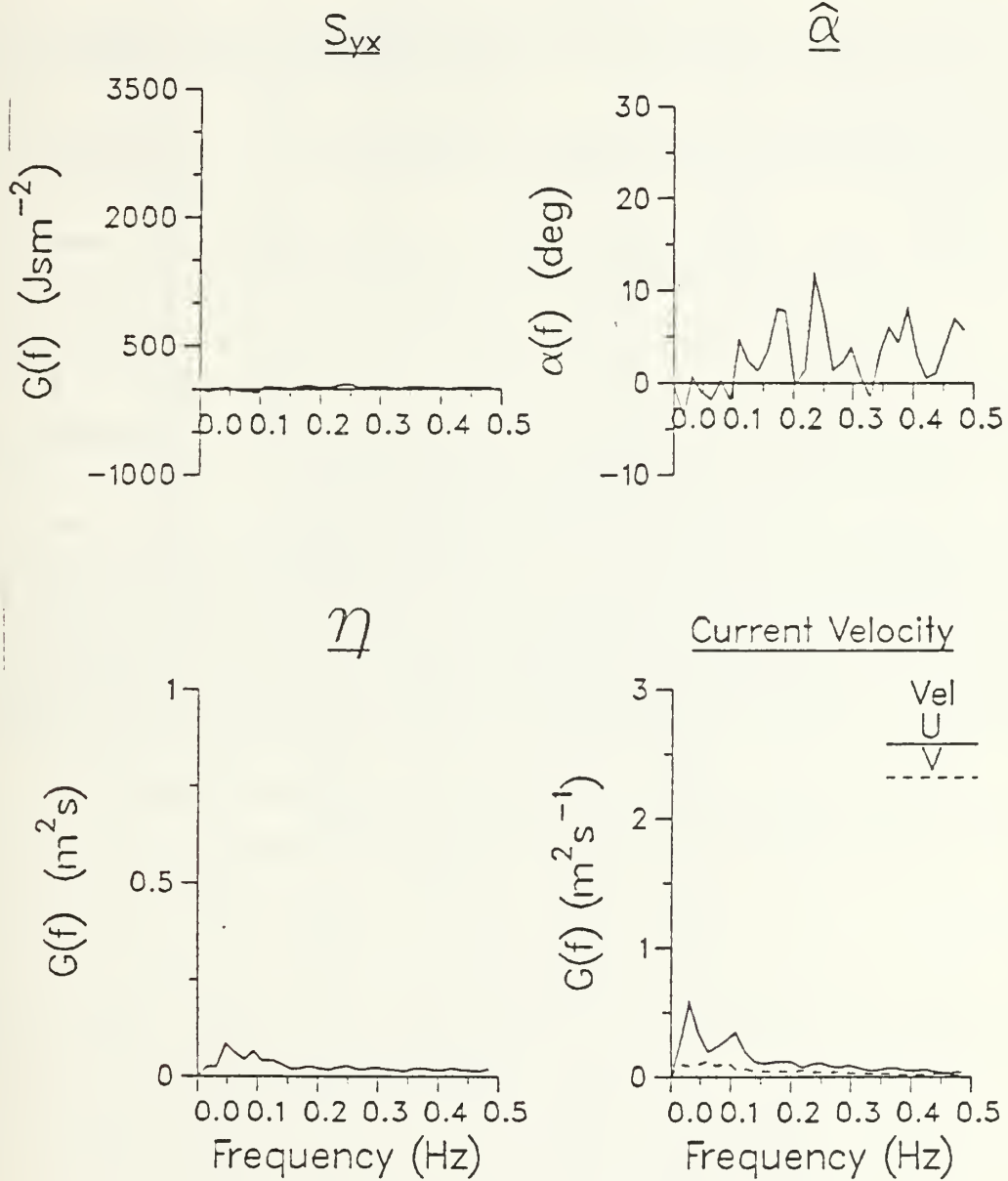


Figure 86. Radiation stress (S_{yx}), sea surface elevation (η), significant wave angle ($\hat{\alpha}$), and current velocity spectra for sled run 18-5.

APPENDIX G. MEAN CURRENT VELOCITIES AND TOTAL RADIATION STRESS FOR EACH SLED CURRENT METER AND RUN

Run	C/M 1 (mid)		C/M 2 (upper)		C/M 4 (lower)		S_{yx}^T (Jm^{-2})		
	V (ms^{-1})	U (ms^{-1})	V (ms^{-1})	U (ms^{-1})	V (ms^{-1})	U (ms^{-1})	C/M 1	C/M 4	C/M 2
111	-0.418	0.367	-0.512	0.266	-0.354	0.407			
112	-0.514	0.195	-0.588	0.155	-0.405	0.154			
113	-0.256	0.074	-0.339	0.130	-0.164	0.005			
121	0.307	0.252	0.259	0.325	0.304	0.173	-134.40	-134.40	-134.40
122	0.165	0.517	0.166	0.365	0.069	0.592	8.88	13.01	17.79
123	-0.246	0.295	-0.320	0.318	-0.189	0.193	-21.60	-8.81	-11.67
125	0.295	0.476	0.280	0.471	0.278	0.449	-66.46	-39.30	-62.55
126	0.219	0.323	0.195	0.287	0.204	0.270	-25.27	-34.55	-27.02
127	0.544	0.118	0.498	0.123	0.476	0.069	5.78	25.20	9.84
151	-0.393	0.068	-0.470	0.108	-0.396	0.153	150.00	150.00	150.00
152	-0.786	0.247	-0.830	0.141	-0.798	0.385	59.47	43.67	78.87
153	-0.773	0.207	-0.882	-0.045	-0.723	0.425	16.84	16.67	45.94
154	-0.719	0.053	-0.824	0.073	-0.669	0.130	36.62	22.32	41.41
162	-0.443	0.011	-0.532	0.052	-0.437	0.074	250.50	250.50	250.50
163	-0.985	0.040	-1.090	0.050	-0.993	0.076	153.50	143.10	156.40
164	-1.209	-0.039	-0.931	-0.320	-1.156	0.111	62.10	52.29	*
165	-1.131	-0.089	-0.892	-0.309	-1.072	0.036	48.40	47.58	*
166	-0.638	-0.008	-0.747	-0.073	-0.605	0.070	27.52	25.64	24.66
171	-0.219	-0.024	-0.301	0.025	-0.191	0.054	61.53	61.53	61.53
172	-0.270	0.015	-0.355	0.078	-0.254	0.086	53.75	53.12	51.66

173	-0.414	-0.037	-0.280	-0.291	-0.382	0.074	25.65	22.62	*
174	-0.327	-0.335	-0.144	-0.144	-0.299	-0.022	*	15.34	*
175	-0.299	-0.485	-0.114	-0.041	-0.376	-0.150	*	10.67	*
176	0.003	-0.163	-0.106	-0.144	0.023	0.028	0.95	1.95	*
177	0.031	-0.074	-0.078	-0.117	0.047	0.055	4.03	3.95	*
178	0.038	-0.045	-0.091	-0.133	0.028	0.065	3.56	1.63	*
181	-0.402	0.010	-0.479	0.060	-0.376	0.077	175.60	175.60	175.60
182	-0.703	0.050	-0.795	0.125	-0.693	0.106	122.00	122.60	129.10
183	-0.981	0.126	-0.708	-0.252	-0.978	0.227	58.04	41.20	*
184	-0.778	-0.290	-0.198	-0.092	-0.896	0.073	*	14.04	*
185	-0.622	-0.022	-0.419	-0.181	-0.554	0.123	3.02	4.39	*
186	-0.651	0.054	-0.748	0.075	-0.656	0.118			
211	-0.023	0.033	-0.086	0.107	-0.012	0.119	-6.82	-6.82	-6.82
212	-0.002	0.209	-0.071	-0.063	0.010	0.331	20.18	27.38	*
213	-0.120	0.240	-0.177	0.218	-0.098	0.343	-22.19	-16.32	-14.64
214	-0.256	0.112	-0.313	0.096	-0.276	0.252	0.83	2.71	2.67
215	-0.183	0.106	-0.285	0.176	-0.121	0.190	11.20	13.86	9.56
216	0.003	-0.053	-0.068	-0.007	0.005	0.064	4.20	4.20	4.20
217	0.060	-0.263	-0.082	-0.228	0.083	-0.036	*	3.44	*
218	-0.150	-0.037	-0.204	-0.140	-0.156	0.171	7.63	3.83	6.93
219	-0.125	0.115	-0.128	-0.042	-0.087	0.173	-11.35	-4.10	1.84

* indicates current meter was not underwater for entire data run

REFERENCES

- Allender, J. H. and J. D. Ditmars, 1981: Field measurements of longshore currents on a barred beach. *Coastal Engr.*, 5, 295-309.
- Amorochio, J. and J. J. DeVries, 1980: A new evaluation of the wind stress coefficient over water surfaces. *J. Geophys. Res.*, 85(C1), 433-442.
- Barry, B. A., 1978: *Errors in Practical Measurement in Science, Engineering, and Technology*. John Wiley and Sons, NY, 183 pp.
- Basco, D. R., 1982: *Surf Zone Currents, Vol. I, State of Knowledge*. U.S. Army Corps of Engineers, Coastal Engr. Res. Ctr. Misc. Rpt. 82-7 (I), Ft. Belvoir, VA.
- Battjes, J. A., 1972a: Set-up due to irregular waves. *Proc. 13th Intl. Coastal Engr. Conf.*, ASCE, 1993-2004.
- _____, 1972b: Radiation stresses in short-crested waves. *J. Mar. Res.*, 30, 56-64.
- _____ and J. P. F. M. Janssen, 1978: Energy loss and set-up due to breaking of random waves. *Proc. 16th Intl. Coastal Engr. Conf.*, ASCE, 569-578.
- _____ and M. J. F. Stive, 1985: Calibration and verification of a dissipation model for random breaking waves. *J. Geophys. Res.*, 90(C5), 9159-9167.
- Baum, S. K. and D. R. Basco, 1987: A numerical investigation of the longshore current profile for multiple bar trough beaches. *Proc. 20th Intl. Coastal Engr. Conf.*, ASCE, accepted for publication.
- Bakker, W. T. and T. Van Dorn, 1978: Near bottom velocities in waves with a current. *Proc. 16th Intl. Coastal Engr. Conf.*, ASCE, 1394-1413.
- Birkemeier, W. A. and R. A. Dalrymple, 1975: Nearshore water circulation induced by wind and waves. *Proc. Symposium on Modeling Technique*, ASCE, 1062-1081.
- _____ and C. Mason, 1984: The CRAB: a unique nearshore surveying vehicle. *J. Surveying Engineering*, 110(1), 1-7.
- _____, H. C. Miller, S. D. Wilhelm, A. E. DeWall, and C. S. Gorbics, 1985: *A User's Guide to the Coastal Engineering Research Center's (CERC's) Field Research Facility*. U. S. Army Corps of Engineers, Waterways Experiment Station, Coastal Engr. Rsch. Ctr., Field Rsch. Facility, Instruction Rpt. CERC-85-1, Vicksburg, MS, 121 pp.
- Bodge, K. R. and R. G. Dean, 1984: Wave measurement with differential pressure gauges. *Proc. 19th Intl. Coastal Engr. Conf.*, ASCE, 755-769.
- Bowen, A. J., 1969: The generation of longshore currents on a plane beach, *J. Mar. Res.*, 27, 206-215.

- Bouws, E., H. Gunther, W. Rosenthal, and C. L. Vincent, 1985: Similarity of the wind wave spectrum in finite depth water, 1. Spectral Form. *J. Geophys. Res.*, 90(C1), 975-986.
- Bretschneider, C. L. and R. O. Read, 1954: *Changes in Wave Height Due to Bottom Friction, Percolation, and Refraction*. Beach Erosion Board, U. S. Army Corps of Engineers, Tech. Memo. 45.
- Businger, J. A., Wyngaard, J. C., and Y. Izumi, 1971: Flux profile relationships in the atmospheric surface layer. *J. Atmos. Sci.*, 28, 181-189.
- Byrne, H. M., 1982: *The variation of the drag coefficient in the marine surface layer due to temporal and spatial variations in the wind and sea state*. Ph.D. Dissertation, Univ. of Washington, Seattle, 118 pp.
- Carter, D. J. T., 1982: Prediction of wave height and period for a constant wind velocity using the JONSWAP results. *Ocean Engng.*, 9(1), 17-33.
- Collins, J. I., 1970: Probabilities of breaking wave characteristics. *Proc. 13th Intl. Coastal Engr. Conf.*, ASCE, 399-412.
- _____, 1972: *Longshore Currents and Wave Statistics in the Surf Zone*. Rpt. No. TC-149-2, Tetra Tech, Inc., Pasadena, CA.
- Crowson, R. A., W. A. Birkemeir, H. M. Klein, and H. C. Miller, 1988: *SUPERDUCK Nearshore Processes Experiment: Summary of Studies*. U.S. Army Corps of Engineers, Waterways Experiment Station, Coastal Engr. Rsch. Ctr., Field Rsch. Facility, Tech. Rpt., Vicksburg, MS. (in press)
- Davidson, K. L., P. J. Boyle, S. R. Fellbaum, and J. Mundy, 1988a: Atmospheric surface and mixed layer properties observed from ships in FASINEX. *Proc. 7th AMS Conf. on Air-sea Interaction*, Anaheim, CA, 161-165.
- Davidson, K. L., W. J. Shaw, and W. G. Large, 1988b: Wind stress results from multi-platform and multi-sensor measurements in FASINEX. *Proc. 7th AMS Conf. on Air-sea Interaction*, Anaheim, CA, 132-136.
- Davis, J. C., 1986: *Statistics and Data Analysis in Geology*. 2nd. ed., John Wiley and Sons, NY, 646 pp.
- Detle, H. H., 1974: *Field study of longshore currents*. Braunschweig. Technischen Universitat. Leichtweiss-Institut fur Wasserbau. Mitteilungen 41, in German with English abstract. (abstract)
- Detle, H. H. and A. Fuhrboter, 1974: Field investigations in surf zones. *Proc. 14th Intl. Coastal Engr. Conf.*, ASCE, 518-537.
- Fox, W. T. and R. A. Davis, 1973: Simulation model for storm cycles and beach erosion on Lake Michigan. *Geol. Soc. Am. Bull.*, 84, 1769-1790.
- Freilich, M. H. and S. S. Pawka, 1987: Statistics of S_{xy} estimates. *J. Phys. Oceanogr.*, 17, 1786-1797.

- Garratt, J. R., 1977: Review of C_d over oceans and continents. *Mon. Wea. Rev.*, 105, 915-929.
- Geernaert, G. L. and K. B. Katsaros, 1986: Incorporation of stratification effects on the oceanic roughness length in the derivation of the neutral drag coefficient. *J. Phys. Oceanogr.*, 16, 1580-1584.
- _____, _____, and K. Richter, 1986: Variation of the drag coefficient and its dependence on sea state. *J. Geophys. Res.*, 91(C6), 7667-7679.
- _____, B. J. Byars, K. L. Davidson, S. E. Larsen, and T. Mikkelsen, 1987a: *Measurements of the drag coefficient during the Tower Ocean Wave and Radar Experiment.* (submitted for publication)
- _____, Larsen, S. E., and F. Hansen, 1987b: Measurements of the wind stress, heat flux, and turbulence intensity during storm conditions over the North Sea. *J. Geophys. Res.*, 92(C12), 13127-13139.
- Gerald, C. F., 1978: *Applied Numerical Analysis*. 2nd. ed., Addison-Wesley, Reading, MA. 518 pp.
- Grant, W. D. and O. S. Madsen, 1979: Combined wave and current interaction with a rough bottom. *J. Geophys. Res.*, 84(C4), 1797-1808.
- _____ and _____, 1982: Moveable bed roughness in unsteady oscillatory flow. *J. Geophys. Res.*, 87(C1), 469-481.
- _____, A. J. Williams, III, and S. M. Glenn, 1984: Bottom stress estimates and their prediction on the northern California continental shelf during CODE-1: The importance of wave current interaction. *J. Phys. Oceanogr.*, 14, 506-527.
- Greenwood, B. and D. J. Sherman, 1983: Shore-parallel flows in a barred nearshore. *Proc. 18th Intl. Coastal Engr. Conf.*, ASCE, 1677-1698.
- _____ and D. J. Sherman, 1986: Longshore current profiles and lateral mixing across the surf zone of a barred nearshore. *Coastal Engr.*, 10, 149-168.
- Guza, R. T., M. C. Clifton, and F. Rezvani, 1986a: *Intercomparisons of Electromagnetic Current Meters in the Nearshore.* Paper presented at Am. Geophys. Union, Fall Mtg., Dec. 9, San Fran., CA.
- _____, and E. B. Thornton, 1978: Variability of longshore currents. *Proc. 16th Intl. Coastal Engr. Conf.*, ASCE, 756-775.
- _____ and _____, 1980: Local and shoaled comparisons of sea surface elevations, pressures, and velocities. *J. Geophys. Res.*, 85(C3), 1524-1530.
- _____, _____ and N. Christensen, Jr., 1986b: Observations of steady longshore currents in the surf zone. *J. Phys. Oceanogr.*, 16(11), 1959-1969.
- Haltiner and Martin, 1957: *Dynamical and Physical Meteorology*. McGraw-Hill, NY, 470 pp.

- Hasselmann, K. and J. I. Collins, 1968: Spectral dissipation of finite depth gravity waves due to turbulent bottom friction. *J. Mar. Res.*, 26, 1-12.
- _____, D. B. Ross, P. Muller, and W. Sell, 1976: A parametrical wave prediction model. *J. Phys. Oceanogr.*, 6, 201-228.
- Haugen, D. A., 1973: *Workshop on Micrometeorology*. Amer. Meteor. Soc., Boston, MA, 392 pp.
- Higgins, A. L., R. J. Seymour, and S. S. Pawka, 1981: A compact representation of ocean wave directionality. *Appl. Ocean. Res.*, 3, 105-112.
- Hsiao, B. A., and O. H. Shemdin, 1978: Bottom dissipation in finite depth water waves. *Proc. 16th Intl. Coastal Engr. Conf.*, ASCE, 434-448.
- Hsu, S. A., 1970: The shear stress of sea breeze on a swash zone. *Proc. 12th Intl. Coastal Engr. Conf.*, ASCE, 243-255.
- _____, 1973: Wind stress on a coastal water surface. *Proc. 13th Intl. Coastal Engr. Conf.*, ASCE, 2531-2541.
- _____, 1974: A dynamic roughness equation and its application to wind stress determination at the air-sea interface. *J. Phys. Oceanogr.*, 4, 116-120.
- _____, 1986a: A mechanism for the increase of wind stress (drag) coefficient with wind speed over water surfaces: a parametric model. *J. Phys. Oceanogr.*, 16, 144-150.
- _____, 1986b: Correction of land-based wind data for offshore applications: A further evaluation. *J. Phys. Oceanogr.*, 16, 390-394.
- _____, 1987: Determination of wind stress (drag) coefficient for coastal waters under various meteorological and oceanographic conditions. *Proc. 20th Intl. Coastal Engr. Conf.*, ASCE, paper accepted for publication.
- Hubertz, J. M., 1986: Observations of local wind effects on longshore currents. *Coastal Engr.*, 10, 275-288.
- Hughes, S. A., 1984: *The TMA Shallow-water Spectrum Description and Applications*. U. S. Army Corps of Engineers, Coastal Engr. Res. Ctr., Tech. Rpt. CERC-84-7, Vicksburg, MS. 39 pp.
- Huntley, D. A., 1976: Lateral and bottom forces on longshore currents. *Proc. 15th Intl. Coastal Engr. Conf.*, ASCE, 645-659.
- _____ and A. J. Bowen, 1975: Comparison of the hydrodynamics of steep and shallow beaches. In *Nearshore Sediment Dynamics and Sedimentation*, John Wiley and Sons, NY, 69-109.
- Huschke, R. E., 1959: *Glossary of Meteorology*. Amer. Meteor. Soc., Boston, MA, 638 pp.

- Inman D. L. and R. A. Bagnold, 1963: Littoral processes. In *The Sea*, 3, Interscience Pub., NY, 529-553.
- _____ and W. H. Quinn, 1951: Currents in the surf zone. *Proc. 2nd Intl. Coastal Engr. Conf.*, ASCE, 24-36.
- Iwagaki, Y. and T. Kakinuma, 1967: On the bottom friction factors off five Japanese coasts. *Coastal Engr. in Japan*, 10, 13-22.
- James, I. D., 1972: *Some Nearshore Effects of Ocean Waves*. Ph.D. Thesis (abstract), No. 8258, Univ. of Cambridge, Cambridge, England.
- _____, 1974a: Non-linear waves in the nearshore region: shoaling and set-up. *Estuarine and Coastal Marine Science*, 2 (3), 207-234. (author's abstract)
- _____, 1974b: A non-linear theory of longshore currents. *Estuarine and Coastal Marine Science*, 2 (3), 235-249. (author's abstract)
- Jenkins, G. M. and D. G. Watts, 1968: *Spectral Analysis and its Applications*. Holden-Day, Oakland, CA, 525 pp.
- Johns, B. and R. J. Jefferson, 1980: The numerical modeling of surface wave propagation in the surf zone. *J. Phys. Oceanogr.*, 10, 1061-1069.
- Johnson, D. W., 1919: *Shore Processes and Shoreline Development*. John Wiley and Sons, NY, 584 pp.
- Jonsson, I. G., 1966: Wave boundary layers and friction factors. *Proc. 10th Intl. Coastal Engr. Conf.*, ASCE, 127-148.
- Jonsson, I. G., O. Skovgaard, and T. S. Jacobsen, 1974: Computation of longshore currents. *Proc. 14th Intl. Coastal Engr. Conf.*, ASCE, 699-714.
- Kamphius, J. W., 1975: Friction factor under oscillatory waves. *J. Waterways, Harbors, Coastal Engr. Div.*, 101, 135-144.
- Kinsman, B., 1965: *Wind Waves, Their Generation and Propagation on the Ocean Surface*. Prentice-Hall, Englewood Cliffs, NJ, 676 pp.
- Kitaigorodskii, S. A., V. P. Krasitsjii, and M. M. Zaslavskii, 1975: On Phillips theory of equilibrium range in the spectra of wind-generated gravity waves. *J. Phys. Oceanogr.*, 5, 410-420.
- Komar, P. D., 1975: Nearshore currents: Generation by obliquely incident waves and longshore variations in breaker height. In *Nearshore Sediment Dynamics and Sedimentation*, J. Hails and A. Carr, eds., Wiley and Sons, Inc., NY, 17-45.
- _____, 1976: Nearshore currents. In *Beach Processes and Sedimentation*, 1st ed., Prentice-Hall, Englewood Cliffs, NJ, 429 pp.
- Kraus, N. C. and T. O. Sasaki, 1979: Influence of wave angle and lateral mixing on the longshore current. *Marine Science Comm.*, 5(2), 91-126.

- Large, W. G. and S. Pond, 1981: Open ocean momentum flux measurements in moderate to strong winds. *J. Phys. Oceanogr.*, *11*, 324-336.
- Liu, P. L. F. and R. A. Dalrymple, 1978: Bottom frictional stresses and longshore currents due to waves with large angles of incidence. *J. Mar. Res.*, *36*(2), 357-375.
- Longuet-Higgins, M. S., 1970a: Longshore currents generated by obliquely incident sea waves, 1. *J. Geophys. Res.*, *75*, 6778-6789.
- _____, 1970b: Longshore currents generated by obliquely incident sea waves, 2. *J. Geophys. Res.*, *75*, 6790-6801.
- _____, 1972a: Recent progress in the study of longshore currents. In *Waves on Beaches and Resulting Sediment Transport*, R. E. Meyer, ed., 1st ed., Academic Press, NY, 203-248.
- _____, 1972b: The mechanics of the surf zone. *Proc. 13th Intl. Congress of Theoretical and Appl. Mech.*, E. Becker and G. K. Mikhailov, eds., Moscow Univ., 213-228. (abstract)
- _____ and R. W. Stewart, 1960: Changes in the form of short gravity waves and tidal currents. *J. Fluid Mech.*, *8*, 565-583.
- _____ and _____. 1961: The changes in amplitude of short gravity waves on steady non-uniform currents. *J. Fluid Mech.*, *10*, 529-549.
- _____ and _____. 1962: Radiation stress and mass transport in gravity waves, with application to "surf beat." *J. Fl. Mech.*, *13*, 481-504.
- _____ and _____. 1963: A note on wave set-up. *J. Fluid Mech.*, *21*, 4-10.
- _____ and _____. 1964: Radiation stress in water waves; a physical discussion, with applications. *Deep Sea Res.*, *11*, 529-562.
- Losada, M. A., A. Sanchez-Arcilla, and C. Vidal, 1987: Another approach to longshore current evaluation. *Proc. 20th Intl. Coastal Engr. Conf.*, ASCE, accepted for publication.
- Lowe, R. L., D. L. Inman, and B. M. Brush, 1972: Simultaneous data system for instrumenting the shelf. *Proc. 13th Intl. Coastal Engr. Conf.*, ASCE, 95-112.
- Lundgren, H., 1972: Turbulent currents in the presence of waves. *Proc. 13th Intl. Coastal Engr. Conf.*, ASCE, 623-634.
- Madsen, O. S., D. W. Ostendorf, and A. S. Reynolds, 1978: A longshore current model. *Symposium on Technical, Environmental, Socioeconomic and Regulatory Aspects of Coastal Zone Management*, ASCE, V3, 2332-2341.
- Martens, D. E. and E. B. Thornton, 1987: Nearshore zone monitoring system. *Proc. Coastal Hydrodynamics Conf.*, ASCE, in publication.

- Meadows, G. A., 1976: Time dependent fluctuations in longshore currents. *Proc. 15th Intl. Coastal Engr. Conf.*, ASCE, 660-680.
- Meadows, G. A., 1978: *A Field Investigation of the Spatial and Temporal Structure of Longshore Currents*. Great Lakes Coastal Res. Lab., Purdue Univ., Tech Rpt. 6, 167 pp.
- Mei, C. C., 1983: *The Applied Dynamics of Ocean Surface Waves*. John Wiley and Sons, NY, 740 pp.
- Melville, W. K., 1977: Wind stress and roughness length over breaking waves. *J. Phys. Oceanogr.*, 7, 702-710.
- Miller, I. and J. E. Freund, 1985: *Probability and Statistics for Engineers*. 2nd. ed., Prentice Hall, Inc., Englewood Cliffs, NJ, 530 pp.
- Nummedal, D. and R. J. Finley, 1978: Wind-generated longshore currents. *Proc. 16th Intl. Coastal Engr. Conf.*, ASCE, 1428-1438.
- Panofsky, H. A. and J. A. Dutton, 1984: *Atmospheric Turbulence, Models and Methods for Engineering Applications*. John Wiley and Sons, NY, 397 pp.
- Paulson, C., 1970: The mathematical representation of windspeed and temperature profiles in the unstable atmospheric surface layer. *J. Appl. Met.*, 9, 857-861.
- Phillips, O. M., 1977: *Dynamics of the Upper Ocean*. Cambridge Univ. Press, NY, 2nd ed., 336 pp.
- Pierson, W. J. and L. Moskowitz, 1964: A proposed spectral form for fully developed wind seas based on the similarity theory of S. A. Kitaigorodskii. *J. Geophys. Res.*, 69, 5181-5190.
- Putnam, J. A. and J. W. Johnson, 1949: The dissipation of wave energy by bottom friction. *Trans. Amer. Geophys. Union*, 30(1), 67-74.
- _____, W. H. Munk, and M. A. Traylor, 1949: The prediction of longshore currents. *Trans. Amer. Geophys. Union*, 30, 337-345.
- Roll, H. U., 1965: *Physics of the Marine Atmosphere*. Academic Press, NY, 426 pp.
- Safaie, B., 1984: Wind stress at air-water interface. *J. Waterway, Port, Coastal and Ocean Engr.*, 110(2), 287-293.
- Sallenger, A. H., Jr. and R. A. Holman, 1985: Wave energy saturation on a natural beach of variable slope. *J. Geophys. Res.*, 90(C6), 11939-11944.
- Schlichting, H., 1968: *Boundary Layer Theory*. McGraw-Hill, NY, 6th ed., 742 pp.
- SethuRaman, S., M. J. Kang, C. E. Long, and J. M. Hubertz, 1987: *SUPERDUCK Marine Meteorological Experiment, Data Summary Report, Vol. I (Mean Values) and Vol. II (Turbulence Parameters)* U. S. Army Corps of Engineers, Coastal Engr. Rsch.

- Ctr., Waterways Experiment Station, Vicksburg, MS. (preliminary report, not yet published)
- Sheng, Y. P., W. Lick, R. T. Gedney, and F. B. Molls, 1978: Numerical computation of three-dimensional circulation in Lake Erie: A comparison of a free-surface model and a rigid-lid model. *J. Phys. Oceanogr.*, 8, 713-727.
- Smith, J. D., 1977: Modeling of sediment transport on continental shelves. In *The Sea*, 6, Wiley, NY, 538-578.
- Smith, S. D., 1980: Wind stress and heat flux over the ocean during gale force winds. *J. Phys. Oceanogr.*, 10, 709-726.
- Sonu, C. J., 1975: *Computer Prediction of Nearshore and Surf Zone Statistics*. Tetra Tech. Inc., Rpt. No. 7C-394, 85 pp.
- Stive, M. J. F. and H. J. de Vriend, 1987: Quasi-3D nearshore current modelling: Wave-induced secondary current. *Proc. Coastal Hydrodynamics Conf.*, ASCE, Univ. of Del., 356-370.
- Svendsen, I. A., J. B. Hansen, and H. A. Schaffer, 1987: Analysis of cross-shore circulation on a beach. *Proc. Coastal Hydrodynamics Conf.*, ASCE, Univ. of Del., 508-520.
- Taylor, G. I., 1916: Skin friction of the wind on the Earth's surface. *Proc. Roy. Soc. London*, A92, 196-199.
- Thompson, E. F. and C. L. Vincent, 1983: Prediction of wave height in shallow water. *Proc. Coastal Structures '83*, ASCE, 1000-1008.
- Thornton, E. B., 1970: Variation of longshore currents across the surf zone. *Proc. 12th Intl. Coastal Engr. Conf.*, ASCE, 291-308.
- _____ and R. T. Guza, 1981: Longshore currents and bed shear stress. *Proc. Directional Wave Spectra Applic. Conf.*, ASCE, Berkeley, CA, 147-164.
- _____ and _____, 1982: Energy saturation and phase speeds measured on a natural beach. *J. Geophys. Res.*, 87, 4931-4938.
- _____ and _____, 1983: Transformation of wave height distribution. *J. Geophys. Res.*, 88, 5925-5938.
- _____ and _____, 1986: Surf zone longshore currents and random waves: field data and models. *J. Phys. Oceanogr.*, 16(7), 1165-1178.
- Vitale, P., 1979: Sand bed friction factors for oscillatory flows. *J. Waterway, Port, Coastal and Ocean Div.*, 105 (WW3), ASCE, 229-245.
- Vugts, H. F. and F. Cannemeijer, 1981: Measurements of drag coefficients and roughness length at a sea-beach interface. *J. Applied Meteor.*, 20(4), 335-340.

- Walters, C. D., 1975: Drag coefficient and roughness length determinations on an Alaskan arctic coast during summer. *Bound. Layer Meteor.*, 8, research note, 235-237.
- Wind, H. G. and C. B. Vreugdenhil, 1986: Rip-current generation near structures. *J. Fluid Mech.*, 171, 459-476.
- Wood, W. L. and G. A. Meadows, 1975: Unsteadiness in longshore currents. *Geophys. Res. Ltrs.*, 2(11), 503-505.
- Wright, L. D., P. Nielson, N. C. Shi, and J. H. List, 1986: Morphodynamics of a bar-trough surf zone. *Mar. Geol.*, 70, 251-285.
- Wu, C. S. and E. B. Thornton, 1986: Wave numbers of linear progressive waves. *J. Waterways, Port, Coastal and Ocean Engr.*, 112(4), 536-540.
- Wu, J., 1980: Wind stress coefficients over the sea surface during near-neutral conditions - a revisit. *J. Phys. Oceanogr.*, 10, 727-740.
- _____, 1982: Wind stress coefficients over sea surface from breeze to hurricane. *J. Geophys. Res.*, 87(C12), 9704-9706.
- Wyngaard, J. C. and O. R. Cote, 1971: The budgets of turbulent kinetic energy and temperature variance in the atmospheric surface layer. *J. Atmos. Sci.*, 28, 190-201.
- Young, H. D., 1962: *Statistical Treatment of Experimental Data*. McGraw-Hill, NY, 172 pp.

INITIAL DISTRIBUTION LIST

		No. Copies
1.	Defense Technical Information Center Cameron Station Alexandria, VA 22304-6145	2
2.	Library, Code 0142 Naval Postgraduate School Monterey, CA 93943-5002	2
3.	Chairman, Department of Oceanography Code 68Co Naval Postgraduate School Monterey, CA 93943-5000	1
4.	Chairman, Department of Meteorology Code 63Rd Naval Postgraduate School Monterey, CA 93940-5000	1
5.	Prof. E. B. Thornton Code 68Tm Department of Oceanography Naval Postgraduate School Monterey, CA 93943-5000	3
6.	Dr. C. S. Wu Code 68Wu Department of Oceanography Naval Postgraduate School Monterey, CA 93940-5000	2
7.	CDR D. J. Whitford, USN Fleet Numerical Oceanography Center Monterey, CA 93940	4
8.	Chairman, Oceanography Department U.S. Naval Academy Annapolis, MD 21402	1
9.	Commanding Officer Naval Environmental Prediction Research Facility Monterey, CA 93940	1
10.	Chief of Naval Research 800 N. Quincy Street Arlington, VA 22217	1

- | | | |
|-----|---|---|
| 11. | Commanding Officer
Naval Oceanographic Office
NSTL Station
Bay St. Louis, MS 39522 | 1 |
| 12. | Commander
Naval Oceanography Command
NSTL Station
Bay St. Louis, MS 39522 | 1 |
| 13. | Oceanographer of the Navy
Chief of Naval Operations (OP-006)
Washington, D.C. 20350 | 1 |
| 14. | Commanding Officer
Naval Ocean Research and Development Activity
NSTL Station
Bay St. Louis, MS 39522 | 1 |
| 15. | Director
U.S. Army Coastal Engineering Research Center
Kingman Building
Ft. Belvoir, VA 22060 | 1 |
| 16. | Library
Scripps Institution of Oceanography
P. O. Box 2367
La Jolla, CA 92037 | 1 |
| 17. | Library
Department of Oceanography
University of Washington
Seattle, WA 98105 | 1 |
| 18. | Mr. William A. Birkemeier
Field Research Facility
SR Box 271
Kitty Hawk, NC 27949 | 1 |
| 19. | Mr. H. Carl Miller
Field Research Facility
SR Box 271
Kitty Hawk, NC 27949 | 1 |
| 20. | Dr. S. SethuRaman
Dept. of Marine, Earth, and Atmospheric Sciences
North Carolina State University
Raleigh, NC 27695 | 1 |
| 21. | Commanding Officer
Fleet Numerical Oceanography Center
Monterey, CA 93940 | 1 |

- | | | |
|-----|--|---|
| 22. | National Sea Grant Program
NOAA
2001 Executive Blvd.
Rockville, MD 20852 | 1 |
| 23. | Physical Oceanography Program
National Science Foundation
1800 G Street, N.W.
Washington, D.C. 20550 | 1 |
| 24. | Library
Department of Physical Oceanography
Woods Hole Oceanographic Institution
Woods Hole, MA 02543 | 1 |
| 25. | Pacific Marine Environmental Laboratory
7600 Sand Point Way NE
Seattle, WA 98115-0070 | 1 |
| 26. | Commanding Officer
Naval Civil Engineering Laboratory
Port Hueneme, CA 93043
Attn: LOSB | 1 |
| 27. | Dr. J. Oltman-Shay
College of Oceanography
Oregon State University
Corvallis, OR 97331 | 1 |
| 28. | Prof. K. L. Davidson
Code 63Ds
Department of Meteorology
Naval Postgraduate School
Monterey, CA 93943-5000 | 1 |

Thesis
W5581 Whitford
c.1 Wind and wave forcing
of longshore currents
across a barred beach.

30 SEP 90
12 11 31

80246
25227

Thesis
W5581 Whitford
c.1 Wind and wave forcing
of longshore currents
across a barred beach.

UERMU



DUDLEY KNOX LIBRARY



3 2768 00034501 1